UNIVERSITY OF SOUTHAMPTON

FACULTY OF ENGINEERING, SCIENCE AND MATHEMATICS

Institute of Sound and Vibration Research

Mode Detection in Turbofan Inlets

by

Fabrice Castres

Thesis for the degree of Doctor of Philosophy

October 2006

In loving memory of

JAMADEEN CASTRES

2/11/2004 - 27/02/2005

UNIVERSITY OF SOUTHAMPTON

ABSTRACT

FACULTY OF ENGINEERING, SCIENCE AND MATHEMATICS

Doctor of Philosophy

by Fabrice Castres

An inverse technique for determining the mode amplitudes generated by turbofan inlets both for tonal and broadband noise is proposed using pressure measurements made in the near-field. The motivation of this research is to make use of the Turbulence Control Screen (TCS). This TCS offers a useful platform for locating microphones to implement a non-intrusive inverse technique since it is often fitted to aero-engines during ground testing to remove the integrated flow. The knowledge of such modal content is very useful for characterizing source mechanisms of broadband noise and for determining the most appropriate mode distribution model for duct liner predictions and for sound power measurements of the radiated sound field. The near-field sound pressure radiated from a duct is modelled by directivity patterns of cut-on modes. The resulting system of equations is ill-posed and it is shown that the conditioning of the inverse problem, which depends greatly on the positions of the microphones, is important in assessing the sensitivity of the modal solution to measurement noise and thus the modal reconstruction accuracy. An optimal array geometry for robust inversion is investigated. It is then shown that the presence of modes with eigenvalues close to a cut-off frequency results in a poorly conditioned directivity matrix. A physical interpretation of the Singular Value Decomposition (SVD) of the directivity matrix throws light on the understanding of the issues of ill conditioning as well as the detection performance of the radiated sound field by a given sensor array. The detection of broadband modes generated by a laboratory-scaled fan inlet is performed using the optimal array geometry. This experiment provides a milestone for detecting modal content of broadband noise produced by real fan inlet engines.

Contents

List of Figures

Nomenclature

$\mathbf{a}$	Vector of mode amplitudes
A	TCS surface area
a	Duct radius
a_{mn}	Mode amplitude
$\hat{\mathbf{a}}_{\mathbf{R}}$	Vector of mode amplitudes from Tikhonov regularisation
$\hat{\mathbf{a}}_{\mathbf{red}}$	Vector of mode amplitudes from the reduced inverse problem
$\hat{\mathbf{a}}_{\mathbf{T}}$	Vector of mode amplitudes from the singular value discarding problem
$\tilde{\mathbf{a}}$	Transformed mode amplitudes
$\tilde{\mathbf{a}}_{\mathbf{R}}$	Regularised transformed modes
$\hat{\mathbf{a}}_{\mathbf{0}}$	Least-squares estimate of mode amplitudes
C_p	Heat capacity at constant pressure
C_v	Heat capacity at constant volume
C_{xx}	Auto-correlation of a signal x
C_{xy}	Cross-correlation of a signal x with a signal y

c	Speed of sound
$\mathbf{D}$	Directivity matrix
$\mathbf{D}_{\mathbf{r}}$	Reduced directivity matrix
D_{mn}	Modal directivity factor
$\mathbf{D}^{+}$	Pseudo-inverse of $\mathbf{D}$
$\mathbf{e}$	Error vector in the inverted solution
$f\left(\gamma_i\right)$	Filter factors of generalised form Tikhonov regularisation
$f\left(\sigma_i\right)$	Filter factors of standard form Tikhonov regularisation
f_s	Sampling frequency
$H_i\left(\omega\right)$	Transfer functions between reference signal and microphones
J	Cost function
j'_{mn}	Modal eigenvalue
$\vec{k}$	Free-space wavenumber vector
K	Number of microphones on the TCS
k_z	Modal axial wavenumber
L	Number of cut-on modes accounted for the inversion
l_e	Element length
m	Modal spinning mode number (i.e. number of radial nodal lines)
$\mathbf{n}$	Vector of measurement noise or modelling errors
n	Radial mode number (i.e. number of polar nodal circles)

N_w	Window length
$\mathbf{p}$	Vector of TCS modelled pressures
p	Radiated acoustic pressure field
p_d	Acoustic pressure field inside the duct
$\tilde{\mathbf{p}}$	Transformed radiated pressures
Q	Number of cut-on modes removed Number of singular values discarded
(k_x, k_y, k_z)	Wavenumber Cartesian coordinates
(x, y, z)	Cartesian coordinatre system in the radiated field
(x_s, y_s, z_s)	Cartesian coordinate system inside the duct
$\mathbf{R}$	Tikhonov regularising matrix
$(\vec{e_x}, \vec{e_y}, \vec{e_z})$	Orthonormal Cartesian coordinate system
(r, θ, φ)	Spherical coordinate system in the radiated field
(r_s, θ_s, z_s)	Cylindrical coordinate system inside the duct
$\vec{r_s}$	Position vector inside the duct with origin at the centre of the duct exit
$\vec{r}$	Position vector in the radiated field with origin at the centre of the duct exit
$\hat{S}_{xx}(\omega)$	Smoothed auto-spectrum of a signal x
$\hat{S}_{xx}(\omega)$	Smoothed cross-spectrum of a signal x with a signal y
S_{xx}	Auto-power spectrum of a signal x
S_{xy}	Cross-power spectrum of a signal x with a signal y

$\hat{\mathbf{S}}_{\mathbf{ee}}$	Matrix of modal errors cross-spectra
$\hat{\mathbf{S}}_{\mathbf{nn}}$	Matrix of noise cross-spectra
$\hat{\mathbf{S}}_{\mathbf{p}\hat{\mathbf{p}}}$	Cross spectral matrix of measured pressures
$\mathbf{S}_{\mathbf{aa}}$	Cross spectral matrix of mode amplitudes
$\mathbf{S}_{\mathbf{pp}}$	Cross spectral matrix of modelled pressures
$\mathbf{u}$	Left singular vector of $\mathbf{D}$ (i.e. column vector of $\mathbf{U}$)
$\mathbf{u}$	Left singular vectors of $\mathbf{D}$ (i.e. column of $\mathbf{U}$)
$\tilde{U}_{mm}$	Hankel transform of order m of u_m
$\vec{U}$	Flow velocity field
u_m	m^{th} Fourier component of the radial surface velocity distribution
U_z	Fourier transform of the axial velocity distribution
u_z	Normal velocity distribution across the opening surface
$\mathbf{U}$	Matrix of left singular vectors of $\mathbf{D}$ Matrix of left generalised singular vectors of $(\mathbf{D},\mathbf{R})$
$\mathbf{V}$	Matrix of right singular vectors of $\mathbf{D}$
$\mathbf{v}$	Right singular vectors of $\mathbf{D}$ (i.e. column vector of $\mathbf{V}$)
$\tilde{W}_i$	Acoustic power of the i^{th} transformed modes
W	Total mean radiated acoustic power
$\tilde{\mathbf{W}}$	Fourier matrix
$\mathbf{X}$	Matrix of right generalised singular vectors of $(\mathbf{D},\mathbf{R})$

α_{mn}	Modal cut-on ratio
β	Tikhonov regularisation parameter
Δf	Frequency resolution
$\mathbf{D}^{\#}$	Regularised inverse of $\mathbf{D}$
$\bar{\eta}$	Modal error
ε	Reconstruction accuracy parameter
$\gamma_{\hat{a}_i\hat{a}_j}$	Modal Coherence Function
γ	Generalised singular values of $(\mathbf{D}, \mathbf{R})$
$\kappa(\mathbf{D})$	Condition number of $\mathbf{D}$
κ_R	Condition number of $\mathbf{D}$ for Tikhonov regularisation in general form
κ_r	The condition number of $\mathbf{D_r}$
κ_T	Condition number of the singular value discarding problem
κ_β	Condition number of $\mathbf{D}$ for Tikhonov regularisation in standard form
κ_{mn}	Modal radial wavenumber
λ	Acoustic wavelength
λ_i	i^{th} Eigenvalue of $\mathbf{D^H D}$
Λ_{mn}	Normalisation constant
μ_η	Mean value of the reconstruction accuracy over 2000 random arrays
μ_κ	Mean value of the condition number over 2000 random arrays
η_r	Reconstruction accuracy from the reduced inverse problem

η_T	Reconstruction accuracy of the singular value discarding problem
Ω	Shaft rotation frequency
ω	Angular frequency
Ψ_{mn}	Mode shape function
$\tilde{\psi}$	Transformed mode shape function
φ	Polar coordinate in the radiated field
ρ	Air density
$\mathbf{\Sigma}^{\#}$	Regularised inverse of $\mathbf{\Sigma}$
Σ	Diagonal matrix of singular values $\mathbf{D}$
σ_i	ith Singular value of $\mathbf{D}$
$\Sigma_{\mathbf{T}}$	Truncated matrix of singular values
σ_η	Standard deviation of the reconstruction accuracy over 2000 random arrays respectively
σ_κ	Standard deviation of the condition number over 2000 random arrays
θ	Azimuthal coordinate in the radiated field
ξ_z	Angle of the normal of the wave front with the duct axis
$\angle$	Phase of complex quantity
$E\left[\,\right]$	Expectation operator

Acknowlegements

Firstly, I would like to thank my supervisor Phillip Joseph for all his support and patience throughout this work. He was the initiator of this project which I turned into a PhD thesis thanks to his very competent guidance. I am very grateful to him as he has always provided me a very pleasant working atmosphere and always responded present when I ever needed his help to understand some important theoretical aspects of duct acoustics. Furthermore, he has provided me an immense amount of support when I had to experience the most painful moment of my life.

I would also like to thank Professor Jeremy Astley for providing me helpful comments and suggestions on this challenging topic and Doctor Rod Self for sharing his invaluable insight on mathematical challenges and derivations. Many special thanks to Sue Brindle and Maureen Mew for their availability, the help provided in sorting out administrative paperwork and more importantly the nice atmosphere they created at the ISVR. I also want to extend my appreciation to the entire staff in the ISVR. Finally, I would like to thank Rolls Royce, which through the UTC in Gas Turbine Noise has provided me the financial support and the equipment to undertake the experimental part of my work and has allowed me to present my work at the AIAA/CEAS Aeroacoustics Conference, the largest international conference in the acoustics applied to aircraft noise and wind turbines.

I would like to thank my colleagues at 15A University Crescent for creating a friendly

atmosphere, which helped me a lot to wake up every morning and go to work. Special thanks to my office mates, Chris Lowis for these endless discussions on duct acoustics and inverse techniques but who also made me discover and like country music, Chris Ham for always being happy and ready for some mathematical challenges and lately Phil McLoughlin for bringing his enjoyable mood in the office.

I am very grateful to my beloved wife for her immense patience and support. Her love and feedback helped me a lot to keep my head cool at some difficult moments. I would like to thank my sons Thelonious and Django for bringing so much happiness in my life. Finally, a very huge tribute to my special son Jamadeen who showed me what the word courage meant and whom I owed the completion of this thesis. Jamadeen, you will remain at the most precious place in my heart.

Chapter 1

Introduction

1.1 The need for modal analysis in engine ducts

The increasing interest in trying to control the sound emissions from aircraft has been motivated by an increase in air traffic and more stringent noise regulations imposed to reduce its impact on communities located near airports. The understanding and reduction of noise produced by commercial aircrafts at take-off and landing is a real engineering challenge. Research effort has been focused on individual noise sources on the engine such as the jet noise radiated from the exhaust nozzle and fan noise radiated from the by-pass and inlet ducts. The noise sources on a turbofan engine are shown in figure 1.1. The interest in this thesis is the measurement of the modal distribution of the noise produced by a turbofan engine and radiated from the inlet. The thesis is primarily concerned with broadband noise although the technique applies equally to tones.

The noise radiated from a turbofan inlet has been extensively measured by engine manufacturers. The noise produced by the fan may be categorised into two types:

1. **Tonal noise**: Characterised by a number of narrow band peaks in the power spectrum
2. **Broadband noise**: Characterised by a smooth continuous spectrum over a wide frequency band

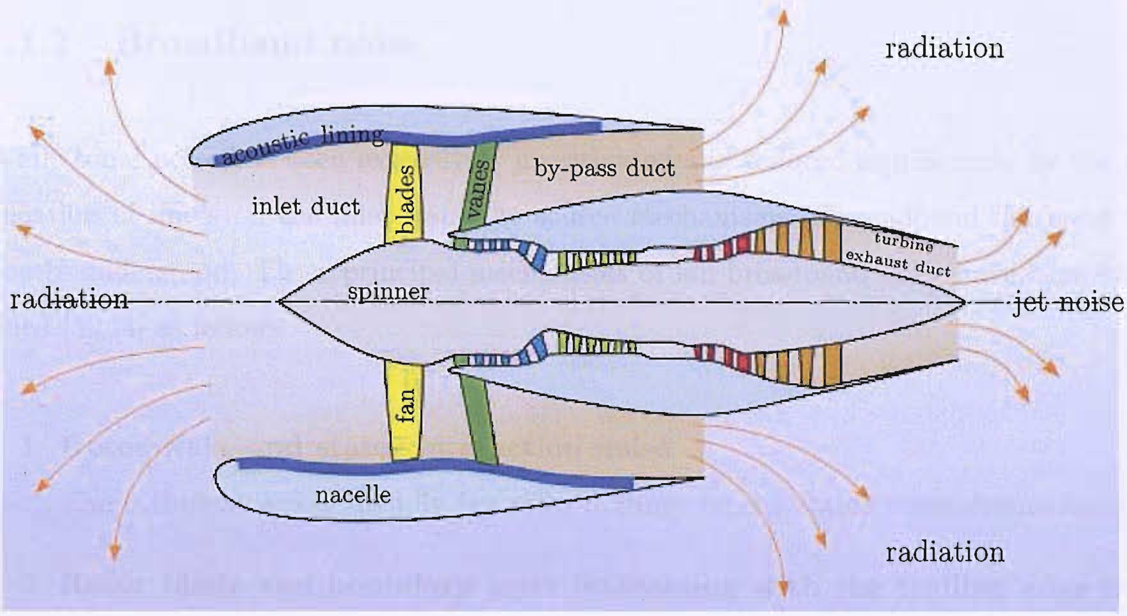

Figure 1.1: Sketch of high-bypass ratio turbofan engine [1]

1.1.1 Tonal noise

Fan tonal noise is a deterministic signal which is related to the shaft rotation frequency Ω. At subsonic tip speeds, it is generated by the interaction between the rotor wakes and stator vanes or struts [2]. The sound field propagates along the duct as a superposition of transverse mode shape patterns that rotate about the duct axis at their circumferential phase speed.

These tones occur at multiples s of the Blade Passage Frequency (BPF) and depend upon the number of rotor blades B and the number of stator vanes V. The modes generated at the s^{th} BPF have a characteristic spinning structure $\approx e^{j\omega t-jm\theta} = e^{jsB\Omega t-j(sB+qV)\theta}$ where θ is the polar coordinate inside the inlet and q is any integer value $[-\infty, \ldots, 0, 1, 2, \ldots, +\infty]$. At supersonic tip speeds, the tones occur at harmonics of the shaft rotation frequency and is called buzz-saw noise. Here, the modes are of the form $e^{js(\Omega t-\theta)}$.

1.1.2 Broadband noise

While tonal noise has been extensively investigated and reduced significantly by the application of liners on the inlet wall, the source mechanisms of broadband fan noise are poorly understood. Three principal mechanisms of fan broadband noise have been identified [3], [4] as follows:

1. **Rotor wake and stator interaction noise**
   The turbulent wakes shed by fan rotor impinge on the stator vanes downstream
2. **Rotor blade and boundary layer interacting with the trailing edge flow noise**
   Turbulence on the rotor blade boundary layer interacts with the blade trailing edge
3. **Inlet boundary layer turbulence-rotor tip interaction**
   The duct wall and hub boundary layer interacts with the tip of the fan blades

Knowledge of the modal content of the broadband noise generated by ducted fans is very useful in characterising these source mechanisms, for determining the most appropriate mode distribution model for duct liner predictions, and for sound power measurements of the radiated field. This thesis discusses one such technique. We first review previous attempts at deducing the mode amplitudes of the broadband noise field.

1.2 Literature review

The first experimental techniques to determine the modal distribution of the radiated sound field were first carried out at the tonal frequencies since these were once the dominant sources in the engine. In recent times, improved liners in the engine inlets and bypass sections, modern fan blade configurations and cut-off design of the fan rotor and its stator (to prevent propagating interaction modes) have become standard noise control solutions. As greater reductions in the levels of the tones were achieved, the broadband sound field has become more important. It is now regarded by some as the most important noise source in modern aero engines. However, it is only in the last 10 years that techniques concerning the detection of broadband modes radiated by a turbofan inlet have been addressed. This is perhaps because such techniques require the use of a large number of microphones resulting in a large number of simultaneous acquisition channels. These have only been available fairly recently. This section reviews the measurement techniques proposed in the literature in order to determine the modal content of noise propagating in a ducted fan. The challenge of mode detection is to implement a non-intrusive technique that does not disturb the sound field to be measured, which allows the determination of tonal, as well as broadband, mode amplitudes.

1.2.1 Rotating circular microphone array

Sutliff *et al* [5] has investigated the use of a rotating rake microphone array to measure the inlet and exhaust duct modes on a full-scale turbofan engine at the first three blade passing frequencies (i.e. $s = 1, 2, 3$). At the inlet, the rake is situated near the throat of the inlet duct and is rotated about the duct axis. The rotating rake rotates at speed $\bar{\Omega}$ that is at an exact fraction of the rotor speed (i.e. $\Omega = \tau\bar{\Omega}$). At the exhaust, the rake was located at the exit plane of the bypass duct, again rotating about the duct axis. The position of a microphone is given by $\theta = \bar{\Omega}t$ and the signal produced by a given spinning mode is therefore proportional to $e^{j(sB-m/\tau)\Omega t}$ and is thus shifted away from the s^{th} BPF. The degree of this Doppler shift depends on the spinning mode order and the angular speed of the rotating device [6]. The spectrum at the s^{th} BPF contains a cluster of closely spaced tones. The synchronisation of the rake speed with the rotor speed must be very precise to be able to resolve the Doppler shift of the measured pressures and relate them to the spinning mode amplitudes. Furthermore, since the microphones are mounted on the rotating rake, noise due to vortex shedding at the inlet and due to wake formation at the exhaust is produced. The measurements made using the rotating rake method thus intrudes inside, and therefore may affect, the sound field. The use of windscreens on all the microphones on the inlet and the exhaust side helps to reduce the effects of this extraneous noise source at the inlet and exhaust. Another feature associated with the rotating rake is the complexity involved in fitting the rake in the inlet and exhaust ducts. While mounting the rake on the exhaust is relatively easier, the mounting on the inlet side is more complicated, particularly when the inlet is enclosed by an Inlet Control Device (ICD). Note that there is no clear extension of this technique to broadband sound fields.

Sutliff *et al* conducted measurements on a full-scale TFE 731-60 turbofan engine to detect the duct modes using the rotating rake microphone array to obtain the modal spectrum for the first three fan harmonics in the inlet and in the exhaust. The mode amplitudes were deduced by fitting, in a least squares sense, the modelled pressures to the measured pressure data. The fan has 22 rotor blades and 52 stator vanes and a speed which ranges between 6000-10000 rpm.

1.2.2 Circular hoop microphone array

Thomas *et al* [7] has performed mode detection of the tonal noise radiated from a turbofan inlet with a microphone array on a circular hoop. The circular hoop, whose diameter is much larger than the fan diameter (about 6 times the fan diameter), is situated in

the far field and the microphones are placed along a radial line originating from the duct centre. In addition, the hoop was mounted on a rail with its axis coincident with that of the fan to move it axially to enable the sound field measurements at different axial positions. Most importantly, unlike the rotating rake method, the circular hoop method is totally non-intrusive. Far field azimuthal directivity patterns radiated from the inlet can be measured by simply rotating the hoop through a number of discrete angular distances. The measurements were acquired at the various azimuthal and polar positions in different sequences.
The authors first tried their modal analysis technique on a 30cm scale model of a turbofan engine with 16 rotor blades and 40 stator vanes, with a tip speed of 300 m/s. The acoustic field was measured at a constant fan rotation speed with a 16-microphone array uniformly located on the circular hoop. At one axial station, the hoop was rotated in increments of 0.5 degrees for a total of 46 azimuthal distances. The measurements were extended to 14 such axial stations.

The analysis carried out by Thomas *et al* [7] and extended by Farassat [8] consisted of applying Fourier analysis of the far field pressure in the azimuthal direction to deduce the spinning mode amplitudes. The radial modes within each spinning mode were deduced by inverting a system of linear equations relating the pressure measurements to the mode amplitudes. The conditioning of the matrix to be inverted was assessed and some regularisation guidelines were proposed to minimise the errors introduced by the poorly conditioned matrix. Their technique was demonstrated to reliably deduce azimuthal directivities and detect mode amplitude distribution at the tones. However this technique requires an extensive number of measurements that is roughly twice the total number of propagating modes to be inverted and is only feasible for tonal noise. It does not readily allow for the inversion of broadband mode amplitudes.

1.2.3 Far field microphone array

Lewy [9] has investigated the problem of deducing the modal amplitudes of the acoustic field generated by a ducted turbofan using far field pressure measurements. The basic idea was, at a given frequency, to calculate a far field directivity due to the propagating modes assuming unit mode amplitudes. The maximum computed Sound Pressure Level (SPL) for each mode is adjusted to the maximum measured SPL at the main radiation angle. This fit corresponds to minimising a parameter σ which is given in dB as follows:

$$10^{\sigma/10} = 10^{|\mathrm{SPL}_{calc} - \mathrm{SPL}_{meas}|/10}$$

This fit does not account for the phase differences between the computed and measured modal pressures. The method was verified with the use of data from the RESOUND tests made by Rolls Royce in its Antsy Noise Compressor Test Facility (ANCTF) [10]. The number of modes that radiate is greater than the number of measurements made during the tests. A limited number of modes are then selected according to *a priori* knowledge of the sources generated at the tones. Although spinning modes, which reliably fit the sound field measured during the tests, are determined this solution has the disadvantage that it requires an *a priori* knowledge about the mode distribution solution and therefore can only be applied to tonal noise. A corresponding lack of information about broadband noise suggests that it cannot be readily extended to this noise source.

In a private communication with the author, it was agreed that the modal solution is not unique using conventional directivity measurements and that mode detection is not improved if the conditioning of the inversion is not investigated. The author also agreed that a special array of microphones is the best way to solve the problem of non-uniqueness of the solution.

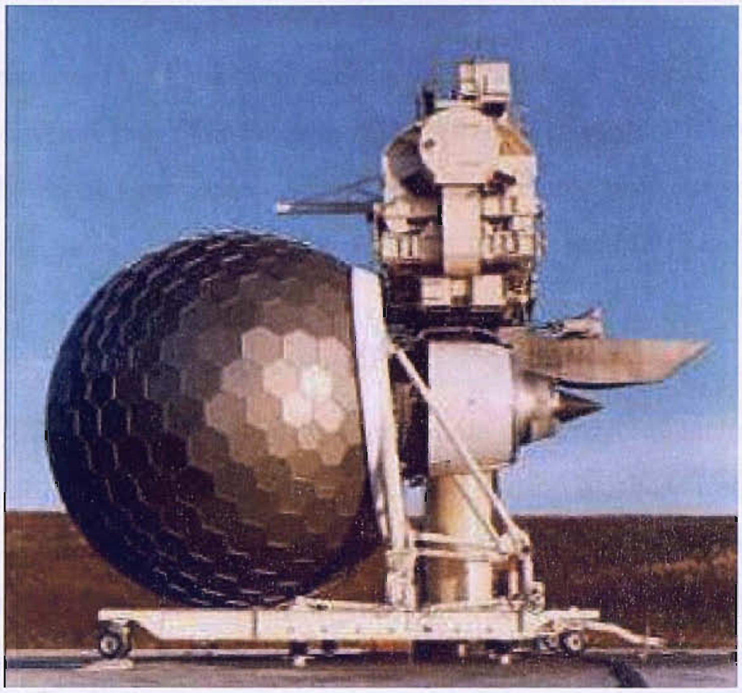

Figure 1.2: Rolls Royce Trent 800 outdoor static engine test using a Turbulence Control Screen

1.2.4 Turbulence Control Screen (TCS) microphone array

Another approach for determining the amplitude of modes radiated from a turbofan inlet is that proposed by Lan *et al* [11]. They adopted an innovative approach for mode detection that uses pressure measurements on the Turbulence Control Screen (TCS). They designed a microphone array distributed over the surface of the TCS. The TCS is an acoustically transparent surface used to remove the ground vortices and incoming turbulence at the inlet during ground testing on test bed, and is shown in figure 1.2. The TCS array has several advantages over other measurement techniques in that it is generally non-intrusive and easy to implement in full-scale engine tests. The microphone array can be permanently installed on a TCS to provide modal information for a variety of engines and inlet configurations. Lan *et al* distributed an array of 40 microphones over the TCS. The array configuration consisted of four rings of 10 non-uniformly spaced microphones in each ring. The measured pressure data $\mathbf{p}$ were related to the mode amplitudes $\mathbf{a}$

via a directivity matrix $\mathbf{D}$. Their approach was to ascertain, by computer simulation, microphone positions on the TCS for which the directivity matrix becomes orthogonal (i.e. $\mathbf{D}^{\mathbf{H}}\mathbf{D} = \mathbf{I}$). In effect, this allows each microphone to sense only one mode. The mode amplitudes are then determined from the pressure measurements $\mathbf{p}$ and the Hermitian transpose of $\mathbf{D}$, i.e.

$$\mathbf{a} = \mathbf{D}^{\mathbf{H}}\mathbf{p}$$

Lan *et al* applied this technique to the first two blade passing frequencies of a 16-bladed rotor combined with 30 stator vanes. Few modes are cut-on at these frequencies. Whilst the number of microphones required in this approach is larger than the number of modes to be inverted, the method has the significant disadvantage that these microphone positions are difficult to identify at any single frequency and probably impossible to obtain over a band of frequencies. The author has had the opportunity to discuss with Lan about his technique. It was agreed that such a microphone array, which leads to an orthogonal transfer matrix, is difficult obtain due to the complexity of the modal radiation patterns.

1.2.5 Microphone array wall-flush mounted

Another type of technique that has been investigated extensively consists of measuring the sound field propagating through the duct by the use of wall-flush mounted microphones. An arrangement of the microphones in a ring allows the circumferential dependence of the modal information to be determined. The use of additional rings of microphones enables the radial modes to be determined in each spinning mode.

Recently, based on the same principle, Enghardt *et al* [12] presented a new experimental technique using an in-duct microphone array to calculate the in-duct transmitted sound power for tones and broadband noise. The technique uses the modal distribution inverted from pressure measurements at the duct wall. The method requires cross-spectral measurements to be made between a number of microphones and a single reference microphone. The pressure cross-spectra inside the duct can be modelled in terms of the constituent modes via a transfer matrix which can be inverted to deduce the mean square mode amplitudes. An essential assumption made in the technique is that individual modes are mutually uncorrelated. Furthermore, the matrix established for modal inversion may be poorly conditioned and extraneous noise contaminating the measurements will be greatly amplified in the modal solution. Enghardt *et al* [12] regularised the solution by discarding small singular values but this is done at the expense of external errors introduced by discarding some of the information. The author has discussed with Enghardt about his technique and found out that the system of equations considered is not positive definite such that negative mean square mode amplitudes can be obtained. It was concluded that the implementation of an iterative least-squares solver is required to give positive mean square mode amplitudes. The technique was applied to a single-stage compressor comprising a 24 bladed fan and 17 stator vanes. An azimuthally traversable duct section is attached downstream of the rotor. The mode detection is performed using 8 microphones installed in the moving duct section and traversed over 36 azimuthal positions. A fixed wall-flush mounted microphone was used as a reference sensor. The sound power deduced from the modal analysis was compared with that obtained from the ISO 5136 standard. The estimate obtained from the mode detection method was found to over-predict the SWL by 2dB. However, this discrepancy could be due to inaccuracies in the ISO standard as from the mode detection technique.

The mode detection techniques discussed above may be summarised in table 1.1. This table suggests that there is no single technique that allows the robust inversion of broadband mode amplitudes.

Technique	Tones	Broadband	Intrusive	Robustness
Rotating circular array [5]	√	×	√	×
Circular hoop array [7]	√	×	×	√
Far field array [9]	√	×	×	×
TCS array [11]	√	×	×	×
Wall-flush mounted induct array [12]	×	√	√	×

Table 1.1: Summary of the mode detection technique

1.3 Aims, objectives and original contribution of the thesis

The previous section has highlighted the lack of a robust technique for the inversion of the mode amplitudes in a turbofan inlet sound field. The aim of this thesis is to investigate the use of inverse techniques to determine broadband mode amplitudes in a duct from measurements of the near field radiated sound pressure. The motivation of this research is to make use of a TCS, as suggested by Lan *et al* of Boeing to mount microphones for near field pressure measurements (as shown in figure 1.2). The great advantage of using the TCS to position the sensors is that it offers a platform from which all modes can be deduced simultaneously, unlike the other mode detection techniques discussed in section 1.2. Although a TCS is used, in both the technique proposed by Lan *et al* and the inversion technique described in this thesis, they are fundamentally different.

In this thesis, emphasis is placed on the conditions on the sensor distribution necessary for a robust and accurate inversion. The detection performance of a given sensor array is investigated and the design of a microphone array which satisfies best these requirements is specified. Unlike Farassat [13], who used a far field prediction model for the acoustic pressure radiated by the inlet, a forward model must be computed to account for the near field radiation since the TCS employed by engine manufacturers has a diameter of 3m and is therefore likely to be in the near field at most of the frequency range of interest.

The original contributions of this thesis are as follows:

- A microphone arrangement on the TCS that allows minimal sensitivity of the modal solution to noise during measurements is investigated. Some guidelines on the design of a sensor array which offers a good coupling with the radiated sound field are given.
- The frequency-dependent behaviour of the inversion robustness and accuracy of a given microphone array is presented. It is shown that inverting the mode amplitudes close to the cut-on frequencies is fundamentally very different.
- The detection performance of the microphone array in reconstructing mode amplitudes is analysed and the effect of the measurement noise upon the inverted mode amplitudes is investigated.
- Regularisation methods for improving the inversion accuracy at frequencies close to the modal cut-on frequencies are investigated and some guidelines for choosing optimal regularisation parameters are given.
- Tonal and broadband mode amplitudes are determined in an experimental rig and compared with the results from an in-duct mode detection technique.
- The level of coherence between different mode amplitudes is presented for the first time.
- Alternative methods based on Fourier analysis which aim at determining the mode amplitudes from the reconstructed velocity distribution are presented.

1.4 Outline of thesis contents

Chapter 2 describes the theoretical background of sound propagation and derives the model for sound radiation from a semi infinite, hard-walled, baffled ducts based on the 1^{st} Rayleigh integral. The numerical integration is performed to compute near field directivity functions, which are then compared with the directivity functions computed from the well-known far field approximation.

Chapter 3 investigates the least-squares inversion of mode amplitudes for both tonal and broadband radiation. This inverse technique requires a number of microphones greater than the number of modes that can radiate but makes no *a priori* assumption about the solution. The importance of the inversion conditioning is defined and discussed in order to assess the robustness and accuracy of the technique. Numerical simulations are performed to investigate the influence of sensor positioning on the robustness and accuracy of the modal inversion.

Chapter 4 presents an analysis of the ill-conditioning at frequencies close to the modal cut-on frequencies. The analysis of radiation problems using the SVD have been extensively investigated [14–19] by expressing the radiated pressure in terms of the velocity distribution on the source plane and a Green function matrix. In this thesis, the radiation problem studied consists of expressing the radiated pressure in terms of the mode amplitudes over the duct exit cross-section and the modal directivity matrix. A physical interpretation the Singular Value Decomposition of the modal directivity matrix is therefore presented to throw light on the understanding of the issues of ill-conditioning as well as the detection performance of the radiated sound field by a given sensor array.

Chapter 5 discusses different methods of improving inversion robustness by means of regularisation. Some guidelines are given on the choice of various regularisation parameters for reducing overall levels of errors.

Chapter 6 presents the details of a Finite Element/Infinite Element model of sound radiation from a fan inlet, which accounts for the sound radiation from more complex duct geometries such as the fan inlet used for the experimental measurements described in chapter 7. The effects of the flange and lip on modal sound radiation are discussed.

Chapter 7 describes the experimental set-up and procedure undertaken during the lab-scale experiments aimed at validating the theory and principles of the inverse techniques. The experiment involves TCS measurements of the pressure radiated from a 9-bladed fan under nearly free field conditions using 110 microphones.

Chapter 8 presents the results deduced from the experiments such as the power radiated from the inlet. The mean square broadband mode amplitudes detected by the TCS arrays are compared with those deduced from an induct wall-flush mounted microphone array. The modal coherence function between the broadband mode amplitudes is presented.

Finally, chapter 9 introduces a different approach to inverting the mode amplitudes based on Fourier analysis of the radiated sound field.

Chapter 2

Acoustic field radiated from a baffled duct

The study of the wave equation in infinite ducts of circular shapes based from the Kirchhoff approximation theory is very useful to engine designers both quantitatively and qualitatively. This theory has been used in many basic papers [2], [20] and [21] and enables to understand many useful results in duct propagation if one wishes to explain some aspects of engine noise. This section introduces the theoretical background to sound propagation and radiation from a semi-infinite, hard-walled duct. It first presents the modal theory of propagation within a circular duct. Modal behaviour for a hard-walled duct is discussed. The sound field radiated from the duct is then studied in detail. Well-known results in duct acoustics are then derived and described such as the mode cut-off concept, the angle of the radiation lobe at peak directivity.

2.1 Sound-field within a circular duct

The sound pressure wave that propagates in a fluid with no external sources must satisfy the wave equation at any position $\vec{r_s}$ within the duct:

$$\left(\nabla^2 - \frac{1}{c^2}\frac{D^2}{Dt^2}\right) p_d\left(\vec{r_s}, t\right) = 0 \tag{2.1.1}$$

where the operator

$$\frac{D}{Dt} \equiv \vec{U} \cdot \vec{\nabla} + \frac{\partial}{\partial t} \tag{2.1.2}$$

is the material derivative operator and $\vec{U}$ is the velocity field of the flow within the duct and c is the speed of sound in the fluid.

The sound field that propagates along the duct can be decomposed into modes, the properties of which depend on the geometry of the duct (constant or varying cross-section), the nature of the wall (hard-walled or lined ducts), and on presence or not of flow. The form of these modes is now discussed.

If no flow is present within the duct, the wave equation 2.1.1 reduces to

$$\left(\nabla^2 - \frac{1}{c^2}\frac{\partial^2}{\partial t^2}\right) p_d(\vec{r_s}, t) = 0 \tag{2.1.3}$$

If the sound waves are assumed to be harmonic, i.e. $p_d(\vec{r_s}, t) = p_d(\vec{r_s})e^{j\omega t}$, the complex pressure $p_d(\vec{r_s})$ satisfies the Helmholtz equation

$$(\nabla^2 + k^2)p_d(\vec{r_s}) = 0 \tag{2.1.4}$$

where k is the free space wavenumber.

The position $\vec{r_s}$ of equation 2.1.4 is expressed in the cylindrical coordinate system (r_s, θ_s, z_s), representing respectively the radial, polar and axial directions. In order to solve equation 2.1.4 for a cylindrical duct the method of separation of variables is used. The pressure is written in the form

$$p_d(r_s, \theta_s, z_s) = R(r_s)\Theta(\theta_s)Z(z_s) \tag{2.1.5}$$

Thus equation (2.1.4) becomes

$$\left(\frac{\partial^2}{\partial r_s^2}+\frac{1}{r_s}\frac{\partial}{\partial r_s}+\frac{1}{r_s^2}\frac{\partial^2}{\partial \theta_s^2}+\frac{\partial^2}{\partial z_s^2}\right)R(r_s)\Theta(\theta_s)Z(z_s)=-k^2R(r_s)\Theta(\theta_s)Z(z_s) \tag{2.1.6}$$

$$\frac{R''(r_s)}{R(r_s)}+\frac{1}{r_s}\frac{R'(r_s)}{R(r_s)}+\frac{1}{r_s^2}\frac{\Theta''(\theta_s)}{\Theta(\theta_s)}+\frac{Z''(z_s)}{Z(z_s)}=-k^2 \tag{2.1.7}$$

where the primes and the double primes are used to denote the first and second derivatives with respect to their dependent variables.

First, the only term in equation 2.1.7, which depends on z_s is $\frac{Z''(z_s)}{Z(z_s)}$ must therefore be constant to satisfy equation 2.1.7. Thus

$$\frac{Z''(z_s)}{Z(z_s)}=-k_z^2 \tag{2.1.8}$$

The solution to equation 2.1.8 is

$$Z\left(z_s\right)=e^{\pm jk_zz_s} \tag{2.1.9}$$

Equation 2.1.7 is

$$r_s^2\frac{R''(r_s)}{R(r_s)}+r_s\frac{R'(r_s)}{R(r_s)}+\frac{\Theta''(\theta_s)}{\Theta(\theta_s)}=r_s^2(k_z^2-k^2) \tag{2.1.10}$$

Again $\frac{\Theta''(\theta_s)}{\Theta(\theta_s)}$ is the only term in equation 2.1.10 which depends on θ_s and must therefore be constant to satisfy equation 2.1.10,

$$\frac{\Theta''(\theta_s)}{\Theta(\theta_s)}=-m^2 \tag{2.1.11}$$

The solutions to equation 2.1.11 are of the form

$$\Theta\left(\theta_s\right)=e^{\pm jm\theta_s} \tag{2.1.12}$$

From equation 2.1.11, m must take integer values due to the periodicity of the sound field in the θ_s-direction. The radial solution may be found by multiplying equation 2.1.10 by $R(r_s)/r_s^2$ to give

$$R''(r_s)+\frac{1}{r_s}R'(r_s)+(\kappa_{mn}^2-\frac{m^2}{r_s^2})R(r_s)=0 \tag{2.1.13}$$

where $\kappa_{mn} = \sqrt{k^2 - k_z^2}$ is the modal radial wavenumber and is chosen to satisfy equation 2.1.14. Equation 2.1.13 is the Bessel's equation, whose solution satisfies following the hard-walled boundary condition

$$\left.\frac{\partial R(r_s)}{\partial r}\right|_{r_s=a} = 0 \tag{2.1.14}$$

This is written as follows

$$R(r_s) = J_m(\kappa_{mn} r_s) \tag{2.1.15}$$

$J_m(\kappa_{mn} r_s)$ is the Bessel function of the first kind and order m. The general solution to equation 2.1.4 is written as a combination of modes, each of which possesses a particular spatial pattern described by the mode shape function $\Psi_{mn}(r_s, \theta_s)$ as shown in figure 2.1. This solution is written as follows

$$p_d(r_s, \theta_s, z_s) = \sum_{m=-\infty}^{+\infty} \sum_{n=1}^{+\infty} a_{mn} \Psi_{mn}(r_s, \theta_s) e^{-jk\sqrt{1-\alpha_{mn}^2} z_s} \tag{2.1.16}$$

The term α_{mn} in equation 2.1.16, of fundamental importance in this thesis is the cut-on ratio defined as

$$\alpha_{mn} = \frac{\kappa_{mn}}{k} \tag{2.1.17}$$

The propagation characteristics of the modes are determined by the axial wavenumber k_z, which from equation 2.1.17 can be written as

$$k_z = k\sqrt{1 - \alpha_{mn}^2} \tag{2.1.18}$$

Two separate situations can thus be deduced

- $\alpha_{mn} \leq 1$, (i.e. $\kappa_{mn} \leq k$), the axial wavenumber is real $k_z = k\sqrt{1 - \alpha_{mn}^2}$
  Here the mode propagates along the duct without attenuation and energy is transported to the far-field. The mode is said to be cut-on

- $\alpha_{mn} > 1$, (i.e. $\kappa_{mn} \geq k$), the axial wavenumber is purely imaginary $k_z = -jk\sqrt{\alpha_{mn}^2 - 1}$
  The mode decays exponentially along the duct and no energy is transported to the far-field. The mode is said to be evanescent and decays exponentially.

At any given frequency, therefore, there will be a finite number of propagating modes. The duct can be regarded as low-pass filter that only allows modes whose natural frequency is below the driving frequency to propagate. In this study only cut-on modes will be considered.

The mode shape function $\Psi_{mn}(r_s, \theta_s)$ in equation 2.1.16 is orthonormal over the duct cross-section and satisfies the following condition

$$\int\int_S \Psi_{mn}(r_s, \theta_s)\, \Psi^*_{pq}(r_s, \theta_s)\, dS = \begin{cases} 0 & m, n \neq p, q \\ S & m, n = p, q \end{cases} \tag{2.1.19}$$

Using the orthogonality property of Bessel functions, it may be shown [22] that

$$\Psi_{mn}(r_s, \theta_s) = \frac{1}{\sqrt{\Lambda_{mn}}} J_m(\kappa_{mn} r_s) e^{-jm\theta_s} \tag{2.1.20}$$

where the mean square amplitude of the cross-duct mode is

$$\Lambda_{mn} = \left(1 - \frac{m^2}{(\kappa_{mn} a)^2}\right) J^2_m(\kappa_{mn} a) \tag{2.1.21}$$

The integer m denotes the spinning mode number and determines the number of radial lines while the second integer n denotes the radial mode number and determines the number of nodal lines. The term a_{mn} is the complex modal amplitude for each (m, n) mode pattern that is determined by the source distribution. The radial wavenumber κ_{mn} is determined by the hard-walled duct boundary conditions stated in equations 2.1.14, which implies that the radial component of the fluid particle velocity at the duct wall (i.e. $r_s = a$) must vanish. This leads to values of κ_{mn} given by

$$\kappa_{mn} = \frac{j'_{mn}}{a} \tag{2.1.22}$$

where j'_{mn} denotes the n^{th} stationary value of the Bessel function of the first kind and order m and is called the modal eigenvalue. Figure 2.1 shows the real part of different mode patterns that are retained as the wave travels along the duct. It should also be noted that $n = 1$ is the minimum allowed value of n, such that the plane mode is the mode (0,1).

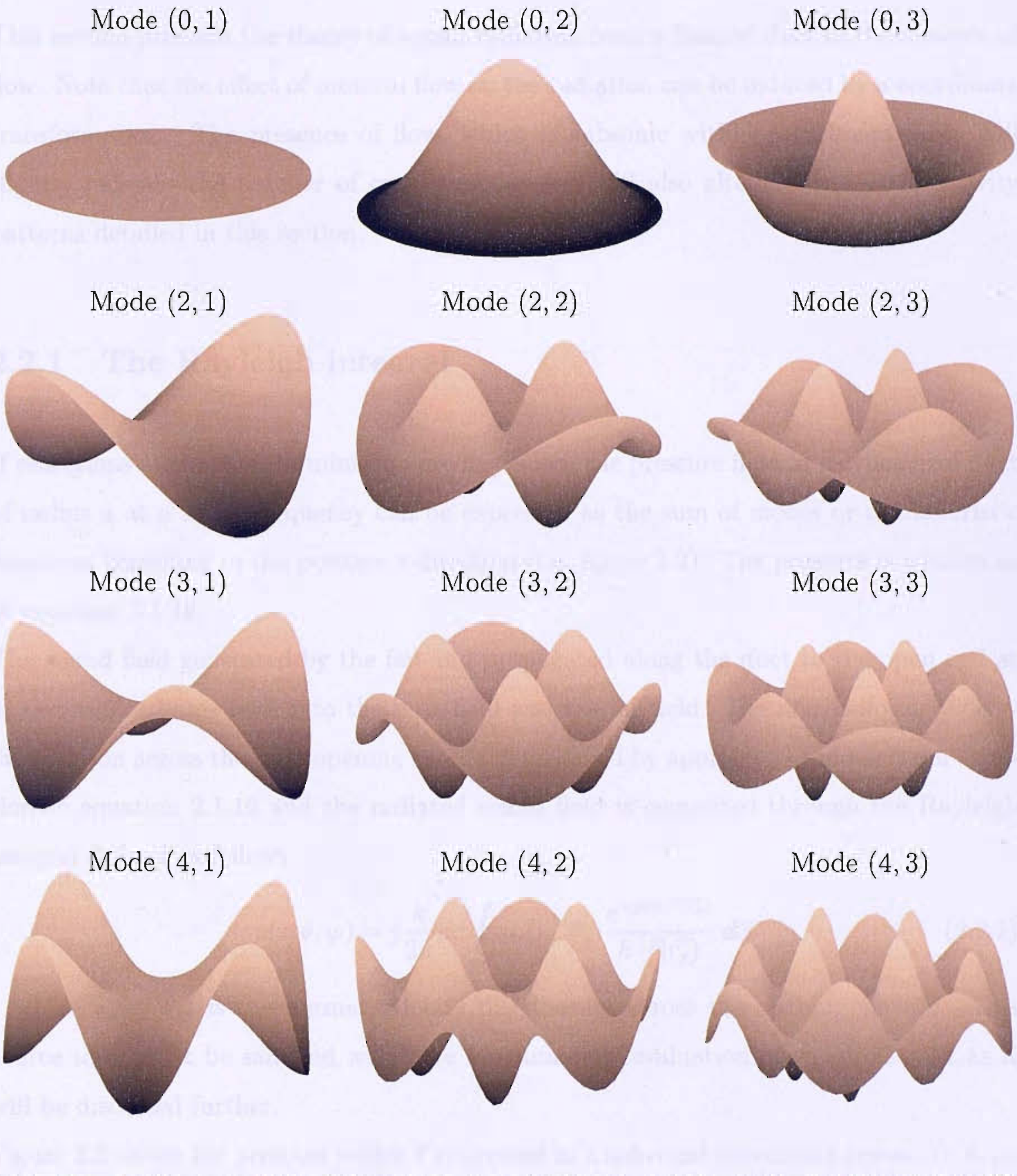

Mode (0, 1) Mode (0, 2) Mode (0, 3)

Mode (2, 1) Mode (2, 2) Mode (2, 3)

Mode (3, 1) Mode (3, 2) Mode (3, 3)

Mode (4, 1) Mode (4, 2) Mode (4, 3)

Figure 2.1: Isometric view of the real part of different mode shape functions travelling along a duct

2.2 Sound field radiated from a duct

This section presents the theory of sound radiation from a flanged duct in the absence of flow. Note that the effect of uniform flow on the radiation can be induced by a coordinate transformation. The presence of flow, which is subsonic within a turbofan inlet, will slightly increase the number of cut-on modes and will also alter the modal directivity patterns detailed in this section.

2.2.1 The Rayleigh integral

If reflections at the duct termination are neglected, the pressure field in a cylindrical duct of radius a at a single frequency can be expressed as the sum of modes or characteristic functions travelling in the positive z-direction (i.e. figure 2.2). The pressure is written as in equation 2.1.16.

The sound field generated by the fan and propagated along the duct to the open end at $z_s = z = 0$ radiates both into the near field and the far field. The non-uniform velocity distribution across the duct opening can be determined by applying the momentum equation to equation 2.1.16 and the radiated sound field is computed through the Rayleigh integral defined as follows

$$p(r,\theta,\varphi) = j\frac{k}{2\pi}\rho c \int_S u_z(r_s,\theta_s)\frac{e^{-jkh(\vec{r}|\vec{r_s})}}{h\left(\vec{r}|\vec{r_s}\right)}\, dS \tag{2.2.1}$$

where $u_z(r_s,\theta_s)$ is the normal velocity distribution across the opening surface. This source term must be sampled with care for numerical evaluation of equation 2.2.1 as it will be discussed further.

Figure 2.2 shows the position vector $\vec{r}$ expressed in a spherical coordinate system (r,θ,φ) with origin the centre of the duct opening and representing respectively the radial, azimuthal and polar directions. The vector $\vec{h}$ represents points in the radiated sound field from an elemental volume source located at a position $\vec{r_s}$ from the duct opening centre.

Namely,

$$\vec{r} = r\sin\varphi\cos\theta\vec{e_x} + r\sin\varphi\sin\theta\vec{e_y} + r\cos\varphi\vec{e_z} \tag{2.2.2}$$

$$\vec{r_s} = r_s\cos\theta_s\vec{e_x} + r_s\sin\theta_s\vec{e_y} \tag{2.2.3}$$

$$\vec{h} = \vec{r} - \vec{r_s}$$

$$\vec{h} = (r\sin\varphi\cos\theta - r_s\cos\theta_s)\vec{e_x} + (r\sin\varphi\sin\theta - r_s\sin\theta_s)\vec{e_y} + r\cos\varphi\vec{e_z} \tag{2.2.4}$$

Thus an expression for the distance of the point in the radiated sound field from each

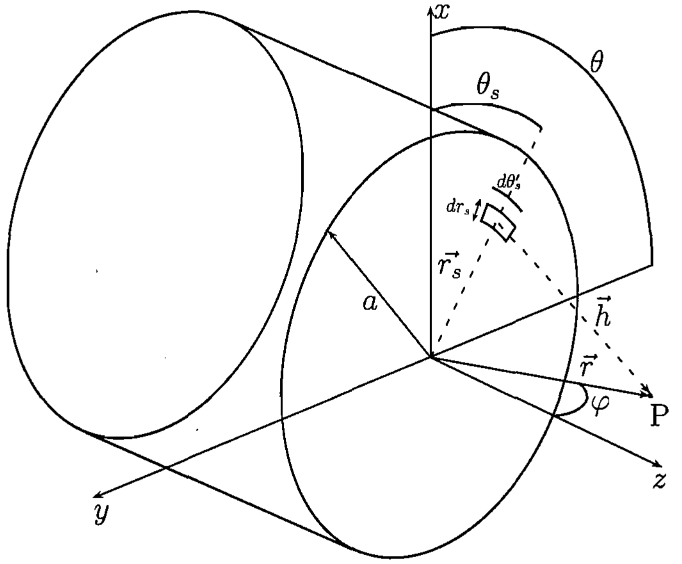

Figure 2.2: Cylindrical coordinate system for duct propagation analysis and spherical coordinate system for radiation analysis

volume source can be found by writing the magnitude of the vector defined in equation 2.2.4.

$$\begin{aligned} h^2 &= \vec{h}\cdot\vec{h} \\ &= r_s^2 + r^2 - 2rr_s\sin\varphi\cos(\theta_s - \theta) \end{aligned} \tag{2.2.5}$$

so that the distance between each individual source element and each radiated point $h(r_s, \theta_s | r, \varphi, \theta)$ is given by

$$h = r\left(1 + \left(\frac{r_s}{r}\right)^2 - 2\frac{r_s}{r}\sin\varphi\cos(\theta_s - \theta)\right)^{1/2} \tag{2.2.6}$$

Equation 2.2.1 assumes that the reflection from the duct opening is negligible that is a reasonable approximation for most modes considered in this study except those near cutoff. The fluid particle velocity normal to the duct opening u_z is defined as

$$u_z = \frac{j}{\omega\rho}\frac{\partial p}{\partial z}\bigg|_{z=0} \tag{2.2.7}$$

This can be found by introducing equation 2.1.16 into equation 2.2.7

$$u_z(r_s, \theta_s) = \sum_{m=-\infty}^{+\infty}\sum_{n=1}^{+\infty}\frac{k_z}{\omega\rho}a_{mn}\Psi_{mn}(r_s, \theta_s) \tag{2.2.8}$$

The radiated pressure may be written as a basis of modal directivity factors D_{mn} weighted by their modal amplitudes

$$p(r, \theta, \varphi) = \sum_{m=-\infty}^{+\infty}\sum_{n=1}^{+\infty}a_{mn}D_{mn}(r, \theta, \varphi) \tag{2.2.9}$$

Introducing equation 2.2.8 into equation 2.2.1, the total radiated pressure is written as

$$p(r, \theta, \varphi) = j\frac{k}{2\pi}\sum_{m=-\infty}^{+\infty}\sum_{n=1}^{+\infty}\sqrt{1 - \alpha_{mn}^2}\,a_{mn}\int_S \Psi_{mn}(r_s, \theta_s)\frac{e^{-jkh}}{h}r_s dr_s d\theta_s \tag{2.2.10}$$

Therefore, the modal directivity factor D_{mn} is given by

$$D_{mn}(r, \theta, \varphi) = j\frac{k_0}{2\pi}\sqrt{1 - \alpha_{mn}^2}\int_S \Psi_{mn}(r_s, \theta_s)\frac{e^{-jkh}}{h}r_s dr_s d\theta_s \tag{2.2.11}$$

The integral term of equation 2.2.11 can be numerically evaluated using the Newton-Cotes formula as follows

$$\begin{aligned}&\int_0^a\int_0^{2\pi}\Psi_{mn}(r_s, \theta_s)\frac{e^{-jkh(r_s,\theta_s)}}{h(r_s, \theta_s)}r_s dr_s d\theta_s = \\ &\qquad \frac{a}{N_r}\frac{2\pi}{N_\theta}\sum_{n_r=1}^{N_r}\sum_{n_\theta=1}^{N_\theta}\Psi_{mn}(r_{n_r}, \theta_{n_\theta})\frac{e^{-jkh(r_{n_r},\theta_{n_\theta})}}{h(r_{n_r}, \theta_{n_\theta})}r_{n_r}w_{r_{n_r}}w_{\theta_{n_\theta}}\end{aligned} \tag{2.2.12}$$

where $w_{r_{n_r}}$ and $w_{\theta_{n_\theta}}$ are weighting coefficients that correspond to the order of numerical integration and, N_r and N_θ are the number of points to perform the integration for r_s and θ_s respectively. For example, the 2-point closed extended rule also known as the extended trapezoidal rule or Romberg integration uses the following weighting coefficients

$$w = [1/2\ 1\ 1\ ...\ 1\ 1\ 1/2] \tag{2.2.13}$$

A number of 100 points in each direction is used to sample the source plane with this order of integration.

2.2.2 Far field approximation

This section discusses the sound radiation properties in the far field and compares them with that of the near field. As detailed in section 2.2.1, the Rayleigh integral which accounts for the duct outlet as a source plane to radiate sound, may be computed numerically and provides a solution for the near field. However using a second order approximation, it also provides an analytic solution for the far field which allows an insight into some important properties of mode radiation. Furthermore, this solution will also be important in mode detection since it will help uncover the nature of the instability of the inverse problem. Finally, the far field approximation allows a Fourier relationship between source distribution across the duct opening and the radiated field, namely the Rayleigh integral defined in equation 2.2.1, to be expressed as a spatial Fourier transform or more particularly a Hankel transform.

A far-field second-order approximation ($r \gg r_s$) can be found from equation 2.2.6 and neglecting terms of order 2

$$h = r\left(1 - 2\frac{r_s}{r}\sin\varphi\cos(\theta_s - \theta)\right)^{1/2} \tag{2.2.14}$$

If one uses the expansion series

$$(1-x)^{1/2} = 1 - \frac{1}{2}x - \frac{1}{8}x^2 - ... \tag{2.2.15}$$

and eliminates the higher-order terms, the distance h can be expressed as

$$h \approx r - r_s \sin\varphi \cos(\theta_s - \theta) + O\left(\frac{r_s}{r}\right)^2 \tag{2.2.16}$$

Equation 2.2.16 can then be introduced into equation 2.2.11 and an analytic solution for the modal directivity factor in the far-field may be derived as in appendix A. The result is given as follows

- $\alpha_{mn}^2 \neq \sin^2\varphi$

$$D_{mn}(r,\theta,\varphi) = j^{m+1}\frac{\sqrt{1-\alpha_{mn}^2}}{\sqrt{\Lambda_{mn}}}\frac{e^{-jkr}}{r}e^{-jm\theta}\frac{a\sin\varphi}{\alpha_{mn}^2-\sin^2\varphi}J_m(\kappa_{mn}a)J'_m(ka\sin\varphi) \tag{2.2.17}$$

- $\alpha_{mn}^2 = \sin^2\varphi$

$$D_{mn}(r,\theta,\varphi) = j^{m+1}\frac{k\sqrt{1-\alpha_{mn}^2}}{\sqrt{\Lambda_{mn}}}\frac{e^{-jkr}}{r}e^{-jm\theta}\frac{a^2}{2}$$
$$\left[J_m^2(\kappa_{mn}a) - \frac{2m}{\kappa_{mn}a}J_m(\kappa_{mn}a)J_{m+1}(\kappa_{mn}a) + J_{m+1}^2(\kappa_{mn}a)\right] \tag{2.2.18}$$

Here, $J'_m(x)$ is the the first derivative of the Bessel function of the first kind with respect to its argument given in [23].

Equations 2.2.17 and 2.2.18 for the far field modal radiation enlightens some important characteristics of single mode radiation which are also likely to be present in the near field.

- The polar angle of the main radiation lobe is $\varphi_{peak} = \sin^{-1}\alpha_{mn}$.
- Modal radiation becomes progressively weaker as $\alpha_{mn} \mapsto 1$ and tending to vanish exactly at cutoff.
- Polar angles of the radiation nulls are located at $\varphi_{null} = \sin^{-1}\alpha_{mi}$ with $i \neq n$.

- Polar angles of side lobes occur roughly mid-way between the angles of the radiation nulls and increase roughly as the frequency squared.

- Only the axisymmetric modes (i.e. $m = 0$) have non-zero radiated pressure in the duct axis (i.e. $\varphi = 0$) and the plane wave mode is the only mode have its main radiation lobe along the duct axis.

The solutions of equations 2.2.12 and 2.2.13, valid for the near field, are now compared with the far-field analytical solutions of equations 2.2.17 and 2.2.18. Figures 2.3 shows

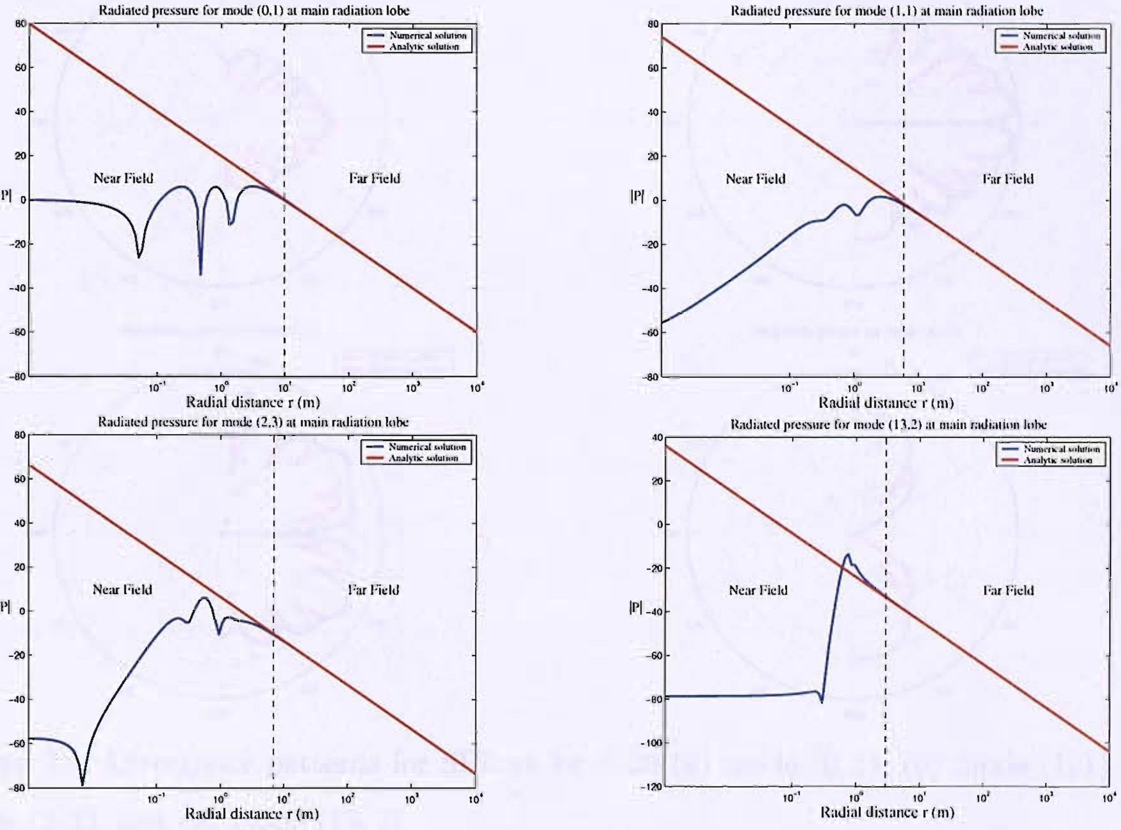

Figure 2.3: Modulus of the radiated pressure at main radiation lobe with radial distance from duct outlet at $ka = 20$ (a) mode $(0,1)$, (b) mode $(1,1)$, (c) mode $(2,3)$, and (d) mode $(13,2)$

the absolute part of the radiated pressure in dB for both the analytic and numerical solutions for the four modes on their respective main radiation lobes at $ka = 20$ plotted versus the radial distance on a logarithmic scale. The same comparison at $ka = 30$ is shown in appendix A. First it is posssible to note that as expected the analytic solution decreases with increasing distance in a $1/r$ fashion. The numerical solution converges to the analytic at a distance that slightly increases with frequency. This distance for which both solutions converge indicates the far field for a particular mode and at a particular frequency, and also indicates that the TCS radius is more than likely to be in the near field for all cut-on modes at frequencies of interest (i.e. $15 < ka < 30$). As the aim of this research is to perform the acoustic inversion for mode decomposition and source characterisation of the sound field within the inlet by use of microphones on the TCS, the analytic solution is therefore not valid. The numerical integration is then appropriate to model the sound pressure if the pressure field is to be measured at the TCS. Figures 2.4 shows the directivity patterns of the four modes above for the Sound Pressure Level (SPL)

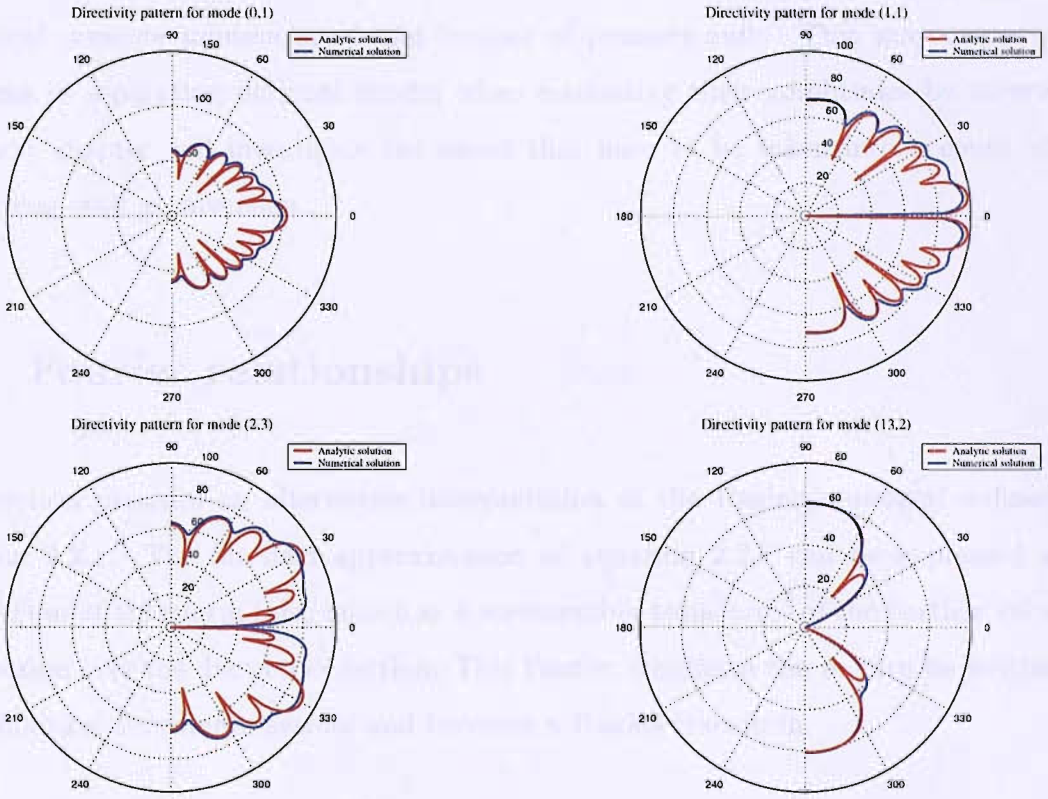

Figure 2.4: Directivity patterns for SPL at $ka = 20$ (a) mode $(0, 1)$, (b) mode $(1, 1)$, (c) mode $(2, 3)$, and (d) mode $(13, 2)$

in dB, at $ka = 19.9$. The directivity patterns of the same four modes modes at $ka = 30$ is shown in appendix A. It is first possible to note that the modal radiation properties discussed above for the analytic solution are encountered on these figures; that all non asymmetric modes have zero SPL on the duct axis (i.e. $\varphi = 0$), and that as frequency increases and modes are becoming increasingly cut-on the principal lobe of radiation shifts towards the axis and the number of side lobes increases. Figure 2.4 also shows that the near-field solution satisfies these modal radiation properties, with the major difference that local pressure minima are found instead of pressure-nulls. This may cause some problems in separating different modes when estimating their amplitudes by inversion. The next chapter will investigate the issues that have to be taken into account when performing such an inversion.

2.3 Fourier relationships

This section presents an alternative interpretation of the Rayleigh integral defined in equation 2.2.1. The far field approximation of equation 2.2.1 can be expressed as a spatial Fourier transform (also known as a wavenumber transform) of the particle velocity distribution over the duct cross-section. This Fourier transform can in turn be written in the cylindrical coordinate system and becomes a Hankel transform.

In the far field $r >> r_s$,

$$\begin{aligned} h &= |\vec{r} - \vec{r}_s| \\ &= \sqrt{r^2 + r_s^2 - 2\vec{r}\vec{r}_s} \\ &= r\sqrt{1 - \frac{2\vec{r}\vec{r}_s}{r^2} + \frac{r_s^2}{r^2}} \\ &\approx r\sqrt{1 - \frac{2\vec{r}\vec{r}_s}{r^2}} \\ &\approx r\left(1 - \frac{1}{2}\frac{2\vec{r}\vec{r}_s}{r^2} - \frac{1}{8}\left(\frac{2\vec{r}\vec{r}_s}{r^2}\right)^2 \ldots\right) \\ &\approx r\left(1 - \frac{\vec{r}\vec{r}_s}{r^2}\right) \approx r\left(1 - \frac{xx_s + yy_s + zz_s}{r^2}\right) \end{aligned} \tag{2.3.1}$$

Since $z_s = 0$

$$|\vec{r} - \vec{r}_s| \approx r - \frac{x}{r}x_s - \frac{y}{r}y_s \tag{2.3.2}$$

In the far-field, $\vec{k}$ and $\vec{r}$ are in the same direction so that

$$\frac{\vec{k}}{k} = \frac{\vec{r}}{r} \tag{2.3.3}$$

thus $\frac{x}{r} = \frac{k_x}{k}$ and $\frac{y}{r} = \frac{k_y}{k}$ and the exponential term in equation 2.2.1 can be written as

$$\frac{e^{-jkh}}{h} \approx \frac{e^{-jkr}}{r}e^{j(k_x x_s + k_y y_s)} \qquad (r >> r_s) \tag{2.3.4}$$

The radiated pressure field given by equation 2.2.1 can therefore be rewritten as

$$\begin{aligned} p(r,\theta,\phi) &= j\rho ck\frac{e^{-jkr}}{r}\int_{-\infty}^{+\infty}\int_{-\infty}^{+\infty} u_z(x_s,y_s)\,\Pi(x_s)\,\Pi(y_s)\,e^{j(k_x x_s + k_y y_s)}dx_s dy_s \\ &= j\rho ck\frac{e^{-jkr}}{r}U_z(k_x,k_y) \end{aligned} \tag{2.3.5}$$

where $U_z(k_x,k_y)$ is the Fourier transform of the axial velocity distribution on the duct outlet and $\Pi(x_s)$ and $\Pi(y_s)$ are window functions defined as

$$\Pi(x_s)\begin{cases} 0 & x_s \notin [0,a] \\ 1 & x_s \in [0,a] \end{cases} \qquad \Pi(y_s)\begin{cases} 0 & y_s \notin [0,a] \\ 1 & y_s \in [0,a] \end{cases} \tag{2.3.6}$$

The radiated sound field is therefore the spatial Fourier transform of the given source field at the duct outlet. The analysis of the source distribution (i.e. the axial velocity at the outlet) in the wavenumber domain merely gives the information of sound radiation. The relationship introduced by this far field approximation leads to some precautions that need to be taken into account. Windowing in each spatial dimension as can be seen in equation 2.3.5 will introduce smearing effects in the wavenumber domain. The choice of accounting only cut-on modes which seems to be a reasonably good approximation will similarly introduce smearing effects in the spatial domain and create a source of errors when inverting for the mode amplitudes.

Now since the source distribution lies in a cylindrical geometry, it may be possible to use a cylindrical coordinate system using the following transformations

$$\begin{cases} x_s = r_s \cos\theta_s \\ y_s = r_s \sin\theta_s \end{cases} \tag{2.3.7}$$

such that $dS = dx_s dy_s = r_s dr_s d\theta_s$ and let $k_r = k\sin\varphi$ so that

$$\begin{cases} k_x = k_r \cos\theta \\ k_y = k_r \sin\theta \end{cases} \tag{2.3.8}$$

the Fourier transform of the surface velocity given in equation 2.3.5 becomes

$$U_z\left(k_r, \theta\right) = \int\limits_0^{2\pi} \int\limits_0^{\infty} u_z\left(r_s, \theta_s\right) e^{jk_r r_s \sin(\theta_s - \theta)} r_s dr_s d\theta_s \tag{2.3.9}$$

Since the velocity distribution in periodic in 2π, it can be written as a Fourier series expansion of the form

$$u_z\left(r_s, \theta_s\right) = \sum_{m=-\infty}^{+\infty} u_m\left(r_s\right) e^{-jm\theta_s} \tag{2.3.10}$$

Substituting equation 2.3.10 into equation 2.3.9 yields

$$U_z\left(k_r, \theta\right) = \sum_{m=-\infty}^{+\infty} \int\limits_0^{2\pi} \int\limits_0^{\infty} u_m\left(r_s\right) e^{j\left(k_r r_s \sin(\theta_s - \theta) - m\theta_s\right)} r_s dr_s d\theta_s \tag{2.3.11}$$

Using the integral representation of the Bessel function

$$J_m(z) = \frac{1}{2\pi}\int_0^{2\pi} e^{j(z\sin\zeta - m\zeta)}\,d\zeta \tag{2.3.12}$$

allows the integral term $\int_0^{2\pi} e^{j(k_r r_s \sin(\theta_s-\theta)-m\theta_s)}\,d\theta_s$ to be written as the following by making the substitution $\theta_s = \zeta_s + \theta$

$$e^{-jm\theta}\int_0^{2\pi} e^{j(k_r r_s \sin\zeta_s - m\zeta_s)}\,d\zeta_s = 2\pi\, e^{-jm\theta} J_m(k_r r_s) \tag{2.3.13}$$

Therefore the Fourier transform can be written as

$$U_z(k_r,\theta) = 2\pi \sum_{m=-\infty}^{+\infty} \tilde{U}_{mm}(k_r)\, e^{-jm\theta} \tag{2.3.14}$$

where

$$\tilde{U}_{mm}(k_r) = \int_0^{\infty} u_m(r_s)\, J_m(k_r r_s)\, r_s dr_s \tag{2.3.15}$$

Equation 2.3.15 is the Hankel transform of order m of the m^{th} Fourier component of the radial surface velocity distribution.

Chapter 3

Inverse problem

This chapter introduces the method for estimating modal amplitudes by inversion of acoustic measurements made over the TCS. The important issues related to the robustness of the inverse problem are discussed. It is shown in this chapter that the stability of the inversion depends strongly on the positioning of the microphones on the TCS. Computer simulations are performed to identify the optimal array geometry over the TCS in terms of the number and the position of sensors that affords the most stable inversion.

3.1 Mode amplitude estimation

The pressure field radiated in the near field of a flanged semi-infinite duct can be estimated from the Rayleigh integral presented in equation 2.2.1. This Kirchhoff approximation used for the flanged duct solution does not require the complexity of Wiener-Hopf factorisations and contour integrals found in the unflanged duct solution and will be sufficiently accurate as a first approximation to the modal directivities from a ducted turbofan engine.

Measurements of the sound radiation from a turbofan inlet, as stated by equation 2.2.10, can be formulated in the following general form

$$\int_{\Omega} \text{input} \times \text{system}\, d\Omega = \text{output} \tag{3.1.1}$$

In this formulation, the forward problem is to compute the output given the input and the mathematical description of the system. The goal of the inverse problem is to determine the input that gives rise to the measurements of the output. An inverse problem is often ill-posed in the sense that the inverted solution may be highly sensitive to changes in the measurement data. The classical example of a linear ill-posed problem is a Fredholm integral equation of the first kind with a square integrable Kernel [24]. This is relevant to the Rayleigh integral computation of duct radiation mentioned above, which can be written in the generic form of equation 3.1.1 as

$$\int_{0}^{k} a\,(k)\, D\,(k, \vec{x})\, d\vec{k} = p\,(\vec{x}) \tag{3.1.2}$$

where the right-hand side p and the Kernel D are known functions while a is the unknown sought solution. The Kernel D is given exactly by the mathematical model while the right-hand side typically consists of measured quantities and is only known with certain accuracy at a finite set of points x_1, ... , x_K.

The forward problem of equation 3.1.2, at a single frequency, can be written in matrix notation as follows

$$\mathbf{D}\mathbf{a} = \mathbf{p} \tag{3.1.3}$$

where

- $\mathbf{p} \in \mathbb{C}^K$ is a complex vector of the radiated pressure field measured at K model sensor outputs.

- $\mathbf{a} \in \mathbb{C}^L$ is a complex vector of modal amplitudes for L modes.

- $\mathbf{D} \in \mathbb{C}^{K \times L}$ is the directivity matrix and contains the radiation directivities of L modes at K sensor outputs in the radiated field at the TCS.

When written in full equation 3.1.3 becomes

$$\begin{bmatrix} D_{11}(\omega) & D_{12}(\omega) & \cdot & \cdot & D_{1L}(\omega) \\ \cdot & & & & \cdot \\ \cdot & & & & \cdot \\ & & & & \\ & & & & \\ \cdot & & & & \cdot \\ D_{K1}(\omega) & & & & D_{KL}(\omega) \end{bmatrix} \begin{bmatrix} a_1(\omega) \\ a_2(\omega) \\ \cdot \\ \\ \cdot \\ \\ a_L(\omega) \end{bmatrix} = \begin{bmatrix} p_1(\omega) \\ p_2(\omega) \\ \cdot \\ \cdot \\ \\ \cdot \\ p_K(\omega) \end{bmatrix} \tag{3.1.4}$$

Note that for the general case $K > L$, the system is said to be overdetermined (i.e. there are more sensors on the TCS than significant radiated modes). A particular case is when the number of sensors is made equal to the number of radiated modes (i.e. $K = L$) for which the directivity matrix is square. Now if $\hat{\mathbf{p}}$ denotes the vector of measured pressures at the K sensor outputs, it can be related to the modelled vector of pressures $\mathbf{p}$ by an error vector $\mathbf{n}$ whose components represent the noise on the error sensors and modelling errors. Thus,

$$\hat{\mathbf{p}} = \mathbf{D}\mathbf{a} + \mathbf{n} \tag{3.1.5}$$

We seek the vector of modal amplitudes $\mathbf{a}$ that ensures the best fit of the modelled pressure field $\mathbf{p}$ to the measured data $\hat{\mathbf{p}}$. In order to deduce this solution, the minimisation of the sum of the squared errors ('residuals') between the measured sensor outputs and the model sensor outputs will be performed (i.e. $\min \|\hat{\mathbf{p}} - \mathbf{D}\mathbf{a}\|_2^2$). This method is called the 'least-squares' solution.

In this case the complex error vector can be written as

$$\mathbf{n} = \hat{\mathbf{p}} - \mathbf{p} = \hat{\mathbf{p}} - \mathbf{D}\mathbf{a} \tag{3.1.6}$$

The least-squares solution minimises the following cost function

$$J = \sum_{k=1}^{K} |n_k(\omega)|^2 = \mathbf{n}^{\mathbf{H}}\mathbf{n} \tag{3.1.7}$$

such that

$$\frac{\partial J}{\partial \mathbf{a}} = 0 \tag{3.1.8}$$

The optimal estimate of the modal amplitudes vector that minimises this cost function, which is a Hermitian quadratic function of the vector of complex amplitudes **a**, is derived in appendix B and is found to be

$$\begin{aligned} \hat{\mathbf{a}}_0 &= \left[\mathbf{D}^{\mathbf{H}}\mathbf{D}\right]^{-1}\mathbf{D}^{\mathbf{H}}\hat{\mathbf{p}} \\ &= \mathbf{D}^{+}\hat{\mathbf{p}} \end{aligned} \tag{3.1.9}$$

where $\mathbf{D}^{+}$ is the pseudo-inverse of the directivity matrix **D**.

Note that when the number of sensors is made equal to the number of radiated modes (i.e. **D** is square), the solution reduces to $\mathbf{a_0} = \mathbf{D}^{-1}\hat{\mathbf{p}}$. This is the minimum requirement for the inversion to be performed as in the case of an underdetermined system (i.e. the number of sensors is lower than the number of radiated modes $K < L$), no solution exists for the modal amplitudes vector unless some further constraint is introduced.

3.2 Mode amplitudes for broadband sound field

Turbofan inlets produce sound field which comprises two components. The first one is the tonal component of the sound field made of tones which are produced by rotor/stator interactions [2]. These tones are characterised by peaks in the sound power spectrum radiated from the inlet and occur at frequencies which are multiples of the Blade Passage frequency $B\Omega$, where B is the number of blades and Ω the shaft frequency. At these frequencies, the modal analysis of the least-squares solution detailed in section 3.1 is valid. The second component denotes the broadband sound field, which occur at any other frequencies, and is produced by more complex mechanisms. Broadband sound field produce random signals which will be assumed to be ergodic in this research. For this reason, the least-squares solution needs to be applied to spectrum analysis in order to give estimates that characterise such random signals. The power spectra and the cross spectra which, define how the pressure signal of a microphone is related with itself and with the signal of another microphone at another instant, are defined respectively. These spectra can be arranged into the cross spectral matrix which, for the modelled pressure is given by

$$\mathbf{S_{pp}} = \lim_{T \mapsto \infty} \frac{1}{T} E \left[\mathbf{pp^H} \right] \tag{3.2.1}$$

$E\,[\,]$ in equation 3.2.1 is the expectation operator. Introducing equation 3.1.3 into equation 3.2.2 yields

$$\mathbf{S_{pp}} = \mathbf{D S_{aa} D^H} \tag{3.2.2}$$

where $\mathbf{S_{aa}}$ is the cross spectral matrix of mode amplitudes defined by

$$\mathbf{S_{aa}} = \lim_{T \mapsto \infty} \frac{1}{T} E \left[\mathbf{aa^H} \right] \tag{3.2.3}$$

If we substitute equation 3.1.9 into equation 3.2.3, the least-square estimate of the mode amplitude cross spectra is then given by

$$\begin{aligned} \mathbf{S_{\hat{a}\hat{a}}} &= \lim_{T \mapsto \infty} \frac{1}{T} E \left[\mathbf{D^+ \hat{p} \hat{p}^H} \left(\mathbf{D^+} \right)^{\mathbf{H}} \right] \\ &= \mathbf{D^+ \hat{S}_{\hat{p}\hat{p}}} \left(\mathbf{D^+} \right)^{\mathbf{H}} \end{aligned} \tag{3.2.4}$$

where $\mathbf{\hat{S}_{\hat{p}\hat{p}}}$ is the matrix of measured pressure cross-spectra as defined in equation 3.2.1. Note that the diagonal elements of the above matrix represent the least-square estimate of the mean square mode amplitudes.

3.3 Condition number of modal directivity matrix

The underdetermined system (with more modes than sensors) mentioned at the end of the previous section is an extreme case and will not be studied further in this thesis. In this case, there will not be sufficient numbers of sensors to obtain the information to invert for all the modes present. However, similar problems to an underdetermined system may arise in the overdetermined case because of inappropriate measurement locations or unfavourable acoustical conditions. If, for example, radiation patterns of different radiated modes are similar, particularly if their main radiation lobes are at the same polar angle, their effect on each of the sensors will therefore also be similar. This leads to redundant information, which gives a system of equation 3.1.3 of similar mathematical form to that in the underdetermined case. The exact least-squares solution to this problem is still mathematically defined, as in equation 3.1.9, but the modal information detected is made very sensitive to the presence of noise. The reason for this sensitivity is that two columns in the directivity matrix **D** are very similar. Such a matrix is said to be 'ill-conditioned'. Similar ambiguity may also arise in another way, which affects the positioning of the microphones on the TCS. Indeed, two microphones that are at the same position, or placed very close together, will lead to rows in the directivity matrix **D** being very similar and thus to ill-conditioning of the system. Just as important is when the matrix elements have a very large dynamic range, which occur close to cutoff as we will show in chapter 4.

We will show in this chapter that the stability of the inverse problem strongly depends on the coupling between modes and sensors. It is therefore important to evaluate the sensitivity of the modal amplitude vector estimate to small perturbations **n** in the measured pressure, for example, due to measurement noise. A suitable parameter for evaluating this sensitivity is the condition number of **D**. This section discusses how the condition number quantifies the sensitivity of the system, which is then used to identify sensor arrays on the TCS that afford robust inversion.

The condition number places a bound on the solution inaccuracies **e** due to inaccuracies **n** in **p** (error of measuring of $\hat{p}_{ij}$, i.e. noise).

The condition number for a rectangular matrix $\mathbf{D} \in \mathbb{C}^{K \times L}$ is defined to be

$$\kappa(\mathbf{D}) = \|\mathbf{D}\|_2 \left\|\mathbf{D}^{+}\right\|_2 \qquad (3.3.1)$$

where $\| \ \|_2$ denotes the 2-norm operator applied to a matrix or a vector.

Deviations $\mathbf{n}$ produce small deviations $\mathbf{e}$ in the solution. According to equation 3.1.3

$$\mathbf{p} + \mathbf{n} = \mathbf{D}\left(\mathbf{a} + \mathbf{e}\right) \tag{3.3.2}$$

Multiplying out and introducing equation 3.1.9 gives

$$\mathbf{e} = \mathbf{D}^{+}\mathbf{n} \tag{3.3.3}$$

The 2-norm of a matrix $\mathbf{A}$ is defined to be [25]

$$\left\|\mathbf{A}\right\|_2 = \max_{x \neq 0} \frac{\left\|\mathbf{A}\mathbf{x}\right\|_2}{\left\|\mathbf{x}\right\|_2} \tag{3.3.4}$$

A useful property of the matrix 2-norm [25] for any matrices $\mathbf{A}$ and $\mathbf{B}$ is that

$$\left\|\mathbf{AB}\right\|_2 \leq \left\|\mathbf{A}\right\|_2 \left\|\mathbf{B}\right\|_2$$

which in equation 3.3.3 leads to the inequality,

$$\left\|\mathbf{e}\right\|_2 \leq \left\|\mathbf{D}^{+}\right\|_2 \left\|\mathbf{n}\right\|_2 \qquad \text{and} \qquad \left\|\mathbf{p}\right\|_2 \leq \left\|\mathbf{D}\right\|_2 \left\|\mathbf{a}\right\|_2 \tag{3.3.5}$$

Therefore, one can write

$$\left\|\mathbf{e}\right\|_2 \left\|\mathbf{p}\right\|_2 \leq \left\|\mathbf{D}\right\|_2 \left\|\mathbf{D}^{+}\right\|_2 \left\|\mathbf{n}\right\|_2 \left\|\mathbf{a}\right\|_2 \tag{3.3.6}$$

Introducing equation (3.3.1) into equation (3.3.6) yields the important inequality

$$\frac{\left\|\mathbf{e}\right\|}{\left\|\mathbf{a}\right\|} \leq \kappa\left(\mathbf{D}\right) \frac{\left\|\mathbf{n}\right\|}{\left\|\mathbf{p}\right\|} \tag{3.3.7}$$

This important and well-established result demonstrates clearly that the sensitivity of the solution for $\mathbf{a}$ is determined by the condition number of the matrix $\mathbf{D}$ to be inverted. Thus a large condition number will greatly amplify small perturbations in $\mathbf{p}$ (i.e. noise). In practical terms, contaminating noise will have disproportionately large effect on the solution for the modal amplitudes vector $\mathbf{a}$ if the matrix is 'badly conditioned', i.e. if it has a large condition number $\kappa\left(\mathbf{D}\right)$. In other words, $\kappa\left(\mathbf{D}\right)$ bounds the relative error in the solution from the relative error in the measurements. The acceptable value of the condition number is subjective and will depend on the level of the noise that contaminates the measurements and the resulting error in the mode amplitudes reconstruction.

If the noise and the pressure signals are uncorrelated, $\hat{\mathbf{S}}_{\hat{\mathbf{p}}\hat{\mathbf{p}}}$ can be related to the modelled pressure cross-spectral matrix $\hat{\mathbf{S}}_{\mathbf{pp}}$ and the matrix of noise cross-spectra $\hat{\mathbf{S}}_{\mathbf{nn}}$ as

$$\hat{\mathbf{S}}_{\hat{\mathbf{p}}\hat{\mathbf{p}}} = \hat{\mathbf{S}}_{\mathbf{pp}} + \hat{\mathbf{S}}_{\mathbf{nn}} \tag{3.3.8}$$

The presence of errors in the modal cross-spectral matrix, $\hat{\mathbf{S}}_{\mathbf{ee}}$, which using equation 3.3.3, may be written as

$$\hat{\mathbf{S}}_{\mathbf{ee}} = \mathbf{D}^{+}\hat{\mathbf{S}}_{\mathbf{nn}}\left(\mathbf{D}^{+}\right)^{\mathbf{H}} \tag{3.3.9}$$

It may be shown [18] that

$$\frac{\left\|\hat{\mathbf{S}}_{\mathbf{ee}}\right\|}{\left\|\hat{\mathbf{S}}_{\hat{\mathbf{a}}\hat{\mathbf{a}}}\right\|} \leq \kappa(\mathbf{D})^{2}\frac{\left\|\hat{\mathbf{S}}_{\mathbf{nn}}\right\|}{\left\|\hat{\mathbf{S}}_{\hat{\mathbf{p}}\hat{\mathbf{p}}}\right\|} \tag{3.3.10}$$

Equation 3.3.10 is the equivalent for broadband noise to equation 3.3.7 for tonal noise. In conclusion, the condition number of the directivity matrix bounds the error in the solution from the error found in the measurements both for tonal and broadband noise.

3.4 Reconstruction accuracy parameter

Whilst equation 3.3.7 is important for specifying bounds on the accuracy of the inverted solution $\|\mathbf{e}\| / \|\mathbf{a}\|$, it cannot quantify the precise value of this error due to measurement noise at the sensors. For this purpose we define a reconstruction accuracy parameter, which evaluates the error found in the solution, as follows

$$\varepsilon = \frac{\|\hat{\mathbf{a}} - \mathbf{a}\|_2}{\|\mathbf{a}\|_2} \tag{3.4.1}$$

The 'noise' vector generated at the sensor array during the simulations performed in this chapter is obtained for a given Signal to Noise Ratio (SNR) as follows

$$\mathbf{n} = \frac{10^{-\frac{SNR}{20}} \left\|\mathbf{p}\right\|_2 e^{j\phi}}{\sqrt{K}} \tag{3.4.2}$$

where ϕ is a vector of randomly distributed phase angles. From equation 3.4.2, and the fact that the inverted mode amplitudes vector $\hat{\mathbf{a}}$ is written as the sum of the original mode amplitude $\mathbf{a}$ and the solution error vector $\mathbf{e}$, a single value that quantifies the global reconstruction accuracy in dB is defined here as follows

$$\eta = 20\log_{10}(\varepsilon) = 20\log_{10}\left(\frac{\left\|\mathbf{e}\right\|_2}{\left\|\mathbf{a}\right\|_2}\right) \tag{3.4.3}$$

The effect of the randomly generated noise of equation 3.4.2 on the modal information radiated from the inlet varies with the phase angle distribution. The noise vector is generated 2000 times and the mean value of the reconstruction accuracy is computed from this ensemble. Numerical simulations carried out on η and on $\bar{\eta}$ defined in section 3.7 will refer to their mean values from here on.

Unlike the condition number, which does not require a *a priori* solution, the reconstruction parameter allows to assess the inversion accuracy only if the original solution is known. While this parameter will not be useful when the mode amplitudes are inverted from experimental data, it is still useful for simulations when the original solution is known. It is important to note that, throughout this thesis, simulations involving reconstruction accuracy, as well as the modal error discussed in section 3.7 are performed with noise contaminating the pressure measurements such that the SNR is 20dB.

3.5 The effect of sensor positioning on inversion robustness and accuracy

It has been shown in chapter 2 that the pressure radiated from the duct at a single frequency may be expressed as a summation of modes, each of which possesses its own directivity pattern. When calculating the directivity matrix $\mathbf{D}$, it is essential to take into account all dominant modes present in the radiated field. Because each mode possesses a different radiation pattern and efficiency, it is possible to see that the positioning of the microphones on the TCS will have a significant effect on how well the detection of these modes can be performed. The effect of the positioning of microphones on the TCS upon the parameters $\kappa(\mathbf{D})$ and η is therefore investigated such that the most useful information of each mode is extracted. It is essential to devise a sensor array, which would couple best with the modal information radiated from the inlet. Such a sensor array is difficult to obtain since the cut-on ratio of each mode, which indicates the location and efficiency of the main radiation lobe, varies with frequency. However, some guidelines about the positioning and the number of microphones on the TCS for robust and accurate inversion are discussed in the following sections.

3.5.1 Random distribution of sensors on the TCS

The importance of sensor positioning on the TCS array for good coupling with the modal radiation has been discussed. As a first attempt to identify array geometries that afford good conditioning of the directivity matrix, a study of the influence of sensor positioning upon the condition number and the reconstruction accuracy parameter is now carried out. Computer simulations are performed to evaluate the sensor array performance in terms of robustness and accuracy. As a preliminary study, the behaviour of both $\kappa(\mathbf{D})$ and η is investigated for randomly distributed microphones over the TCS.The simulations are performed for sets of 2000 realisations of randomly distributed sensors at $ka = 10$, $ka = 15$ and $ka = 20$ respectively for different numbers of sensors. The mean value and the standard deviation of the condition number $\kappa(\mathbf{D})$, denoted by μ_κ and σ_κ respectively, are computed alongside the mean and the standard deviation of η denoted by μ_η and σ_η.

Figure 3.1 shows μ_κ, σ_κ, μ_η and σ_η plotted against K/L at $ka = 20$. The results for frequencies $ka = 10$ and $ka = 15$ are given in appendix E. This figure clearly indicates that the condition number and the reconstruction accuracy are significantly improved by adding a few more microphones than the total number of cut-on modes accounted by the inversion. For numbers of sensors K corresponding to $K/L \approx 1.3$, the mean value and the standard deviation cease to have significant improvement for both the condition number and the reconstruction accuracy parameter. Very little improvement in the inversion robustness and accuracy is made at a high cost of microphones on the TCS. This study reveals that the number of microphones used for the computation of mode amplitudes has an important influence on the inversion robustness and accuracy. At a given frequency,

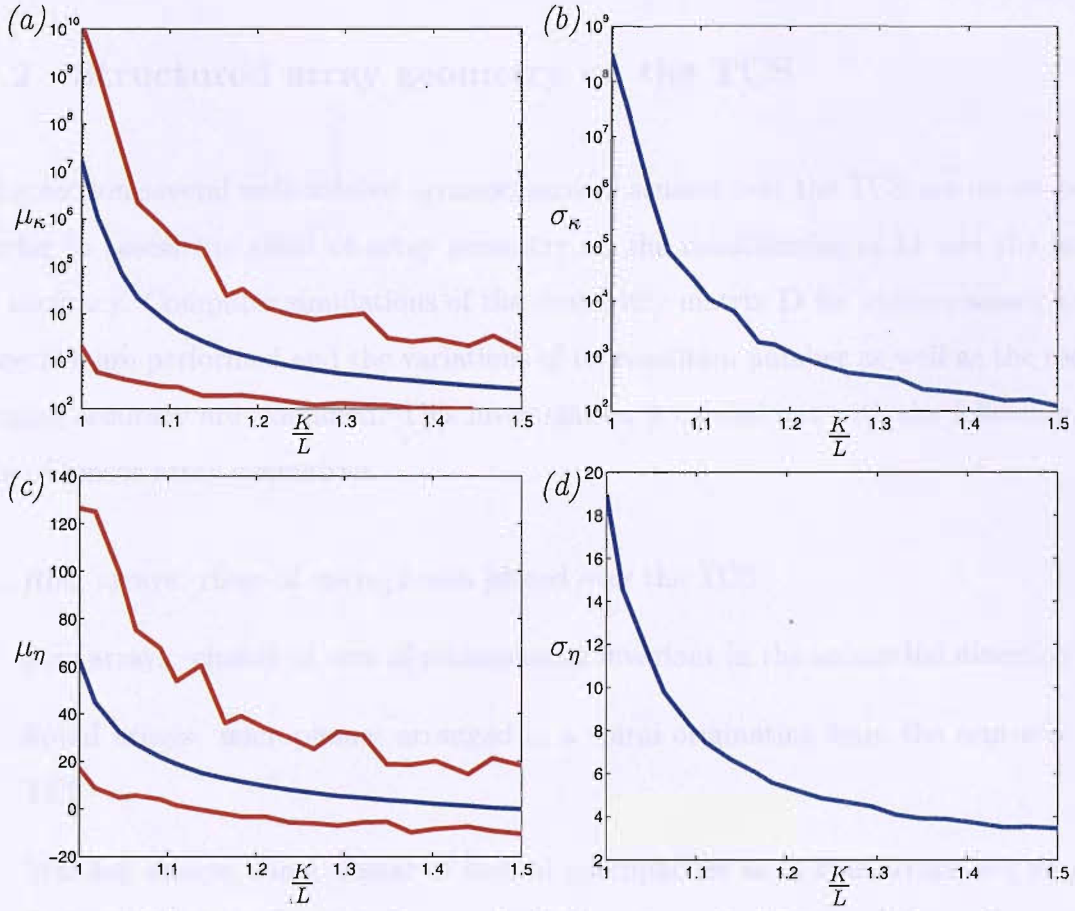

Figure 3.1: (*a*) Mean value and (*b*) standard deviation of $\kappa(\mathbf{D})$, (*c*) Mean value and (*d*) standard deviation η at $ka = 20$ of 2000 randomly distributed sensor arrays

— gives the minimum and maximum values of μ_κ and μ_η

the TCS array devised for this inverse technique will therefore employ a number of sensors such that $K/L \approx 1.3$. This study, however, does not provide any guidelines relating to particular array geometries.

3.5.2 Structured array geometry on the TCS

In this section several well-ordered arrangements of sensors over the TCS are investigated in order to assess the effect of array geometry on the conditioning of $\mathbf{D}$ and the inversion accuracy. Computer simulations of the directivity matrix $\mathbf{D}$ for various sensor array geometries are performed and the variations of its condition number as well as the reconstruction accuracy are examined. This investigation is carried out with the following five types of sensor array geometries

1. Ring arrays: rings of microphones placed over the TCS
2. Star arrays: cluster of arcs of microphones invariant in the azimuthal direction
3. Spiral arrays: microphones arranged in a spiral originating from the centre of the TCS
4. Star-fish arrays: same cluster of arcs of microphones as in star arrays but varying in the azimuthal direction
5. Geodesic sensor arrays: uniform distribution of microphones over the TCS each of which occupying an equal surface area

On the array geometries 2, 3 and 4, the microphones are either uniformly or piecewise distributed. For a given number of microphones L, the piecewise distribution is arranged to satisfy the following distribution in the polar direction

- $9\,\%$, $\varphi \in [0^o, 15^o]$

- 57 %, $\varphi \in [15^o, 80^o]$
- 33 %, $\varphi \in [80^o, 90^o]$

Such a piecewise distribution is chosen for two reasons: limiting the concentration of microphones close to the axis (i.e. $\varphi \in [0^o, 15^o]$) which aims at preventing redundant measurements over this section of the TCS while a high concentration of sensors at edges of the TCS (i.e. $\varphi \in [80^o, 90^o]$) is ought to enhance the modal information close to the sideline of nearly cut-off modes. This is an attempt of detecting these modes which radiate weak acoustic energy. An illustration of the types of arrays investigated is shown in figure 3.2.

3.5.3 Ring Arrays

Ring arrays consists simply of rings of microphones arranged concentrically around the TCS axis. Each ring possesses a different number of microphones. The behaviour of the condition number at $ka = 20$ versus the number of rings for different K/L ratios is shown in figures 3.3(a) and 3.3(b) and that of the reconstruction accuracy in figures 3.3(c) and 3.3(d). This simulation is performed for 3 different numbers of microphones. These figures indicate that $\kappa(\mathbf{D})$ is extremely large, i.e. of the order of 10^{15}, when there is not a sufficient number of rings over the TCS. When the number of rings is comprised between 7 and 9 the inversion robustness and accuracy are significantly improved as shown in figures 3.3(b) and 3.3(d). The condition number is of order 10^3 at the best when $K/L < 2$. Despite this improvement, it is clear that rings of microphones over the TCS do not allow robust and accurate inversion and that several sensors detect similar modal information. This is due to the fact that this type of arrays has insufficient microphone coverage over the polar angle and thus cannot detect the modal information independently, especially at high frequencies (i.e. $ka > 20$) when the spreading of mode radiation becomes more concentrated over the polar angle.

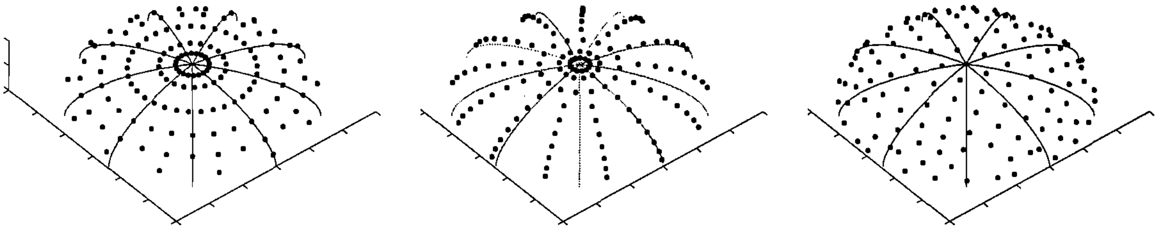

6 Ring array 10 Ring array $\nu = 5$ Geodesic array

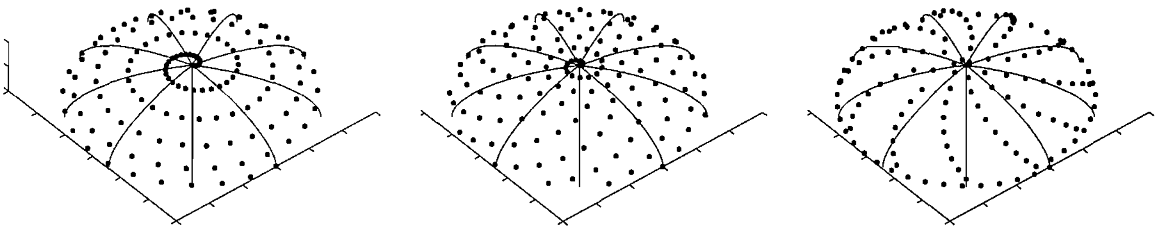

uniform 5 Spiral array uniform 10 Spiral array piecewise 10 Spiral array

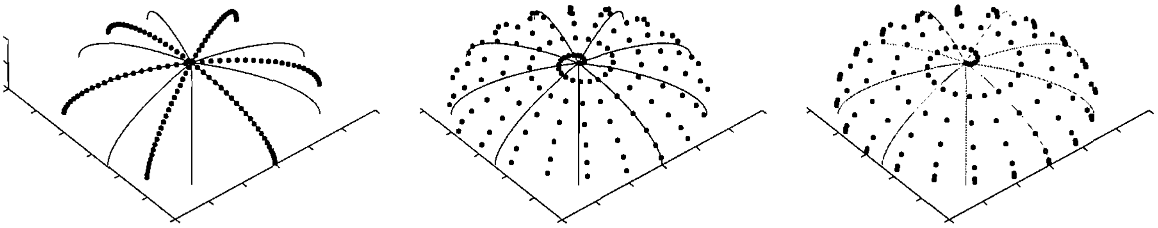

uniform 6 legs Star array uniform 10 legs Star array piecewise 10 legs Star array

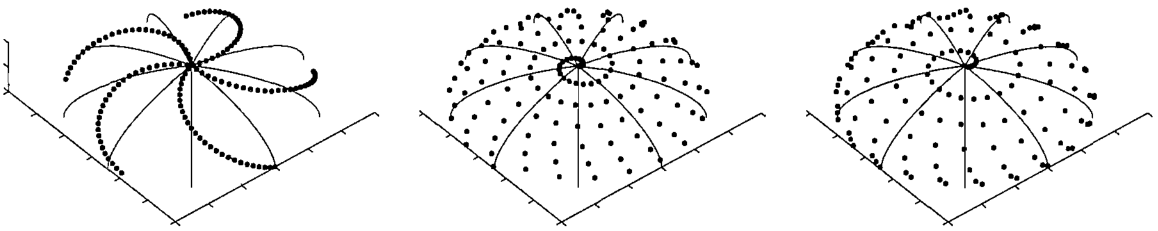

uniform 6 legs
Starfish array

uniform 10 legs
Starfish array

piecewise 10 legs
Starfish array

Figure 3.2: Illustration of sensor array geometries investigated

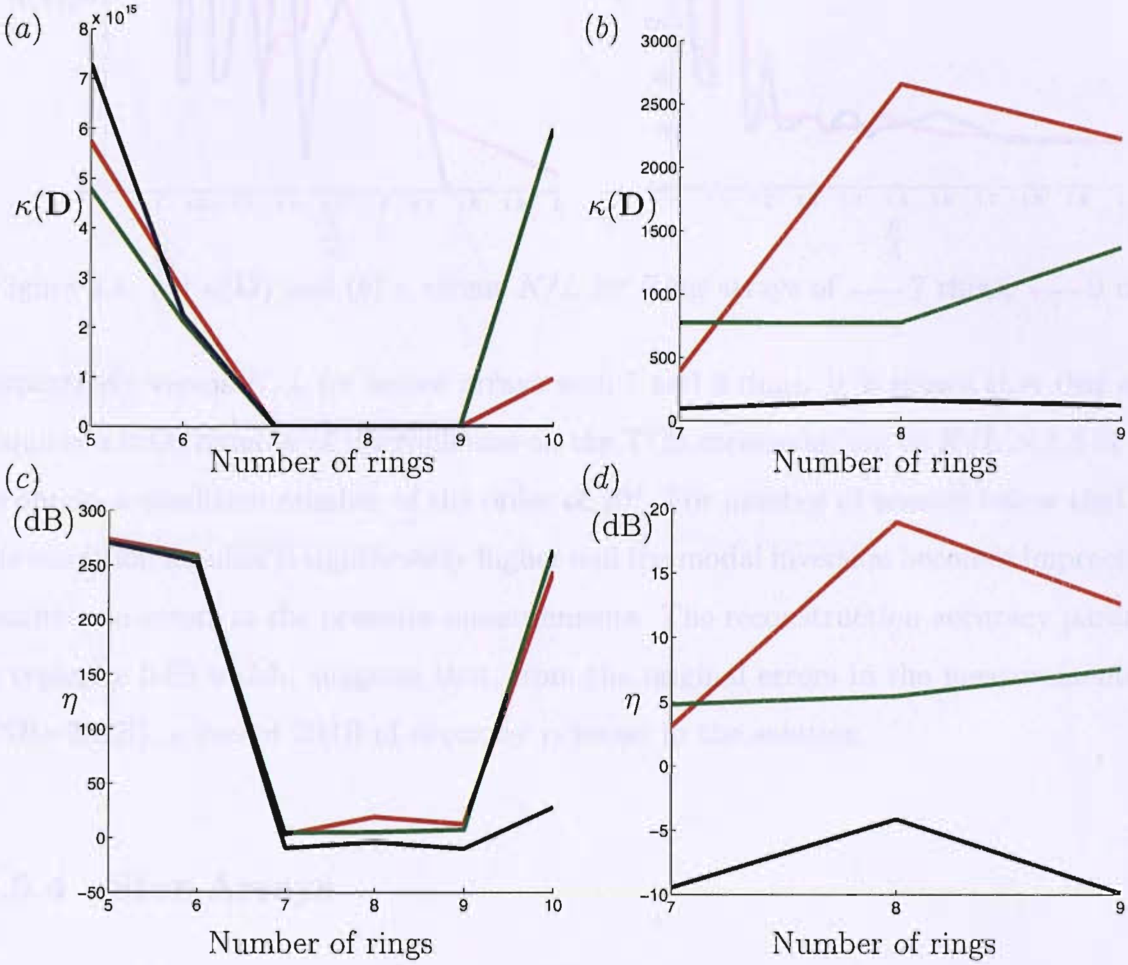

Figure 3.3: (*a*), (*b*) $\kappa(\mathbf{D})$ and (*c*), (*d*) η for Ring arrays
—— $K/L = 1.26$, —— $K/L = 1.5$ and —— $K/L = 2$

Figures 3.4(a) and 3.4(b) show the condition number and the reconstruction accuracy respectively versus K/L for sensor arrays with 7 and 9 rings. It is shown that ring arrays requires a total number of microphones on the TCS corresponding to $K/L > 1.3$ in order to obtain a condition number of the order of 10^3. For number of sensors below that ratio the condition number is significantly higher and the modal inversion becomes impractically sensitive to errors in the pressure measurements. The reconstruction accuracy parameter is typically 0dB which, suggests that, from the original errors in the measurements (i.e. SNR=20dB), a loss of 20dB of accuracy is found in the solution.

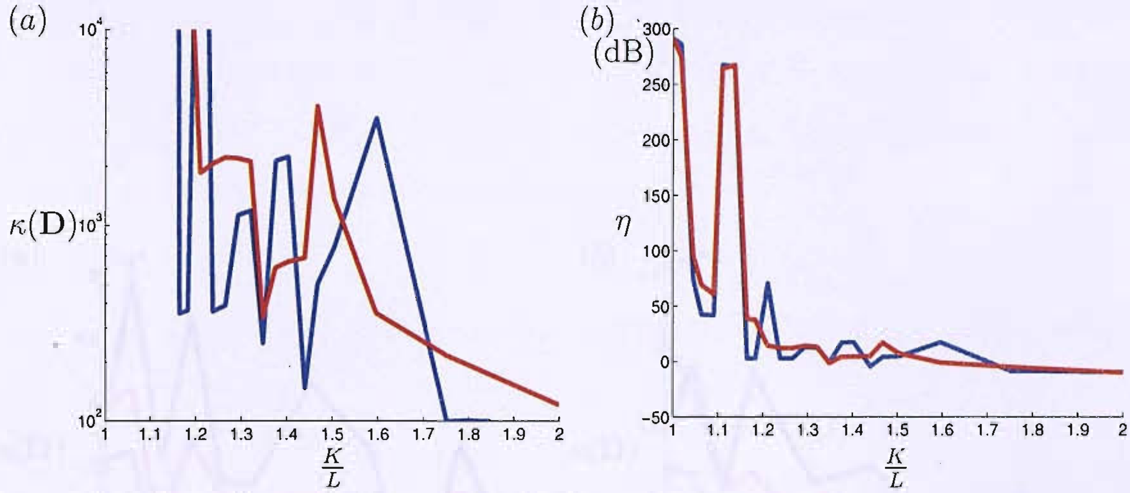

Figure 3.4: (a) $\kappa(\mathbf{D})$ and (b) η versus K/L for Ring arrays of —— 7 rings, —— 9 rings

3.5.4 Star Arrays

Star arrays favours spreading microphones over the polar angle and forms a cluster of arcs invariant with the azimuthal direction. The number of legs of the star is then varied over the TCS. Unlike ring arrays, these arrays involve a broad spreading of microphones over the polar angle. However, this is achieved at the expense of only a few azimuthal locations covered by these Star arrays. The variation of $\kappa(\mathbf{D})$ and η with the number of legs are presented in figures 3.5(a), 3.5(b) and 3.5(c), 3.5(d) respectively. These figures show that both the uniform and piecewise star arrays do not allow robust and accurate

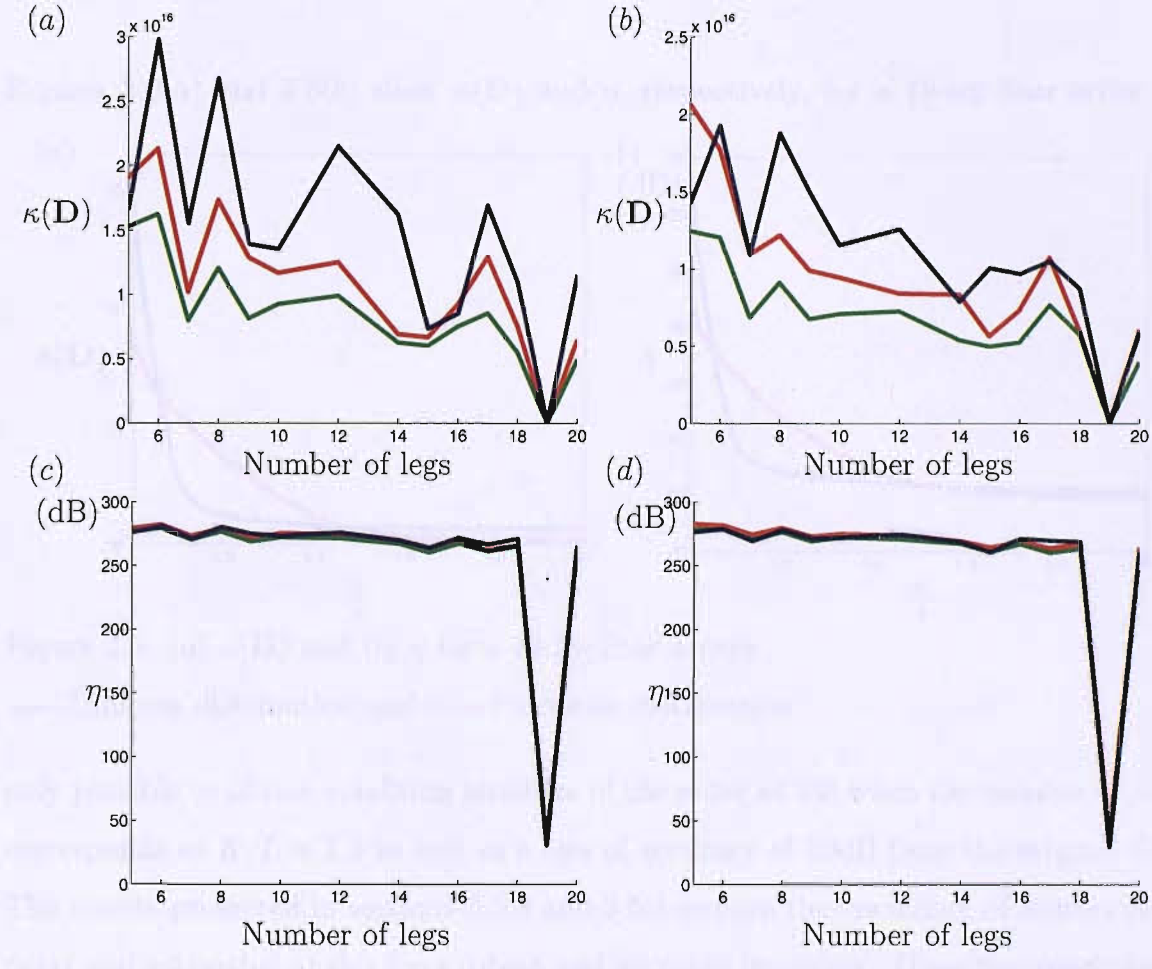

Figure 3.5: (a), (b) $\kappa(\mathbf{D})$ and (c), (d) η for uniform and piecewise Star arrays
— $K/L = 1.26$, — $K/L = 1.5$ and — $K/L = 2$

inversion. The condition number is very large in most cases (i.e. of order 10^{16}) and the reconstruction accuracy parameter is extremely low when the number of legs on the TCS is very low. Although there is a strong dependence of the modal radiation over the polar angle, it is also very important to spread microphones in the azimuthal direction in order to resolve modes independently from each other.

Figures 3.6(*a*) and 3.6(*b*) show $\kappa(\mathbf{D})$ and η, respectively, for a 19-leg Star array. It is only possible to obtain condition numbers of the order of 10^4 when the number of sensors corresponds to $K/L \approx 1.3$ as well as a loss of accuracy of 50dB from the original SNR. The results presented in sections 3.5.3 and 3.5.4 require the spreading of sensors in both polar and azimuthal angles for a robust and accurate inversion. These two conditions are fulfilled by the next two array geometries.

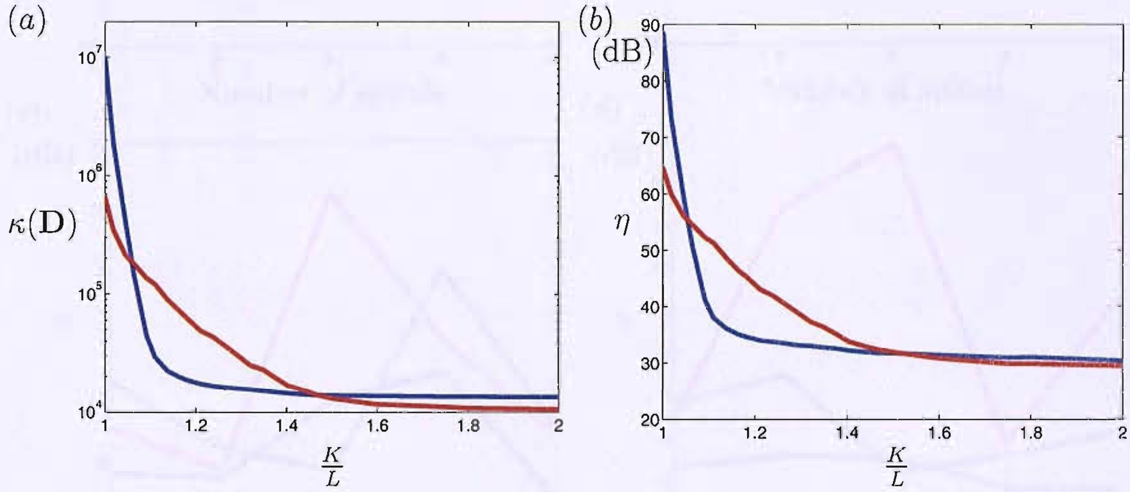

Figure 3.6: (*a*) $\kappa(\mathbf{D})$ and (*b*) η for a 19 leg Star arrays

—— Uniform distribution and —— Piecewise distribution

3.5.5 Spiral Arrays

Spiral array geometries form spiral of microphones over the TCS, the number of which may be varied. This geometry features a wide spread of sensors over the polar and azimuthal directions. While the previous array geometries produced extremely large condition num-

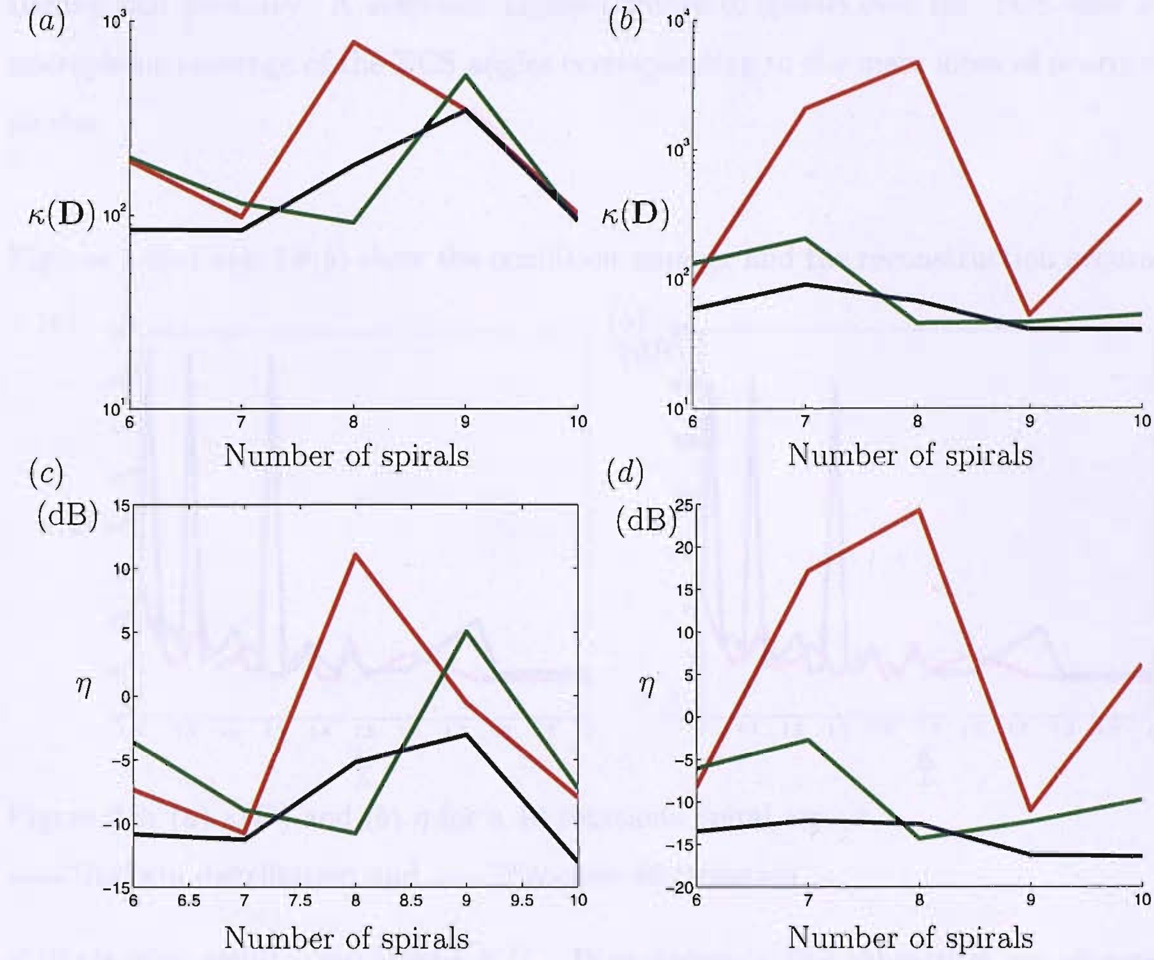

Figure 3.7: (*a*), (*b*) $\kappa(\mathbf{D})$ and (*c*), (*d*) η for uniform and piecewise Spiral arrays —— $K/L = 1.26$, —— $K/L = 1.5$ and —— $K/L = 2$

bers and poor reconstruction accuracy, spiral arrays are observed to considerably enhance the directivity matrix conditioning, as shown in figure 3.7, for both uniform and piecewise distributions. Spiral arrays lead to condition numbers of order 10^2 at best and only a loss of accuracy of 10 to 5dB compared to the original SNR. Comparatively large fluctuations of $\kappa(\mathbf{D})$ and η with the number of rotations may be observed. These fluctuations may be explained by the fact that as the number of spirals is increased, the sensors are shifted to a radiation angle that is not well coupled to the modal information. This sensitivity to number of spirals effect may be greatly reduced by just adding extra microphones. Note also that piecewise distributions do not offer any improvements in the inversion conditioning and accuracy. A sufficient highly number of spirals over the TCS offer a good microphone coverage of the TCS angles corresponding to the main lobes of nearly cut-off modes.

Figures 3.8(a) and 3.8(b) show the condition number and the reconstruction accuracy for

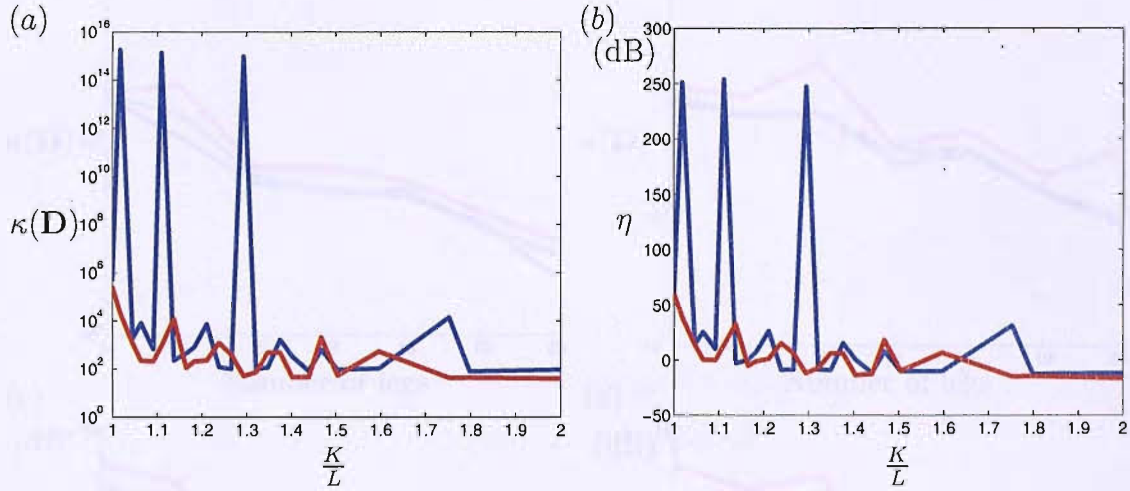

Figure 3.8: (a) $\kappa(\mathbf{D})$ and (b) η for a 10 rotations Spiral arrays
—— Uniform distribution and —— Piecewise distribution

a 10-rotation spiral array versus K/L. Poor accuracy and robustness are observed for 3 numbers of sensors on the spiral arrays. The shift of sensors in the polar direction to obtain a 10 spiral array with a particular number of sensors can uncouple the sensor array to the radiated modal information.

3.5.6 Star-fish Arrays

Star-fish arrays, as star arrays, have a cluster of arcs of microphones that offer good microphone coverage in the polar direction but arcs vary with the azimuthal direction. This geometry, unlike star arrays, has therefore the advantage of possessing a wide spread of sensors over both the polar and azimuthal angles. As for the spiral arrays in section

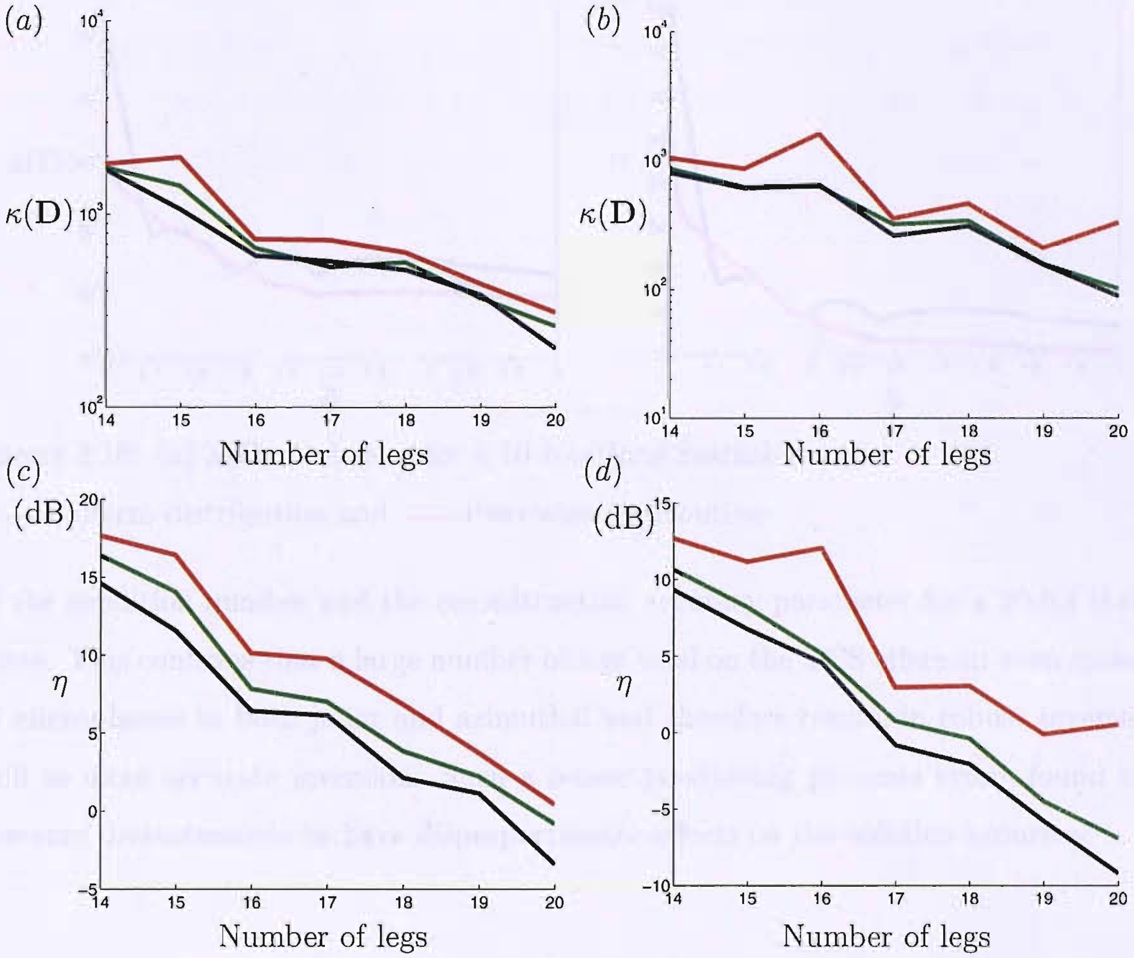

Figure 3.9: (*a*), (*b*) $\kappa(\mathbf{D})$ and (*c*), (*d*) η for uniform and piecewise Starfish arrays — $K/L = 1.26$, — $K/L = 1.5$ and — $K/L = 2$

3.5.5, the star-fish arrays allow condition numbers of order 10^2 and losses of reconstruction accuracy of 10 to 15dB from the original SNR. Likewise, star-fish arrays offer a good coverage of the TCS section of nearly cut-off modal radiation, since the piecewise arrays do not enhance the inversion conditioning. Figures 3.10(*a*) and 3.10(*b*) show the behaviour of the condition number and the reconstruction accuracy parameter for a 20-leg star-fish array. This confirms that a large number of legs used on the TCS offers an even spreading of microphones in both polar and azimuthal and therefore results in robust inversion as well as more accurate inversion. Such a sensor positioning prevents errors found in the pressure measurements to have disproportionate effects on the solution accuracy.

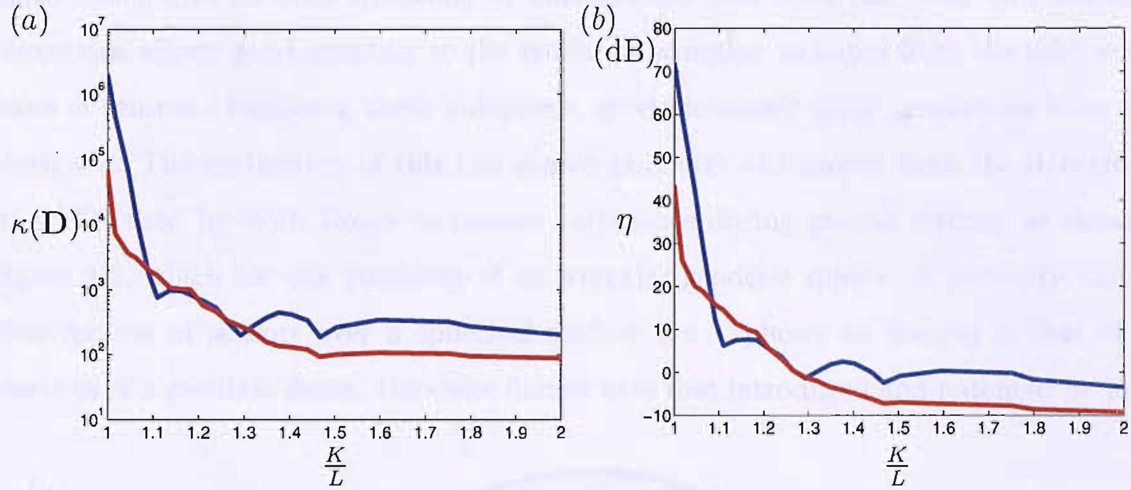

Figure 3.10: (*a*) $\kappa(\mathbf{D})$ and (*b*) η for a 10 rotations Starfish arrays
—— Uniform distribution and —— Piecewise distribution

3.5.7 Geodesic sensor arrays

This section details the sensor array geometry that leads to the best conditioning of the inverse problem and hence an accurate reconstruction of mode amplitudes. As discussed in section 3.5.2, increasing the number of microphones above the number of cut-on modes greatly improves the conditioning of the inversion. The more microphones used, in general, the more robust the inversion. However, the cost and the implementation of using many hundreds of microphones may be prohibitive. It is therefore important to examine the number of microphones that allows the best trade-off between robustness, accuracy, and the number of sensors. The computer simulations in sections 3.5.3, 3.5.4, 3.5.5 and 3.5.6 have found that an even spreading of microphones over both the polar and azimuthal directions allows good coupling to the modal information radiated from the inlet with a save of sensors. Following these guidelines, geodesic sensor array geometries have been designed. The motivation of this last sensor geometry also comes from the structure of the TCS used by Rolls Royce to remove turbulence during ground testing, as shown in figure 1.2, which has the geometry of an irregular geodesic sphere. A perfectly uniform distribution of sensors over a spherical surface (i.e. spheres or domes) is that of the vertices of a geodesic dome. Geodesic domes were first introduced and patented by Fuller in 1954 and discussed in [26]. The geodesic structure is a polyhedron, also denoted

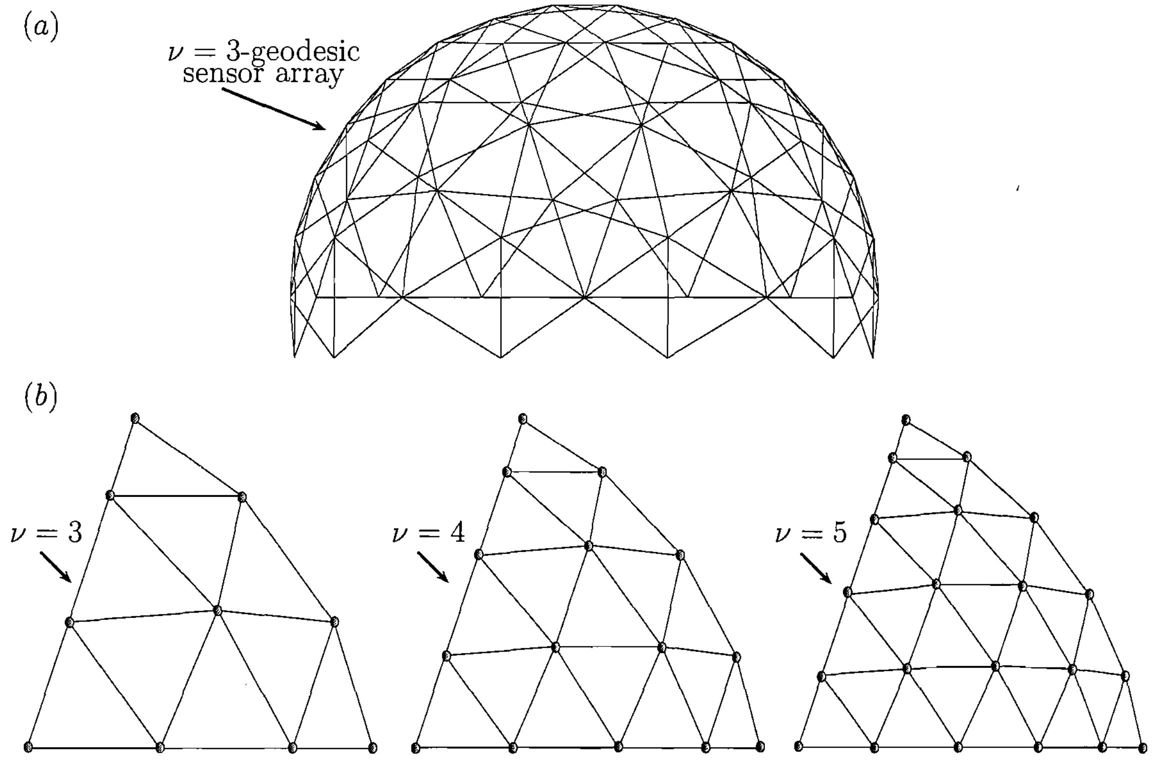

Figure 3.11: Illustration of geodesic structure for Geodesic sensor array

as a platonic solid, the vertices of which are inscribed within a sphere. The design of various geodesic structures may be found in [27]. The geodesic array investigated here is based on an icosahedron, (i.e. 20 face polyhedron) the faces of which are made up by isosceles triangles of similar surface area. The arrangement of microphones are given by the positions of the vertices of that geometry, which enables to define facets of equal surface area. At each increment of ν a number of new vertices are produced by pushing out to the radius of the sphere intermediate points found on each edge. A geodesic sphere of frequency $\nu = 3$ is illustrated in figure 3.11(a). However such sensor array can only be implemented at a limited number of microphones which varies as the square of the geodesic frequency ν. The hemispherical array with a geodesic geometry is built from the half of a given ν-geodesic sphere.

The number K of sensors is given by

$$K = \frac{10\nu^2 + 2}{2} \quad \nu\,\text{odd} \qquad K = \frac{10\nu^2 + 2}{2} + \frac{5\nu}{2} \quad \nu\,\text{even} \tag{3.5.1}$$

At $ka = 20$, a geodesic array of frequency $\nu = 5$ and $\nu = 6$ with 126 and 196 microphones respectively satisfies the requirement of $K/L \geq 1.3$ and are considered here.

The condition number of $\mathbf{D}$ corresponding to this geometry at this frequency is significantly smaller than that found with the Spiral and Starfish arrays. It is found $\kappa(\mathbf{D}) = 49$ and $\kappa(\mathbf{D}) = 25$ for geodesic sensor array of frequency $\nu = 5$ and $\nu = 6$ respectively. The reconstruction accuracy deduced from these two geodesic sensor arrays is found to be -10dB and -15dB respectively. Remembering 20dB SNR, this therefore leads to a loss of accuracy of 10 and 5dB.

3.6 Robustness and accuracy over a frequency band

An important consideration in designing a TCS array for mode detection concerns its robustness and accuracy over a band of frequencies. The condition number $\kappa(\mathbf{D})$ and the reconstruction accuracy η are examined over the band of frequencies $10 < ka < 20$. Figures 3.12(a) and 3.12(b) show the variations of $\kappa(\mathbf{D})$ with frequency and figures 3.12(c) and 3.12(d) the variations of η for the $\nu = 5$ and $\nu = 6$-geodesic sensor arrays respectively. A series of peaks are observed to coincide with the modal cut-on frequencies. Figures 3.12(b) and 3.12(d) are magnified versions of figure 3.12(a) and 3.12(c) for frequencies $14 \leq ka \geq 16$ and $17 \leq ka \geq 19$ respectively. The inversion conditioning and accuracy are significantly poorer at frequencies in the vicinity of cut-on frequencies, as indicated by black dotted lines. The noise present in the measurements leads to subsequent inaccuracies in the solution at these frequencies. This reason will be discussed in chapter 4.

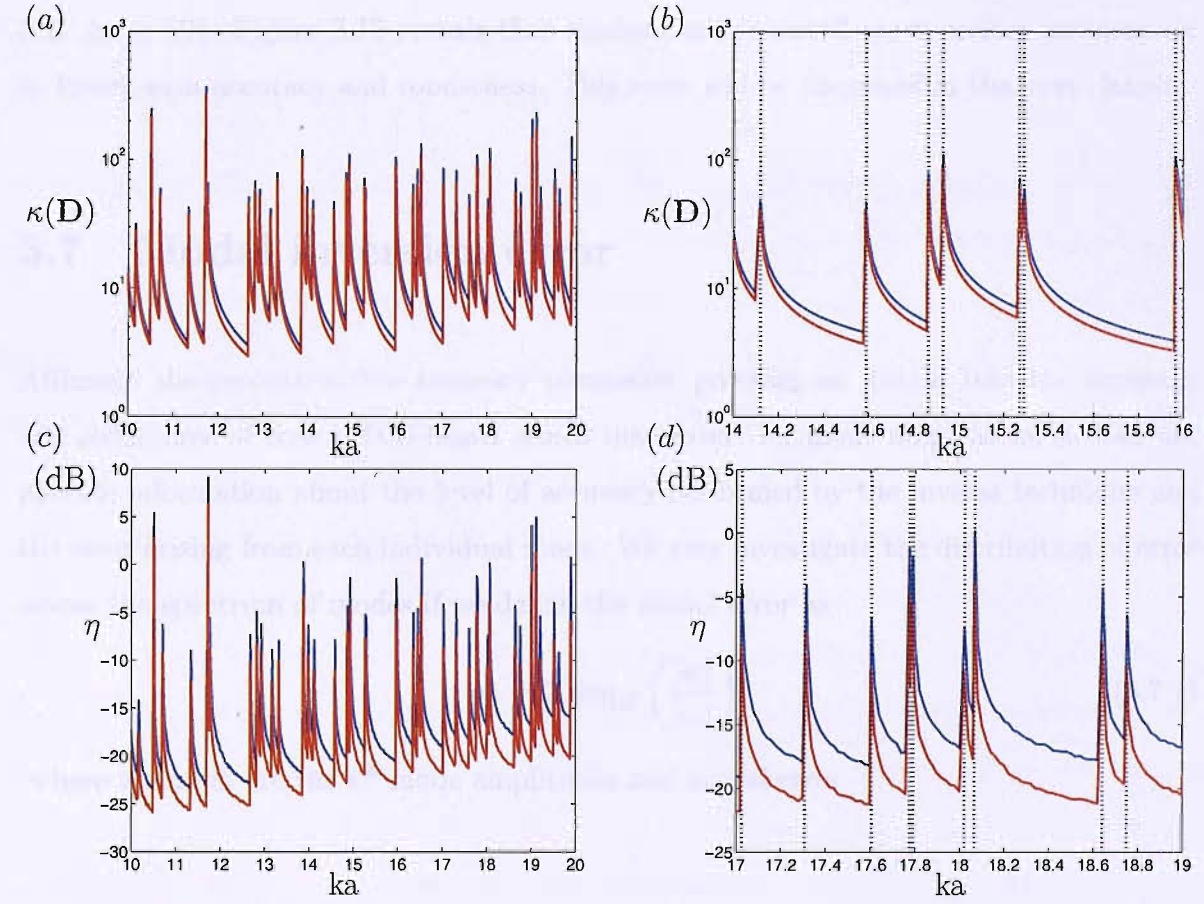

Figure 3.12: (a), (b) $\kappa(\mathbf{D})$ and (c), (d) η versus frequency for — $\nu = 5$ geodesic array and — $\nu = 6$ geodesic sensor array

Figure 3.12(c) also shows that the reconstruction accuracy tend to levels similar to that of the SNR at low frequencies when the number of cut-on modes accounted by the inversion is much lower than that of the number of sensors. The reason for this will be discussed in chapter 4. Note that between cut-on frequencies, the reconstruction accuracy only differs from a few dB between the 2 geodesic sensor arrays discussed in these simulations. This indicates that increasing the number of microphones (i.e. 70 microphones added on the TCS for the $\nu = 6$-geodesic array) does not enhance greatly the inversion accuracy and therefore demonstrates that geodesic arrays offer a good coupling between sensor positioning and complicated modal information radiated from the inlet. The $\nu = 6$-geodesic array only allows robust and accurate inversion at higher frequencies (i.e. $ka \geq 20$). Figure 3.12 reveals that modes close to cutoff are therefore problematic to invert with accuracy and robustness. This issue will be discussed in the next chapter.

3.7 Modal inversion error

Although the reconstruction accuracy parameter provides an insight into the accuracy and robustness of how a TCS-based sensor may invert for mode amplitudes, it does not provide information about the level of accuracy performed by the inverse technique and the error arising from each individual mode. We may investigate the distribution of error across the spectrum of modes if we define the modal error as

$$\bar{\eta}_i = 20\log_{10}\left(\frac{|e_i|}{|a_i|}\right) \tag{3.7.1}$$

where a_i and e_i are the i^{th} mode amplitudes and modal error.

The reconstruction accuracy parameter η provides a global measure of reconstruction accuracy averaged over all modes. The error in individual modes as defined in equation 3.7.1 is now investigated. This provides an insight into the accuracy with which modes are inverted independently and to understand which particular modes are causing inversion inaccuracies found in figure 3.12(*b*). Figures 3.13(*a*) and 3.13(*b*) show the modal error

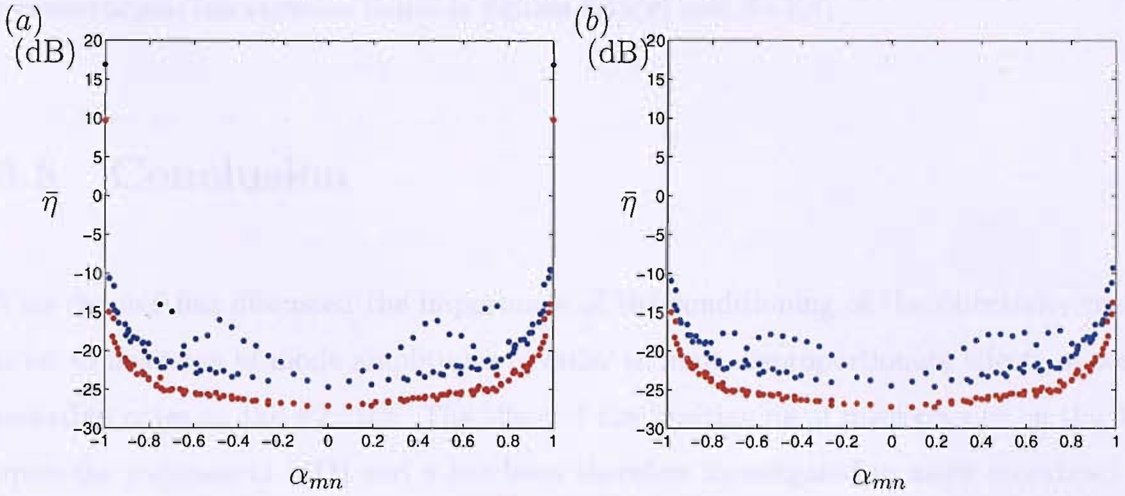

Figure 3.13: Modal error $\bar{\eta}$ (*a*) at 19.885 and (*b*) at $ka = 19.88$

● $\nu = 5$-geodesic array and ● $\nu = 6$-geodesic array

obtained from the inversion at frequencies $ka = 19.885$ and just before $ka = 19.88$, respectively, plotted against the cut-on ratio. The frequency $ka = 19.885$ coincides with a cut-on frequency. Although these two frequencies are very close, they differ in one important respect since the frequency $ka = 19.88$ is far from the previous cut-on frequency. These two frequencies are chosen to ensure the study at a cut-on frequency and away from a cut-on frequency. For ease of presentation, cut-on ratios with a negative sign denote negative spinning mode number. It is possible to observe that the modal errors across the spectrum of modes is very similar between the two frequencies shown in figure 3.13, with many modes having an inversion error of the same order as that of the SNR. The important difference between figures 3.13(*a*) and 3.13(*b*) is the additional two modes just cut-on at $ka = 19.885$, which are cutoff at $ka = 19.88$. For these two modes, $|\alpha_{mn}| = 0.999$, the modal error is found to be $\bar{\eta} \approx 20$dB. At frequencies in the vicinity of cut-on frequencies, therefore, the global reconstruction accuracy parameter η is a misleading indicator of inversion accuracy. Extremely large errors within these two modes are found to be around 40dB greater than that in most of the modes inverted. At $ka = 19.88$, just before the cut-on frequency, the range of errors across the spectrum of modes is found to be of around

12dB. Therefore, this confirms that modes close to cutoff are responsible for the large reconstruction inaccuracies found in figures 3.12(*c*) and 3.12(*d*).

3.8 Conclusion

This chapter has discussed the importance of the conditioning of the directivity matrix prior to inversion of mode amplitudes in order to limit disproportionate effects of contaminating noise on the solution. The effect of the positioning of microphones on the TCS upon the parameters $\kappa(\mathbf{D})$ and η has been therefore investigated in order to extract the most useful information of each mode. It has been shown that optimal coupling between modal radiation patterns, which form the core of the sound field, and sensor positioning, plays an important role in allowing a robust and accurate mode detection from inverse techniques. Some guidelines for the design of an optimal array geometry on the TCS have been made. Although modal information radiated from the inlet has a strong dependence on the polar direction, it has been proven that covering the TCS by sensors on both the polar and the azimuthal angles is essential to enhance the conditioning and the accuracy of the inverse problem. The study of chapter 2 showed that the modal cut-on ratio determine the main polar lobe of radiation. As the number of mode increases with frequency, the main radiation lobe of each are getting closer from one another and tending towards the duct axis. The resolution of modes with similar cut-on ratio is made from spreading of microphones over the azimuthal position. Finally, it has been shown in this chapter that measurement noise greatly contaminates modes close to cutoff and therefore damages their detection. These nearly cut-off modes strongly affect the robustness and accuracy of the full inversion. Chapter 4 investigates this problem and shows that it is inherent to the sound field radiated from the inlet and very little that can be done to get significant improvement without external numerical treatment. A broad distribution of sensors in both polar and azimuthal angles is required for robust inversion. Spiral and star-fish arrays with sufficient high number of rotations and branches satisfy this criterion. The geodesic array geometry, which offer an even spreading of microphones over the TCS, also seem to couple best the modal information since the best condition numbers and reconstruction accuracy parameters are achieved by this array geometry.

Chapter 4

Interpretation of the modal inverse problem by Singular Value Decomposition (SVD) of the modal directivity matrix

This chapter investigates the link between inversion robustness, accuracy and the presence of nearly cut-off modes. The Singular Value Decomposition (SVD) is introduced as a powerful tool for dealing with matrix inversion that enables a better understanding of the characteristics of the ill-conditioned directivity matrices discussed in section 3.3. It is also shown to be essential for describing how the condition number quantifies the sensitivity of the inversion and identifies the cause ill-conditioning.

4.1 SVD of the directivity matrix

The SVD of the modal directivity matrix **D** is a useful means of analysing the coupling between the modal distribution and the sensor position. The SVD technique essentially factorises the matrix into a product of two square unitary matrices and diagonal matrix. Any directivity matrix **D** can be decomposed into the following form

$$\mathbf{D} = \mathbf{U\Sigma V^H} \tag{4.1.1}$$

where $\mathbf{U} \in \mathbb{C}^{\mathrm{K \times K}}$ and $\mathbf{V} \in \mathbb{C}^{\mathrm{L \times L}}$ are unitary matrices and $\mathbf{\Sigma} \in \Re^{K \times L}$ is a diagonal matrix, which for an overdetermined system $K > L$ is given by

$$\Sigma = \begin{bmatrix} \sigma_1 & \cdot & \cdot & \cdot & \cdot & 0 \\ \cdot & \sigma_2 & \cdot & \cdot & \cdot & \cdot \\ \cdot & \cdot & \cdot & \cdot & \cdot & \cdot \\ \cdot & \cdot & \cdot & \cdot & \cdot & \sigma_L \\ \cdot & \cdot & \cdot & \cdot & \cdot & \cdot \\ \cdot & \cdot & \cdot & \cdot & \cdot & \cdot \\ 0 & \cdot & \cdot & \cdot & \cdot & 0 \end{bmatrix} \tag{4.1.2}$$

First consider the Hermitian matrix $\mathbf{D^H D}$, whose inverse is required in the least-squares solution of equation 3.1.9. Using equation 4.1.1 and the unitary properties of **U** and **V**

$$\mathbf{V^H V} = \mathbf{V^{-1} V} = \mathbf{U^H U} = \mathbf{U^{-1} U} = \mathbf{I} \tag{4.1.3}$$

$\mathbf{D^H D}$ can be written as

$$\mathbf{D^H D} = \mathbf{V \Sigma^T \Sigma V^H} \tag{4.1.4}$$

Comparison of equation 4.1.4 with equation 4.1.1 implies that the diagonal matrix $\mathbf{\Sigma^T \Sigma}$ contains the real and nonnegative eigenvalues of the matrix $\mathbf{D^H D}$ of size $L \times L$ and that the unitary **V** matrix contains its corresponding eigenvectors. For a matrix **D** of rank N (i.e. with $N < L$), if these eigenvalues are arranged in descending order,

$$\lambda_1 \geq \lambda_2 \geq \cdots \geq \lambda_N > \lambda_{N+1} = \lambda_{N+2} = \cdots = \lambda_L = 0 \tag{4.1.5}$$

it then follows that the elements of $\mathbf{\Sigma}$ are the square root of the corresponding eigenvalues of the matrix $\mathbf{D^H D}$, that is $\sigma_i = \sqrt{\lambda_i}$. These are called the singular values of the directivity matrix $\mathbf{D}$. The rank of the matrix $\mathbf{D}$ is equal to the number of its non-zero singular values in equation 4.1.2. If, for example, $\mathbf{D}$ had N *non-zero* singular values, so that $\sigma_{N+1},...,\sigma_L$ are zero (i.e. see equation 4.1.5), then $\mathbf{D}$ would be rank deficient and no solution would be available for $\hat{\mathbf{a}}_0$.

It is interesting to note that similar to equation 4.1.4, $\mathbf{DD^H}$ can also be expanded as

$$\mathbf{DD^H} = \mathbf{U\Sigma\Sigma^T U^H} \tag{4.1.6}$$

so that the diagonal matrix $\mathbf{\Sigma\Sigma^T}$ contains L non-zero eigenvalues of the matrix $\mathbf{DD^H}$ of size $K \times K$ and $K - L$ zero elements.

Using the properties of the unitary matrices $\mathbf{V}$ and $\mathbf{U}$ of equation 4.1.3, the pseudo-inverse of the directivity matrix, given by equation 3.1.9 may be expressed in terms of $\mathbf{U}$, $\mathbf{\Sigma}$ and $\mathbf{V}$ as follows

$$\mathbf{D^+} = \mathbf{V\Sigma^+U^H} \tag{4.1.7}$$

where $\mathbf{\Sigma^+}$ is the pseudo-inverse of $\mathbf{\Sigma}$ and can be written as

$$\mathbf{\Sigma^+} = \begin{bmatrix} 1/\sigma_1 & 0 & \cdot & \cdot & \cdot & 0 & \cdot & \cdot & 0 \\ 0 & 1/\sigma_2 & & & & \cdot & & & \cdot \\ \cdot & \cdot & & & & \cdot & & & \cdot \\ \cdot & & & & & & & & \\ 0 & 0 & & & 1/\sigma_L & 0 & & & 0 \end{bmatrix} \tag{4.1.8}$$

Substituting equation 4.1.7 into equation 3.1.9 gives the optimal estimate of the modal amplitudes vector in terms of the eigenvectors and eigenvalues of $\mathbf{D}$ as

$$\hat{\mathbf{a}}_0 = \mathbf{V\Sigma^+U^H}\hat{\mathbf{p}} \tag{4.1.9}$$

Inspection of equation 4.1.8 shows that any zero or very small singular value σ_i will result in extremely large elements of the matrix $\mathbf{\Sigma^+}$. This is extremely undesirable as demonstrated in the next section.

4.2 Interpretation of the inversion conditioning in terms of singular value distribution

Section 3.3 has shown that the conditioning of the directivity matrix to be inverted for the estimation of the mode amplitude vector $\hat{\mathbf{a}}_0$ is related to its condition number. Appendix C shows that the condition number $\kappa(\mathbf{D})$ may be related to the minimum and maximum singular values of the matrix $\mathbf{D}$, σ_{min} and σ_{max} respectively, as follows

$$\kappa\left(\mathbf{D}\right) = \frac{\sigma_{\max}}{\sigma_{\min}} \tag{4.2.1}$$

Equation 4.2.1 shows that the presence of singular values that tend to zero will cause the condition number to tend to infinity and hence will reduce the robustness of the inversion. Moreover, the behaviour of the singular value distribution also characterises the type of ill-conditioning of $\mathbf{D}$. Two classes of ill-conditioned problems typically encountered in inversion problems [28] can be determined from the 'shape' of the singular value distribution, as illustrated in figure 4.1.

The first class of problems arises from rank-deficiency problems that are characterised by a cluster of small singular values separated from the large values by a well-determined gap. This kind of singular value spectrum is illustrated in blue in figure 4.1. This implies nearly linear combinations between some of the rows or columns of the matrix $\mathbf{D}$. The directivity matrix in this case contains almost redundant information. As outlined in chapter 3 the design of an TCS array can be optimised to avoid modal information redundancies.

Another class of problems arises from ill-posedness that result from the discretisation of ill-posed problems defined in equation 3.1.2, such as the Rayleigh integral for the mode detection problem. In this case, all singular values on average gradually decay to zero. This kind of singular value spectrum is illustrated in red in figure 4.1. Since there is no well-defined gap in the singular value spectrum, there is no notion of a numerical rank for $\mathbf{D}$. The goal is to define another cost function from that defined in equation 3.1.7,

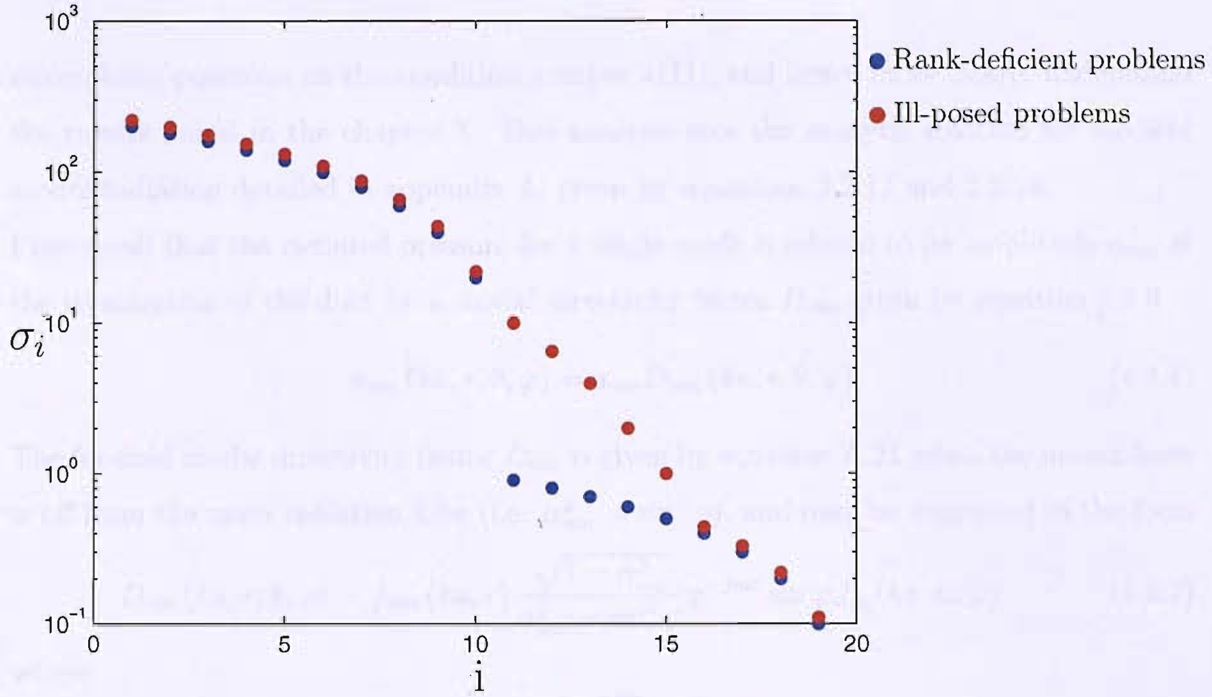

Figure 4.1: Illustration of singular value spectra

which consists of applying an additional constraint on the solution such that it minimises the residual norm $||\hat{\mathbf{p}} - \mathbf{p}||_2$ and the norm of the expected computed solution. Several approaches to the stabilisation of the optimal estimate of the modal amplitudes vector will be considered in chapter 5.

4.3 The simple case of the inversion of a few modes from pressure measurements at few microphone positions

Prior to investigating how the SVD relates to the ill-conditioning of $\mathbf{D}$, it is enlightening to study the simple case of inverting for two or three modes with two or three microphones. This will allow the analytic examination of the relationship between modal radiation and microphone positions on the condition number $\kappa(\mathbf{D})$, and hence more clearly understand the results found in the chapter 3. This analysis uses the analytic solution for far-field modal radiation detailed in appendix A, given by equations 2.2.17 and 2.2.18.

First recall that the radiated pressure for a single mode is related to its amplitude a_{mn} at the termination of the duct by a modal directivity factor D_{mn} given by equation 2.2.9

$$p_{mn}\left(ka,r,\theta,\varphi\right)=a_{mn}D_{mn}\left(ka,r,\theta,\varphi\right) \tag{4.3.1}$$

The far-field modal directivity factor D_{mn} is given by equation A.21 when the microphone is off from the main radiation lobe (i.e. $\alpha^2_{mn}\neq\sin^2\varphi$), and may be expressed in the form

$$D_{mn}\left(ka,r,\theta,\varphi\right)=f_{mn}\left(ka,r\right)\frac{\sqrt{1-\alpha^2_{mn}}}{\alpha^2_{mn}-\sin^2\varphi}e^{-jm\theta}\sin\varphi J'_m\left(ka\sin\varphi\right) \tag{4.3.2}$$

where

$$f_{mn}\left(ka,r\right)=j^{m+1}\frac{e^{-jkr}}{r}\frac{a}{\sqrt{\Lambda_{mn}}}J_m\left(\kappa_{mn}a\right) \tag{4.3.3}$$

4.3.1 Two modes and two sensors

For simplicity we first assume that only two modes are present and their radiation measured by two microphones. The pressure can then be related to the mode amplitudes by

$$\begin{bmatrix} p_1 \\ p_2 \end{bmatrix}=\begin{bmatrix} D_{11} & D_{12} \\ D_{21} & D_{22} \end{bmatrix}\begin{bmatrix} a_1 \\ a_2 \end{bmatrix} \tag{4.3.4}$$

Since it has been shown in section 4 that the eigenvalues of the matrix $\mathbf{G}=\mathbf{D^HD}$ are found to be the square of singular values of $\mathbf{D}$, the condition number can be written as

$$\kappa\left(\mathbf{D}\right)=\sqrt{\frac{\lambda_{\max}}{\lambda_{\min}}} \tag{4.3.5}$$

where λ_{min} and λ_{max} are the eigenvalues of the matrix $\mathbf{D^HD}$.

The matrix $\mathbf{G}=\mathbf{D^HD}$ is written as

$$\begin{bmatrix} G_{11} & G_{12} \\ G_{21} & G_{22} \end{bmatrix}=\begin{bmatrix} D^*_{11}D_{11}+D^*_{21}D_{21} & D^*_{11}D_{12}+D^*_{21}D_{22} \\ D^*_{12}D_{11}+D^*_{22}D_{21} & D^*_{12}D_{12}+D^*_{22}D_{22} \end{bmatrix} \tag{4.3.6}$$

whose eigenvalues are deduced from

$$\det\left(\mathbf{G}-\lambda\mathbf{I}\right)=0 \tag{4.3.7}$$

Solving for λ, the condition number can be written in the form

$$\kappa\left(\mathbf{D}\right)=\sqrt{\frac{1+\sqrt{1-4A}}{1-\sqrt{1-4A}}} \tag{4.3.8}$$

where

$$A=\frac{G_{11}G_{22}-G_{12}G_{21}}{\left(G_{11}+G_{22}\right)^2} \tag{4.3.9}$$

$\kappa(\mathbf{D})\mapsto\infty$ for $A\mapsto 0$, i.e. when $G_{11}G_{22}-G_{12}G_{21}\mapsto 0$ since the denominator of equation 4.3.9 cannot go to zero. If the sensors are located at (φ_1,θ_1) and $(\varphi_2,\theta_1+\Delta\theta)$, equation 4.3.9 can be written using equation 4.3.2.

Thus $A=0$ when

$$\left(1-\alpha_1^2\right)\left(1-\alpha_2^2\right)H_{m_1m_2n_1n_2}\left(ka,\varphi_1,\varphi_2,\theta\right)=0 \tag{4.3.10}$$

where $H_{m_1m_2n_1n_2}\left(ka,\varphi_1,\varphi_2,\theta\right)$ written in full is a complicated factor, which involves combinations of Bessel functions whose details are unimportant for the purpose of this analysis. The factor H can only equal zero due to an unfortunate and unlikely choice of modes and sensor positions. The sensors at these locations are therefore said to be not well-coupled with the modes. This may be prevented by designing an appropriate TCS sensor array as investigated in chapter 3, and by employing more sensors than modes.

Equation 4.3.10 demonstrates clearly that the condition number tends to infinity if at least one mode is excited at frequencies close to the cut-on frequency, i.e. $\alpha_{mn}\approx 1$. In this case, a robust inversion may not be performed regardless of where the microphones are positioned.

If at least one of these two modes is excited close to its cut-on frequency, say $\alpha_1\approx 1$, $A<<1$, and the denominator of equation 4.3.8 may be approximated by

$$\sqrt{1-\sqrt{1-4A}}\approx\sqrt{2A}\qquad(A<<1) \tag{4.3.11}$$

The condition number in this limit converges to

$$\kappa(\mathbf{D}) \mapsto \sqrt{\frac{1-A}{A}} \approx \frac{1}{\sqrt{A}} \qquad (A \mapsto 1) \qquad (4.3.12)$$

From equation 4.3.10, the condition number at frequencies close to a single cut-on frequency behaves as

$$\kappa(\mathbf{D}) \mapsto \frac{B_1(ka)}{\sqrt{1-\alpha_1^2}} \qquad (\alpha_1 \mapsto 1) \qquad (4.3.13)$$

where B_1 is a complicated factor involving combinations of Bessel functions and is a slowly varying function of frequency.

However, in practice, cut-on frequencies of the non axi-symmetric modes (i.e. $m \neq 0$) occur in pairs such for every (m, n) mode there is a corresponding $(-m, n)$ mode with identical cut-on ratio α_{mn}. In this case, the lowest number of sensors and modes which incorporates the behaviour of $\kappa(\mathbf{D})$ in the vicinity of a cut-on frequency containing such a pair of modes is three.

4.3.2 Three modes and three sensors

The details of the inversion of three modes by three microphones at a cut-on frequency are given in appendix D. It is shown that the behaviour of the condition number of $\mathbf{D}$ for three modes and three sensors, where two modes with identical cut-on frequencies and cut-on ratios α_{mn} are excited at frequencies close to these cut-on frequencies, varies according to

$$\kappa(\mathbf{D}) \mapsto \frac{B_2}{\sqrt{1-\alpha_{mn}^2}} \qquad (\alpha_{mn} \mapsto 1) \qquad (4.3.14)$$

This expression is identical to equation 4.3.13 but with a different factor B.

Even though this analysis is carried out in sections 4.3.1 and 4.3.2 for the inversion of a few modes, equations 4.3.13 and 4.3.14 also apply at frequencies close to a modal cut-on frequency while inverting for a much larger number of modes using a greater number of microphones. It is interesting to note that such behaviour of the condition number $\kappa(\mathbf{D})$ is affected only by the presence of the pair of modes closest to cutoff. The TCS sensor geometries, discussed in chapter 3, that aims to give good coupling between the modes and the sensor positions will not allow robust inversion at frequencies close to a cut-on frequency. The ill-conditioning that arises due to the presence of nearly cut-off modes is therefore the most problematic, particularly at high ka, when the modal density is high and the likelihood of at least one mode being close to cut-off is high. This likelihood is addressed in section 4.4

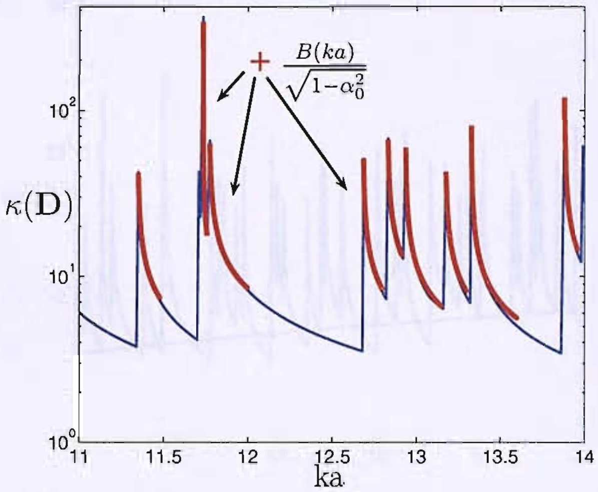

Figure 4.2: Asymptotic behaviour of the condition number at the cut-on frequencies

The variation of the condition number with frequency for the $\nu = 6$-geodesic sensor array, already shown in figure 3.12, is reproduced below in blue in figure 4.2. Also shown in red is the function defined in equations 4.3.13 and 4.3.14 where B is chosen such that the function fits with $\kappa(\mathbf{D})$. The asymptotic function $(1-\alpha_{mn}^2)^{-1/2}$ is found to be in very close agreement with the exact variation of $\kappa(\mathbf{D})$ at frequencies in the vicinity of the cut-on frequencies.

The presence of modes that are just cut-on is therefore critical for the conditioning of the directivity matrix. These modes radiate inefficiently and thus their detection is greatly affected by noise contaminating the measurements. Techniques aimed at enhancing the conditioning of **D** by introducing some further constraints on the solution will be discussed in chapter 5.

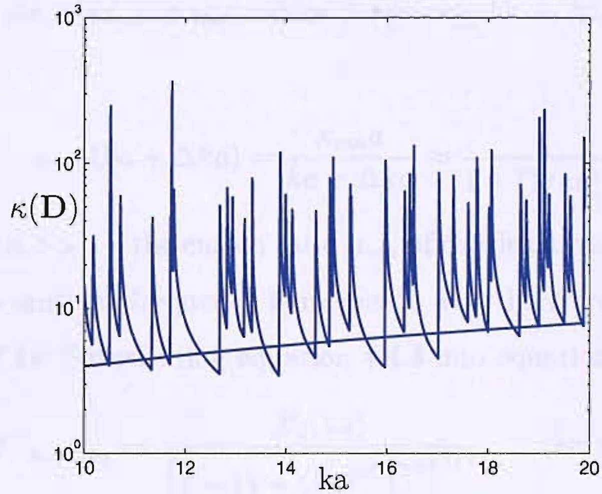

Figure 4.3: Behaviour of the 'minimum' condition number. The function 'ka' follows the overall variation between the cut-on frequencies

4.4 Frequency dependence of the 'minimum' condition number

In this section we investigate the behaviour of $\kappa(\mathbf{D})$ between cut-on frequencies. In the absence of flow, the number of modes L with cut-on frequencies below a frequency ka is approximately given by [29]

$$L\,(ka) \approx \frac{1}{2}ka + \left(\frac{1}{2}ka\right)^2 \tag{4.4.1}$$

The number of propagating modes within a unit frequency band is therefore given by

$$l\,(ka) = \frac{L\,(ka + \delta ka) - L\,(ka)}{\delta ka} \approx \frac{dL}{d\,(ka)} \approx ka \tag{4.4.2}$$

It therefore follows that the average frequency separation between adjacent cut-on modes is

$$\Delta ka \approx \frac{1}{ka} \tag{4.4.3}$$

Consider a single mode excited at its cut-on frequency, $ka = \kappa_{mn}a$, such that $\alpha(ka) = 1$. Its cut-on ratio at the next average cut-on frequency $ka + \Delta ka$, from equation 4.4.3 therefore becomes

$$\alpha_{mn}(ka + \Delta ka) = \frac{\kappa_{mn}a}{ka + \Delta ka} \approx \frac{1}{1 + (1/ka)^2} \tag{4.4.4}$$

At high frequency ($ka >> 1$), the cut-on ratio α_{mn} of this least cut-on mode will therefore also remain close to unity as frequency is increased and therefore also contribute to the poor conditioning of $\mathbf{D}$. Substituting equation 4.4.4 into equation 4.3.14 gives

$$\kappa(\mathbf{D})|_{ka+\Delta ka} \mapsto \frac{B_3(ka)}{\left[1 - \left(1 + (ka)^{-2}\right)^{-2}\right]^{1/2}} \qquad (ka \neq \kappa_{mn}a) \tag{4.4.5}$$

A series expansion of $\kappa(\mathbf{D})$ in ka, to leading term, is of the form

$$\kappa(\mathbf{D})|_{ka+\Delta ka} \mapsto \frac{B_3(ka)}{\left[1 - \left(1 - 2(ka)^{-2}\right)\right]^{1/2}} \mapsto B_3(ka) \cdot ka \tag{4.4.6}$$

The function given by equation 4.4.6 is shown in figure 4.3 and is on close agreement with the variation of the 'minimum' value of $\kappa(\mathbf{D})$ with a value of B_3 that depends on the sensor positioning. This lower bound value is observed to increase over the whole range of frequencies shown in figure 4.3. The function given by equation 4.4.6 clearly shows that the overall increase is due to an increase of modes to be inverted while the number of sensors remains fixed.

The singular value analysis of the directivity matrix has been shown to be useful in understanding the essential problem of mode inversion in the vicinity of the cut-on frequencies. It is also useful in finding a compromise that provides the best trade-off between robustness and accuracy. The interpretation of the singular values and singular vectors afforded by the SVD is discussed below. It will provide a diagnosis of how well the TCS array is coupled with the radiated sound field and what modal information is sensitive to the presence of external noise measurements following inversion.

4.5 Interpretation of the SVD of the Directivity matrix

Recall that using the SVD of **D**, the vector of radiated pressures **p** at the TCS can be expressed as

$$\mathbf{p} = \mathbf{U}\Sigma\mathbf{V}^{\mathbf{H}}\mathbf{a} \tag{4.5.1}$$

Now using the unitary property of the matrix **U** (i.e. $\mathbf{U}^{\mathbf{H}}\mathbf{U} = \mathbf{I}$), pre-multiplication of this equation by $\mathbf{U}^{\mathbf{H}}$ results in

$$\mathbf{U}^{\mathbf{H}}\mathbf{p} = \Sigma\mathbf{V}^{\mathbf{H}}\mathbf{a} \tag{4.5.2}$$

Multiplying a vector quantity by either one of these unitary matrices **U** or **V** is equivalent to applying a transformation, which enables the investigation inherent of the properties of this quantity in terms of another set of basis functions. If we define the vector of transformed complex pressures as

$$\tilde{\mathbf{p}} = \mathbf{U}^{\mathbf{H}}\mathbf{p} \tag{4.5.3}$$

and the transformed set of amplitudes as

$$\tilde{\mathbf{a}} = \mathbf{V}^{\mathbf{H}}\mathbf{a} \tag{4.5.4}$$

equation 4.5.2 shows that

$$\tilde{\mathbf{p}} = \Sigma\tilde{\mathbf{a}} \tag{4.5.5}$$

Thus the vector of transformed mode amplitudes is related to the vector of transformed acoustic pressures by the singular values of the directivity matrix. The vector of transformed mode amplitudes and the vector of transformed pressures are both linear combinations of their respective original vectors, namely the vectors of mode amplitudes and of pressure measurements. The unitary property of **U** and **V** enables the investigation of the radiated pressures and mode amplitudes into another set of basis functions [14], [30] and [18] which is also an essential property of Fourier wavenumber transforms (spatial

Fourier transforms). These transformed vectors depend on the TCS sensor array and therefore determine how the modal distribution over the duct outlet cross-section is coupled with the radiated sound field detected by the TCS sensor array.

Following equation 4.5.5 the right singular vectors contained in the unitary matrix $\mathbf{V}$ possess information about the modal distribution over the duct outlet cross-section. Similarly, the left singular vectors contained in the unitary matrix $\mathbf{U}$ possess information relating to the radiated sound field. It should be noted that, at a single frequency, the transformation process associated with the SVD is dependent upon the geometry of the TCS array. In other words, the elements of $\mathbf{U}$ and $\mathbf{V}$ are thus entirely determined by mode distribution/TCS sensor coupling. The mapping of the mode distribution over the duct outlet cross-section into the radiated sound field performed by equation 4.5.5 is related by the real singular values and quantifies this coupling. It will therefore be important to investigate the behaviour of the singular values as well as the right and left singular vectors of the directivity matrix, for the various TCS arrays. The former determines the efficiency of each transformed mode in the radiated field detected by the TCS while the latter specifies the modal content of these transformations.

Equation 4.5.5 shows that the transformed acoustic pressures, given by the column vectors of the unitary matrix $\mathbf{U}$, result from L different transformed mode amplitudes. Each of these transformed mode amplitudes is weighted by its associated singular value and forms a basis of acoustic modes defined by the column vectors of the unitary matrix $\mathbf{V}$, as shown in equation 4.5.6. Since the singular values are sorted in decreasing order, most of the radiation informations detected by the TCS sensor array are found within the singular vectors associated with high singular values. If $\mathbf{v_i}$ denotes the i^{th} column vector of the matrix $\mathbf{V}$, the i^{th} transformed mode amplitude is given by

$$\tilde{a}_i = \sum_{j=1}^{L} v_{ji}^{*} a_j \tag{4.5.6}$$

Each transformed mode amplitude $\tilde{a}_i$ is therefore a linear combination of acoustic modes.

Its associated singular value indicates how well $\tilde{a}_i$ is detected by the TCS array and its associated right singular vector $\mathbf{v_i}$ quantifies the content of acoustic modes. In other words, the TCS sensor array detects most strongly acoustic modes that are dominant within right singular vectors associated with large singular values. Conversely, acoustic modes principally found within right singular vectors associated with small singular values will not be strongly detected. Section 4.2 showed the influence of singular values in the conditioning of the directivity matrix. Inspection of the right and left singular vectors provides a more complete analysis of the inverse problem as it will determine which acoustic modes are sensitive to measurement noise and those which are not.

4.5.1 Singular value distribution

In this section we provide an interpretation of the singular values of **D**. The singular value analysis can be performed to give an expression for the radiation efficiency. This is done by recalling that the total mean radiated acoustic power is given by

$$W = \frac{1}{2\rho c}\mathbf{p^H p}\delta A \tag{4.5.7}$$

where ρ and c are the air density and speed of sound and δA is the average surface area defined by a single microphone on the TCS.

Using the relationship between the acoustic and transformed pressures $\mathbf{p} = \mathbf{U}\tilde{\mathbf{p}}$ and the unitary properties of the matrix **U** leads to an expression for the radiated power

$$W = \frac{1}{2\rho c}\tilde{\mathbf{p}}^{\mathbf{H}}\tilde{\mathbf{p}}\delta \mathbf{A} \tag{4.5.8}$$

Equation 4.5.8 is analoguous to a Parseval's theorem in sprectral analysis. Introducing equation 4.5.5 into equation 4.5.8 gives

$$\begin{aligned} W &= \frac{1}{2\rho c}\tilde{\mathbf{a}}^{\mathbf{H}}\Sigma^{\mathbf{T}}\Sigma\tilde{\mathbf{a}}\delta A \\ &= \frac{\delta A}{2\rho c}\sum_{i=1}^{L}\sigma_i^2|\tilde{a}_i|^2 \end{aligned} \tag{4.5.9}$$

Equation 4.5.9 suggests that the sound power can be expressed as the sum of the acoustic powers $\tilde{W}_i$ of L transformed modes

$$W = \sum_{i=1}^{L} \tilde{W}_i \tag{4.5.10}$$

The singular values are therefore directly related to the radiation efficiency of the transformed mode

$$\sigma_i^2 = \frac{2\rho c \tilde{W}_i}{|\tilde{a}_i|^2 \delta A} \tag{4.5.11}$$

Small singular values are therefore related with inefficiently radiating transformed modes. Figure 4.4(a) shows the variation frequency of the 3 largest singular values. These maximum singular value describe the radiation efficiency of transformed modes and have similar trend to the radiation efficiency of acoustic duct modes as shown in Morfey [20]. On the other hand, the variation with frequency of the smallest singular value shown in figure 4.4(b) has a totally different behaviour. This singular value decreases significantly at cut-on frequencies. This clearly demonstrates that this minimum singular value is responsible for the large order of magnitudes of the condition number at cut-on frequencies as shown in figure 4.2. The radiation efficiency of the transformed mode associated with this singular value is indeed very low at cut-on frequencies.

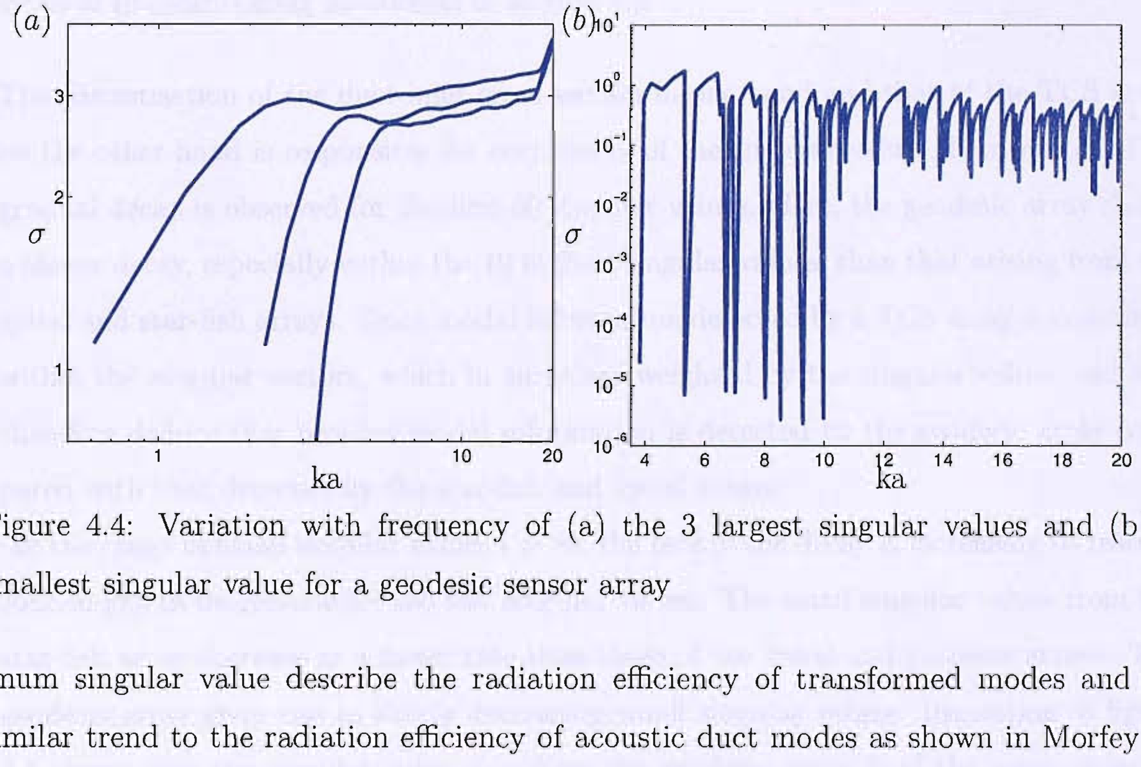

Figure 4.4: Variation with frequency of (a) the 3 largest singular values and (b) the smallest singular value for a geodesic sensor array

The distribution of singular values is important in determining which 'modes' dominate the sound field detected by the TCS array. Robust inversion would be achieved if all transformed modes were detected by the TCS array with equal efficiency. Ideally, from equation 4.2.1, one would expect the singular values to be all equal for a well-conditioned directivity matrix so that it results in a condition number of unity (the smallest theoretical value of κ). Figure 4.5 shows the spectra of singular values of the modal directivity matrix resulting from a spiral, a star-fish and a geodesic sensor arrays respectively at a frequency of $ka = 20$. These spectra display a gradual decay of singular values followed by well-defined gap followed by very small singular values. Thus figure 4.5 displays both types of ill-conditioning mentioned in section 4.2.

The discretisation of the duct inlet cross-section in one hand and that of the TCS array on the other hand is responsible for such decay of the singular values distribution. This gradual decay is observed for the first 80 singular values. Here, the geodesic array shows a slower decay, especially within the 10 highest singular values, than that arising from the spiral and star-fish arrays. Since modal information detected by a TCS array is contained within the singular vectors, which in turns are weighted by the singular values, one can therefore deduce that broader modal information is detected by the geodesic array compared with that detected by the star-fish and spiral arrays.

In the range of small singular values $i > 80$, the rate of the decay is increasing to reach a sudden gap in magnitude for the last singular values. The small singular values from the star-fish array decrease at a faster rate than those of the spiral and geodesic arrays. The geodesic array gives rise to slowly decreasing small singular values. Inspection of figure 4.5 shows that the singular value σ_{107} from the geodesic array is of the same order as σ_{100} and σ_{94} from the spiral and star-fish array respectively. Since singular values define the level of contribution of their corresponding singular vectors, each of which has the potential of modal information detected by the sensor array, one can again expect the geodesic array to detect broader modal information than spiral and star-fish arrays.

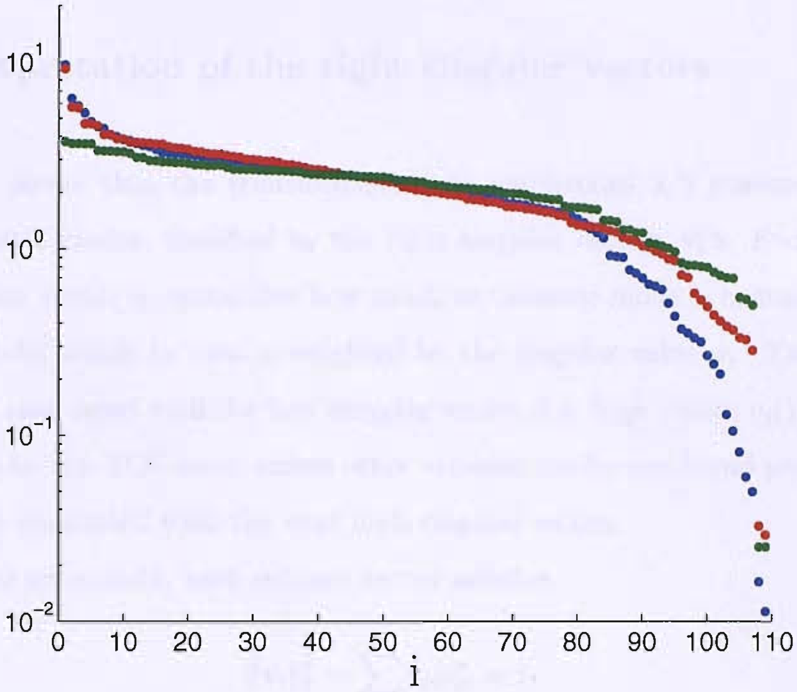

Figure 4.5: Spectra of singular values at $ka = 19.885$ for ● Uniform 20 leg star-fish array ● Uniform 10 rotation spiral array ● $\nu = 5$ geodesic array

One of the various scheme for enhancing the conditioning of $\mathbf{D}$ discussed in chapter 5 consists of discarding small singular values. This common method of improving inversion robustness introduces some inherent inaccuracies into the reconstructed solution. The size of this error increases with the number of singular values discarded. Consequently, a flat singular value spectrum is therefore desired in order to reduce the need of discarding many singular values. It is therefore possible to see from figure 4.5 that discarding only 2 singular values from the geodesic array enhances greatly the condition number while a greater effort corresponding to around 25 singular values discarded is required to achieve the same improvement for star-fish and spiral arrays therefore introduces larger inaccuracies. This again underlines the importance of sensor positioning for robust inversion at the cut-on frequencies.

4.5.2 Interpretation of the right singular vectors

Equation 4.5.6 shows that the transformed mode amplitudes $\tilde{a}_i$'s possess a particular content of acoustic modes, specified by the right singular vectors $\mathbf{v}_i$'s. Each element j^{th} of the i^{th} singular vector v_{ji} quantifies how much an acoustic mode is contained in the i^{th} transformed mode, which in turn is weighted by the singular value σ_i. Thus, dominant acoustic modes associated with the first singular vector (i.e. high values v_{j1}) are the 'best' detected modes by the TCS array unless other acoustic modes are found present in many singular vectors associated with the next high singular values.

Since $\mathbf{V}$ is a unitary matrix, each column vector satisfies

$$\|\mathbf{v}_i\|_2^2 = \sum_{j=1}^{L} v_{ji} v_{ij}^* = 1 \tag{4.5.12}$$

so that $|v_{ij}|^2$ quantifies the fractional contribution to the i^{th} singular vector by the j^{th} acoustic mode.

Figures 4.6 and 4.7 show the first 9 and last 9 singular vectors $\mathbf{v}_i$ plotted against the cut-on ratio α_{mn} respectively. The $\nu = 5$ and $\nu = 6$-geodesic sensor arrays are shown in blue and red respectively in figures 4.6 and 4.7. Again, for clarity of presentation, modes with negative spinning mode numbers are identified by a negative cut-on ratio.

It is clear that the content of singular vectors associated with the largest singular values comprise mostly of well cut-on modes (i.e. $|\alpha_{mn}| < 0.5$). Modes close to cutoff (i.e.$|\alpha_{mn}| > 0.8$) , however, are found in the singular vectors associated with small singular values ($i > 80$). This is particularly true for the singular vectors associated with the pair of smallest singular values shown in figure 4.5. They contain only the two modes that are just cut-on at this frequency (i.e. $|\alpha_{mn}| \approx 1$). This confirms the presence of near cut-off modes as being responsible for high condition numbers, and hence the cause of the difficulty in inverting for all modes with accuracy in the presence of noise. One can also observe from figures 4.6 and 4.7 that only a few acoustic modes are contained

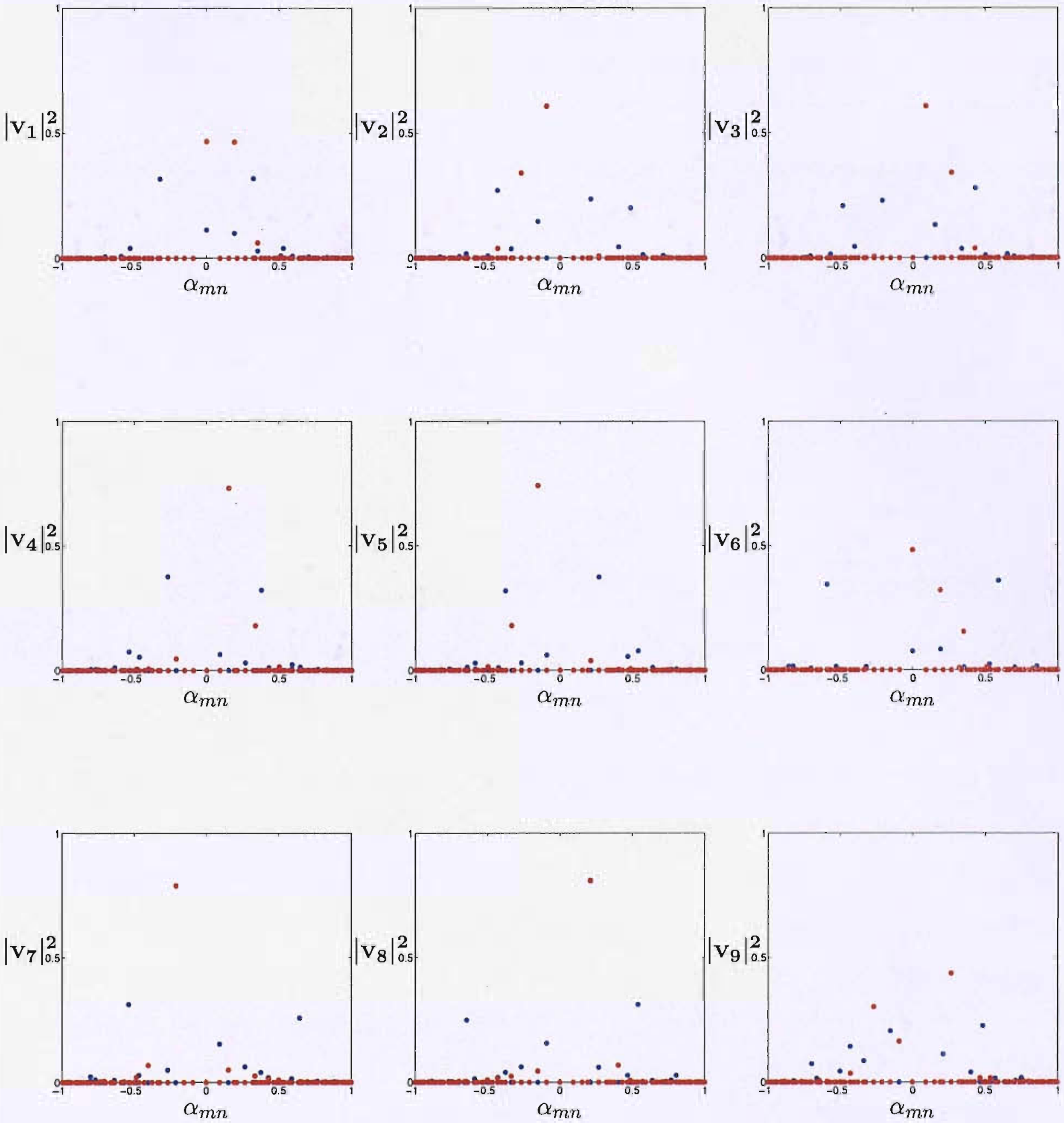

Figure 4.6: First 9 right singular vectors against α_{mn} at $ka = 19.885$

● $\nu = 5$-geodesic array ● $\nu = 6$-geodesic array

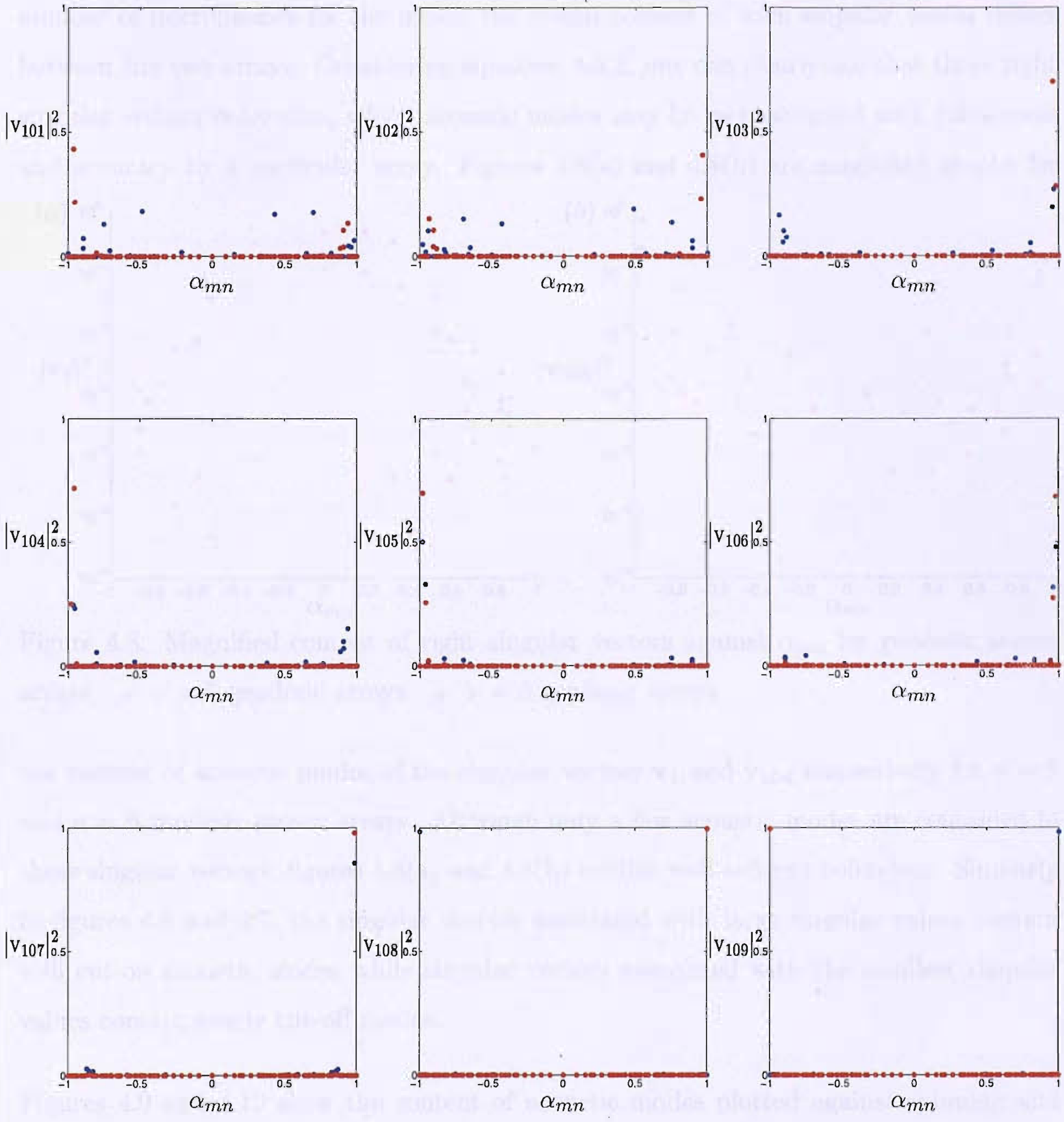

Figure 4.7: Last 9 right singular vectors against α_{mn} at $ka = 19.885$

● ν = 5-geodesic array ● ν = 6-geodesic array within each right singular vector. Although the geometry of $\nu = 5$ and $\nu = 6$-geodesic sensor arrays follow the same distribution of microphones over the TCS but with a larger number of microphones for the latter, the modal content of each singular vector differs between the two arrays. Considering equation 4.5.2, one can clearly see that these right singular vectors determine, which acoustic modes may be reconstructed with robustness and accuracy by a particular array. Figures 4.8(a) and 4.8(b) are magnified graphs for the content of acoustic modes of the singular vectors $\mathbf{v}_1$ and $\mathbf{v}_{104}$ respectively for $\nu = 5$ and $\nu = 6$-geodesic sensor arrays. Although only a few acoustic modes are contained in these singular vectors, figures 4.8(a) and 4.8(b) exhibit well-ordered behaviour. Similarly to figures 4.6 and 4.7, the singular vectors associated with large singular values contain well cut-on acoustic modes while singular vectors associated with the smallest singular values contain nearly cut-off modes.

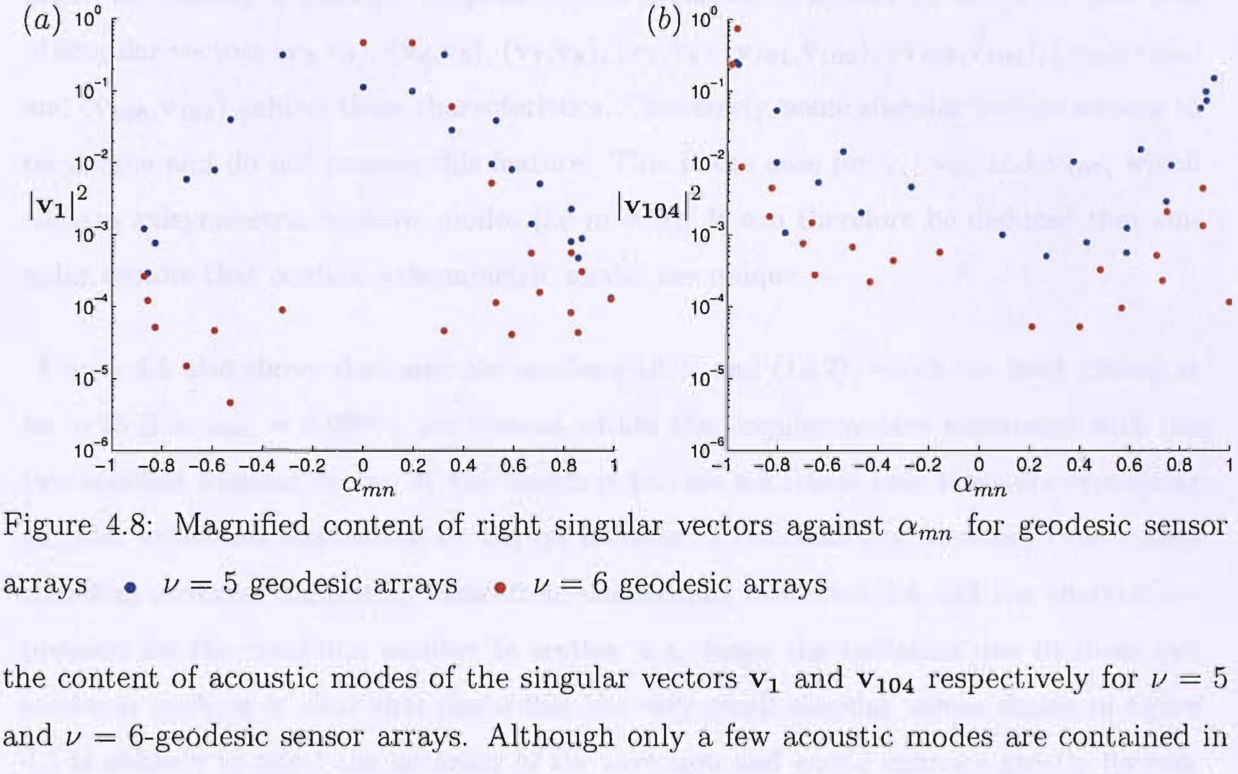

Figure 4.8: Magnified content of right singular vectors against α_{mn} for geodesic sensor arrays ● $\nu = 5$ geodesic arrays ● $\nu = 6$ geodesic arrays

Figures 4.9 and 4.10 show the content of acoustic modes plotted against spinning and radial mode numbers (m, n) within the right singular vectors associated with the largest and smallest singular values respectively for a $\nu = 6$-geodesic array. These figures show a high degree of symmetry between different pairs of right singular vectors. It is interesting to note that these pairs are formed from two consecutive right singular vectors and are shown in blue and red (i.e. see figures 4.9(b) and 4.9(c) for example). The acoustic modes within these pairs are found to be identical but with the spinning mode number of these modes reversed in sign. This property follows from the symmetry of the directivity matrix $\mathbf{D}$, in which for every term with the factor $e^{-jm\theta}$ (i.e. $m \neq 0$), there is an equivalent term $e^{jm\theta}$. Equivalently, this pairing could also be written in terms of $\sin\theta$ and $\cos\theta$. This explains the pairing of the right singular vectors presented in figures 4.9 and 4.10. The pair of singular vectors ($\mathbf{v}_2$,$\mathbf{v}_3$), ($\mathbf{v}_4$,$\mathbf{v}_5$), ($\mathbf{v}_7$,$\mathbf{v}_8$), ($\mathbf{v}_7$,$\mathbf{v}_8$) ($\mathbf{v}_{101}$,$\mathbf{v}_{102}$), ($\mathbf{v}_{103}$,$\mathbf{v}_{104}$), ($\mathbf{v}_{105}$,$\mathbf{v}_{106}$) and ($\mathbf{v}_{108}$,$\mathbf{v}_{109}$) exhibit these characteristics. Conversely, some singular vectors appear to be unique and do not possess this feature. This is the case for $\mathbf{v}_1$, $\mathbf{v}_6$, and $\mathbf{v}_{107}$, which contain axisymmetric acoustic modes (i.e $m = 0$). It can therefore be deduced that singular vectors that contain axisymmetric modes are unique.

Figure 4.5 also shows that only the modes (-13,2) and (13,2), which are least cut-on at $ka = 20$ (i.e. $\alpha_{mn} = 0.9996$), are present within the singular vectors associated with the two smallest singular values. It was shown in section 4.5.1 that only these corresponding singular values are responsible for abrupt increase of the condition number. This feature therefore confirms the results found from simulations in section 3.6 and the analytic expression for the condition number in section 4.3. Since the radiation due to these two modes is weak, it is clear that discarding the very small singular values shown in figure 4.5 is unlikely to affect the accuracy of the inversion and would enhance greatly its conditioning. Some other forms of regularisation may also be more effective for other sensor geometries that lead to different singular value spectra and different right singular vectors. Various forms of numerical treatment for stabilising the solution will be discussed in chapter 5.

The right singular vectors contained in $\mathbf{V}$ possess information about the modal distribution over the duct outlet cross-section. By analogy with equation 4.5.6, the TCS sensor array detects a set of transformed mode shape functions over the duct outlet cross-section

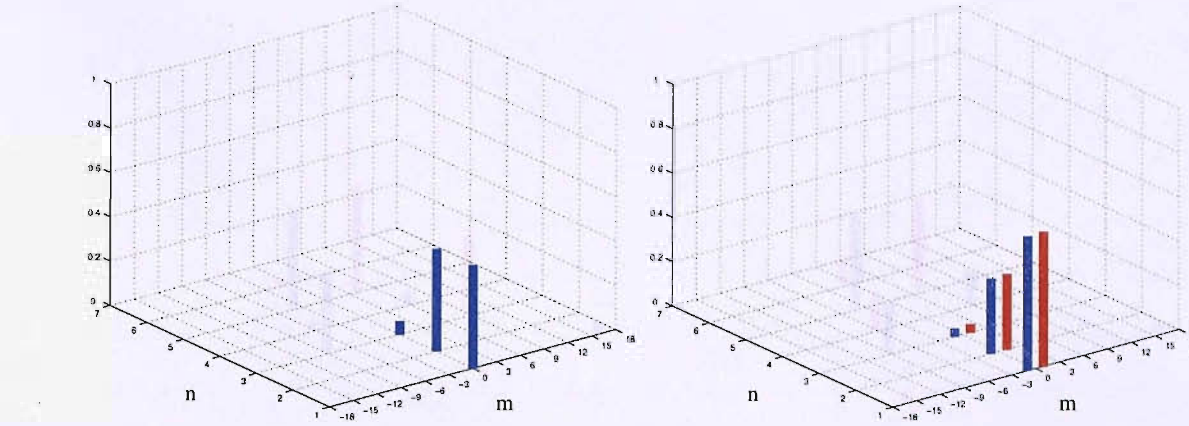

(a) $\mathbf{v_1}$ (b) $\mathbf{v_2}$ & $\mathbf{v_3}$

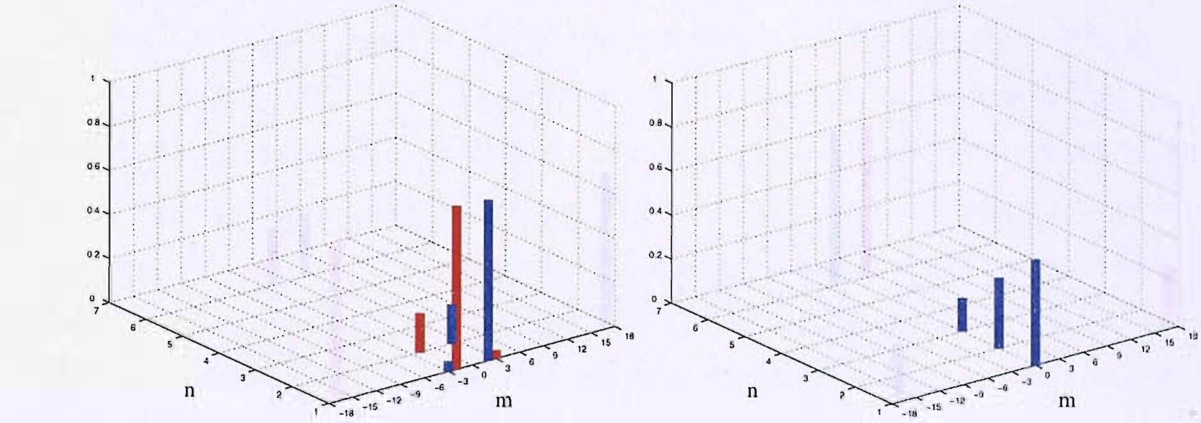

(c) $\mathbf{v_4}$ & $\mathbf{v_5}$ (d) $\mathbf{v_6}$

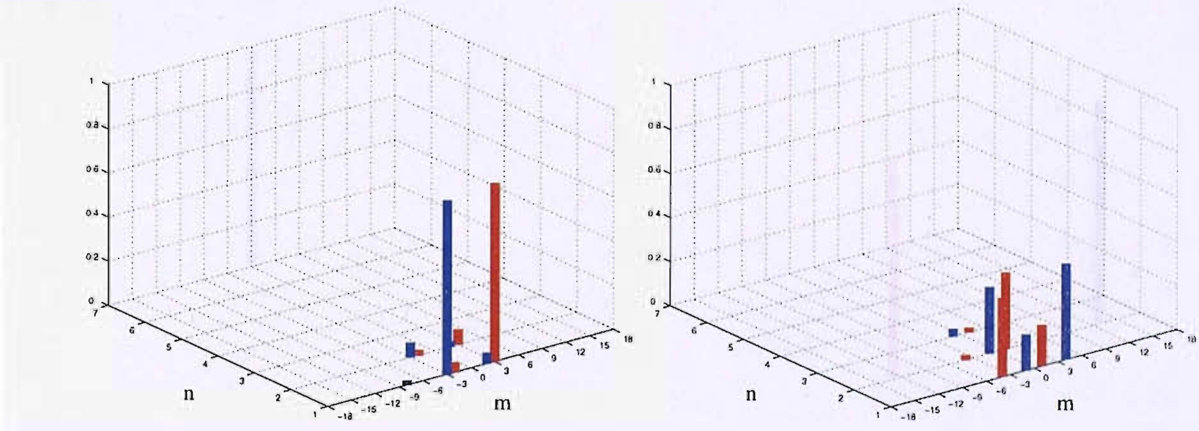

(e) $\mathbf{v_7}$ & $\mathbf{v_8}$ (f) $\mathbf{v_9}$ & $\mathbf{v_{10}}$

Figure 4.9: Modal content in right singular vectors associated with large singular values for a $\nu = 6$-geodesic sensor array

— and — show pairs formed by 2 consecutive singular vectors

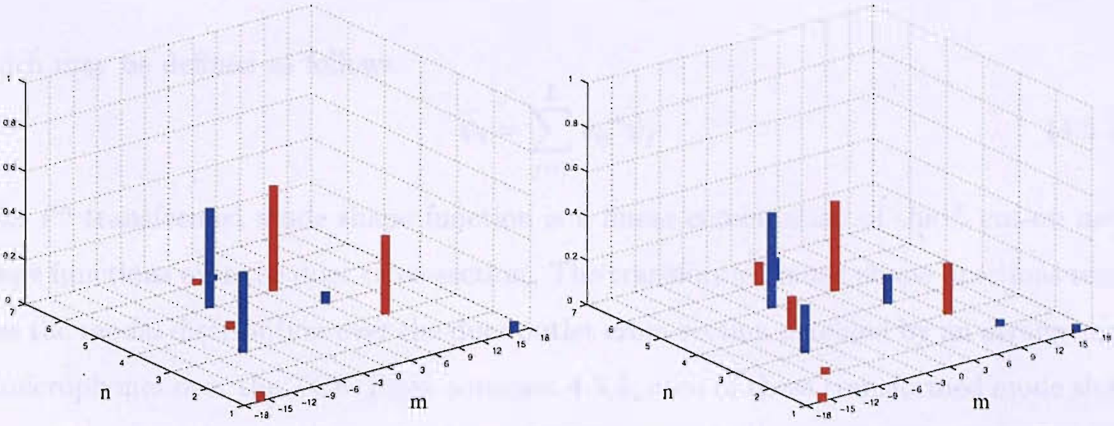

(a) $\mathbf{v}_{99}$ & $\mathbf{v}_{100}$ (b) $\mathbf{v}_{101}$ & $\mathbf{v}_{102}$

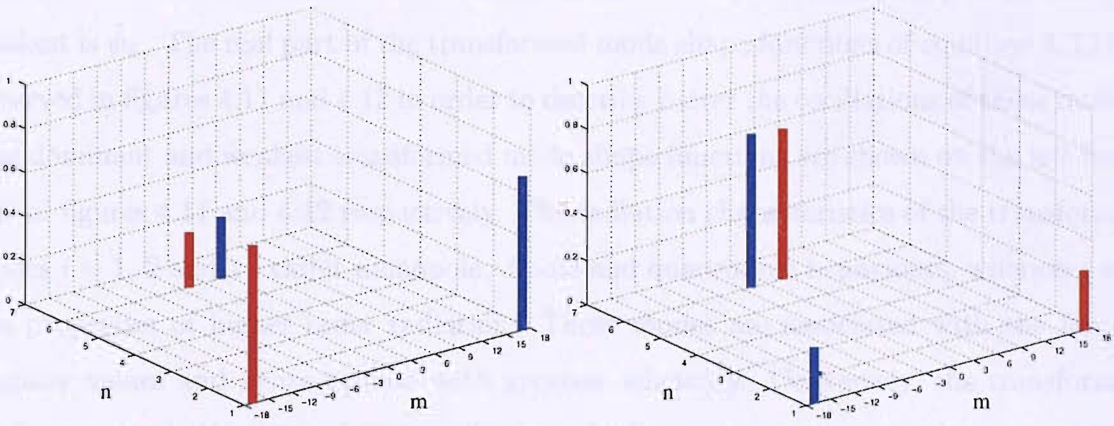

(c) $\mathbf{v}_{103}$ & $\mathbf{v}_{104}$ (d) $\mathbf{v}_{105}$ & $\mathbf{v}_{106}$

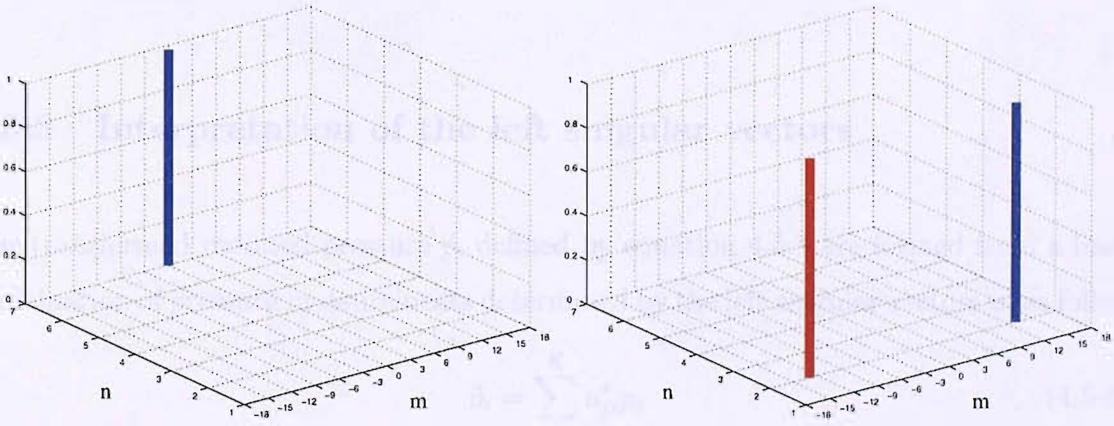

(e) $\mathbf{v}_{107}$ (f) $\mathbf{v}_{108}$ & $\mathbf{v}_{109}$

Figure 4.10: Modal content in right singular vectors associated with small singular values for a $\nu = 6$-geodesic sensor array

—— and —— show pairs formed by 2 consecutive singular vectors which may be defined as follows

$$\tilde{\psi}_i = \sum_{j=1}^{L} v_{ij}{}^* \psi_j \tag{4.5.13}$$

The i^{th} transformed mode shape function is a linear combination of the L cut-on mode shape functions over the duct cross-section. The transformed mode shape functions represent the modal distribution over the duct outlet cross-section detected by an arrangement of microphones over the TCS. From equation 4.5.5, each of these transformed mode shape functions are weighted by their singular values representing their radiation efficiencies such that the most dominant mode shape function detected by the TCS array is $\tilde{\psi}_1$ and the weakest is $\tilde{\psi}_L$. The real part of the transformed mode shape functions of equation 4.5.13 is observed in figures 4.11 and 4.12 in order to describe better the oscillations of these modes. The dominant and weakest transformed mode shape functions are shown on the left-hand side of figures 4.11 and 4.12 respectively. The radiation characteristics of the transformed modes $i = 1$, 2 and 4 exhibit monopole, dipole and quadrupole behaviours, whereas $i = 7$ has properties of higher order radiation. These modes are associated with the largest singular values and hence radiate with greatest efficiency. Conversely, the transformed modes $i = 103$, 015, 107 and 109 exhibit very high order radiation and therefore radiate very inefficiently.

4.5.3 Interpretation of the left singular vectors

The transformed radiated pressure $\tilde{p}_i$ defined by equation 4.5.3 are formed from a linear combination of pressure measurements determined by the left singular vectors $\mathbf{u}_i$ as follows

$$\tilde{p}_i = \sum_{j=1}^{K} u_{ji}^* p_j \tag{4.5.14}$$

From equation 4.5.5, they describe how the TCS sensor array is coupled to the acoustic modes. From equation 4.5.14, the j^{th} element of a left singular vector $\mathbf{u}_i$ determines how much radiation information of the j^{th} acoustic mode is found within the i^{th} transformed

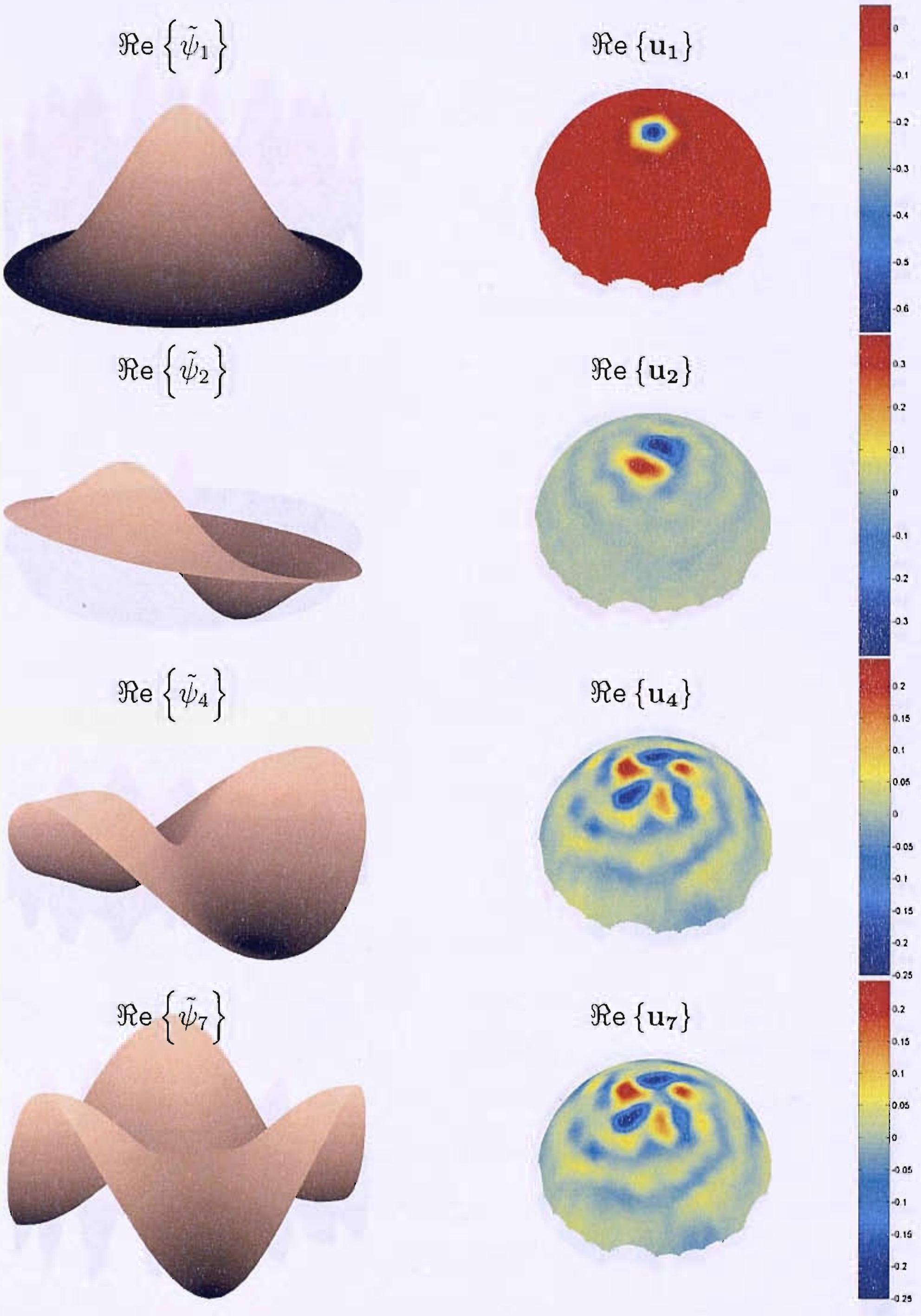

Figure 4.11: Real part of transformed mode shape functions (left hand-side) and transformed (right hand side) acoustic pressures associated with large singular values

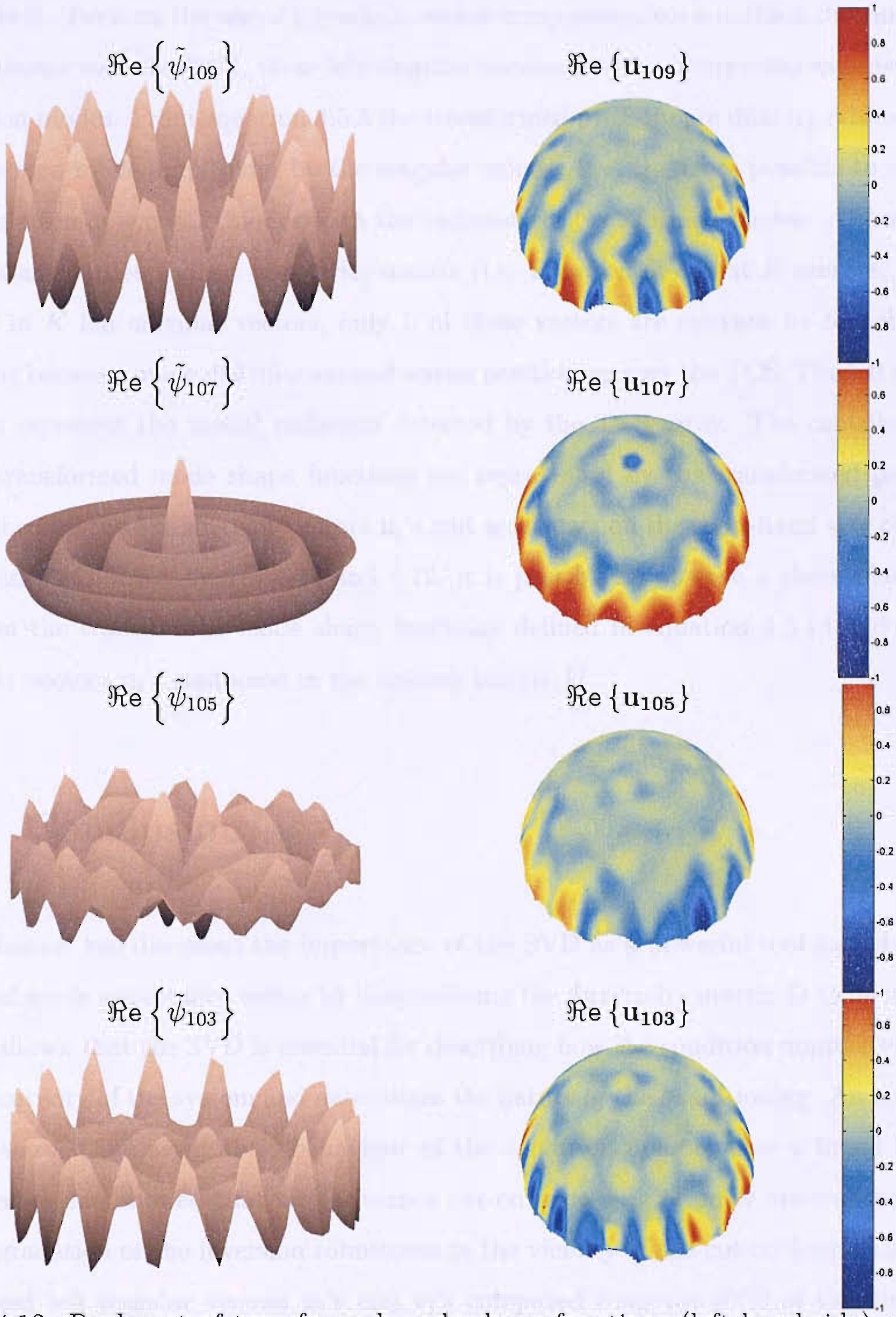

Figure 4.12: Real part of transformed mode shape functions (left hand-side) and transformed (right hand side) acoustic pressures associated with small singular values

pressure $\tilde{p}_i$. Because the use of a geodesic sensor array comprises a uniform distribution of microphones over the TCS, these left singular vectors may be interpreted as a new set of radiation modes. From equation 4.5.5 the transformed pressure are directly related to the transformed mode amplitudes by the singular values. It is therefore possible to compare the radiation of acoustic modes with the radiation of transformed modes. Although the SVD of an overdetermined directivity matrix (i.e. L cut-on modes at K sensors, $K > L$) results in K left singular vectors, only L of these vectors are relevant to describing the coupling between mode distribution and sensor positioning over the TCS. The left singular vectors represent the modal radiation detected by the TCS array. The contribution of these transformed mode shape functions are represented by the transformed pressures, prescribed by the left singular vectors $\mathbf{u}_i$'s and are shown on the right-hand side of figures 4.11 and 4.12. From figures 4.11 and 4.12, it is possible to observe a close relationship between the transformed mode shape functions defined in equation 4.5.13 and the left singular vectors $\mathbf{u}_i$'s contained in the unitary matrix $\mathbf{U}$.

4.6 Conclusion

This chapter has discussed the importance of the SVD as a powerful tool for solving the inverted mode amplitudes vector by diagonalizing the directivity matrix $\mathbf{D}$ to be inverted. It has shown that the SVD is essential for describing how the condition number evaluates the sensitivity of the system and determines the nature of the conditioning. An analytical study showed the asymptotic behaviour of the condition number over a broad band of frequencies and showed that modes with a cut-on ratio α_{mn} of unity are responsible for the degradation of the inversion robustness in the vicinity of the cut-on frequencies. The right and left singular vectors $\mathbf{u}_i$'s and $\mathbf{v}_i$'s computed from the SVD of the directivity matrix $\mathbf{D}$ allowed to diagnose the coupling between the modal distribution over the duct outlet cross-section and the sensor positioning over the TCS. It was shown that the right and left singular vectors determine the mode distribution on the source plane and the mode radiation detected by the TCS sensor array respectively. Some consecutive right singular vectors showed a high degree of symmetry in their modal content such that they formed a pair of identical modal content but with the spinning mode number m of these modes reversed in sign. Conversely, some right singular vectors, which contain axisymmetric modes (i.e. $m = 0$), do not possess this feature and are said to be unique.

More importantly, the inspection of singular vectors also showed that well cut-on modes are found within singular vectors associated with high singular values while modes close to cutoff are contained within singular vectors associated with small singular values. It can thus be deduced that the inversion of well cut-on modes is likely to be less damaged by the presence of external noise measurement than that of modes close to cutoff. More particularly, modes with a cut-on ratio of unity were only found within singular vectors associated with the smallest singular values, responsible for the ill-conditioning, therefore agreeing with the fact that least cut-on modes damage considerably the inversion robustness.

Finally, the SVD provided the analysis necessary to understand why ill-conditioning arises in the mode inversion problem and enlightened the need of external numerical treatment to be applied on the directivity matrix **D** which consists of constraining the solution to enhance inversion robustness. Again the SVD will play a central role in finding the best trade-off between robustness and inaccuracies that such constrain will introduce. This numerical treatment is denoted as regularisation and its various schemes will be discussed in the next chapter.

Chapter 5

Methods for improving inversion robustness

The previous chapter has highlighted the conditioning of **D** as a fundamentally important issue on the robustness of the inversion technique. The sensitivity to errors in the inverted solution caused by noise in the measurements or by modelling errors is quantified by the condition number. As discussed previously, it is essential that the condition number is reduced as far as possible by finding appropriate sensor positions on the TCS.

The study in chapter 3 on the sensor positioning and its effect on the conditioning has shown that the condition number may be significantly lowered if one considers carefully the positions of microphones on the TCS and employs a number of microphones higher than the number of modes to be inverted. However, it was shown in chapter 4 that these precautions did not necessarily lead to good conditioning for robust mode reconstruction to be performed at the cut-on frequencies. Section 4.3 has shown that the presence of nearly cut-off modes damages dramatically the conditioning of the directivity matrix **D** and in the meantime leads to substantially large solution norms. This may be problematic particularly at high ka when the modal density is high and the likelihood of at least one mode being close to cutoff is high. In this case, some external numerical treatments are therefore required to stabilise the solution. Such regularisation schemes introduce additional constraints on the solution and thus allow some tighter perturbation bounds [31,32]. This prevents disproportional effects from measurement perturbation on one hand but leads, on the other hand, to a degrading effect upon the solution accuracy because of these additional constraints. A trade-off between conditioning and mode reconstruction accuracy will have a key role in choosing parameters that will configure the regularisation technique.

This chapter investigates different schemes for regularising the directivity matrix **D** and discusses their effect that arises on the conditioning and reconstruction accuracy of the modal amplitude inversion. The first scheme consists of modifying the original forward problem by simply removing the modes that are very close to cutoff. The second scheme uses the original forward problem considered in the previous chapters and discards a number of the very small singular values responsible for the high condition number. The last scheme uses Tikhonov regularisation methods, both in its standard and general form, which is one of the most conventional stabilising methods in inverse techniques.

5.1 Removal of modes close to cutoff

Chapter 3 has shown that the conditioning of the directivity matrix is very poor in the vicinity of the cut-on frequencies. Chapter 4 has proven, by the study of a simple analytical case, that the condition number varies as $(1-\alpha_0^2)^{-1/2}$ with $\alpha_0 \approx 1$. The inverse problem stated in equation 3.1.9 is modified by simply removing in **D** the elements due to modes close to cutoff. This yields the solution of the reduced inverse problem

$$\hat{\mathbf{a}}_{\mathbf{red}} = \mathbf{D}_{\mathbf{r}}^{+}\hat{\mathbf{p}} \tag{5.1.1}$$

where $\mathbf{D_r}$ is the directivity matrix given in equation 3.1.4 with the column vectors associated with the modes close to cutoff removed, whose condition number is significantly reduced compared to the original directivity matrix $\mathbf{D}$. The least square estimate is then given by

$$\hat{\mathbf{a}}_0 = \begin{bmatrix} \hat{\mathbf{a}}_{\mathbf{red}} \\ \mathbf{0} \end{bmatrix} \tag{5.1.2}$$

This methods is first studied at a cut-off frequency, namely $ka = 19.885$, and then investigated over a band of frequencies ($10 \leq ka \leq 20$) and is applied with the $\nu = 5$-geodesic array.

Figures 5.1(a) and 5.1(b) show the variation of the condition number κ_r of this reduced directivity matrix and the reconstruction accuracy η_r for a measurement SNR of 20dB respectively, versus the number of cut-on modes is removed Q. It is important to note that Q increases with decreasing cut-on ratio. A sharp improvement, for both arrays, is achieved in both robustness and accuracy when two modes are precluded from the directivity matrix prior reconstructing the mode amplitudes. Since the first two modes removed in this simulation are modes closest to cutoff, it confirms the essential problem encountered with nearly cut-off modes as discussed in chapters 3 and 4. The fact that both robustness and accuracy are enhanced when these two modes are not taken into

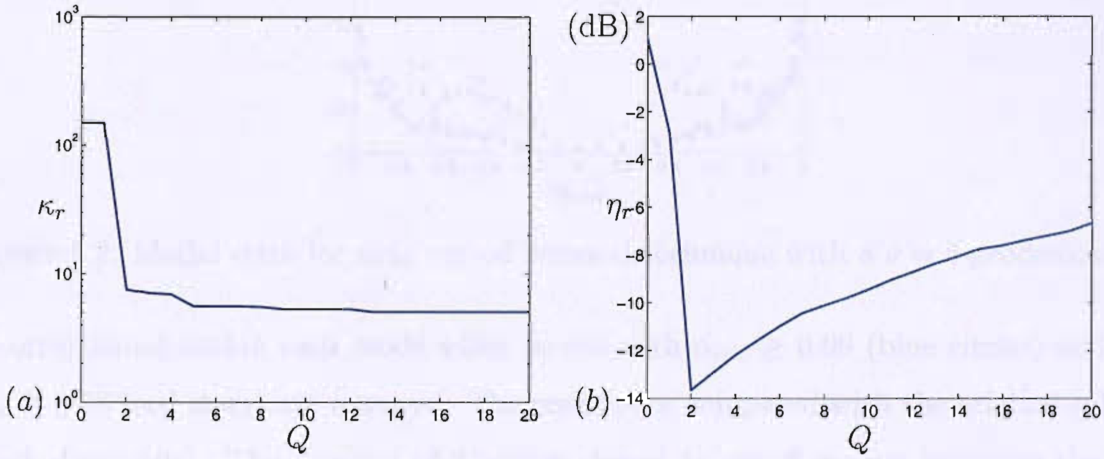

Figure 5.1: Condition number (a) and reconstruction accuracy (b) with number of cut-on modes removed for a $\nu = 5$-geodesic array

account during the inversion process suggests that their presence may be neglected. A gain of accuracy of 14dB is achieved when these two modes are omitted.

At this frequency of $ka = 19.885$, only two modes have a cut-on ratio $\alpha_{mn} \geq 0.99$ while it is necessary to go up to $Q = 5$ in order to remove all modes with a cut-on ratio $\alpha_{mn} \geq 0.98$. As expected, the conditioning is slightly improved when $Q > 2$, but this improvement is not accompanied by additional accuracies in the solution. Information contained in the modes $0.98 \geq \alpha_{mn} \leq 0.99$ contribute within some limits to the original problem since a loss of accuracy of 2 or 3dB is observed when subsequently removed. Figure 5.2 shows the error found within each mode when modes with $\alpha_{mn} \geq 0.99$ (blue circles) and with $\alpha_{mn} \geq 0.98$ (red stars) are removed. The results are compared with the original solution (black diamonds). The removal of 2 modes closest to cutoff mainly improves the large inaccuracies found in these two modes.

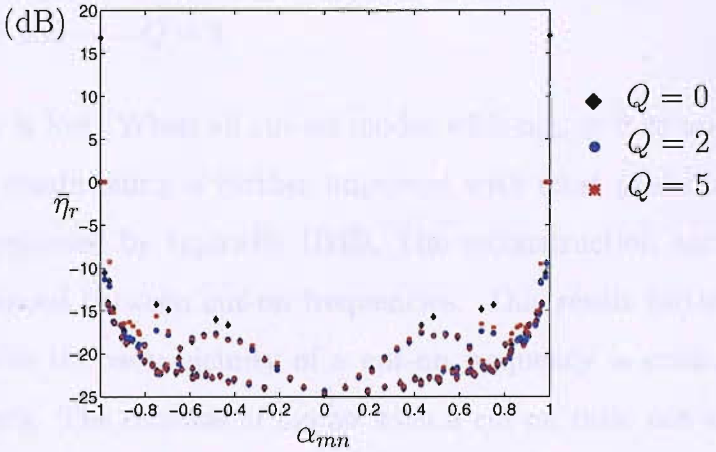

Figure 5.2: Modal error for near cut-off removal technique with a ν = 5-geodesic array

Figures 5.3(a) and 5.3(b) show the variation of the condition number κ_r and the reconstruction accuracy η_r with frequency ka for $Q = 2$ and $Q = 5$. Also shown is the original solution with all modes included, i.e. $Q = 0$. All peaks in κ and η at the cut-off frequencies are now suppressed when only cut-on modes with $\alpha_{mn} \geq 0.99$ are discarded. In the vicinity of the cut-on frequencies, when the modes for which $\alpha_{mn} \geq 0.98$ rather than 0.99

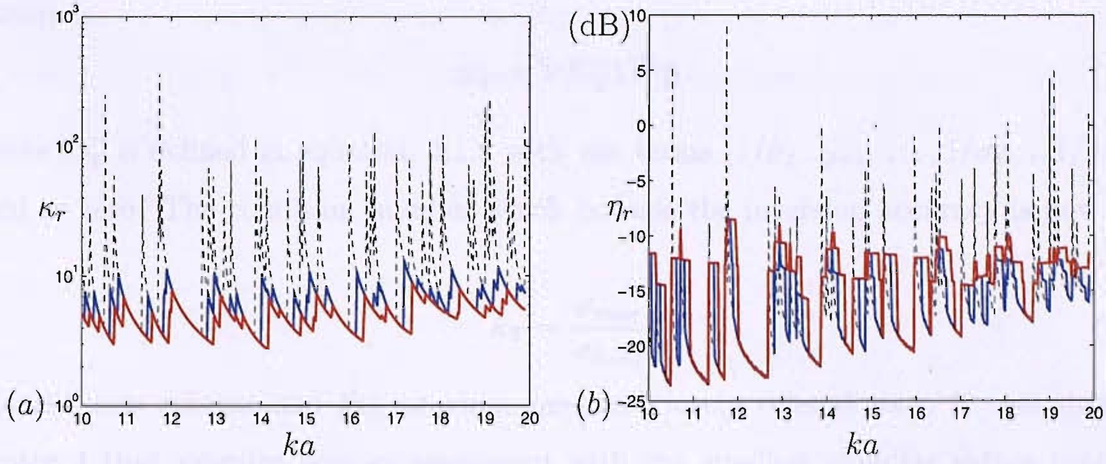

Figure 5.3: (a) κ_r and (b) η_r versus ka for a $\nu = 5$-geodesic array
----$Q = 0$ ——$Q = 2$ and ——$Q = 5$

are removed, accuracy is lost. When all cut-on modes with $\alpha_{mn} \geq 0.98$ are not accounted for the inversion, the conditioning is further improved with most peaks in the condition number spectrum suppressed by typically 10dB. The reconstruction accuracy observed for $Q = 2$ is not enhanced between cut-on frequencies. This result further confirms the fact that only modes in the very vicinity of a cut-on frequency is critical for inversion robustness and accuracy. The removal of modes with a cut-on ratio not sufficiently close to unity clearly damages the reconstruction accuracy, not only at the cut-on frequencies but also at frequencies in between. Therefore, the presence of these modes indicates a significant contribution to the radiated sound field that cannot be neglected. In summary, modes with $\alpha_{mn} \geq 0.99$ should not be included in $\mathbf{D}$.

5.2 Truncated Singular Value Decomposition

The second scheme of regularisation investigated in this chapter consists of performing the inversion of all cut-on modes and then discarding the $L - Q$ smallest singular values, where Q here denotes the number of discarded singular values. The solution is then written as

$$\hat{\mathbf{a}}_{\mathrm{T}} = \mathbf{V}\Sigma_{\mathrm{T}}^{+}\mathbf{U}^{\mathrm{H}}\hat{\mathbf{p}} \tag{5.2.1}$$

where Σ_{T}^{+} is defined in equation 4.1.8 with the terms $(1/\sigma_{L-Q+1}, \ldots, 1/\sigma_{L-1}, 1/\sigma_L)$ set equal to zero. The condition number which bounds the inversion accuracy is now given by

$$\kappa_T = \frac{\sigma_{max}}{\sigma_{L-Q}} \tag{5.2.2}$$

Clearly, this scheme and the previous one are closely related since it was shown in chapter 4 that singular vectors associated with the smallest singular values contain a single dominant mode which is increasingly more cut-on for increasing singular values index. As the magnitude of the singular values increases, the number of dominant modes contained within associated singular vectors generally increases from 2 to 3. Figures 5.4(a) and 5.4(b) show the variation of κ_T and η_T against the number Q of singular values discarded respectively and are compared with κ_r and η_r against the number Q of cut-on modes removed. These figures clearly demonstrates that discarding the 2 smallest singular values is equivalent to discarding the 2 modes closest to cutoff prior inversion since both κ and η remain unchanged. This confirms again that these 2 smallest singular values are associated with singular vectors containing the 2 modes closest to cutoff. As

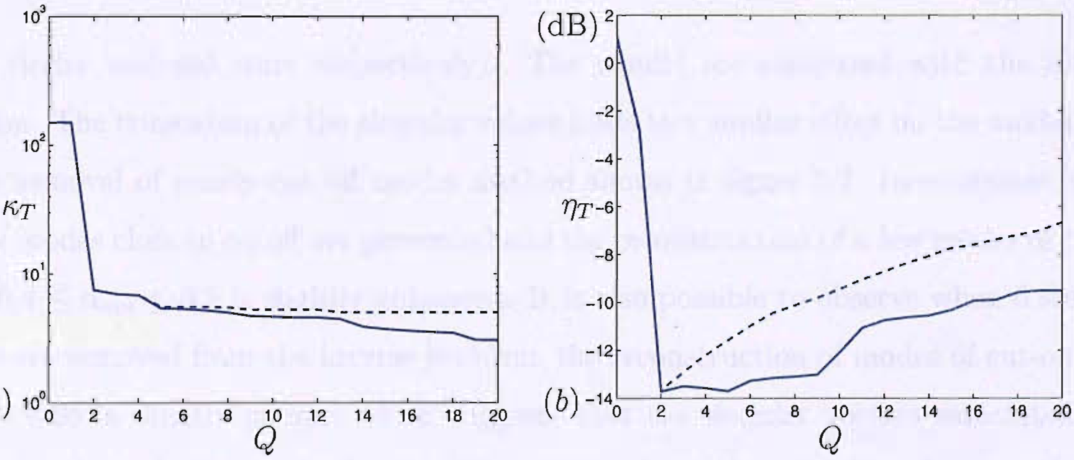

Figure 5.4: Condition number (a) and reconstruction accuracy (b) versus the number of singular values discarded ----shows the comparison with the mode discarding method

the number of singular values to be discarded increases, modal information contained in the corresponding singular vectors have not been entirely discarded when $2 < Q \leq 6$ since inaccuracies increases at a slower rate. A small part of this modal information may be found in singular vectors of index greater than 5.

Figure 5.5 shows the error within each mode when 2 or 6 singular values are discarded

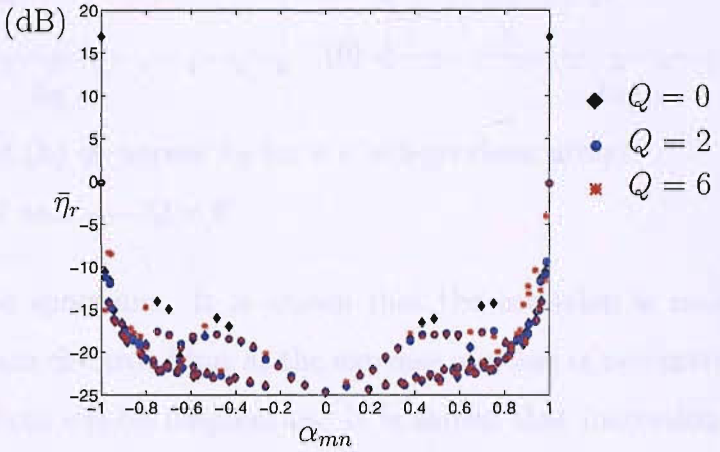

Figure 5.5: Modal error for singular value discarding with a ν = 5-geodesic array

(blue circles and red stars respectively). The results are compared with the original solution. The truncation of the singular values leads to a similar effect on the modal error to the removal of nearly cut-off modes method shown in figure 5.2. Inaccuracies on the pair of modes close to cutoff are prevented and the reconstruction of a few modes of cut-on ratio $0.4 \leq \alpha_{mn} \leq 0.8$ is slightly enhanced. It is also possible to observe when 6 singular values are removed from the inverse problem, the reconstruction of modes of cut-on ratio $\alpha_{mn} \approx 0.98$ is slightly poorer, which suggests that the singular vectors associated with these singular values contained some information about these modes. Again, only very small singular values should be removed from the original inverse problem since a loss of accuracy is found for very little enhancement of the inversion robustness.

Figures 5.6(a) and 5.6(b) show the conditioning and the reconstruction accuracy versus the non-dimensional frequency ka when 2 and 6 singular values are removed from the

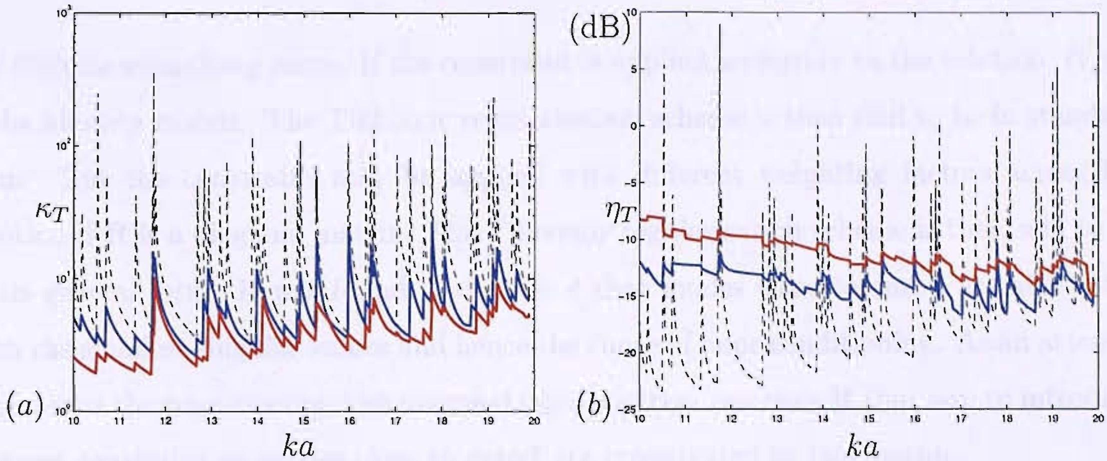

Figure 5.6: (a) κ_T and (b) η_T versus ka for a $\nu = 5$-geodesic array

----$Q = 0$ —— $Q = 2$ and —— $Q = 6$

original singular value spectrum. It is shown that the inversion is made more robust when singular values are discarded but at the expense of a loss of reconstruction accuracy at frequencies away from cut-on frequencies. It is shown that increasing the number of discarded singular values causes poorer inversion accuracy, both at, and between, cut-on frequencies. This method is effective at the cut-on frequencies when the smallest singular values are discarded. By contrast, the mode discarding method scheme affects only the frequencies close to the cut-off frequencies as shown in figure 5.3.

5.3 Tikhonov regularisation

This section discusses one of the most common methods of regularisation. The Tikhonov regularisation consists of adding to the original scheme of least-squares estimation an additional constraint on the size of the solution. This can be summarised as follows

$$J = \|\hat{\mathbf{p}} - \mathbf{D}\mathbf{a}\|_2^2 + \beta \|\mathbf{R}\mathbf{a}\|_2^2 \tag{5.3.1}$$

where β is a specified weighting factor and often called the Tikhonov parameter. The regularising matrix $\mathbf{R}$ describes some measure of the norm of the solution and is termed the discrete smoothing norm. If the constraint is applied uniformly to the solution, $\mathbf{R} = \mathbf{I}$ is the identity matrix. The Tikhonov regularisation scheme is then said to be in standard form. But the constraint may be applied with different weighting factors across the solution if $\mathbf{R}$ is a diagonal matrix. The Tikhonov regularisation scheme is then said to be in its general form. It was found in chapter 4 that modes close to cutoff are associated with the smallest singular values and hence the cause of poor conditioning. As an attempt to improve the conditioning, two diagonal regularisation matrices $\mathbf{R}$ that aim to introduce a larger constraint on modes close to cutoff are investigated in this section.

5.3.1 Regularised mode amplitudes estimation

The Tikhonov regularisation scheme given by equation 5.3.1 minimises the 'residuals' plus a weighted form of the size of the solution specified by

$$\mathbf{y} = \sqrt{\beta}\,\mathbf{R}\mathbf{a} \tag{5.3.2}$$

Thus the cost function to be minimised in this method is then defined by

$$J = \sum_{k=1}^{K} |n_k(\omega)|^2 + \sum_{k=1}^{P} |y_k(\omega)|^2 = \mathbf{n}^{\mathbf{H}}\mathbf{n} + \mathbf{y}^{\mathbf{H}}\mathbf{y} \tag{5.3.3}$$

It is important to note the dimensions of $\mathbf{D} \in \mathbb{C}^{\mathbf{K}\times\mathbf{L}}$ and $\mathbf{R} \in \mathbb{C}^{\mathbf{L}\times\mathbf{L}}$. Therefore the modal amplitude vector that minimises this cost function can be found using a similar derivation to that given in section 3.1 for the 'least-squares' solution, namely $\partial J/\partial \mathbf{a} = \mathbf{0}$. Introducing equation 3.1.6 and equation 5.3.2 into equation 5.3.3 leads to

$$\begin{aligned} J &= \mathbf{a}^{\mathbf{H}}\mathbf{D}^{\mathbf{H}}\mathbf{D}\mathbf{a} - \hat{\mathbf{p}}^{\mathbf{H}}\mathbf{D}\mathbf{a} - \mathbf{a}^{\mathbf{H}}\mathbf{D}^{\mathbf{H}}\mathbf{p} + \hat{\mathbf{p}}^{\mathbf{H}}\mathbf{p} + \beta\,\mathbf{a}^{\mathbf{H}}\mathbf{R}^{\mathbf{H}}\mathbf{R}\mathbf{a} \\ &= \mathbf{a}^{\mathbf{H}}\left(\mathbf{D}^{\mathbf{H}}\mathbf{D} + \beta\,\mathbf{R}^{\mathbf{H}}\mathbf{R}\right)\mathbf{a} - \hat{\mathbf{p}}^{\mathbf{H}}\mathbf{D}\mathbf{a} - \mathbf{a}^{\mathbf{H}}\mathbf{D}^{\mathbf{H}}\hat{\mathbf{p}} + \hat{\mathbf{p}}^{\mathbf{H}}\mathbf{p} \end{aligned} \tag{5.3.4}$$

Similar to appendix B for the unconstrained 'least-squares' solution, one can define $\mathbf{G} = \mathbf{D}^{\mathbf{H}}\mathbf{D} + \beta\,\mathbf{R}^{\mathbf{H}}\mathbf{R}$, $\mathbf{b} = -\mathbf{D}^{\mathbf{H}}\hat{\mathbf{p}}$ and the real scalar quantity $c = \hat{\mathbf{p}}^{\mathbf{H}}\mathbf{p}$. Equation 5.3.4

then becomes identical to equation B.7. The solution may again be written in the form of equation B.18, which in turn leads to the optimal estimate of the regularised modal amplitudes vector given by

$$\begin{aligned}\hat{\mathbf{a}}_{\mathrm{R}} &= \left[\mathbf{D}^{\mathbf{H}}\mathbf{D} + \beta\,\mathbf{R}^{\mathbf{H}}\mathbf{R}\right]^{-1}\mathbf{D}^{\mathbf{H}}\hat{\mathbf{p}} \\ &= \mathbf{D}^{\#}\hat{\mathbf{p}}\end{aligned} \tag{5.3.5}$$

where $\mathbf{D}^{\#}$ is the regularised inverse of the directivity matrix $\mathbf{D}$.

Note that when the Tikhonov regularisation scheme is in its standard form (i.e. $\mathbf{R}$ is simply the identity matrix), the solution reduces to

$$\hat{\mathbf{a}}_{\mathrm{R}} = \left[\mathbf{D}^{\mathbf{H}}\mathbf{D} + \beta\,\mathbf{I}\right]^{-1}\mathbf{D}^{\mathbf{H}}\hat{\mathbf{p}} \tag{5.3.6}$$

As in section 4.1, we now consider the Generalised Singular Value Decomposition (GSVD) of equation 5.3.5 as a means of interpreting its behaviour.

5.3.2 Generalised Singular Value Decomposition

The GSVD of the matrix pair ($\mathbf{D}$, $\mathbf{R}$) is a generalisation of the SVD in the sense that the main objective is to factorise both matrices into a unitary, a nonsingular and diagonal matrices and that the generalised singular values extracted from this operation are essentially the square roots of the generalised eigenvalues of the matrix pair ($\mathbf{D}^{\mathbf{H}}\mathbf{D}$, $\mathbf{R}^{\mathbf{H}}\mathbf{R}$), hence its name. The matrix pair involved in Tikhonov method, namely the directivity matrix $\mathbf{D}$ and its regularising matrix $\mathbf{R}$ can be decomposed as follows

$$\mathbf{D} = \mathbf{U\Sigma X}^{-1} \tag{5.3.7}$$

and

$$\mathbf{R} = \mathbf{VMX}^{-1} \tag{5.3.8}$$

where

- $\mathbf{U} \in \mathbf{C}^{K \times L}$ is unitary
- $\mathbf{V} \in \mathbf{C}^{L \times L}$ is unitary
- $\mathbf{X} \in \mathbf{C}^{L \times L}$ is nonsingular
- $\mathbf{\Sigma} \in \mathbf{C}^{L \times L}$ is diagonal
- $\mathbf{M} \in \mathbf{C}^{L \times L}$ is diagonal

and $\mathbf{\Sigma}$ and $\mathbf{M}$ are diagonal matrices given by

$$\mathbf{\Sigma} = \texttt{diag}(\sigma_i) \qquad \mathbf{M} = \texttt{diag}(\mu_i) \tag{5.3.9}$$

whose diagonal elements satisfy $\sigma_i^2 + \mu_i^2 = 1$ and are ordered such that

$$0 \leq \sigma_1 \leq \cdots \leq \sigma_L \qquad 1 \geq \mu_1 \geq \cdots \geq \mu_L \tag{5.3.10}$$

If one considers the Hermitian matrices $\mathbf{D^H D}$ and $\mathbf{R^H R}$ it can be readily shown that

$$\mathbf{D^H D} = \left(\mathbf{X}^{-1}\right)^{\mathbf{H}} \mathbf{\Sigma}^2 \mathbf{X}^{-1} \qquad \mathbf{R^H R} = \left(\mathbf{X}^{-1}\right)^{\mathbf{H}} \mathbf{M}^2 \mathbf{X}^{-1} \tag{5.3.11}$$

Defining the generalized singular values γ_i of the matrix pair $(\mathbf{D}, \mathbf{R})$ as the ratios

$$\gamma_i = \frac{\sigma_i}{\mu_i} \tag{5.3.12}$$

so that they appear to be arranged in ascending order, it can be seen that γ_i^2 are the generalised eigenvalues associated with the matrix $\mathbf{X}$ containing the generalised eigenvectors of the matrix pair $\left(\mathbf{D^H D}, \mathbf{R^H R}\right)$.

Note that there is a difficulty of notation between the SVD and the GSVD because the matrices $\mathbf{U}$ and $\mathbf{V}$ and the elements of $\mathbf{\Sigma}$ in the GSVD of $(\mathbf{D}, \mathbf{R})$ are different from their respective counterparts in the SVD of $\mathbf{D}$. However, when the Tikhonov regularisation scheme is in its standard form (i.e. equation 5.3.6), $\mathbf{U}$ and $\mathbf{V}$ of the GSVD are identical to that of the SVD and the generalised singular values of $(\mathbf{D}, \mathbf{R})$ are identical to the singular values of $\mathbf{D}$, except for the reverse ordering of the singular values and vectors.

The latter remark is obvious as the standard form does not indeed involve any regularising matrix **R**, hence the SVD remains in that particular case the appropriate tool to diagnosing the cause of ill-conditioning. It is also important to bear in mind that even for the general form of regularisation, the generalised singular values will have a similar variation to that of the ordinary singular values. Because the very small singular values of **D** will have a dramatic effect on the conditioning as shown in equation 4.2.1, one can readily deduce that the main objective of regularisation will be a matter of identifying erroneous SVD components and to suppress somehow these singular values in order to prevent them from being very small, leading to very high condition number. In order to better understand what regularisation does and how the action of filtering is carried out, it is useful to develop in more details the regularised solution in both standard and general forms and to introduce the notion of filter factors.

5.3.3 Regularised solution in standard form

Tikhonov regularisation in standard form does not involve modifying the basis vectors originating from the directivity matrix **D**. As a result, it does not involve the use of the GSVD. First recall that the regularised solution in its standard form is given by equation 5.3.6 and that the use of the SVD of **D** from equation 4.1.1 yields

$$\mathbf{V}\left(\mathbf{\Sigma}^2+\beta\mathbf{I}\right)\mathbf{V}^{\mathbf{H}}\hat{\mathbf{a}}_{\mathbf{R}} = \mathbf{V}\mathbf{\Sigma}^{\mathbf{T}}\mathbf{U}^{\mathbf{H}}\hat{\mathbf{p}} \tag{5.3.13}$$

Multiplying to the left both sides of equation 5.3.13 by $\mathbf{V}^{\mathbf{H}}$ gives

$$\left(\mathbf{\Sigma}^2+\beta\mathbf{I}\right)\mathbf{V}^{\mathbf{H}}\hat{\mathbf{a}}_{\mathbf{R}} = \mathbf{\Sigma}^{\mathbf{T}}\mathbf{U}^{\mathbf{H}}\hat{\mathbf{p}} \tag{5.3.14}$$

Therefore the regularised solution can be written as

$$\hat{\mathbf{a}}_{\mathbf{R}} = \mathbf{V}\left(\mathbf{\Sigma}^2+\beta\mathbf{I}\right)^{-1}\mathbf{\Sigma}^{\mathbf{T}}\mathbf{U}^{\mathbf{H}}\hat{\mathbf{p}} \tag{5.3.15}$$

The property of diagonal matrices allows us to multiply by $\mathbf{\Sigma}^{\mathbf{T}}$ and $\mathbf{\Sigma}^{-1}$ without altering equation 5.3.15

$$\hat{\mathbf{a}}_{\mathbf{R}} = \mathbf{V}\mathbf{\Sigma}^{-1}\left(\mathbf{\Sigma}^{2}+\beta\,\mathbf{I}\right)^{-1}\mathbf{\Sigma}^{2}\mathbf{U}^{\mathbf{H}}\hat{\mathbf{p}}$$

$$\hat{\mathbf{a}}_{\mathbf{R}} = \mathbf{V}\mathbf{\Sigma}^{-1}\mathbf{\Lambda}\mathbf{U}^{\mathbf{H}}\hat{\mathbf{p}} \tag{5.3.16}$$

where $\mathbf{\Lambda} = \left(\mathbf{\Sigma}^{2}+\beta\,\mathbf{I}\right)^{-1}\mathbf{\Sigma}^{2}$ is a diagonal matrix whose elements are the filter factors from the Tikhonov filter function given as follows

$$f\left(\sigma_i\right) = \frac{\sigma_i^2}{\sigma_i^2+\beta} = \frac{1}{1+\beta/\sigma_i^2} \tag{5.3.17}$$

Thus the regularised solution is rewritten in terms of these filter factors as

$$\hat{\mathbf{a}}_{\mathbf{R}} = \sum_{i=1}^{L} f\left(\sigma_i\right)\frac{\mathbf{u}_{\mathbf{i}}^{\mathbf{H}}\hat{\mathbf{p}}}{\sigma_i}\mathbf{v}_{\mathbf{i}} \tag{5.3.18}$$

The Tikhonov filter penalises vectors which are associated with $\sigma_i \ll \beta$. Tikhonov regularisation therefore damps the singular vectors which are associated with very small singular values. Now the product of the two diagonal matrices of equation 5.3.16, $\mathbf{\Sigma}^{-1}$ and $\mathbf{\Lambda}$, yields another diagonal matrix. The regularised solution can thus be written in terms of the SVD of the directivity matrix $\mathbf{D}$ as

$$\hat{\mathbf{a}}_{\mathbf{R}} = \mathbf{V}\mathbf{\Sigma}^{\#}\mathbf{U}^{\mathbf{H}}\hat{\mathbf{p}} \tag{5.3.19}$$

where $\mathbf{\Sigma}^{\#} \in \mathbf{C}^{\mathbf{L}\times\mathbf{K}}$ is the regularised inverse of $\mathbf{\Sigma}$ given by

$$\mathbf{\Sigma}^{\#} = \begin{bmatrix} \frac{\sigma_1}{\sigma_1^2+\beta} & 0 & \cdot & \cdot & 0 & \cdot & 0 \\ 0 & \frac{\sigma_2}{\sigma_2^2+\beta} & & & & & \\ & & & & & & \\ \cdot & & & & & & \cdot \\ 0 & & & \frac{\sigma_L}{\sigma_L^2+\beta} & 0 & \cdot & 0 \end{bmatrix} \tag{5.3.20}$$

Pre-multiplying both sides of equation 5.3.19 by $\mathbf{V}^{\mathbf{H}}$ gives the regularised transformed modes in the form

$$\tilde{\mathbf{a}}_{\mathbf{R}} = \mathbf{\Sigma}^{\#}\tilde{\mathbf{p}} \tag{5.3.21}$$

5.3.4 Regularised solution in general form

In addition to filtering out erroneous singular values, the main purpose of Tikhonov regularisation in general form is to modify the set of basis functions originating from the directivity matrix $\mathbf{D}$. As a result, the use of the GSVD is at the core of a diagnosis tool for revealing which radiated field components are not appropriate for the desired regularised solution. First recall that the regularised solution in its general form is given by equation 5.3.5 and together with the use of the GSVD of the matrix pair $(\mathbf{D}, \mathbf{R})$ of equations 5.3.7 and 5.3.8, yields

$$\left[\left(\mathbf{X}^{-1}\right)^{\mathbf{H}}\left(\boldsymbol{\Sigma}^{2}+\beta\mathbf{M}^{2}\right)\mathbf{X}^{-1}\right]\hat{\mathbf{a}}_{\mathbf{R}}=\left(\mathbf{X}^{-1}\right)^{\mathbf{H}}\boldsymbol{\Sigma}^{\mathbf{T}}\mathbf{U}^{\mathbf{H}}\hat{\mathbf{p}} \tag{5.3.22}$$

Multiplying to the left both sides of equation 5.3.22 by $\mathbf{X}^{\mathbf{H}}$ gives

$$\left(\boldsymbol{\Sigma}^{2}+\beta\mathbf{M}^{2}\right)\mathbf{X}^{-1}\hat{\mathbf{a}}_{\mathbf{R}}=\boldsymbol{\Sigma}^{\mathbf{T}}\mathbf{U}^{\mathbf{H}}\hat{\mathbf{p}} \tag{5.3.23}$$

Therefore the regularised solution can be written as

$$\hat{\mathbf{a}}_{\mathbf{R}}=\mathbf{X}\left(\boldsymbol{\Sigma}^{2}+\beta\mathbf{M}^{2}\right)^{-1}\boldsymbol{\Sigma}^{\mathbf{T}}\mathbf{U}^{\mathbf{H}}\hat{\mathbf{p}} \tag{5.3.24}$$

Again, the property of diagonal matrices allows us to multiply by $\boldsymbol{\Sigma}^{\mathbf{T}}$ and $\boldsymbol{\Sigma}^{-1}$ without altering equation 5.3.24

$$\begin{aligned}\hat{\mathbf{a}}_{\mathbf{R}}&=\mathbf{X}\boldsymbol{\Sigma}^{-1}\left(\boldsymbol{\Sigma}^{2}+\beta\mathbf{M}^{2}\right)^{-1}\boldsymbol{\Sigma}^{2}\mathbf{U}^{\mathbf{H}}\hat{\mathbf{p}}\\ \hat{\mathbf{a}}_{\mathbf{R}}&=\mathbf{X}\boldsymbol{\Sigma}^{-1}\boldsymbol{\Lambda}\mathbf{U}^{\mathbf{H}}\hat{\mathbf{p}}\end{aligned} \tag{5.3.25}$$

where here $\boldsymbol{\Lambda}=\left(\boldsymbol{\Sigma}^{2}+\beta\mathbf{M}^{2}\right)^{-1}\boldsymbol{\Sigma}^{2}$ is a diagonal matrix whose elements are the filter factors from the Tikhonov filter function given in terms of the generalised singular values as follows

$$f\left(\gamma_{i}\right)=\frac{\gamma_{i}^{2}}{\gamma_{i}^{2}+\beta}=\frac{1}{1+\beta/\gamma_{i}^{2}} \tag{5.3.26}$$

Thus the regularised solution is rewritten in terms of these filter factors as

$$\hat{\mathbf{a}}_{\mathbf{R}}=\sum_{i=1}^{L}f(\gamma_{i})\frac{\mathbf{u}_{\mathrm{i}}^{\mathbf{H}}\hat{\mathbf{p}}}{\sigma_{i}}\mathbf{x}_{\mathrm{i}} \tag{5.3.27}$$

Again, in a similar fashion to the standard form Tikhonov filter, the general form Tikhonov filter penalises vectors associated with $\gamma_i \ll \beta$ such that Tikhonov regularisation damps generalised singular vectors that are associated with very small generalised singular values. Now the product of the two diagonal matrices of equation 5.3.25, $\mathbf{\Sigma}^{-1}$ and $\mathbf{\Lambda}$, yields another diagonal matrix. The regularised solution can thus be written in terms of the GSVD of the directivity matrix $\mathbf{D}$ as

$$\hat{\mathbf{a}}_{\mathbf{R}} = \mathbf{X}\mathbf{\Sigma}^{\#}\mathbf{U}^{\mathbf{H}}\hat{\mathbf{p}} \tag{5.3.28}$$

Since the generalised singular values γ_i are defined in equation 5.3.13, $\mathbf{\Sigma}^{\#} \in \mathbf{C}^{\mathbf{L}\times\mathbf{K}}$ is the regularised inverse of $\mathbf{\Sigma}$ given by

$$\mathbf{\Sigma}^{\#} = \begin{bmatrix} \frac{\gamma_1}{\sigma_1\left(\gamma_1^2+\beta\right)} & 0 & \cdot\ \cdot & 0 \\ 0 & \frac{\gamma_2}{\sigma_2\left(\gamma_2^2+\beta\right)} & & \cdot \\ \cdot & & & \\ & & & \cdot \\ 0 & 0 & \cdot & \frac{\gamma_L}{\sigma_L\left(\gamma_L^2+\beta\right)} \end{bmatrix} \tag{5.3.29}$$

In this case, the pair of parameters (σ_i, β) together forms the filter coefficients that suppress small generalised singular values γ_i.

For a $L \times L$ matrix $\mathbf{R}$, pre-multiplying both sides of equation 5.3.28 by $\mathbf{X}^{-1}$ gives the transformed mode amplitude vector in the form

$$\tilde{\mathbf{a}}_{\mathbf{R}} = \mathbf{\Sigma}^{\#}\tilde{\mathbf{p}} \tag{5.3.30}$$

where $\tilde{\mathbf{a}}_{\mathbf{R}} = \mathbf{X}^{-1}\hat{\mathbf{a}}_{\mathbf{R}}$ and $\tilde{\mathbf{p}} = \mathbf{U}^{\mathbf{H}}\hat{\mathbf{p}}$ are the regularised transformed modes and transformed pressures vectors respectively.

5.3.5 Perturbation bounds for the constrained least-squares solution

Unlike the unconstrained least-squares estimate, Tikhonov regularisation essentially modifies the inverse problem such that the solution given by equations 5.3.5 and 5.3.6 involves terms other than the Directivity matrix **D**. A different parameter that bounds the errors in the constrained least-squares solution from the noise found in the pressure measurements is therefore required. Research on perturbation bounds for the regularised solution have been extensively carried out and derived for the standard and general-form Tikhonov regularisation by Schock [33], and Hansen [31, 32], respectively.

If $\beta \in [\sigma_1, \sigma_L]$, $\mathbf{a_R}$ denotes the regularisation solution for the unperturbed constrained problem, i.e. $\left[\mathbf{D^H D} + \beta \mathbf{R^H R}\right]^{-1} \mathbf{D^H p}$, and $\mathbf{\hat{a}_R}$ the regularisation solution for the perturbed problem of equation 5.3.6, the condition number related to standard-form Tikhonov regularisation when the pressure measurements only are perturbed, may be shown to satisfy the following relationship [33]

$$\frac{\|\mathbf{a_R} - \mathbf{\hat{a}_R}\|}{\|\mathbf{a_R}\|} \leq \kappa_\beta \frac{\|\mathbf{e}\|}{\|\mathbf{\hat{p}}\|} \tag{5.3.31}$$

where κ_β is defined as follows

$$\kappa_\beta = \begin{cases} \frac{\sigma_1}{\sqrt{\beta}} & \beta \leq \sigma_1 \sigma_L \\ \frac{\sqrt{\beta}}{\sigma_L} & \beta > \sigma_1 \sigma_L \end{cases} \tag{5.3.32}$$

Similarly, it may be shown [31, 32] that the condition number κ_R for the general-form Tikhonov regularisation satisfies the following relationship

$$\frac{\|\mathbf{a_R} - \mathbf{\hat{a}_R}\|}{\|\mathbf{a_R}\|} \leq \kappa_R \frac{\|\mathbf{e}\|}{\|\mathbf{\hat{p}}\|} \tag{5.3.33}$$

where κ_R is defined as follows

$$\kappa_R = \frac{\|\mathbf{D}\| \, \|\mathbf{R^{-1}}\|}{2\sqrt{\beta}} \tag{5.3.34}$$

The behaviour of κ_β as well as κ_R is investigated in the next section as the function of the Tikhonov parameter β. Computer simulations are also performed in order to choose this parameter that satisfies the best trade-off between the minimisation of residual error and that of the error induced by the regularisation.

5.3.6 GSVD Analysis

It was shown in chapter 4 that the singular values of **D** play an important role in determining which singular vectors, and thus acoustic modes, are sensitive to noise. Singular vectors associated with the smallest singular values, when inverted, are responsible of the large bias the noise can generate upon the size of the solution. It was also demonstrated that, in an ideally conditioned directivity matrix, the singular value spectrum would be perfectly flat and the solution would be maximally robust to measurement noise.

Two regularising matrices **R** are now investigated in order to 'flatten' the singular value spectrum and make the solution more stable. The first regularising matrix $\mathbf{R_1}$ is the diagonal matrix defined as

$$\mathbf{R_1} = \begin{bmatrix} \frac{1}{1-\alpha_1^2} & 0 & \cdot & 0 \\ 0 & \frac{1}{1-\alpha_2^2} & & \cdot \\ \cdot & & & \\ & & & \\ 0 & & & \frac{1}{1-\alpha_L^2} \end{bmatrix} \qquad (5.3.35)$$

Following earlier work, the motivation of this regularising matrix is to incorporate *a priori* knowledge of the solution which takes into account the radiation efficiency parameter of each individual acoustic mode. The second regularising matrix is a slight variant of the first one defined as

$$\mathbf{R_2} = \begin{bmatrix} 1 & 0 & \cdot & 0 \\ 0 & 1 & & \cdot \\ \cdot & & & \\ & & & \\ 0 & & & \frac{1}{1-\alpha_L^2} \end{bmatrix} \qquad (5.3.36)$$

The diagonal elements of $\mathbf{R_2}$ associated with modes with a cut-on ratio $\alpha_{mn} < 0.99$ are unity and the remaining elements are identical to that of $\mathbf{R_1}$.

The general form of Tikhonov regularisation aims at 'flattening' the singular value spectrum as well as at modifying the basis of vectors. It was shown from equation 5.3.30 that the vectors contained in the matrix $\mathbf{X}^{-1}$ from the GSVD of $(\mathbf{D}, \mathbf{R})$ has the same role in the regularised least-squares solution as the vectors contained in the matrix $\mathbf{V^H}$ from the SVD of $\mathbf{D}$ in the unconstrained least-squares solution. Notice that these vectors do not form any longer an orthonormal basis. Figure 5.7 shows the spectrum of generalised singular values γ_i resulting from the GSVD of pairs $(\mathbf{D}, \mathbf{R_1})$ and $(\mathbf{D}, \mathbf{R_2})$ respectively, the order of which is reversed to make the comparison with the singular values σ_i of $\mathbf{D}$. Figure 5.7 shows that the generalised singular values of $(\mathbf{D}, \mathbf{R_2})$ has an identical behaviour to that of the singular values of $\mathbf{D}$ except for the two smallest singular values which are associated with the acoustic modes of cut-on ratio $\alpha_{mn} > 0.99$. This is not surprising since $\mathbf{R_2}$ differs from the identity matrix only for these modes. A description of the filtered singular values, once the constraint parameter β is applied, is given in the next section. The vectors

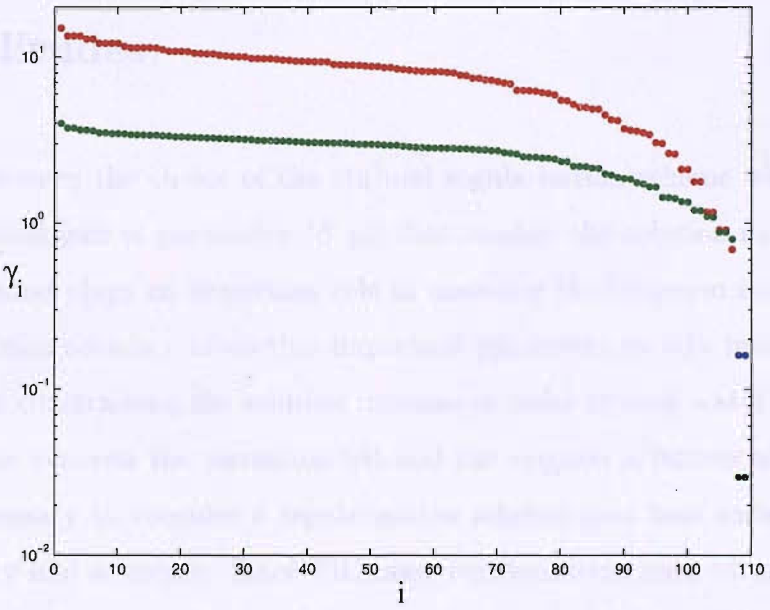

Figure 5.7: Spectra of singular values of: ● $\mathbf{D}$, ● $(\mathbf{D}, \mathbf{R_1})$, and ● $(\mathbf{D}, \mathbf{R_2})$

contained in the matrix $\mathbf{X^{-1}}$ determine the transformed modes and are shown alongside the unitary vectors of $\mathbf{U^H}$ in figures 5.8 and 5.9 for the GSVD of $(\mathbf{D}, \mathbf{R_2})$. Note some strong similarities between the transformed modes and the pressures of the unconstrained least-squares solution and that of the regularised least-squares solution when these figures are compared with figures 4.11 and 4.12. The important difference between these regularised transformed modes and pressures from the original basis of singular vectors is in their differing orders of magnitude.

5.4 Optimal constraint parameter for regularised mode amplitudes

This section discusses the choice of the optimal regularisation scheme which consists of finding the optimal pair of parameter (β, μ_i) that renders the solution more stable. The perturbation bound plays an important role in assessing the inversion robustness. However, reconstruction accuracy is another important parameter to take into consideration. As the efforts of constraining the solution increase in order to seek a stable solution, the chances of errors between the reconstructed and the original solutions also increase. It is therefore necessary to consider a regularisation scheme that best satisfies a trade-off between stability and accuracy. Since Tikhonov regularisation aims at minimising both the residuals and the norm of the solution, another trade off between the error due to regularisation and the error due to noise measurements is to be considered. The L-curve helps in determining this trade-off.

Figure 5.10 shows the variation κ_β, κ_{R_1} and κ_{R_2} and their respective reconstruction accuracies plotted against the constraint parameter β. It shows that values of β of order 10^{-2} are required for the standard form of Tikhonov regularisation as well as for the regularising matrix $\mathbf{R_1}$ to improve the stability of the modal inversion, while lower values of β are

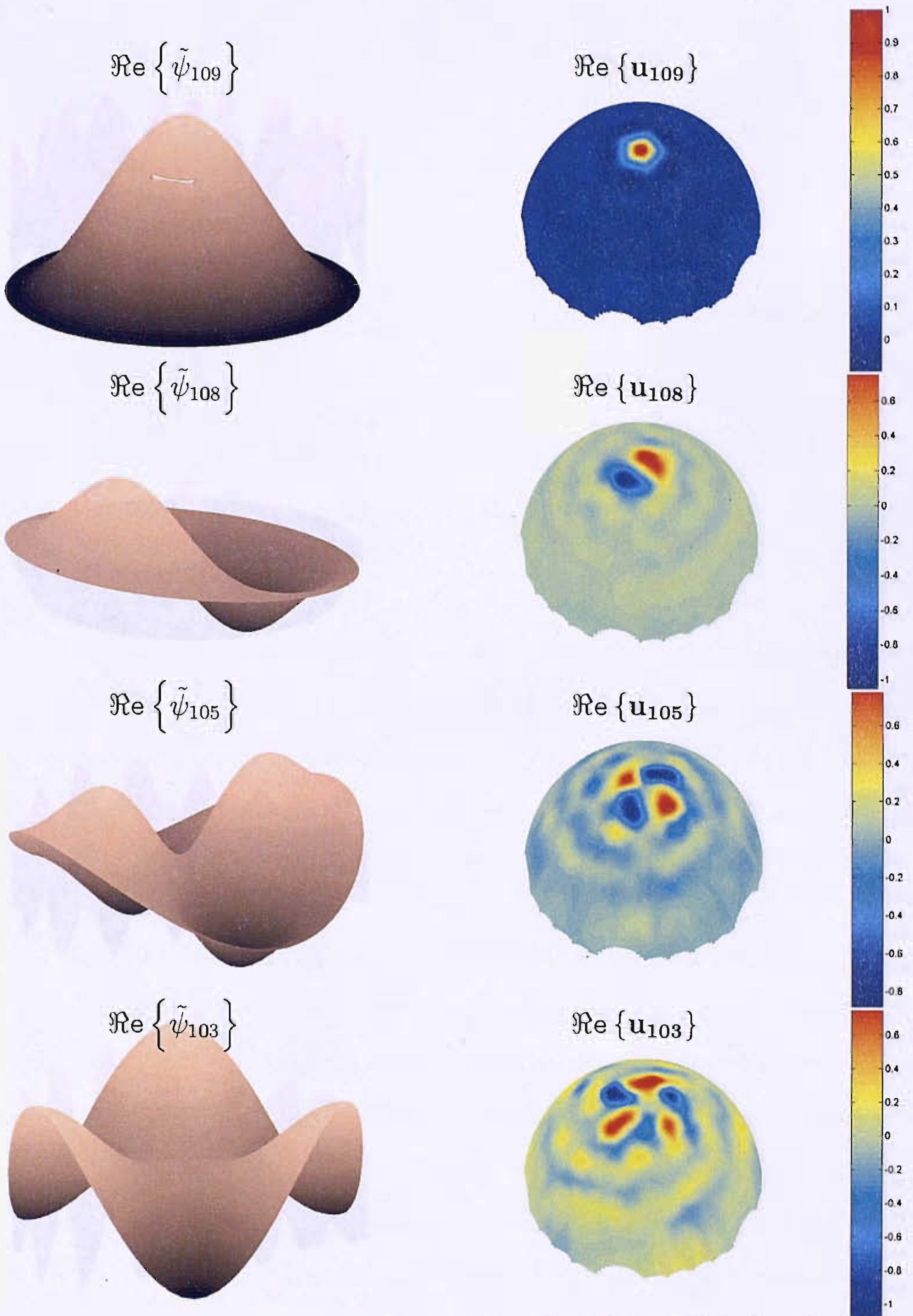

Figure 5.8: Real part of transformed mode shape functions (right hand-side) and transformed acoustic pressures (left hand side) associated with large singular values from the GSVD of $(\mathbf{D}, \mathbf{R_2})$

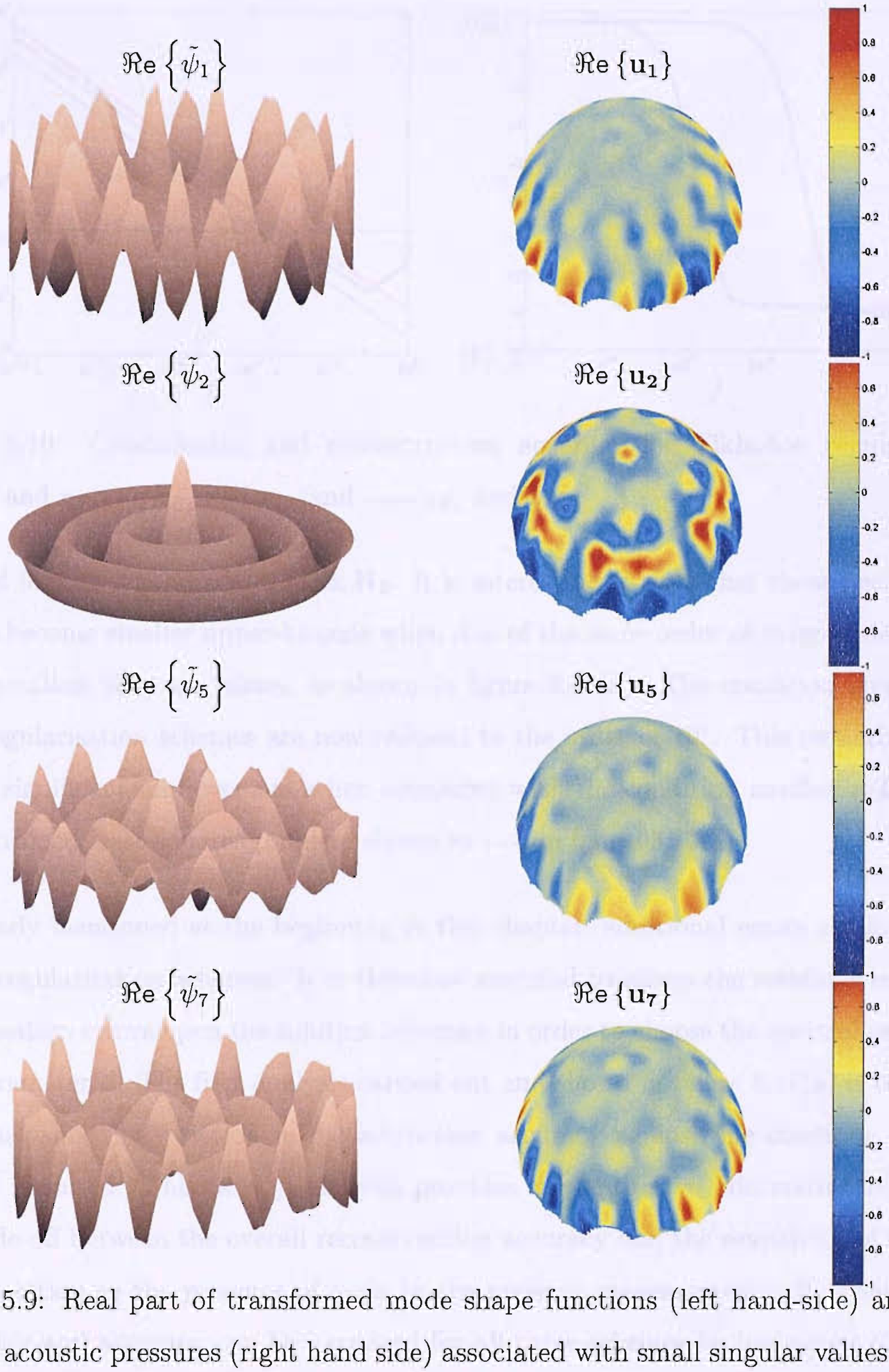

Figure 5.9: Real part of transformed mode shape functions (left hand-side) and transformed acoustic pressures (right hand side) associated with small singular values from the GSVD of $(\mathbf{D}, \mathbf{R_2})$

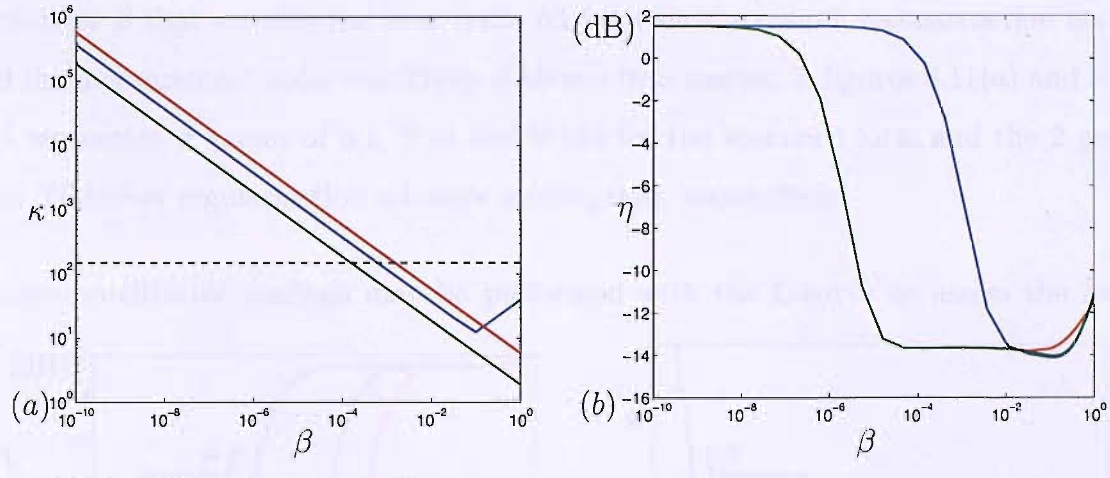

Figure 5.10: Conditioning and reconstruction accuracy for Tikhonov regularisation —— κ_β and η_β —— κ_{R_1} and η_{R_2} and —— κ_{R_2} and η_{R_2}

required for the regularising matrix $\mathbf{R_2}$. It is interesting to note that these perturbation bounds become smaller upper-bounds when β is of the same order of magnitudes as that of the smallest singular values, as shown in figure 5.10(a). The condition numbers for these regularisation schemes are now reduced to the order of 10^1. This reduction represents a significant improvement when compared with the condition number $\kappa(\mathbf{D})$ of the unconstrained least-squares problem shown in ---- in figure 5.10(a).

As already mentioned at the beginning of this chapter, additional errors are introduced by the regularisation schemes. It is therefore essential to assess the residuals errors and regularisation errors upon the solution accuracy in order to choose the optimal regularisation parameter β. The first analysis carried out and shown in figure 5.11(a) is concerned with analysing the variation in reconstruction accuracy against the condition numbers when β is varied. This $(\kappa - \eta)$ analysis provides a quantitative information relating to the trade-off between the overall reconstruction accuracy and the sensitivity of the computed solution to the presence of noise in the pressure measurements. It is shown that sensitivity and accuracy can be improved for all three schemes by increasing β up until 0.2. Above that value the accuracy ceases to improve. This suggests that errors due to regularisation are greater than the residual errors $\|\mathbf{p} - \mathbf{Da}\|$. The optimal regularisation parameter β that satisfies the best trade off between the overall reconstruction accuracy and the measurement noise sensitivity is shown by a marker in figures 5.11(a) and 5.11(b) and represents β values of 0.1, 0.14 and 0.194 for the standard-form and the 2 general-form Tikhonov regularisation schemes investigated, respectively.

A more qualitative analysis may be performed with the L-curve to assess the amount of errors in the solution due to the presence of noise measurements and level of regularisation. The L-curves corresponding to each regularisation scheme are shown in figure 5.11(b). In the general case ($\mathbf{R} \neq \mathbf{I_L}$), the error in the solution is given by

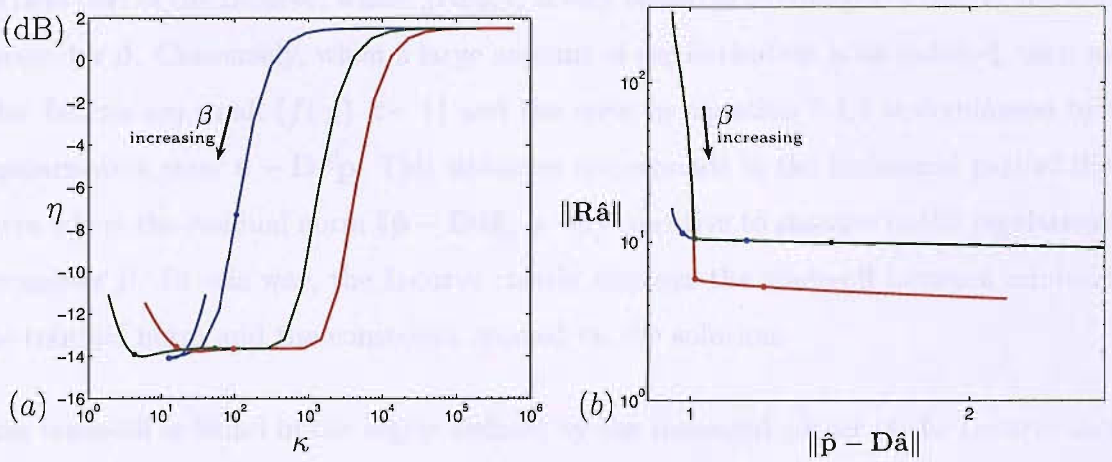

Figure 5.11: Reconstruction accuracy against condition number (a) and L-curve (b) for Tikhonov regularisation —$\mathbf{R} = \mathbf{I_L}$ —$\mathbf{R} = \mathbf{R_1}$ and —$\mathbf{R} = \mathbf{R_2}$

$$\mathbf{a} - \hat{\mathbf{a}}_\mathbf{R} = \mathbf{D}^+\mathbf{p} - \mathbf{D}^\#\hat{\mathbf{p}}$$

$$\mathbf{a} - \hat{\mathbf{a}}_\mathbf{R} = \left(\mathbf{D}^+ - \mathbf{D}^\#\right)\mathbf{p} - \mathbf{D}^\#\mathbf{n} \tag{5.4.1}$$

The final result may be written as

$$\mathbf{a} - \hat{\mathbf{a}}_\mathbf{R} = \left(\mathbf{X}\Sigma^{-1}\mathbf{U}^\mathbf{H} - \mathbf{X}\Sigma^{-1}\Lambda\mathbf{U}^\mathbf{H}\right)\mathbf{p} - \mathbf{X}\Sigma^{-1}\Lambda\mathbf{U}^\mathbf{H}\mathbf{n} \tag{5.4.2}$$

Here Λ is a diagonal matrix whose elements are the filter factors given by equation 5.3.26. Alternatively, this error may be written in terms of the filter factors defined in equation 5.3.17

$$\mathbf{a} - \hat{\mathbf{a}}_\mathbf{R} = \sum_{i=1}^{L}\left[1 - f(\gamma_i)\right]\frac{\mathbf{u_i^H p}}{\sigma_i}\mathbf{x_i} - \sum_{i=1}^{L} f(\gamma_i)\frac{\mathbf{u_i^H n}}{\sigma_i}\mathbf{x_i} \tag{5.4.3}$$

This error consist of two components. One is the perturbation error $\mathbf{D}^{\#}\mathbf{n}$ due to the noise measurement $\mathbf{n}$ and the other is the regularisation error $\mathbf{a} - \mathbf{D}^{\#}\mathbf{p}$ due to regularisation of the noise free measurement $\mathbf{p}$. When very little regularisation is introduced ($\beta << 1$), most of the filter factors of equation 5.3.17 are approximately unity and the error in the solution is dominated by the residuals found in $\mathbf{D}^{\#}\mathbf{n}$. This situation corresponds to the vertical part of the L-curve, where $||\mathbf{R}\hat{\mathbf{a}}_{\mathbf{R}}||_2$ is very sensitive to changes in the regularisation parameter β. Conversely, when a large amount of regularisation is introduced, then most filter factors are small ($f(\gamma_i) << 1$) and the error in equation 5.4.3 is dominated by the regularisation error $\mathbf{a} - \mathbf{D}^{\#}\mathbf{p}$. This situation corresponds to the horizontal part of the L-curve where the residual norm $||\hat{\mathbf{p}} - \mathbf{D}\hat{\mathbf{a}}||_2$ is very sensitive to changes in the regularisation parameter β. In this way, the L-curve clearly displays the trade-off between minimising the residual norm and the constraint applied on the solution.

This trade-off is found in the region defined by the L-shaped corner of the L-curve shown in figure 5.11(b). For given pressure measurements $\hat{\mathbf{p}}$, there is obviously an optimal regularisation parameter that balances the measurement noise and the regularisation error in $\hat{\mathbf{a}}_{\mathbf{R}}$ and is shown by a diamond in figure 5.11(b). It is also seen from this figure that the regularisation parameter that satisfies the trade-off between reconstruction accuracy and noise sensitivity is found in the part of the L-curve which corresponds to an overall error in the solution dominated by the error due to regularisation for each regularisation scheme. A significant amount of regularisation is required in order to reduced the sensitivity of the modal solution to measurement noise. However, the regularisation scheme that involves the regularising matrix $\mathbf{R_2}$ and a parameter β which balances the error due to noise and regularisation allows for an accurate and robust inversion. This scheme presents the particularity of having larger constraint on modes close to cutoff than on well cut-on modes.

Figures 5.12 shows the conditioning and the reconstruction accuracy plotted against *ka* for the 3 regularisation schemes used with their optimal regularisation parameter found from the $(\kappa - \eta)$ analysis. It is shown that significant improvement in the inversion robustness and accuracy can be achieved at the cut-on frequencies. The regularisation scheme using $\mathbf{R_2}$ is seen to provide a highly robust inversion with similar reconstruction accuracy as that of the ones using $\mathbf{I_L}$ and $\mathbf{R_1}$. Condition numbers of order 2 to 3 can be achieved over the whole range of frequencies studied here. The regularisation scheme which imposes most constraint on the modes close to cutoff minimises the residuals without constraining exclusively radiation that contains important information from efficient modes.

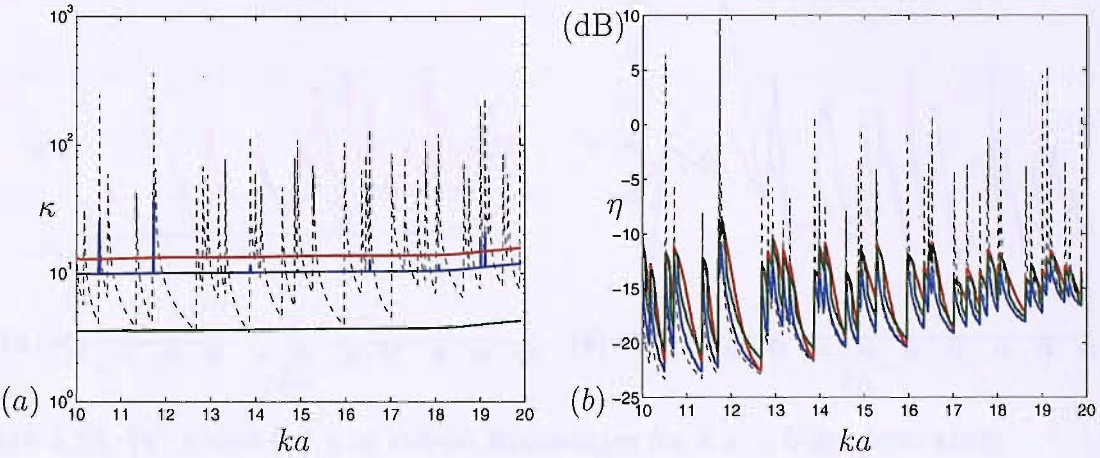

Figure 5.12: (a) κ and (b) η versus ka for a ν = 5-geodesic array ---- no regularisation —— $(\mathbf{R} = \mathbf{I_L}, \beta = 10^{-1})$, —— $(\mathbf{R} = \mathbf{R_1}, \beta = 1.4 \cdot 10^{-1})$ and —— $(\mathbf{R} = \mathbf{R_2}, \beta = 1.94 \cdot 10^{-1})$

5.5 Comparison between the different methods of regularisation

Figures 5.13(a) and 5.13(b) show the condition numbers and the reconstruction accuracy parameters at the cut-on frequencies respectively and allow a comparison of the cut-on mode discarding, the singular value discarding and the Tikhonov regularisation techniques in terms of robustness and accuracy. It is shown that these schemes are essentially similar within a few decibels in terms of reconstruction accuracy. However it is interesting to note that the Tikhonov regularisation technique using $\mathbf{R} = \mathbf{R_2}$ and $\beta = 1.94 \cdot 10^{-1}$ achieve much more robust inversion than the other schemes. During the experiments, we can only have access of condition number which bounds the perturbation in the solution from the measurement noise and thus allows to assess the performance of the inversion technique. Therefore the Tikhonov regularisation technique shown here turns out to be very useful and will be applied on the experimental data.

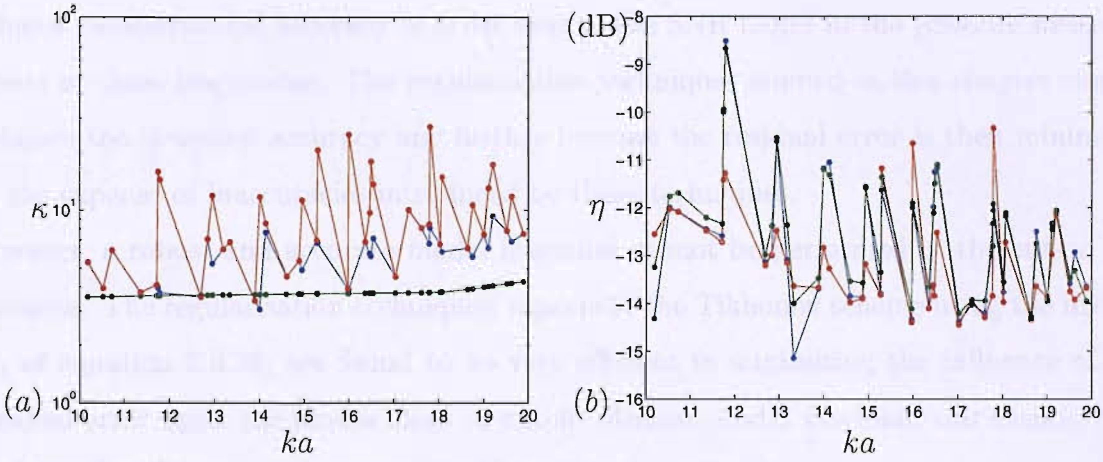

Figure 5.13: (a) κ and (b) η at cut-on frequencies for a ν = 5-geodesic array
● 2 Nearly cut-off modes discarding, ● 2 singular values discarding and
● Tikhonov regularisation ($\mathbf{R} = \mathbf{R_2}$, $\beta = 1.94 \cdot 10^{-1}$)

5.6 Conclusion

In this chapter different methods for improving inversion robustness and accuracy at the modal cut-on frequencies have been investigated. Although, in practice, the reconstruction accuracy parameter remains unknown when the inversion is performed from experimental data, the computer-based simulations of this parameter have been useful to control if these regularisation techniques perform accurate solution while reducing the sensitivity to noise measurements. It is seen that the inversion robustness as well as the reconstruction accuracy can be significantly enhanced at the cut-on frequencies for the regularisation techniques investigated. It is also shown that these techniques performed on geodesic arrays, which were found to couple best with the modal information radiated from the inlet, are efficient only at the cut-on frequencies. The study on sensor geometry is therefore essential in implementing a robust and accurate modal inversion away from the cut-on frequencies. It was shown in chapter 3 that geodesic sensor arrays can almost achieve reconstruction accuracy of order that of the SNR found in the pressure measurements at these frequencies. The regularisation techniques studied in this chapter cannot enhance the inversion accuracy any further because the residual error is then minimised at the expense of inaccuracies introduced by these techniques.

However, a robust and accurate modal inversion cannot be performed at the cut-on frequencies. The regularisation techniques, especially the Tikhonov scheme using the matrix $\mathbf{R_2}$ of equation 5.3.36, are found to be very efficient in minimising the influence of the residual error upon the modes close to cutoff. Robust modal inversion can therefore be performed with improved accuracy at the cut-on frequencies.

Chapter 6

Finite Element/Infinite Element Radiation Model

Chapter 3 has shown that an essential aspect of the inversion procedure proposed in this thesis is the accurate modelling of the modal directivity factor. The numerical integration of the Rayleigh integral as discussed in section 2.2.1 provides a simple model of the sound radiation in the near field from a flanged duct. This model was used so far as a first approximation to simulate the essential radiation properties of acoustic duct modes and to investigate the issues that arises in the reconstruction of mode amplitudes from inversion of sound pressure measurements on the TCS. However, actual duct inlets have complex geometrical features that cannot be modelled with sufficient accuracy using the Kirchhoff approximation. In this chapter, a numerical model using a finite element (FE) and infinite element (IE) analysis is performed to compute the sound field radiation from a duct into an unbounded domain. The commercial software ACTRAN is used to perform such an analysis. The effect on the radiation of the bellmouth as well as the effects of removing the flange at the inlet exit, that are not accounted for with the numerical Rayleigh integral are now incorporated. This chapter discusses the method used to perform the FE/IE model, details of the various meshes carried out, and presents the results obtained for the modal radiation. These are then compared with that obtained from the numerical Rayleigh integral.

6.1 FE/IE analysis procedure

A FE/IE analysis of sound propagation and radiation using Actran generally involves a four step procedure, which can be summarised as follows:

- **Step 1** Creation of a finite mesh of the surrounding acoustic domain
- **Step 2** Definition of material properties and boundary conditions
- **Step 3** Creation of an Actran input file, which is run in batch mode and converted into output files
- **Step 4** Post-processing of the output files to investigate the results

6.1.1 Creating a FE/IE mesh

It was shown in sections 2.1 and 2.2 that sound propagation within a duct (i.e. equation 2.1.16) and its sound radiation (i.e. equations 2.2.17 and 2.2.18) define an axisymmetric problem with a spatial dependence in the azimuthal direction of the form $e^{-jm\theta}$. The solution of the 3D problem may therefore be obtained from a 2D mesh accounting for the polar dependence only. The acoustic domain near the source is then modelled by a 2D mesh with acoustic finite elements and the entire unbounded domain is modelled by acoustic infinite elements. Infinite elements are a special type of elements modelling the sound radiation beyond the finite element mesh and are materialised by their faces at a finite distance defined by the FE/IE interface. The discretisation of the mesh depends on the frequency studied, such that the element length l_e satisfies

$$l_e \leq \frac{\lambda}{8} \tag{6.1.1}$$

where λ is the free-space wavelength. A mesh refinement is carried out in the area of the duct termination especially around the duct lip (e.g. the bellmouth). In this region, the element length satisfies

$$l_e \leq \frac{\lambda}{16} \tag{6.1.2}$$

Such size of elements is necessary to model lip or unflanged effects [34] accurately but increases the computation time, which is compensated for by the 2D meshing. Another requirement to improve accuracy of computation is the choice of quadrangular, rather than triangular, elements. Quadrangular elements are a type of element that uses a quadratic polynomial, which tends to reduce pollution effects while keeping the same number of degrees of freedom and therefore allows a good trade-off between accuracy and computational time [35], [36]. This element topology is formed by 8 nodes and is shown in figure 6.1(a). Sound radiation beyond the domain modelled with finite elements is then modelled by a layer of infinite elements, which is placed along the free external faces

(a)

8 nodes quadrangular finite element

(b)

3 nodes linear infinite element

Figure 6.1: Finite Element and Infinite Element topology

of the acoustic finite element mesh. In order to complete the FE/IE interface, the IE topology used is the line element, which like the FE uses a quadratic polynomial. These are formed by 3 pre-existing nodes and are shown in figure 6.1(b) from the finite element free external faces. The sound field in each infinite element is modelled by a multipole expansion of the following form

$$p \approx \sum_{n} \frac{e^{-jkr}}{r} \left(a_0 + \frac{a_1}{r} + \frac{a_2}{r^2} + \cdots + \frac{a_n}{r^n} \right) \tag{6.1.3}$$

where n is the infinite element radial interpolation order. Since the radiation is computed in the near-field, the FE domain is small, and so the sound field in the IE domain cannot be approximated by a low order multipole expansion. Therefore a high radial interpolation order (i.e. $n = 15$) is adopted.

6.1.2 Defining material properties and boundary conditions

Material properties characterising the acoustical behaviour of FE must be assigned to the mesh. The acoustic fluid assigned to the FE mesh, namely air at room temperature, is characterised by the following parameters:

- Density ρ
- Speed of sound c
- Heat capacity at constant pressure C_p
- Heat capacity at constant volume C_v

The boundary conditions for this problem are that of a hard-walled duct with the corresponding mode shape functions distributed over the duct outlet cross-section. This boundary conditions then couples the acoustic FE mesh with the modal component of incident duct modes as defined in equation 2.1.16 with unit pressure mode amplitude. Similar to the FE/IE interface, this modal basis is assigned onto 3 node linear elements placed along the free external faces of the acoustic FE mesh.

Finally, the results will be computed at field points created by nodes within the acoustic IE domain, which are equally spaced along a polar arc at 1m away from the inlet. These field points must be thought of as virtual microphones at which the software Actran calculates and stores relevant output quantities.

6.1.3 Mesh generation

The mesh data (i.e. node and element ID's) discussed in section 6.1.1, and the parameters detailed in section 6.1.2, are defined in an input file. The input file used by the software Actran is an ASCII file made of many different section or sub-section types that are denoted as data blocks and contains all the necessary information for the calculation performed by the software Actran.

6.2 Results for the FE/IE solution

6.2.1 Validation of the FE/IE procedure

A mesh for a flanged duct was created following the procedure detailed in the previous section to compute the radiated sound field with Actran and is shown in figure 6.2. In this simulation the duct radius was set to $a = 0.315$m and the radial distance from the centre of the duct exit cross-section was set to $r = 1$m. Polar directivities at $ka = 15$ for all cut-on modes are computed with the FE/IE mesh and are compared with those computed from the numerical evaluation of the Rayleigh integral detailed in chapter 2.

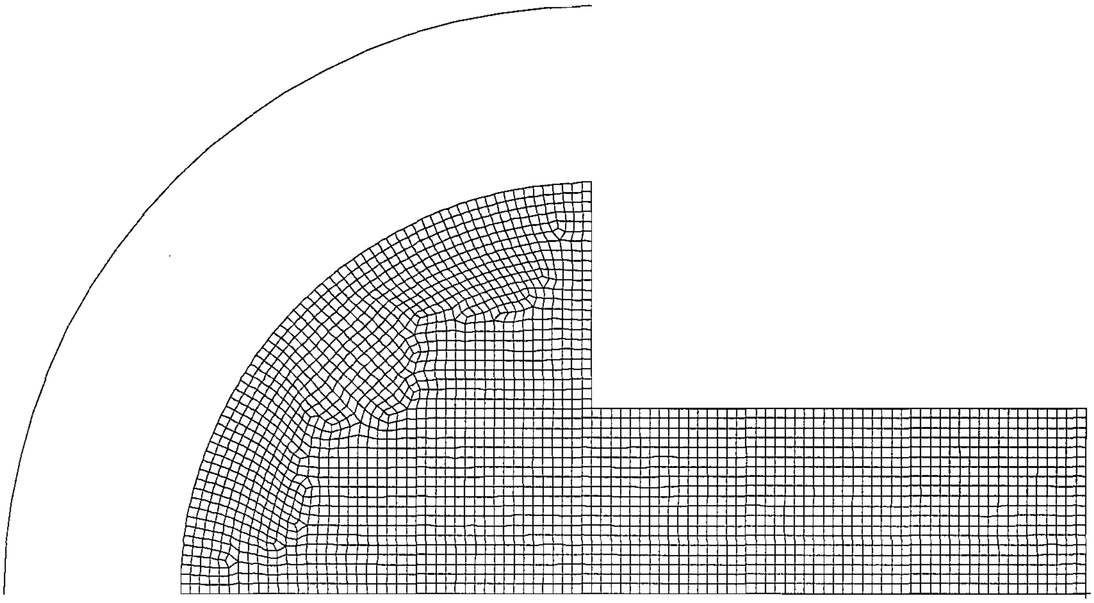

Figure 6.2: Finite Element/Infinite Element mesh for a flanged duct

This comparison for various modes of different cut-on ratios is shown in figures 6.3 and 6.4 and allows the validation of the procedure detailed in section 6.1 prior to modelling more complex geometries. Good agreement between the two solutions both in magnitude and phase is generally observed, especially for the modes that are well cut-on $\alpha_{mn} < 0.8$. For modes close to cutoff, i.e. $\alpha_{mn} > 0.8$, significant differences in the polar directivities are observed in amplitude and phase.

The reasons for these differences arise from the fact that the numerical integration of the Rayleigh integral does not account for reflection and refraction at the duct termination (i.e. see equation 2.1.16), while these effects are necessarily included in the Actran solution. The energy carried by well cut-on modes is radiating with no reflection, and refraction effects at the duct exit shoulder is negligible as the energy is mainly radiating near the duct axis. As a result the FE/IE solution agrees well both in magnitude and phase with the prediction obtained from the Rayleigh integral. As cut-off is approached, the duct termination becomes more reflective and refractive. The differences between the

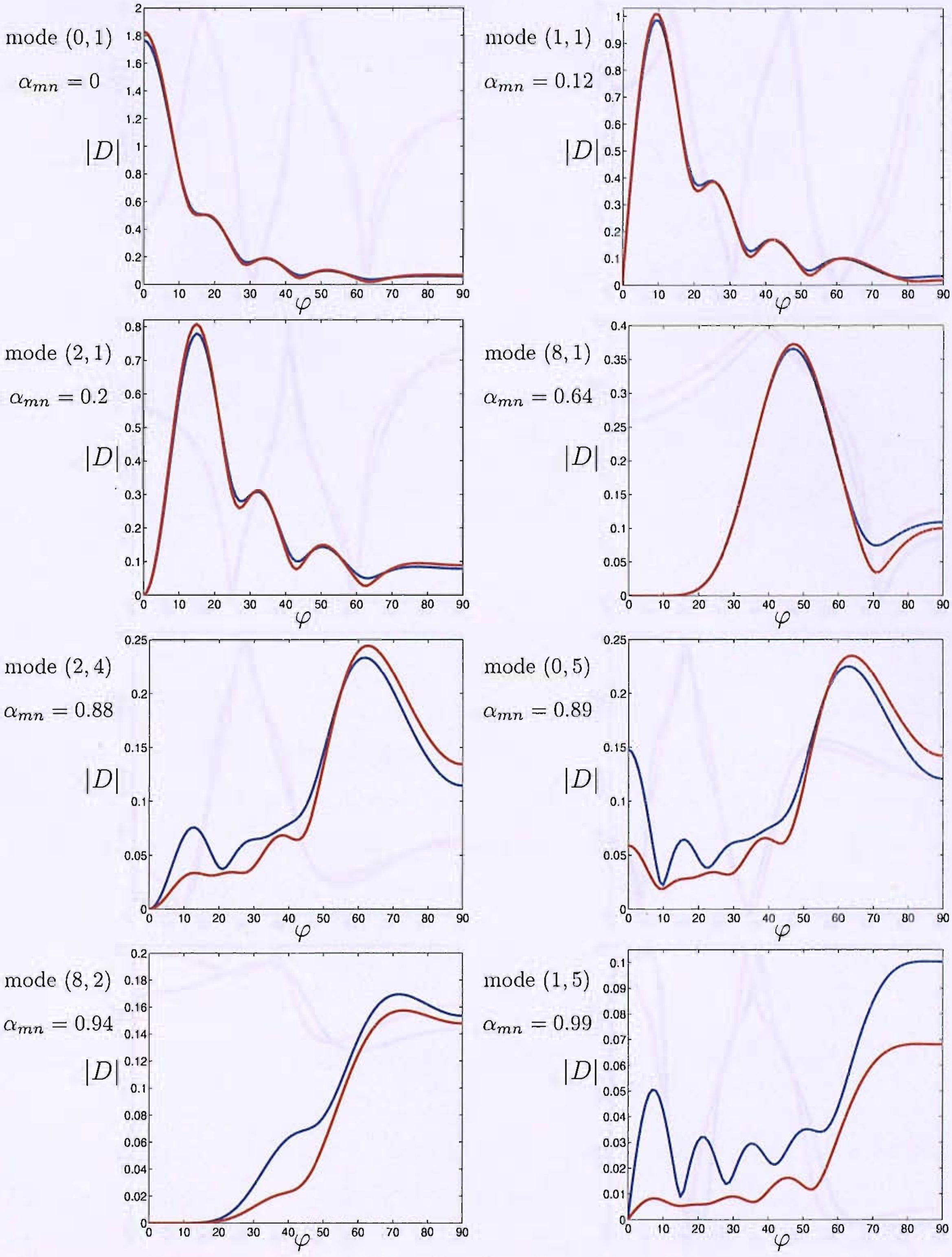

Figure 6.3: Comparison of modulus of polar directivities D at $ka = 15$ between the Rayleigh integral and the Actran model for a flanged duct

—— Actran model —— Numerical integration

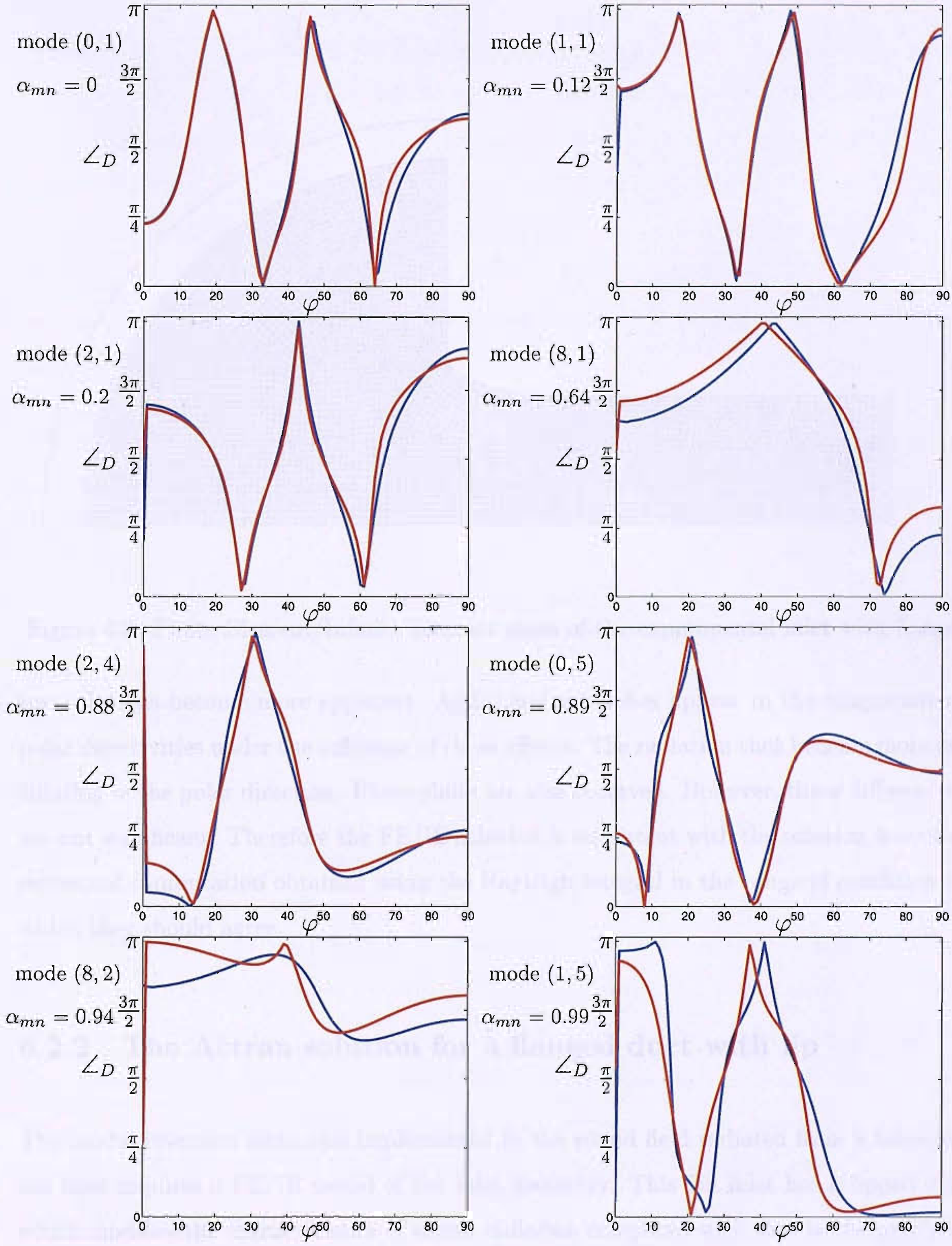

Figure 6.4: Comparison of phase of polar directivities D at $ka = 15$ between the Rayleigh integral and the Actran model for a flanged duct

— Actran model — Numerical integration

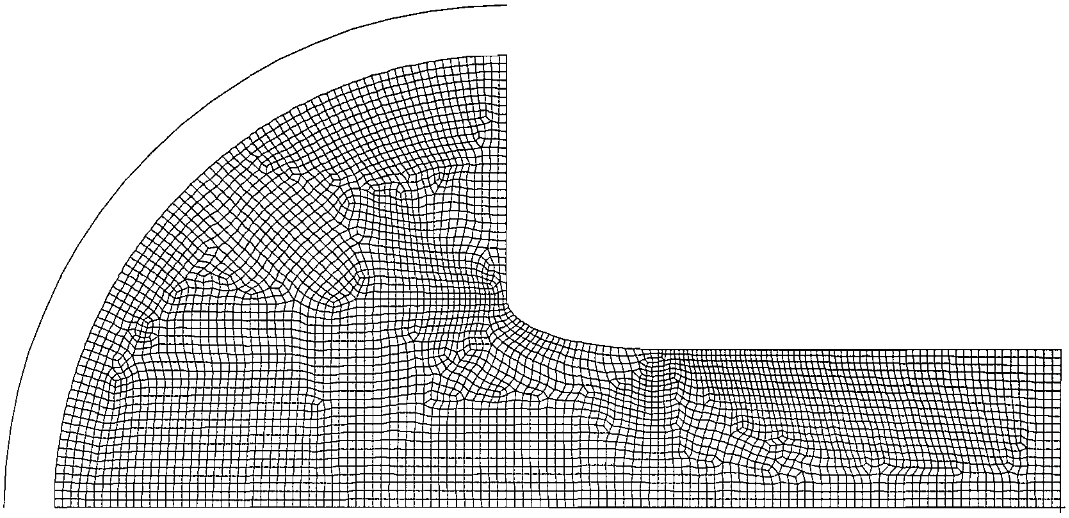

Figure 6.5: Finite Element/Infinite Element mesh of the experimental inlet with flange

two solutions become more apparent. Additional side lobes appear in the magnitude of polar directivities under the influence of these effects. The radiation thus become more oscillating in the polar direction. Phase shifts are also observed. However, these differences, are not significant. Therefore the FE/IE solution is consistent with the solution from the numerical computation obtained using the Rayleigh integral in the range of condition in which they should agree.

6.2.2 The Actran solution for a flanged duct with lip

The modal inversion technique implemented to the sound field radiated from a lab-scale fan inlet requires a FE/IE model of the inlet geometry. This fan inlet has a lipped exit which modifies the characteristics of sound radiation compared with that in the previous section for a flanged duct. In order to understand the influence of the lip on sound radiation, an FE/IE model of the inlet with a flange was performed as shown in figure 6.5. The polar directivities deduced from this model are compared with the duct with sharp edge shown in figure 6.2. This comparison for the modulus and phase of these polar directivities D is shown in figures 6.6 and 6.7 respectively. Figures 6.6 and 6.7 show that the lip has a significant effect on the sound radiation, particularly for modes close to cutoff. The influence of the lip on sound radiation for well cut-on modes (i.e. $\alpha_{mn} < 0.5$) and modes approaching cutoff has been analysed by Rice [37]. The main results of this analysis is described below.

From the theory developed in chapter 2, the angle ξ_z of the normal of the wave front with the duct axis which denotes the phase velocity can be readily found by

$$\cos\xi_z = \frac{\sqrt{k^2 - \kappa_{mn}^2}}{k} = \sqrt{1 - \alpha_{mn}^2} \tag{6.2.1}$$

Figure 6.6 shows that the main radiation lobe of well cut-on modes tends to shift away from the duct axis while the side lobes are smoothed out. Radiation energy from the main radiation lobe seems to have been transferred to the troughs of radiation of the straight duct.

As cutoff is approached (i.e. $\alpha_{mn} > 0.5$), the main lobe of radiation tends to shift towards the duct axis. This shift increases for modes excited closer to cutoff. At cutoff, a mode propagates in a straight inlet with an angle $\xi_z \approx \pi/2$ which can be seen to bounce back and forth between the duct walls before radiating. The growing radial dimension of the bellmouth as the mode propagates causes the cut-on ratio α_{mn} to decrease. This mode progresses in the bellmouth with a phase velocity which decreases gradually towards the duct axis until the phase velocity angle equals the bellmouth wall slope. The pressure wave is no longer constrained by the bellmouth and escapes in the near field.

Finally, the lip enhances the side lobes observed in figure 6.3 and become more important than the main radiation lobe.

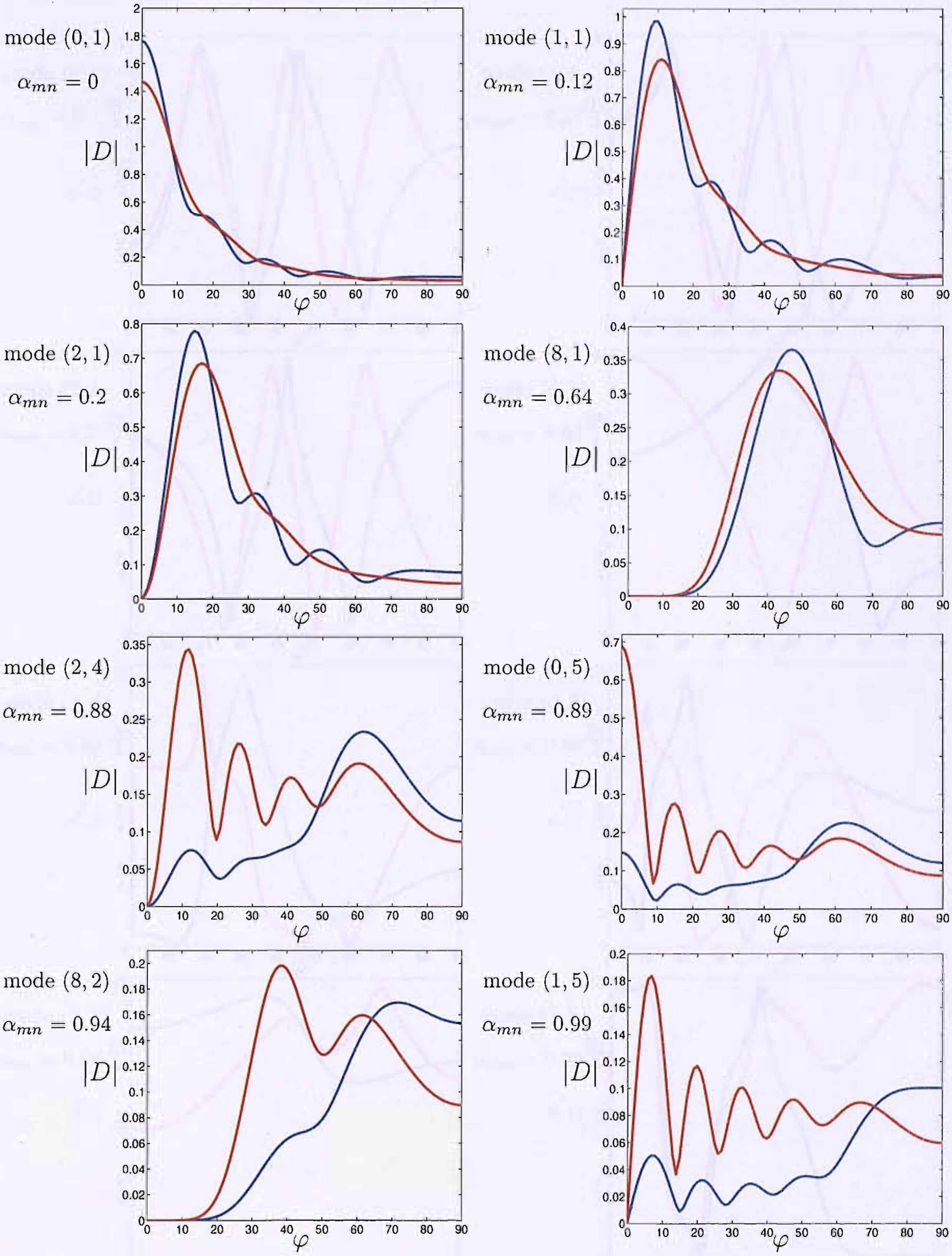

Figure 6.6: Comparison of modulus of polar directivities D at $ka = 15$ between the straight and lipped ducts with flange using Actran

—— straight duct —— lipped duct

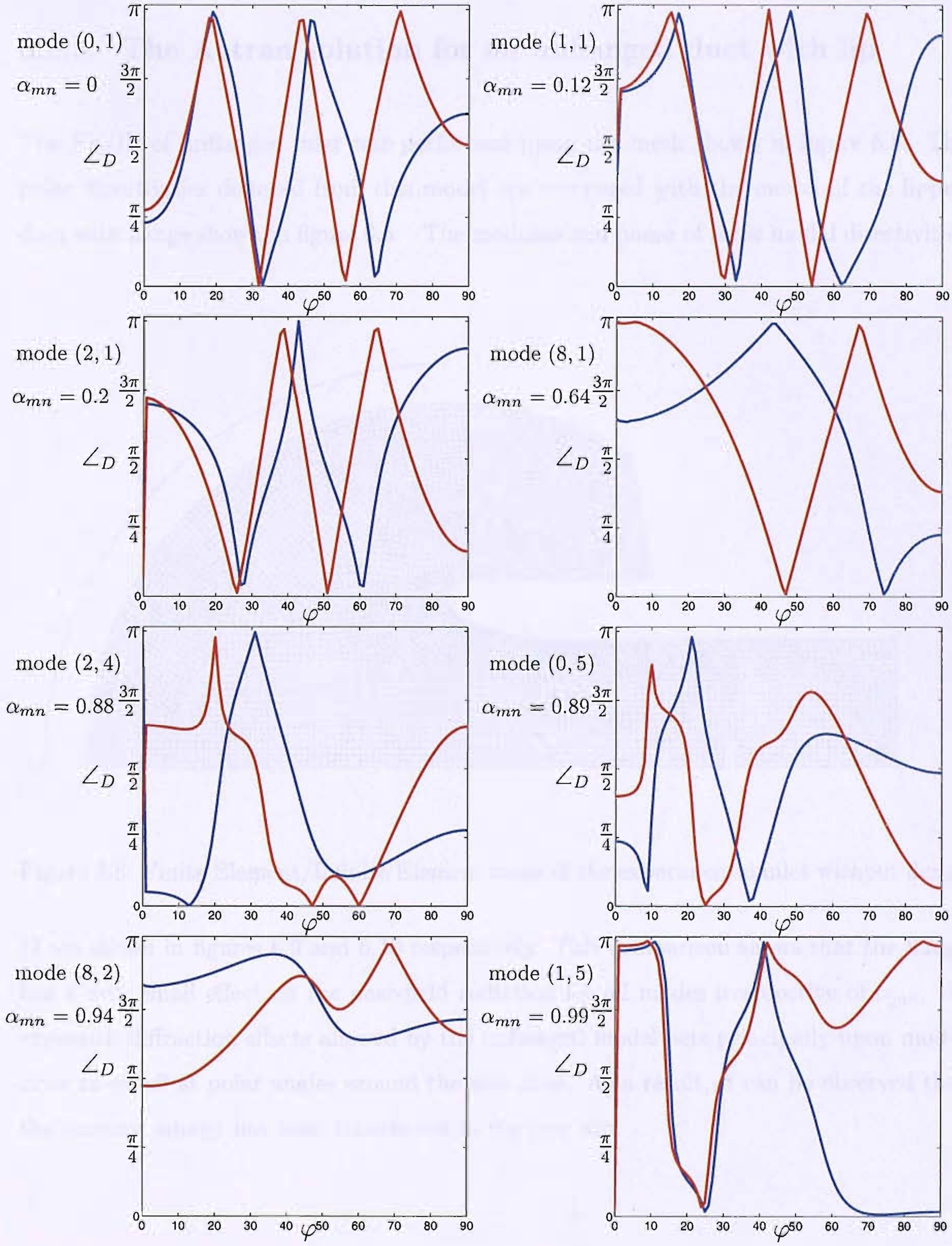

Figure 6.7: Comparison of phase of polar directivities D at $ka = 15$ between the straight and lipped ducts with flange using Actran

—— straight duct —— lipped duct

6.2.3 The Actran solution for an unflanged duct with lip

The FE/IE of unflanged inlet was performed using the mesh shown in figure 6.8. The polar directivities deduced from this model are compared with the model of the lipped duct with flange shown in figure 6.5. The modulus and phase of these modal directivities D are shown in figures 6.9 and 6.10 respectively. This comparison shows that the flange has a very small effect on the near-field radiation for all modes irrepsective of α_{mn}. As expected, diffraction effects allowed by the unflanged model acts principally upon modes close to cutoff at polar angles around the side lines. As a result, it can be observed that the acoustic energy has been transferred in the rear arc.

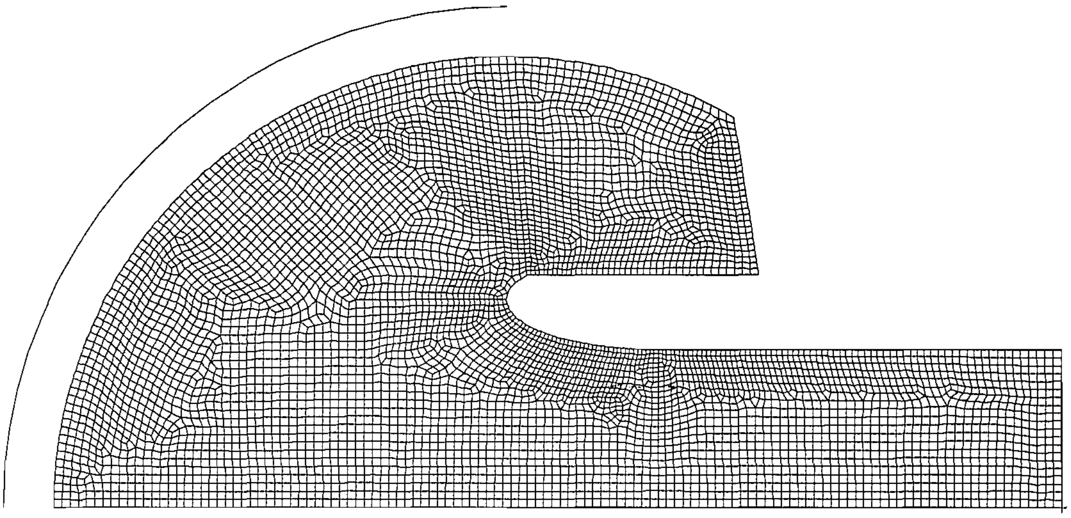

Figure 6.8: Finite Element/Infinite Element mesh of the experimental inlet without flange

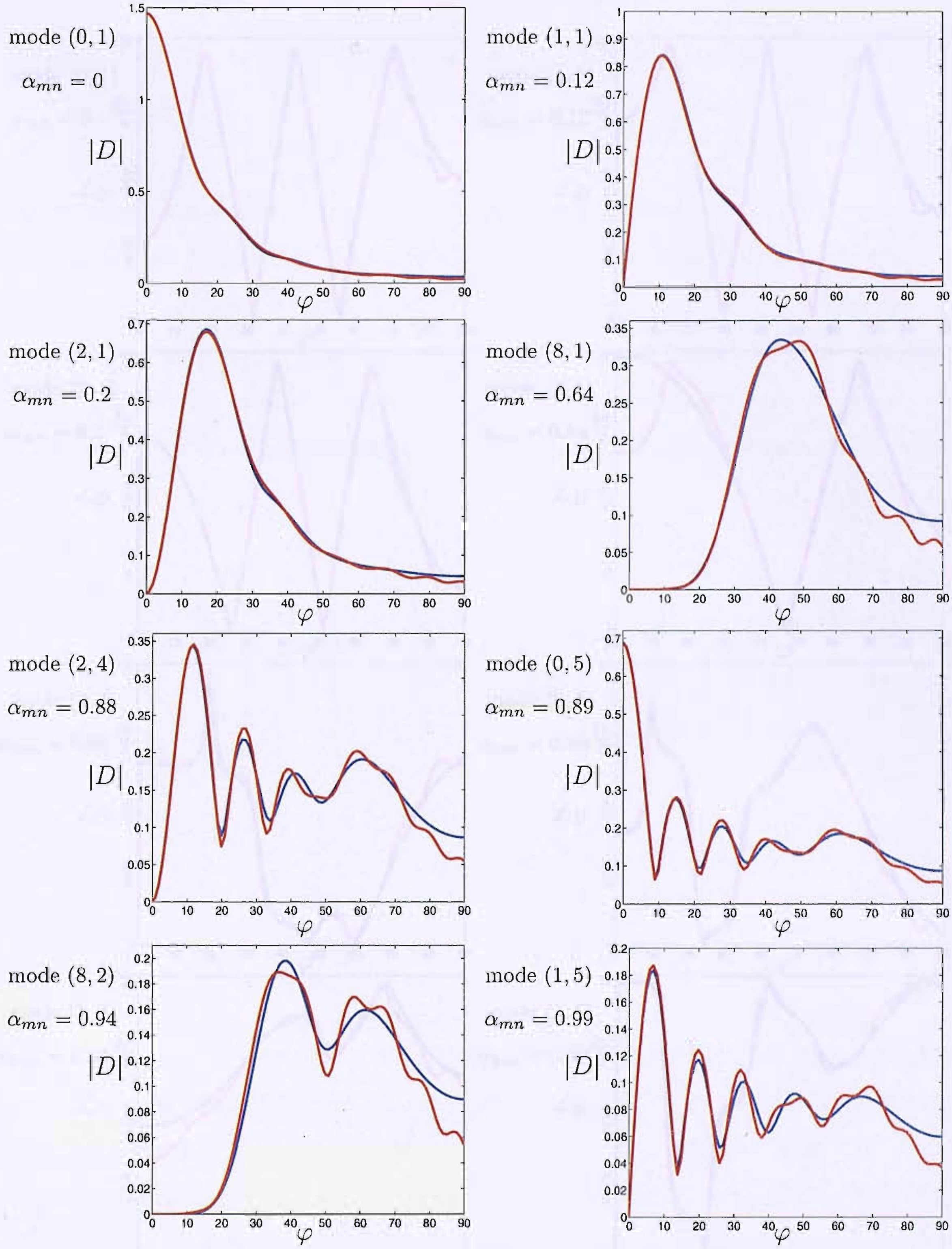

Figure 6.9: Comparison of modulus of polar directivities D at $ka = 15$ between the flanged and unflanged lipped ducts using Actran

—— flanged inlet —— unflanged inlet

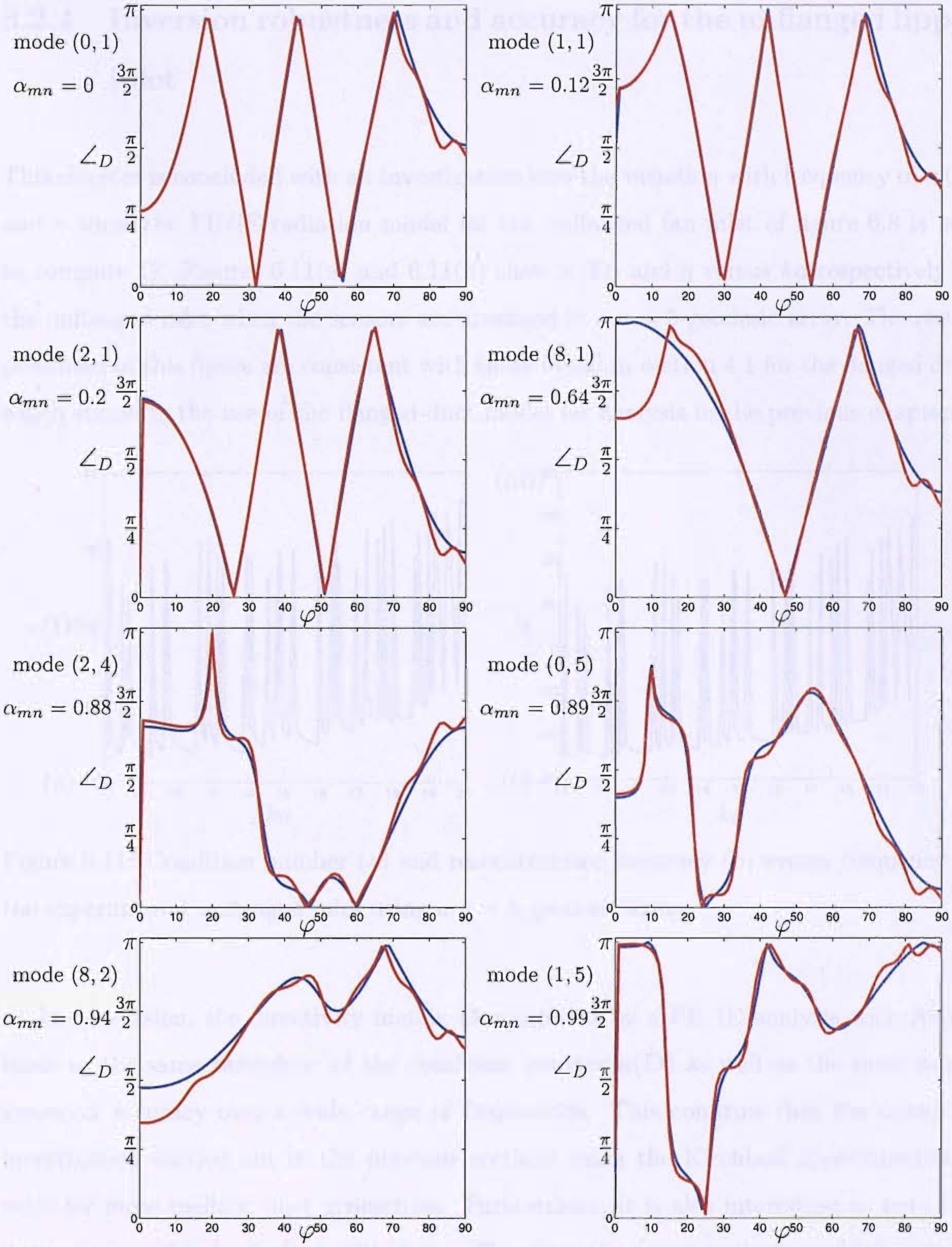

Figure 6.10: Comparison of phase of polar directivities D at $ka = 15$ between the flanged and unflanged lipped ducts using Actran

—— flanged inlet —— unflanged inlet

6.2.4 Inversion robustness and accuracy for the unflanged lipped inlet

This chapter is concluded with an investigation into the variation with frequency of $\kappa(\mathbf{D})$ and η when the FE/IE radiation model for the unflanged fan inlet of figure 6.8 is used to compute $\mathbf{D}$. Figures 6.11(a) and 6.11(b) show $\kappa(\mathbf{D})$ and η versus ka respectively for the unflanged inlet when the sensors are arranged in a $\nu = 5$-geodesic array. The results presented in this figure are consistent with those found in section 4.1 for the flanged duct, which supports the use of the flanged-duct model for analysis in the previous chapters.

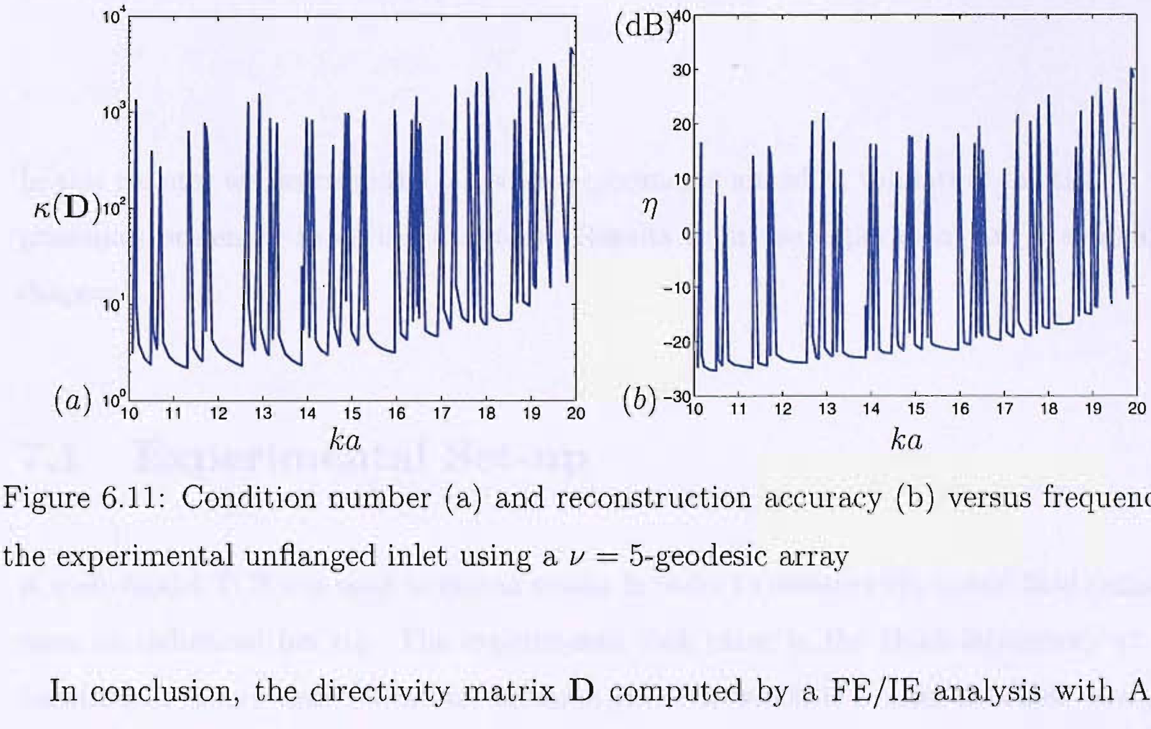

Figure 6.11: Condition number (a) and reconstruction accuracy (b) versus frequency for the experimental unflanged inlet using a $\nu = 5$-geodesic array

In conclusion, the directivity matrix $\mathbf{D}$ computed by a FE/IE analysis with Actran leads to the same behaviour of the condition number $\kappa(\mathbf{D})$ as well as the same modal inversion accuracy over a wide range of frequencies. This confirms that the numerical investigation carried out in the previous sections using the Kirchhoff approximation is valid for more realistic duct geometries. Furhtermore, it is also interesting to note that Actran is capable in dealing with flow. Therefore the same analysis could be readily performed to model the modal directivity functions in the presence of flow.

Chapter 7

TCS Near-field measurements

In this chapter we describe the lab-scale experiments aimed at validating the theory and principles presented in earlier chapters. Results from the experiment are presented in chapter 8.

7.1 Experimental Set-up

A scale-model TCS was used to mount sensor in order to measure the sound field radiated from an industrial fan rig. The experiments took place in the Doak laboratory at the Institute of Sound and Vibration Research (ISVR), which is a semi anechoic chamber that enables measurements of the acoustic radiation from the inlet to be made under nearly free-field conditions.

7.1.1 Fan rig

The duct surrounding the fan is made from steel of radius $a = 0.315$m. The fan comprises 9 blades and is situated a distance of 0.84m from the duct exit. The maximum rotational speed of the fan is 50Hz, which produces an axial flow speed of $M \approx 0.1$. The fan rig and the fan blades are shown in figure 7.1(a) and 7.1(b) respectively.

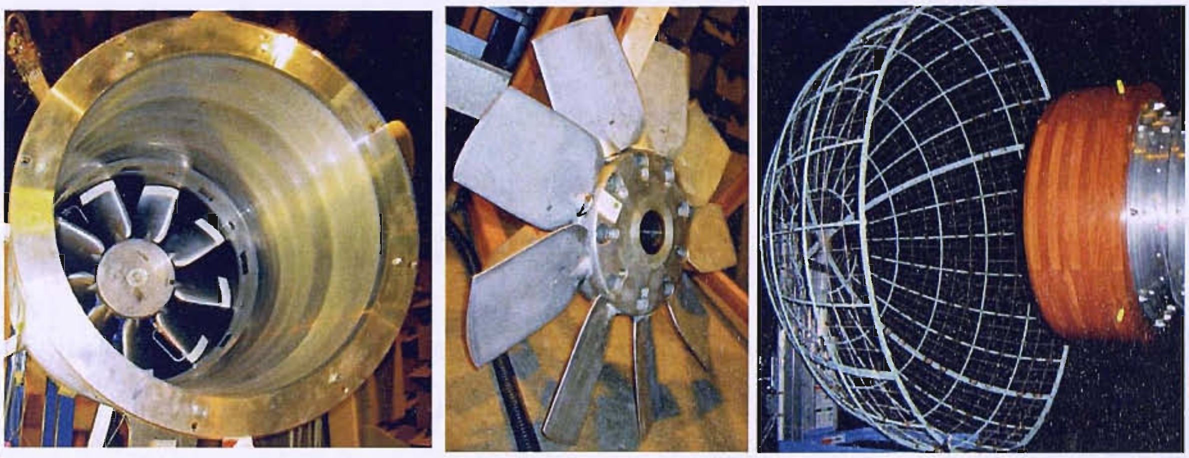

(a) The steel-walled fan inlet

(b) The 9 bladed fan

(c) Inlet with bellmouth and hemispherical rig

Figure 7.1: The steel-walled fan inlet used during the experiment

The duct wall has a series of small holes that allow rings of wall-flush mounted microphones to be inserted for in-duct modal analysis. A single ring of 24 microphones is used to perform a spinning modal decomposition by way of validating the mode amplitudes inverted from the TCS pressure measurements.

A wooden bellmouth with dimensions given in chapter 6 and shown in figure 7.1(c) is fixed to the end of the duct to model the acoustic behaviour of the lip usually present in the turbofan inlets of real aircraft engines. The lip is a smooth wooden varnished surface. It has been shown in chapter 6 that the bellmouth modifies the modal radiation charac-

(a) TCS mounted in near-field of inlet by a crane

(b) Microphones mounted on the TCS

(c) Close look of a microphone clipped on the TCS

Figure 7.2: Experimental set-up of microphones on the laboratory-scale TCS

teristics compared with that when it is absent and hence it is important to incorporate this effect in the experimental duct.

7.1.2 Scale-model TCS array

A hemispherical wire-frame made from a series of steel bars bent into an arc and positioned at every 15^o, both in the polar and azimuthal angles, is used to simulate the TCS. In order to achieve a finer positioning of the microphones, strings are stretched over the rig at every 5^o in both angles, as shown in figure 7.1(c). The TCS is mounted at the inlet exit by a crane as shown in figure 7.2(a). The TCS is of 1m radius which corresponds to a ratio r/a of 3.2. The TCS used on real engines corresponds to a ratio r/a of 6. The model TCS is therefore located slightly closer in the near field than that of a full-scale TCS.

The acoustic measurements are made using Brüel & Kjaer Falcon $1/4''$ microphones mounted on pegs for affixing them to the strings and bars of the TCS. The microphones are arranged such their diaphragms face the inlet centre. The dimensions of the pegs and bars are significantly smaller than the maximum wavelength of interest and should therefore not affect significantly the sound field. The mounting of microphones on the TCS is shown in figures 7.2(b) and 7.2(c).

Four sensor array geometries are investigated. These are: 7 ring, 7 leg star-fish and 5 rotation spiral sensor arrays of 110 microphones, and a $\nu = 4$-geodesic sensor array of 91 microphones. As a way of independently verifying the modal amplitude estimates from the TCS array, modal analysis was performed of the in-duct sound field using in-duct microphones mounted within plastic holders and inserted within holes found in the duct wall and arranged in a ring. Signals captured by the microphones are then fed into four ISVR custom-built pre-amplifiers each comprising 33 input channels. The cabling of the microphones is shown in figures 7.3(a) and 7.3(b). For reasons of practicality, microphone cables are tied in groups of five prior to connecting to amplifier input channels as shown in figure 7.3(a). Amplifiers outputs are then connected to two SONY SIR 1000 digital recording systems with 64 channels each. These are synchronised to record signals simultaneously on DAT magnetic tapes (i.e. see figure 7.3).

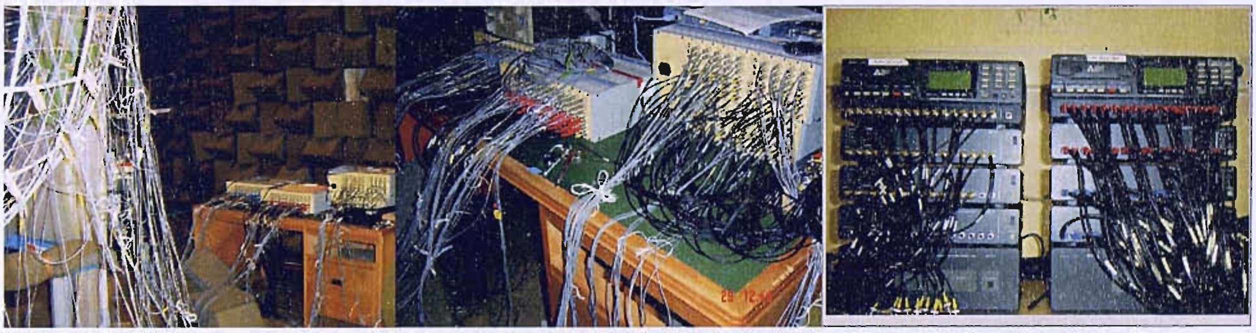

(a)

Microphones connected to amplifiers

(b)

Close look of amplifier connections

(c)

Interface cables connected to DAT recorders

Figure 7.3: Experimental hardware

7.2 Power Spectrum Estimation

Broadband sound fields produce random signals which are then discretised by the A/D card. These random signals are assumed to be ergodic. The autocorrelation C_{xx} and the cross-correlation C_{xy} functions, which determine how a random signal $x(n)$ is related with itself and with another random signal $y(n)$ at another instant respectively, are defined as

$$\begin{aligned} C_{xx}(m) &= \tfrac{1}{N}\sum_{n=0}^{N-|m|-1} x(n)x^*(n+m) \\ C_{xy}(m) &= \tfrac{1}{N}\sum_{n=0}^{N-|m|-1} x(n)y^*(n+m) \end{aligned} \tag{7.2.1}$$

where N is the total number of samples in a single data sequence.

The auto-power and cross-power spectra are the Fourier transforms of the above autocorrelation and cross-correlation functions and are defined as follows:

$$\begin{aligned} S_{xx}(\omega) &= \sum_{m=-(N-1)}^{N-1} C_{xx}(m)\, e^{-jm\omega} = \tfrac{1}{N}\left|X(\omega)\right|^2 \\ S_{xy}(\omega) &= \sum_{m=-(N-1)}^{N-1} C_{xy}(m)\, e^{-jm\omega} = \tfrac{1}{N}X(\omega)\,Y^*(\omega) \end{aligned} \tag{7.2.2}$$

where $X(\omega)$ and $Y(\omega)$ denote the Fourier transform of $x(n)$ and $y(n)$ respectively. For a given random process, the parameters defined in equations 7.2.1 and 7.2.2 are also random processes. An estimate of these parameters, say $\hat{\alpha}$, averaged over the sequence of N samples satisfies the following:

$$E\left[(\hat{\alpha}-\alpha)^2\right] = \sigma_{\hat{\alpha}}^2 + B^2 \qquad \text{as N} \mapsto \infty \tag{7.2.3}$$

where B and $\sigma_{\hat{\alpha}}$ are the bias and the variance of the estimator respectively, defined as

$$B = \alpha - E\left[\hat{\alpha}\right] \tag{7.2.4}$$

and

$$\sigma_{\hat{\alpha}}^2 = E\left[(\hat{\alpha} - E\left[\hat{\alpha}\right])^2\right] \tag{7.2.5}$$

Ideally, we wish to compute an unbiased estimate of these parameters such that their mean value $\mu_{\hat{\alpha}}$ and variance $\sigma_{\hat{\alpha}}$ converge to the ensemble averaged true values μ_{α} and σ_{α}.

Such an estimator is said to be consistent, if as $N \mapsto \infty$, the bias B and the variance $\sigma^2_{\hat{\alpha}}$ both tend to zero. It may be shown [38], [39] that the Fourier transforms of the auto or cross-correlation defined in equation 7.2.2 are not consistent estimates of the power spectrum since the variance does not approach zero as the record length N increases. It is then necessary to compute another estimate of the power spectrum as first introduced by Welch [40]. The data record is sectioned into $K = N/M$ segments of M samples, defined as

$$x^{(i)}(n) = x(n + iM - M), \qquad 0 \leq n \leq M-1, 1 \leq i \leq K \tag{7.2.6}$$

A Hanning window $w(n)$ is applied directly to the data segments before computation of the power spectrum. A modified power spectrum is performed on each segment i to give K power spectra as follows

$$\begin{aligned} S^i_{xx}(\omega) &= \tfrac{1}{MU}\left|\hat{X}_i(\omega)\right|^2 \\ S^i_{xy}(\omega) &= \tfrac{1}{MU}\hat{X}_i(\omega)\,\hat{Y}^*_i(\omega) \end{aligned} \tag{7.2.7}$$

where

$$\begin{aligned} \hat{X}_i(\omega) &= X_i(\omega) * W(\omega) \\ \hat{Y}_i(\omega) &= Y_i(\omega) * W(\omega) \end{aligned} \tag{7.2.8}$$

and

$$U = \frac{1}{M}\sum_{n=0}^{M-1} |w(\omega)|^2 \tag{7.2.9}$$

and $W(\omega)$ is the Fourier transform of the Haninng window $w(n)$. The smoothed auto and cross-power spectrum $\hat{S}_{xx}(\omega)$ and $\hat{S}_{xy}(\omega)$ are given by

$$\begin{aligned} \hat{S}_{xx}(\omega) &= \tfrac{1}{K}\sum_{i=1}^{K} S^i_{xx}(\omega) \\ \hat{S}_{xy}(\omega) &= \tfrac{1}{K}\sum_{i=1}^{K} S^i_{xy}(\omega) \end{aligned} \tag{7.2.10}$$

The calibration of the microphones as well as the modal decomposition from external and in-duct microphones detailed in chapter 8, will be obtained from spectra computed using equation 7.2.10.

7.3 Experimental Procedure

This section details the experimental procedure involved in setting up the TCS sensor array and acquiring measurements of the broadband radiated sound field. This involves the simultaneous measurements of the 110 sensors arranged on the TCS.

Each spectrum is formed from the acquisition of 60 seconds of data. The signals are discretized at a sampling rate of 12kHz. The data sequence is divided into 1500 segments of 43 ms on which a 512 point Fast Fourier Transforms (FFT) is performed to compute the power spectrum using equation 7.2.7. If $f_s = 12\text{kHz}$ denotes the sampling frequency and $N_w = 512$ the window length, the frequency resolution is then

$$\Delta f = \frac{f_s}{N_w} = 23.44\,\text{Hz} \tag{7.3.1}$$

which corresponds to

$$\Delta ka = \frac{2\pi a \Delta f}{c} = 0.1364 \tag{7.3.2}$$

This allows the estimation of the power spectra at 257 different frequency bins over the frequency range 0 to 6kHz. Anti-alias filters built into the SONY SIR 1000 digital recorders prevents aliasing of high frequency components above the Nyquist frequency.

Since the amplifier channels may have a different frequency response, care is taken to ensure that each sensor remains connected to the same amplifier channel for all measurements after calibration. Broadband noise produced by the fan at speeds varying from 20 to 50Hz at 10Hz increments is measured by the 4 sensor array geometries discussed in section 7.1. Before measurement, however, it was necessary to calibrate the microphones. This procedure is discussed in the next section.

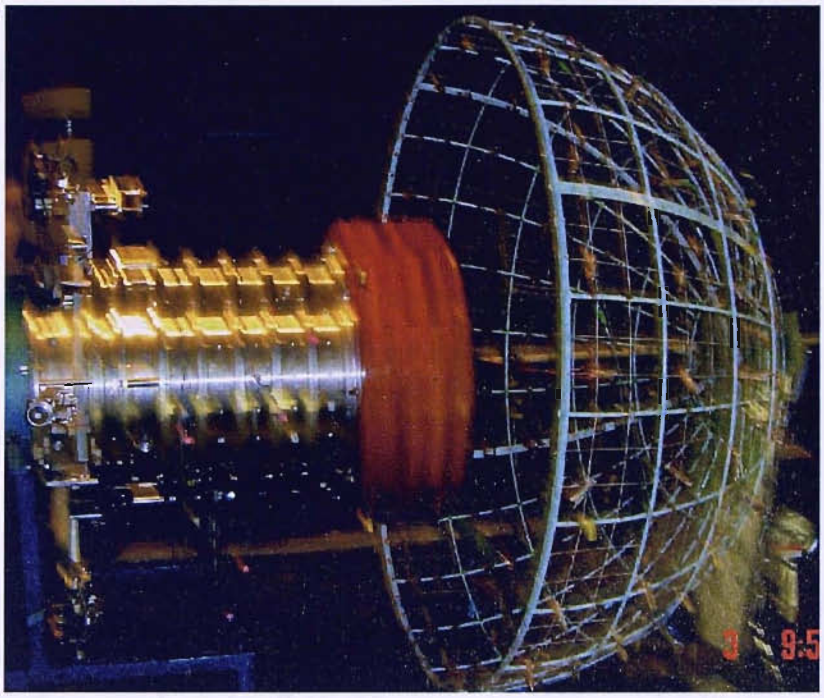

Figure 7.4: Experimental rig in operation

7.4 Microphone calibration

The TCS sensor array for measuring the broadband sound field requires microphones that are calibrated both in magnitude and in phase. The TCS sensors are calibrated relative to a reference microphone which will be used as a common phase reference and will later be mounted on the TCS axis. This is done by measurements of the transfer function between a calibrated reference microphone and each microphone on the TCS using a loudspeaker driven by a white noise signal.

The transfer function between the i^{th} microphone x_i and the reference signal x_1 is defined here as

$$H_i(\omega) = \frac{\hat{S}_{x_1 x_i}(\omega)}{\hat{S}_{x_1 x_1}(\omega)} \tag{7.4.1}$$

The pressure $\hat{p}_i(\omega)$ corrected for magnitude and phase relative to the reference microphone may be computed from

$$\hat{p}_i(\omega) = H_i(\omega)\, p_i(\omega) \tag{7.4.2}$$

where $p_i(\omega)$ is the pressure spectrum at the i^{th} microphone. The power spectrum estimate with the sensor sensitivities removed is given by

$$\hat{S}_{\hat{p}_i\hat{p}_j}(\omega) = \frac{\pi}{T}E\left[\hat{p}_i(\omega)\hat{p}_j^*(\omega)\right] = H_i(\omega)H_j^*(\omega)\hat{S}_{p_ip_j}(\omega) \tag{7.4.3}$$

where $\hat{S}_{p_ip_j}(\omega)$ is the power cross-spectrum estimate of the pressure signal between the i^{th} and j^{th} microphone on the TCS.

It was found to be important to calibrate the in-duct microphones in-situ since they are mounted within plastic holders prior insertion into the holes in the duct wall and their sensitivities were found to change during insertion. In order to do so, a reference microphone is flush mounted onto a flange and the loudspeaker is directly placed onto the reference microphone with an insulating layer to prevent any cavity resonances. Again pressure measurements were made relative to a reference sensor by the use of a transfer function $H_0(\omega)$ between the loudspeaker signal x_l and the calibrated reference microphone signal x_0,

$$H_0(\omega) = \frac{\hat{S}_{x_lx_0}(\omega)}{\hat{S}_{x_lx_l}(\omega)} \tag{7.4.4}$$

The loudspeaker is then placed onto each microphone placed inside the duct and the transfer function between the loudspeaker signal and any in-duct microphone signal can be measured

$$H_i(\omega) = \frac{\hat{S}_{x_lx_i}(\omega)}{\hat{S}_{x_lx_l}(\omega)} \tag{7.4.5}$$

By defining the corrected pressure spectrum

$$\hat{p}_i(\omega) = \frac{H_i(\omega)}{H_0(\omega)}p_i(\omega) \tag{7.4.6}$$

the cross power spectrum estimate made relative to the reference calibrated microphone is given by

$$\hat{S}_{\hat{p}_i\hat{p}_j}(\omega) = \frac{H_i(\omega)H_j^*(\omega)}{|H_0(\omega)|^2}\hat{S}_{p_ip_j}(\omega) \tag{7.4.7}$$

Modal inversion results obtained using this measured data is presented in the next chapter.

Chapter 8

Experimental Results

In this chapter, the inverse technique for deducing the amplitudes of the modes radiated from the engine duct, including schemes for stabilising the solution, is applied to experimental data. The sound power radiated from the fan inlet and the coherence function between different modal amplitudes will also be presented.

8.1 The cross-spectral matrix of radiated acoustic pressure

Broadband sound field generated by a ducted fan produces acoustic energy distributed over a band of frequencies. The information detected by the sensors of the array is quantified through the auto and cross-power spectra of the measured pressure fluctuations. The power spectra between any two microphones are computed using the Welch estimator [40] as detailed in section 7.2, and are adjusted to account for differences in microphone sensitivities by equations 7.4.3 and 7.4.7.

As shown in chapter 3, the inversion procedure for computing the cross spectral matrix of mode amplitudes requires the measurement of $\hat{\mathbf{S}}_{\hat{\mathbf{p}}\hat{\mathbf{p}}}$ defined as the cross-spectral matrix of measured pressures in the analysis frequency bandwidth $\Delta\omega$ by

$$\hat{\mathbf{S}}_{\hat{\mathbf{p}}\hat{\mathbf{p}}}(\omega) = \begin{bmatrix} \hat{S}_{\hat{p}_1\hat{p}_1}(\omega) & & \hat{S}_{\hat{p}_K\hat{p}_1}(\omega) \\ & \cdot & \\ & \hat{S}_{\hat{p}_j\hat{p}_j}(\omega) & \\ & & \cdot \\ \hat{S}_{\hat{p}_1\hat{p}_K}(\omega) & & \hat{S}_{\hat{p}_K\hat{p}_K}(\omega) \end{bmatrix} \tag{8.1.1}$$

The diagonal of this matrix represents the mean-square pressure radiated from the fan inlet. Off-diagonal terms of the matrix defined in equation 8.1.1, appropriately normalised, provide an indication of the level of coherence between any two microphones.

8.1.1 Spectrum of sound power

By making the usual far-field approximation and using the property of the geodesic array that each microphone occupies an equal surface area of $\Delta A = 2\pi r^2/K$, the spectral density of sound power radiated from the fan inlet is given by

$$W(\omega) = \frac{1}{\rho c}\sum_{i=1}^{K} \hat{S}_{\hat{p}_i\hat{p}_i}(\theta_i, \varphi_i, \omega)\,\Delta A \tag{8.1.2}$$

The sound power radiated from the inlet at the four fan speeds, measured by the geodesic sensor array, is plotted in figure 8.1 against the dimensionless frequency ka. Peaks in the spectrum are found to occur at multiples of the Blade Passage Frequency (BPF), which corresponds to 180, 270, 360 and 450Hz (i.e. ka =1.05, 1.57, 2.1 and 2.62) for the fan speeds 20, 30, 40 and 50Hz, respectively. However, apart from the first tone in each spectrum with a level of 10dB above the broadband level, the peaks of subsequent tones are only about 5 dB above the broadband level. These tones also have a significant frequency bandwidth of around 60Hz. These peaks therefore correspond to pseudo-tones that are most likely due to the interaction between the upstream flow distortion and the

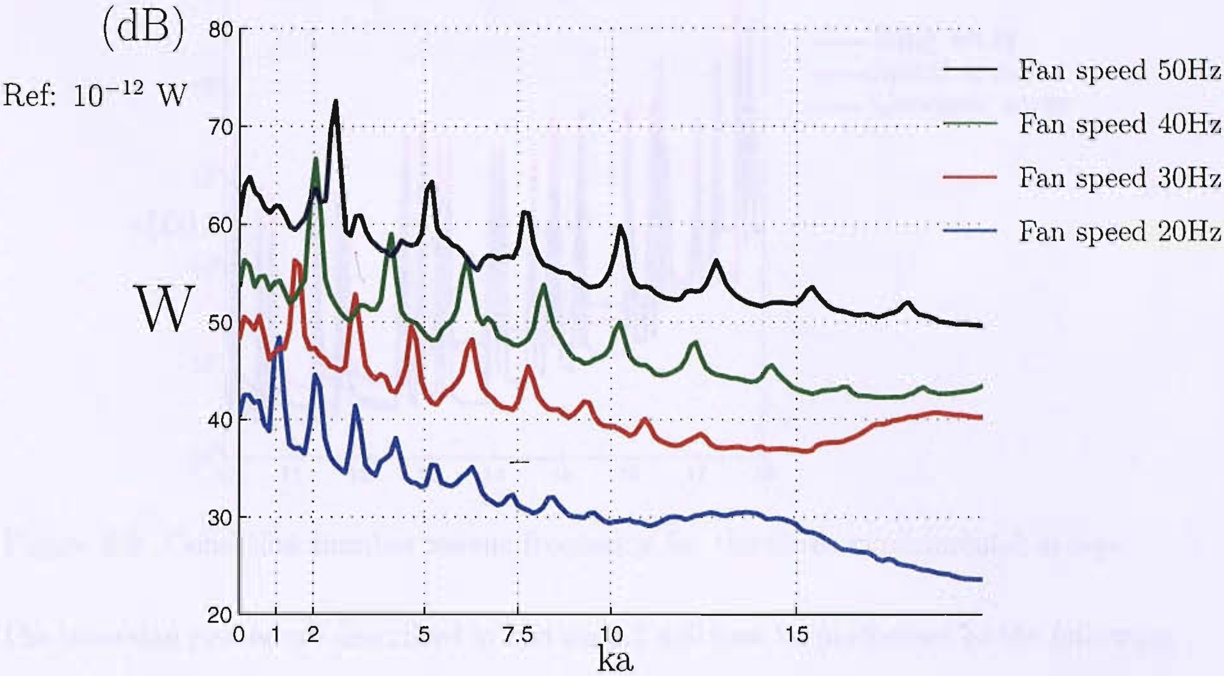

Figure 8.1: The power radiated from the fan inlet and measured by the geodesic sensor array for fan speeds 20, 30, 40 and 50Hz

fan blades. Here, the frequencies of these peaks are referred to as tones to distinguish them from the frequencies at which purely broadband noise occurs. Finally, Signal to Noise Ratios (SNR) of 25 and 30dB are found for the fan speeds 20 and 30Hz while 40 and 45dB SNR is achieved for the 40 and 50Hz fan speeds. The latter fan speeds therefore allows reasonable SNR levels at high frequencies (i.e. $ka \geq 10$). To maximise the SNR, and hence minimise the sensitivity of the solution to noise, the modal inversion is performed at the 40 and 50Hz fan speeds.

Figure 8.2 shows the behaviour of the condition number of **D** computed from the FE/IE computation for the three arrays used during the experiments. As already shown in chapter 3, figure 8.2 confirms the fact that the geodesic array leads to better conditioned inversions at frequencies between the cut-on frequencies by a factor of approximately 2 to 3 than the other two arrays under investigation.

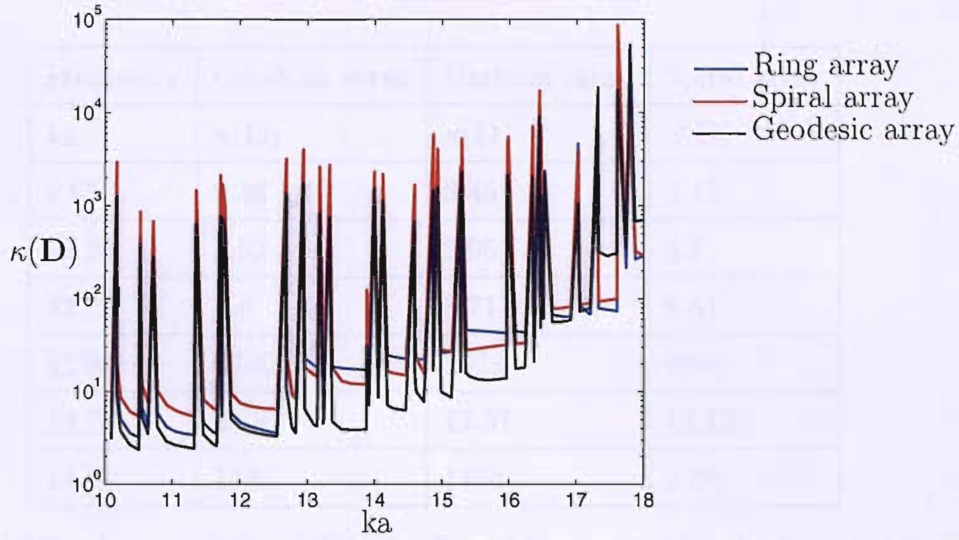

Figure 8.2: Condition number versus frequency for the three experimental arrays

The inversion procedure described in section 3.2 will now be performed at the following three frequencies in the frequency bandwidth of Δka=0.1364.

1. **Broadband noise:**

   $ka = 9.65$ and $ka = 13.78$, frequencies at which broadband sound field dominates

2. **BPF:**

   $ka = 12.28$ and $ka = 12.82$, corresponding to 6^{th} BPF at 40Hz fan speed and 5^{th} BPF at 50Hz fan speed, respectively

3. **Modal cut-on frequencies:**

   $ka = 12.93$ and $ka = 14.12$, corresponding to the cut-on frequencies of the $(\pm 7, 1)$ and $(\pm 8, 1)$ modes, respectively.

At these frequencies, the condition number of the matrix $\mathbf{D}$ for the three sensor arrays is given in table 8.1. We now consider the cross spectral matrices of pressures $\hat{\mathrm{S}}_{\hat{\mathbf{p}}\hat{\mathbf{p}}}$ and $\bar{\mathrm{S}}_{\hat{\mathbf{p}}\hat{\mathbf{p}}}$ defined in section 3.2 formed directly from the measured pressures and that obtained from the reconstructed mode amplitudes, respectively. Comparison between the two gives an indication of the quality of the inversion. The variation of the mean square pressure

Frequency	Geodesic array	Uniform array	Spiral array
ka	$\kappa(\mathbf{D})$	$\kappa(\mathbf{D})$	$\kappa(\mathbf{D})$
9.65	2.36	3.45	5.13
12.28	3.52	3.95	6.7
12.82	3.6	8.71	8.51
12.93	1746	2623	4050
13.78	3.88	17.57	12.12
14.11	1135	1430	2196

Table 8.1: Condition number $\kappa(\mathbf{D})$ at different frequencies for the 3 sensor arrays

over the TCS can be normalised by

$$Q(\theta, \varphi, \omega) = \frac{\hat{S}_{\hat{p}\hat{p}}(\theta_i, \varphi_i, \omega)\, A}{\rho c W(\omega)} = \frac{\hat{S}_{\hat{p}\hat{p}}(\theta_i, \varphi_i, \omega)}{\frac{1}{A}\int_A \hat{S}_{\hat{p}\hat{p}}(\theta_i, \varphi_i, \omega)\, dA} \tag{8.1.3}$$

such that $\frac{1}{A}\int_A Q\, dA = 1$.

The dimensionless mean square pressure computed from the measured pressure data is denoted by $\hat{Q}$. The dimensionless mean square pressure $\bar{Q}$ computed from the reconstructed mode amplitudes makes use of $\hat{S}_{\hat{p}\hat{p}}$ computed from the diagonal elements of the matrix given in equation 3.2.2 with $\hat{\mathbf{S}}_{\hat{\mathbf{a}}\hat{\mathbf{a}}}$ given by equation 3.2.4.

Figures 8.3 and 8.4 show colour maps of $\hat{Q}$ and $\bar{Q}$ obtained from the geodesic array measurements at the three frequencies 1, 2 and 3 listed above. These figures show the mean square pressure variation over the hemispherical surface of the TCS as viewed along the duct axis. Comparison between $\hat{Q}$ and $\bar{Q}$ allows an assessment of the residual error, i.e. $||\hat{\mathbf{p}} - \mathbf{p}||$ resulting from modelling errors and errors due to noise on the sensors. Good agreement between $\hat{Q}$ and $\bar{Q}$ can generally be observed. Agreement of 3dB or less is achieved across the surface of the TCS at most frequencies. An exception is at the cut-on frequencies where differences of 6 to 8dB are observed in the sideline directions (i.e. $\varphi \in [80^o, 90^o]$). This confirms that the errors generally occur in the near cut-off modes. The mean square pressure variation may therefore be reconstructed to within 3dB of the

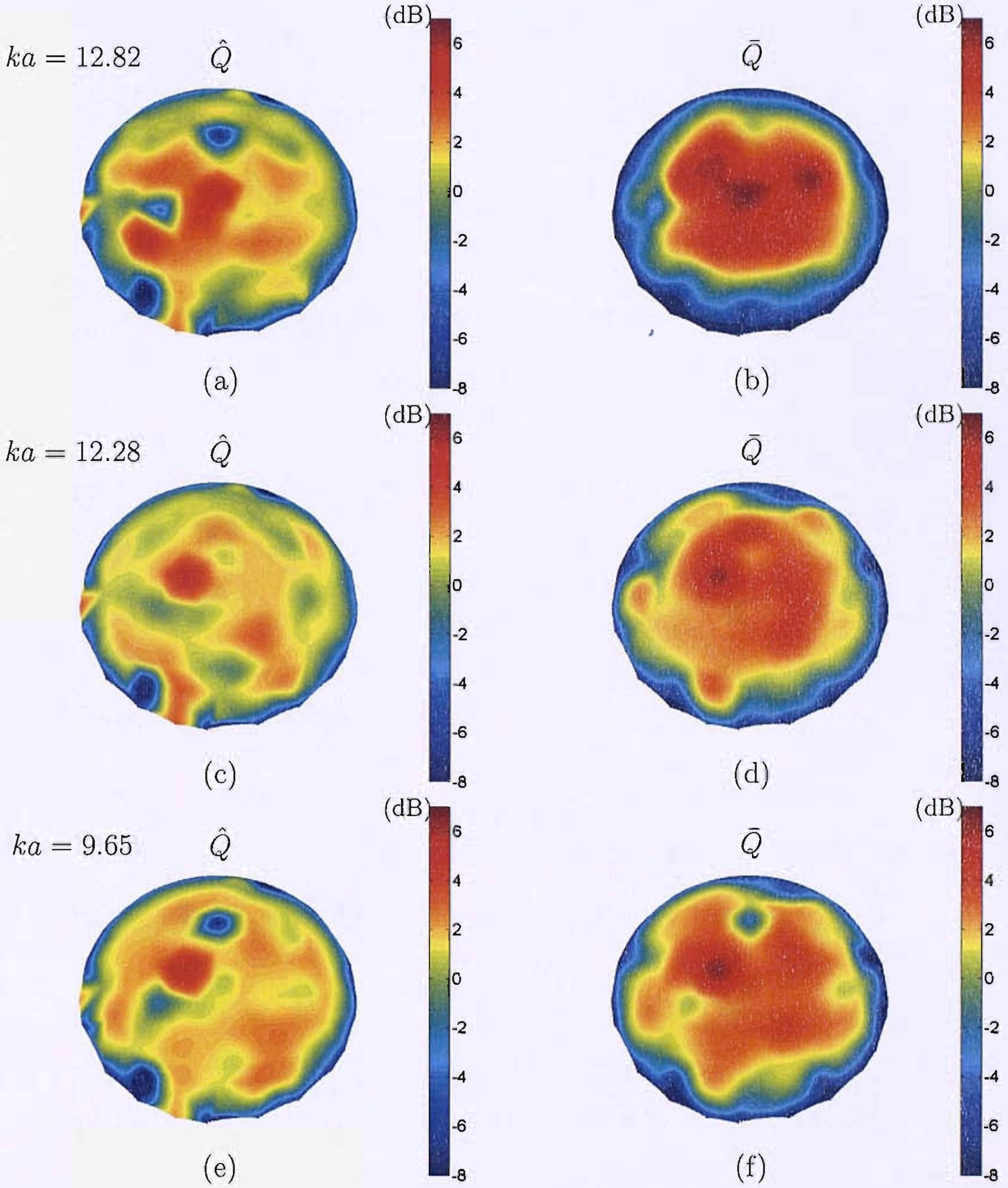

Figure 8.3: Normalised mean-square pressure representation over the TCS hemispherical surface looking from above at (a),(b) $ka = 12.82$, (c),(d) $ka = 12.28$ and (e),(f) $ka = 9.65$

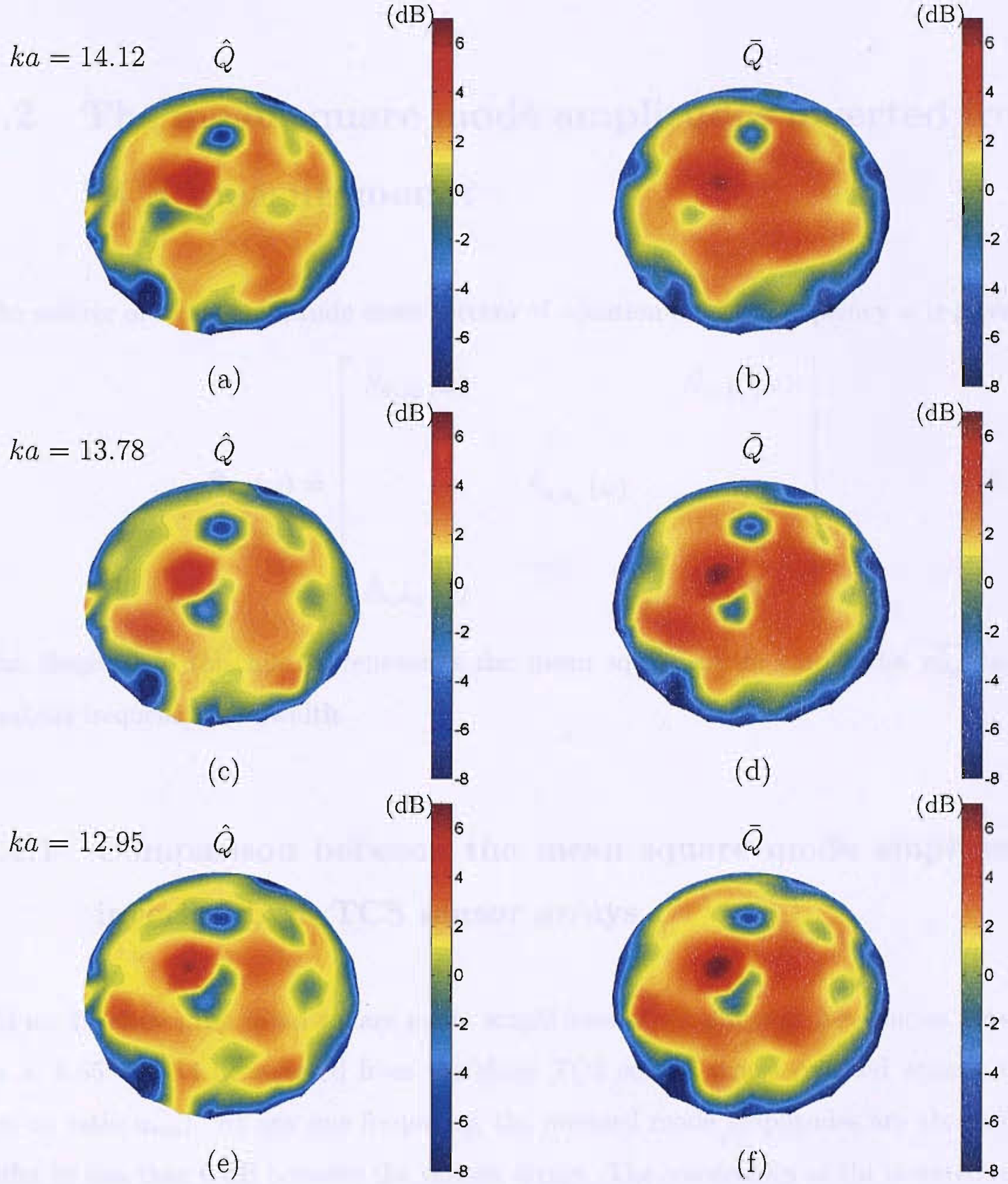

Figure 8.4: Normalised mean-square pressure representation over the TCS hemispherical surface looking from above at (a),(b) $ka = 12.95$, (c),(d) $ka = 13.78$ and (e),(f) $ka = 14.12$

actual pressure at most frequencies studied here, suggesting that the modal amplitudes should be inverted to the same level of accuracy for arrays with good conditioning.

8.2 The mean square mode amplitudes inverted from TCS measurements

The matrix of mode amplitude cross-spectra of equation 3.2.4 at frequency ω is given by

$$\hat{\mathbf{S}}_{\hat{\mathbf{a}}\hat{\mathbf{a}}}(\omega) = \begin{bmatrix} \hat{S}_{\hat{a}_1\hat{a}_1}(\omega) & & \hat{S}_{\hat{a}_L\hat{a}_1}(\omega) \\ & \ddots & \\ & \hat{S}_{\hat{a}_j\hat{a}_j}(\omega) & \\ & \ddots & \\ \hat{S}_{\hat{a}_1\hat{a}_L}(\omega) & & \hat{S}_{\hat{a}_L\hat{a}_L}(\omega) \end{bmatrix} \tag{8.2.1}$$

The diagonal of this matrix represents the mean square mode amplitudes $\overline{a_{mn}^2}$ in the analysis frequency bandwidth.

8.2.1 Comparison between the mean square mode amplitudes inverted by 3 TCS sensor arrays

Figure 8.5 shows the mean square mode amplitudes at six different frequencies between $ka = 9.65$ and 14.12 inverted from the three TCS sensor arrays (plotted against their cut-on ratio α_{mn}). At any one frequency, the inverted mode amplitudes are observed to differ by less than 6 dB between the various arrays. The consistency of the inverted mode amplitudes from the three different arrays gives confidence in the inversion results. At the cut-on frequencies $ka = 12.95$ and $ka = 13.78$ in figures 8.5(d) and 8.5(e) respectively, the nearly cut-off modes, i.e. $\alpha_{mn} > 0.99$, are considerably over-estimated by the inversion procedure, as expected from the theoretical study of the modal error in chapter 3. The regularisation procedure necessary to enhance robustness of these inversion results at these cut-on frequencies, as discussed in chapter 5, is presented in the next section.

Further evidence for the plausibility of the inversion results for the modes not too close to cutoff is that their α-distribution appears to follow reasonably well an 'equal energy per mode' model. This model is widely used for representing the mode distribution in fan broadband noise. Joseph *et al* in [41] has investigated this mode amplitude distribution source model, in which all cut-on modes carry equal power and shown that, for zero flow,

$$\overline{a_{mn}^2} = \rho c \frac{\varpi}{S\sqrt{1-\alpha_{mn}^2}} \tag{8.2.2}$$

where ϖ is the time-averaged acoustic sound power carried by each cut-on mode at the frequency of interest. Equation 8.2.2 is plotted as ---- in figure 8.5 and appears to follow reasonably well the trend of the mode amplitudes with α_{mn} inverted using the geodesic sensor array. The regularisation procedure discussed in chapter 5 will now be applied to the experimental data in order to improve the quality of the inversion of the modes near cutoff.

8.2.2 The effect of regularisation on the inversion results

Regularisation techniques detailed in chapter 5 can help considerably in producing a stable solution in the presence of noise for the near cut-off modes. Tikhonov regularisation in its standard form, as well as in its general form using the matrix $\mathbf{R_2}$ defined in equation 5.3.36, is applied to the broadband experimental data. The mode amplitude cross spectral matrix $\hat{\mathbf{S}}_{\hat{\mathbf{a}}_\mathbf{R}\hat{\mathbf{a}}_\mathbf{R}}$ obtained from the constrained inversion can be obtained by substituting the regularised Tikhonov solution $\hat{\mathbf{a}}_\mathbf{R}$ of equation 5.3.5 into equation 3.2.3,

$$\hat{\mathbf{S}}_{\hat{\mathbf{a}}_\mathbf{R}\hat{\mathbf{a}}_\mathbf{R}} = \mathbf{D}^{\#}\hat{\mathbf{S}}_{\hat{\mathbf{p}}\hat{\mathbf{p}}}\left(\mathbf{D}^{\#}\right)^{\mathbf{H}} \tag{8.2.3}$$

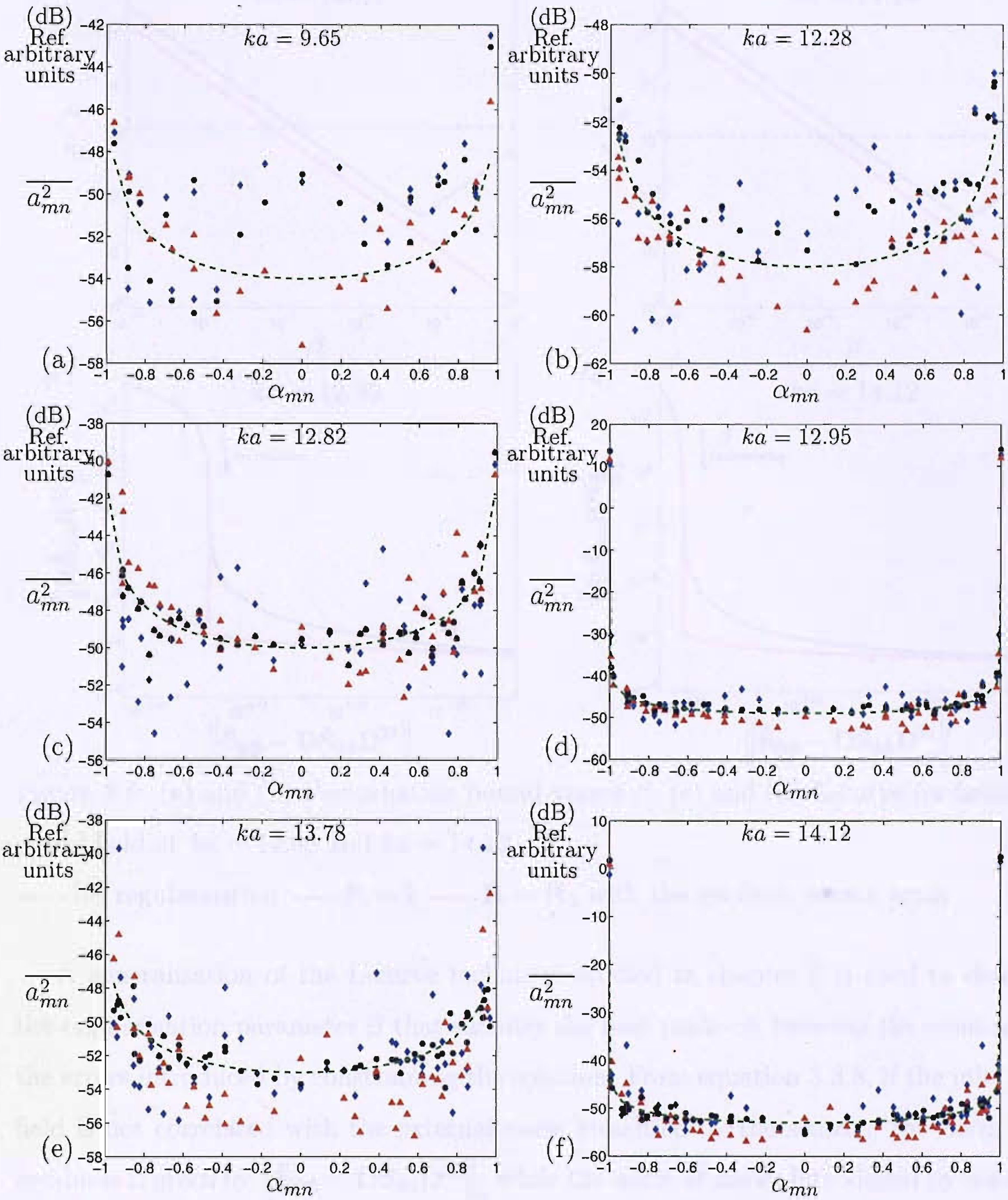

Figure 8.5: Mean square mode amplitudes against α_{mn} inverted from ◆ Ring array ▲ Spiral array • Geodesic array and ---- $\approx (1-\alpha_{mn}^2)^{-1/2}$
(a) $ka = 9.65$,(b) $ka = 12.28$, (c) $ka = 12.82$, (d) $ka = 12.95$ (e) $ka = 13.78$ and (f) $ka = 14.12$

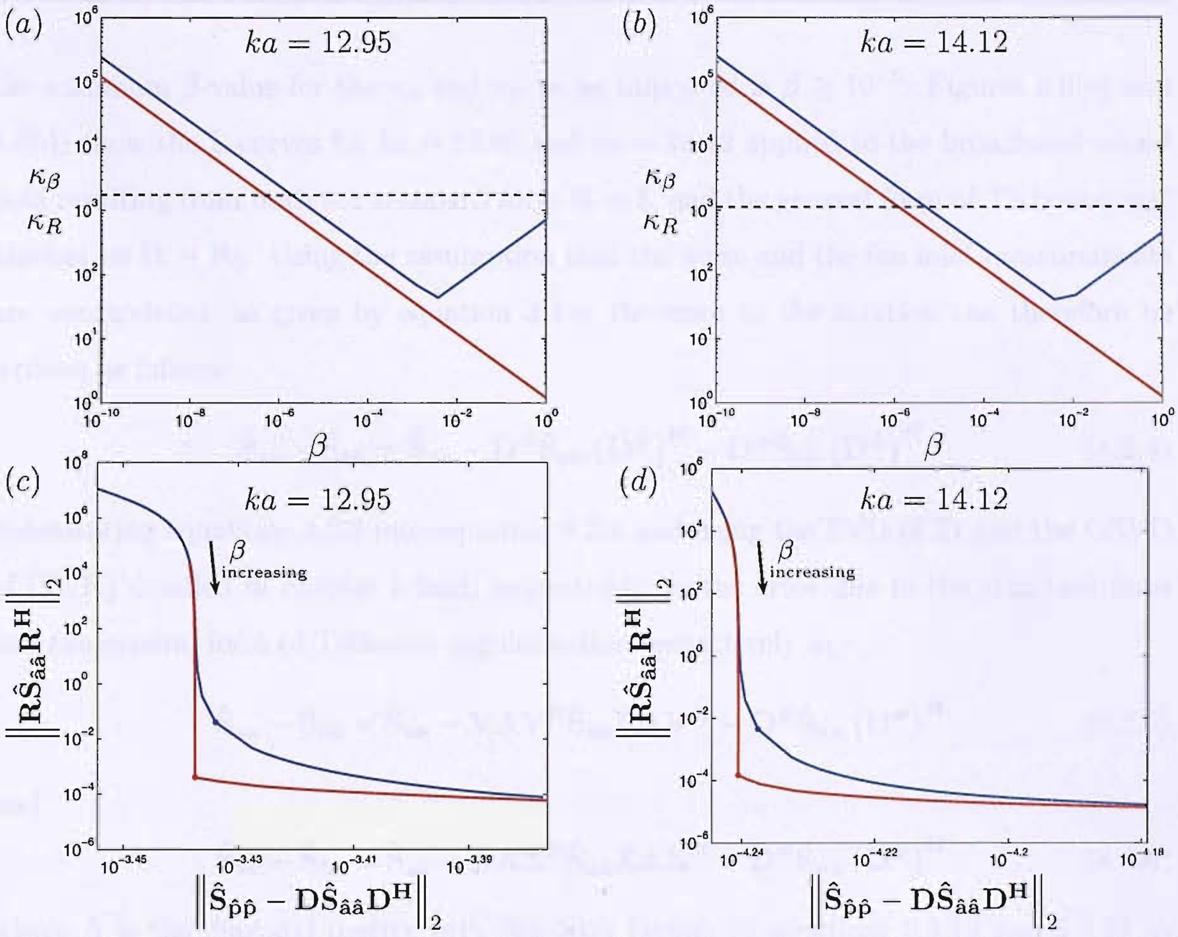

Figure 8.6: (a) and (b) Perturbation bound versus β, (c) and (d) L-curve for broadband sound field at $ka = 12.95$ and $ka = 14.12$

----No regularisation ——$\mathbf{R} = \mathbf{I}$ ——$\mathbf{R} = \mathbf{R_2}$ with the geodesic sensor array

A generalisation of the L-curve technique studied in chapter 5 is used to determine the regularisation parameter β that satisfies the best trade-off between the residuals and the errors introduced by constraining the solution. From equation 3.3.8, if the inlet sound field is not correlated with the external noise measured by the sensors, the norm of the residuals is given by $\left\|\hat{\mathbf{S}}_{\hat{p}\hat{p}} - \mathbf{D}\hat{\mathbf{S}}_{\hat{a}\hat{a}}\mathbf{D}^{\mathbf{H}}\right\|_2$ while the norm of errors introduced by constraining the solution is $\left\|\mathbf{R}\hat{\mathbf{S}}_{\hat{a}\hat{a}}\mathbf{R}^{\mathbf{H}}\right\|_2$.

Figures 8.6(a) and 8.6(b) show the variation of κ_β and κ_R with the regularisation parameter β at the cut-on frequencies, $ka = 12.95$ and $ka = 14.12$. A horizontal dashed line is used to denote the value of $\kappa(\mathbf{D})$ for the unconstrained case. It is shown that in this case, the minimum β-value for the κ_β and κ_R to be improved is $\beta \geq 10^{-5}$. Figures 8.6(c) and 8.6(d) show the L-curves for $ka = 12.95$ and $ka = 14.12$ applied to the broadband sound field resulting from both the standard form $\mathbf{R} = \mathbf{I}$, and the general form of Tikhonov regularisation $\mathbf{R} = \mathbf{R_2}$. Using the assumption that the noise and the fan inlet measurements are uncorrelated, as given by equation 3.3.8, the error in the solution can therefore be written as follows

$$\mathbf{\hat{S}_{aa}} - \mathbf{\hat{S}_{\hat{a}\hat{a}}} = \mathbf{\hat{S}_{aa}} - \mathbf{D}^{\#}\mathbf{\hat{S}_{pp}}\left(\mathbf{D}^{\#}\right)^{\mathbf{H}} - \mathbf{D}^{\#}\mathbf{\hat{S}_{nn}}\left(\mathbf{D}^{\#}\right)^{\mathbf{H}} \tag{8.2.4}$$

Substituting equations 3.2.2 into equation 8.2.4 and using the SVD of $\mathbf{D}$ and the GSVD of $(\mathbf{D}, \mathbf{R})$ detailed in chapter 5 lead, respectively, to the error due to the standard form and the general form of Tikhonov regularisation respectively as

$$\mathbf{\hat{S}_{aa}} - \mathbf{\hat{S}_{\hat{a}\hat{a}}} = \mathbf{\hat{S}_{aa}} - \mathbf{V\Lambda V^{H}\hat{S}_{aa}V\Lambda V^{H}} - \mathbf{D}^{\#}\mathbf{\hat{S}_{nn}}\left(\mathbf{D}^{\#}\right)^{\mathbf{H}} \tag{8.2.5}$$

and

$$\mathbf{\hat{S}_{aa}} - \mathbf{\hat{S}_{\hat{a}\hat{a}}} = \mathbf{\hat{S}_{aa}} - \mathbf{X\Lambda X^{H}\hat{S}_{aa}X\Lambda X^{H}} - \mathbf{D}^{\#}\mathbf{\hat{S}_{nn}}\left(\mathbf{D}^{\#}\right)^{\mathbf{H}} \tag{8.2.6}$$

where $\mathbf{\Lambda}$ is the diagonal matrix with the filter factors of equations 5.3.18 and 5.3.27 as diagonal elements. It can be readily seen from equations 8.2.5 and 8.2.6 that, in the case of broadband noise, the errors due to regularisation are controlled by the elements of the matrix $\mathbf{V\Lambda V^{H}}$ and $\mathbf{X\Lambda X^{H}}$, which represents the filtered modal components (i.e. $\Lambda_i = \sigma_i^2/\sigma_i^2+\beta$ and $\Lambda_i = \gamma_i^2/\gamma_i^2+\beta$ respectively), while the term $\mathbf{D}^{\#}\mathbf{\hat{S}_{nn}}\left(\mathbf{D}^{\#}\right)^{\mathbf{H}}$ represents error due to the presence of background noise in the measurements. When very little regularisation is introduced, most of the filter factors tend to unity so that $\mathbf{V\Lambda V^{H}} \mapsto \mathbf{I_L}$. The errors are then dominated by $\mathbf{D}^{\#}\mathbf{\hat{S}_{nn}}\left(\mathbf{D}^{\#}\right)^{\mathbf{H}}$. The solution is said to be undersmoothed. This corresponds to the uppermost part of the L-curve while the rightmost part corresponds to the oversmoothed solution (i.e. $\beta >> \gamma_i$) when the filter factors are small. Figures 8.6(c) and 8.6(d) show that the general form of Tikhonov regularisation using $\mathbf{R_2}$ displays a sharper corner on the L-curve. This regularising scheme allows a sharper trade-off between the minimisation of the residuals and that of the errors introduced by the constraint applied to the solution. In this scheme, a regularisation parameter of

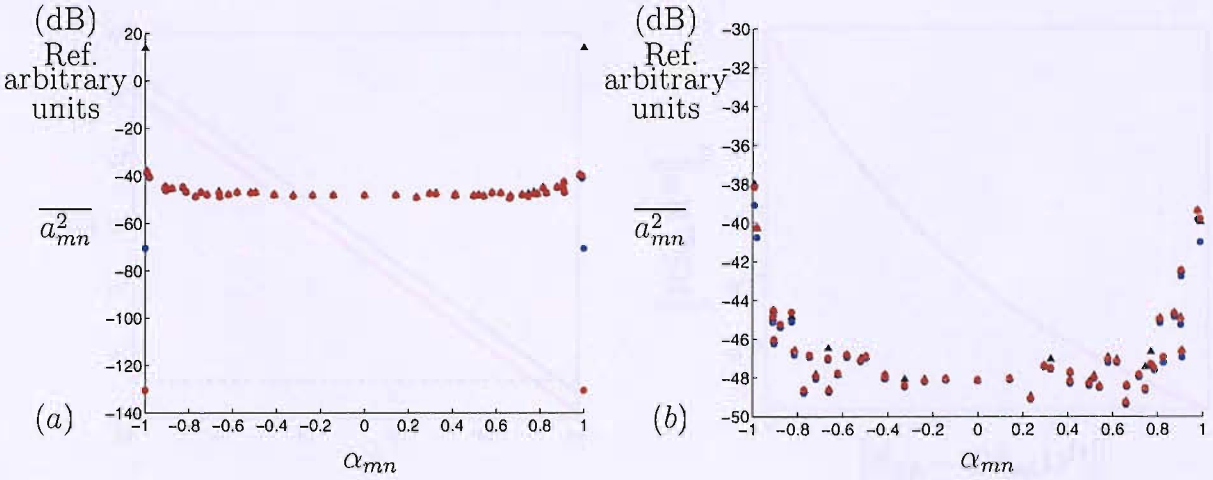

Figure 8.7: (a) Comparison of mean square mode amplitudes between unconstrained and constrained solutions at $ka = 12.95$ ▲ No regularisation • $\mathbf{R} = \mathbf{I}$ • $\mathbf{R} = \mathbf{R_2}$ with the geodesic sensor array, (b) magnified version of (a)

$\beta = 8.5 \cdot 10^{-5}$ for $ka = 12.95$ and $ka = 14.12$ coincides with the L-curve corner and hence satisfies this trade-off. The resulting regularised and unconstrained solutions are compared in figures 8.7(a) and 8.7(b) for $ka = 12.95$, where 8.7(b) is identical to 8.7(a) but plotted over a smaller scale. The application of regularisation is seen to affect only the two modes very close to cutoff. This is because they are filtered out and hence they no longer give rise to large solution norms in the unconstrained case. Figure 8.7(b) confirms the fact that the influence of regularisation upon other modes of cut-on ratio $\alpha_{mn} \leq 0.99$ is negligible. This confirms again that the modes close to cutoff are therefore responsible for large solution norms. Note that similar results are found at the other cut-on frequency of $ka = 14.12$.

Figure 8.8(a) shows an example of the variation of κ_β and κ_R with the regularisation parameter β at $ka = 13.78$, which is well away from a cut-on frequency. It shows that a greater regularisation effort is required than that at the cut-on frequencies in order to improve κ_β and κ_R. Now required β are values of order 10^{-1} to obtain a tighter bound on the modal solution errors than $\kappa(\mathbf{D})$ already provides in the unconstrained least squares solution. This is due to the fact that the directivity matrix $\mathbf{D}$ inverted at these frequencies

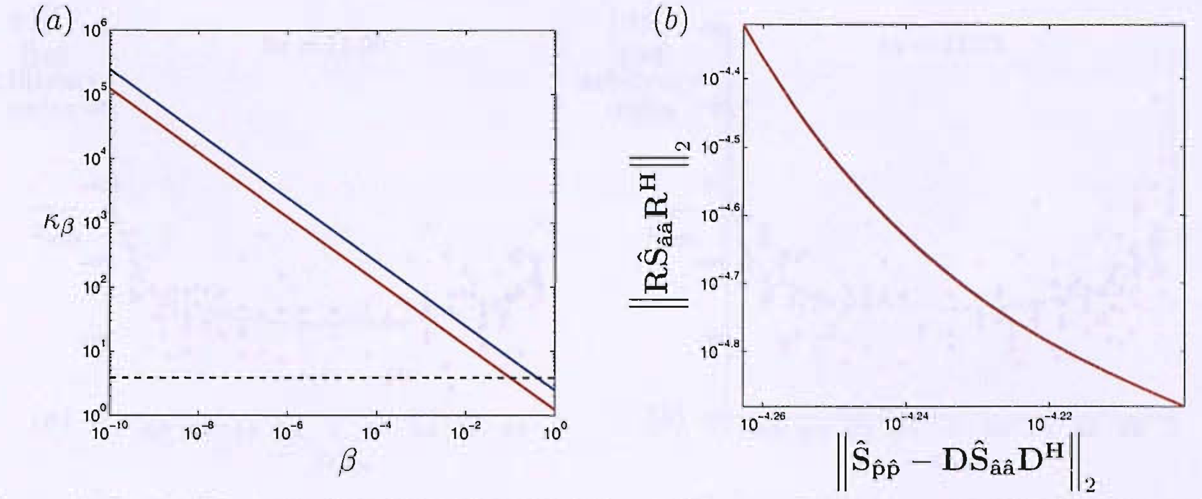

Figure 8.8: (a) Perturbation bound versus β ----No regularisation and (b) L-curve for broadband sound field at $ka = 13.78$
——$\mathbf{R} = \mathbf{I}$ ——$\mathbf{R} = \mathbf{R_2}$ with the geodesic sensor array

is very well conditioned, i.e. $\kappa(\mathbf{D})$ <4, for the geodesic sensor array and therefore possesses small singular values of order 10^{-1}. Section 4.5.1 showed that the singular values were proportional to the radiated power of each of the transformed modes. The modal information associated with these smallest singular values may still have a relative importance to the overall radiated sound field at $ka = 13.78$ and therefore may not be filtered. Figure 8.8(b) shows the L-curve for the two Tikhonov regularisation schemes investigated. No significant differences are observed and more importantly, no shoulders appear on the graph of figure 8.8(b) suggesting that the residual errors can only be minimised at the expense of regularisation errors. Again, a slow rate of decreasing singular values in $\mathbf{D}$ is responsible for the absence of 'knees' in the L-curve. There is therefore no real trade-off between the minimisation of the residuals and the errors introduced by regularisation. The improvement in reducing the residuals is compensated for by the errors introduced by regularisation. This confirms that the application of regularisation is not beneficial at frequencies away from the cut-on frequencies. Thus, the 'well-conditioned' inverse problem arising from the geodesic array at this frequency cannot be improved any further.

Figures 8.9(a) and 8.9(b) show the inverted mean square mode amplitudes following regu-

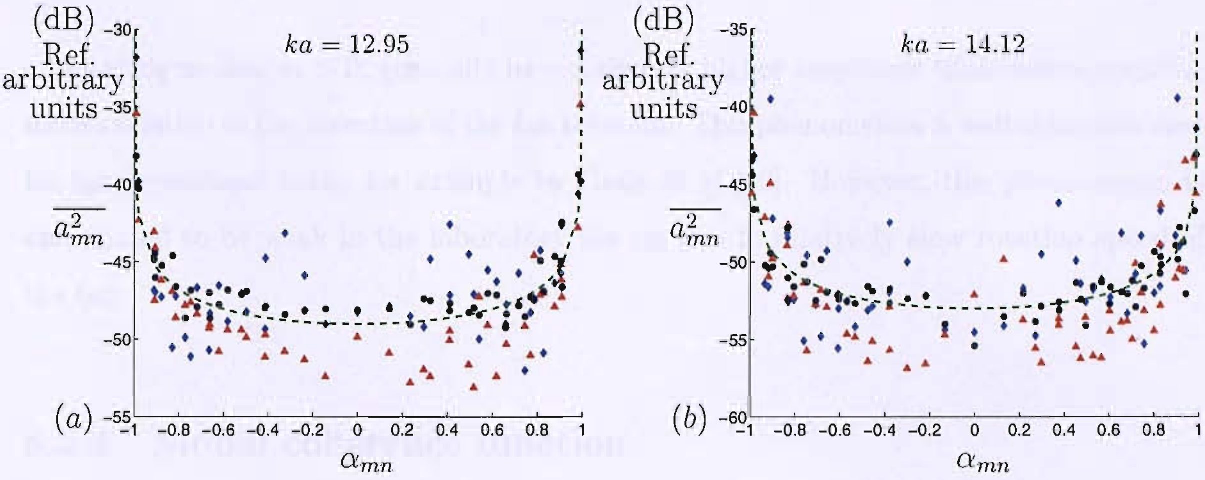

Figure 8.9: Mean square mode amplitudes against α_{mn} inverted from ◆ Ring array ▲ Spiral array ● Geodesic array and ---- $\approx (1-\alpha_{mn}^2)^{-1/2}$
(a),(b) $ka = 12.95$, (c),(d) $ka = 14.12$

larisation at the cut-on frequencies, $ka = 12.95$ and $ka = 14.12$ respectively. They can be compared with figures 8.5(d) and 8.5(f) with no regularisation applied. It can readily be observed that the mode amplitudes for the nearly cut-off modes, which are over-estimated in figures 8.5(d) and 8.5(f), now follow the 'equal energy per mode' model much more closely, suggesting that these new results are much closer to their actual values than when regularisation is absent.

8.2.3 Mean square mode amplitudes inverted from the geodesic sensor array

As an alternative representation of the inverted mode amplitude, figure 8.10 shows the mean square mode amplitudes on a colour scale, deduced from the geodesic sensor array, for the 3 frequency cases (1), (2) and (3), plotted against their spinning and radial mode number m and n. In general, the mean square mode amplitudes are observed to vary by no more than 10 to 12dB. As in figure 8.5, modes near cutoff, i.e. those along the edge of the modal triangle, have greatest amplitude. Another interesting observation is that co-rotating modes, $m > 0$, generally have a slightly higher amplitude than contra-rotating modes relative to the direction of the fan rotation. This phenomenon is well-demonstrated for fan broadband noise, for example by Ganz *et al* [42]. However, this phenomenon is anticipated to be weak in the laboratory fan rig due to relatively slow rotation speed of the fan.

8.2.4 Modal coherence function

The modal coherence function, which quantifies the degree of statistical inter-dependence between two modes $\hat{a}_i$ and $\hat{a}_j$, can be defined as follows:

$$\gamma^2_{\hat{a}_i\hat{a}_j}(\omega) = \frac{\left|S_{\hat{a}_i\hat{a}_j}(\omega)\right|^2}{S_{\hat{a}_i\hat{a}_i}(\omega)\,S_{\hat{a}_j\hat{a}_j}(\omega)} \tag{8.2.7}$$

and has the property $0 \leq \gamma_{\hat{a}_i\hat{a}_j} \geq 1$.

It is often assumed that the modes generated in an engine duct, in the broadband part of the pressure spectrum, are incoherent. To the author's knowledge no experimental evidence to support assertion is available. Figure 8.11 shows the modal coherence function of equation 8.2.7 computed from the geodesic sensor arrays at the frequencies investigated previously in section 8.2.1. Note that $\gamma_{\hat{a}_i\hat{a}_i} = 1$. These values have been omitted from the figure to aid clarity of presentation. The modal coherence is generally found to be less than 0.2 for most of the modal combinations at all frequencies investigated. An exception occurs at $ka = 9.65$ where a few modes exist with a coherence greater than 0.6. Note that no significant coherence values between any modes is observed at $ka = 12.28$ and $ka = 12.82$ corresponding to the 5^{th} and 6^{th} BPF's at 40Hz and 50Hz fan speed respectively. The absence of good modal coherence at these pseudo-tones is essentially due to the fact that the peaks observed in figure 8.1 are not pure tones created by rotor-stator interaction but the result of an interaction between upstream flow distortion in the duct and the fan blades. It also possible that coherence levels may be improved by reducing the analysis bandwidth, which is currently Δka =0.1364.

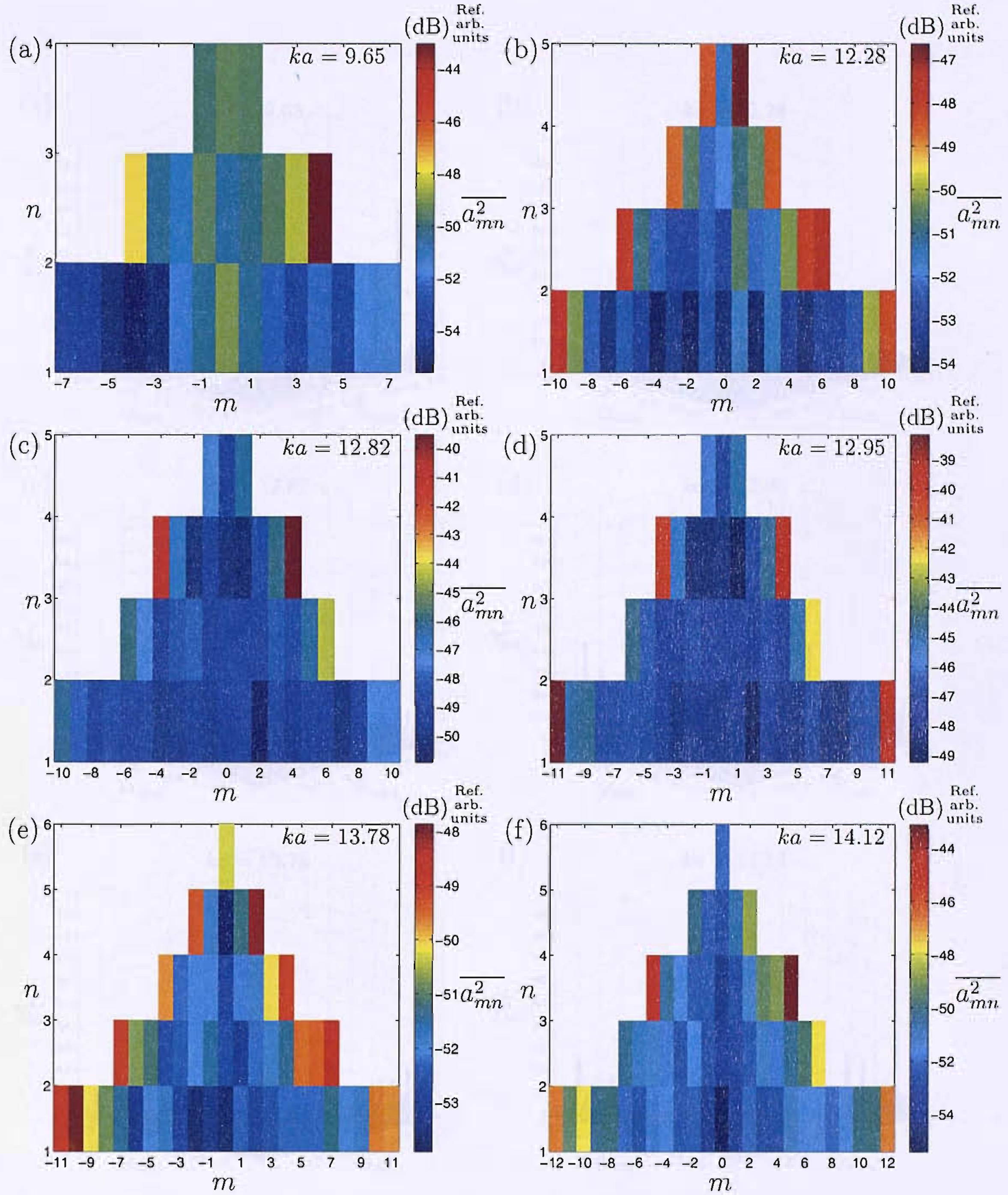

Figure 8.10: Mean square mode amplitudes against spinning and radial mode number m and n detected by the Geodesic array

(a) $ka = 9.65$,(b) $ka = 12.28$, (c) $ka = 12.82$, (d) $ka = 12.95$ (e) $ka = 13.78$ and (f) $ka = 14.12$

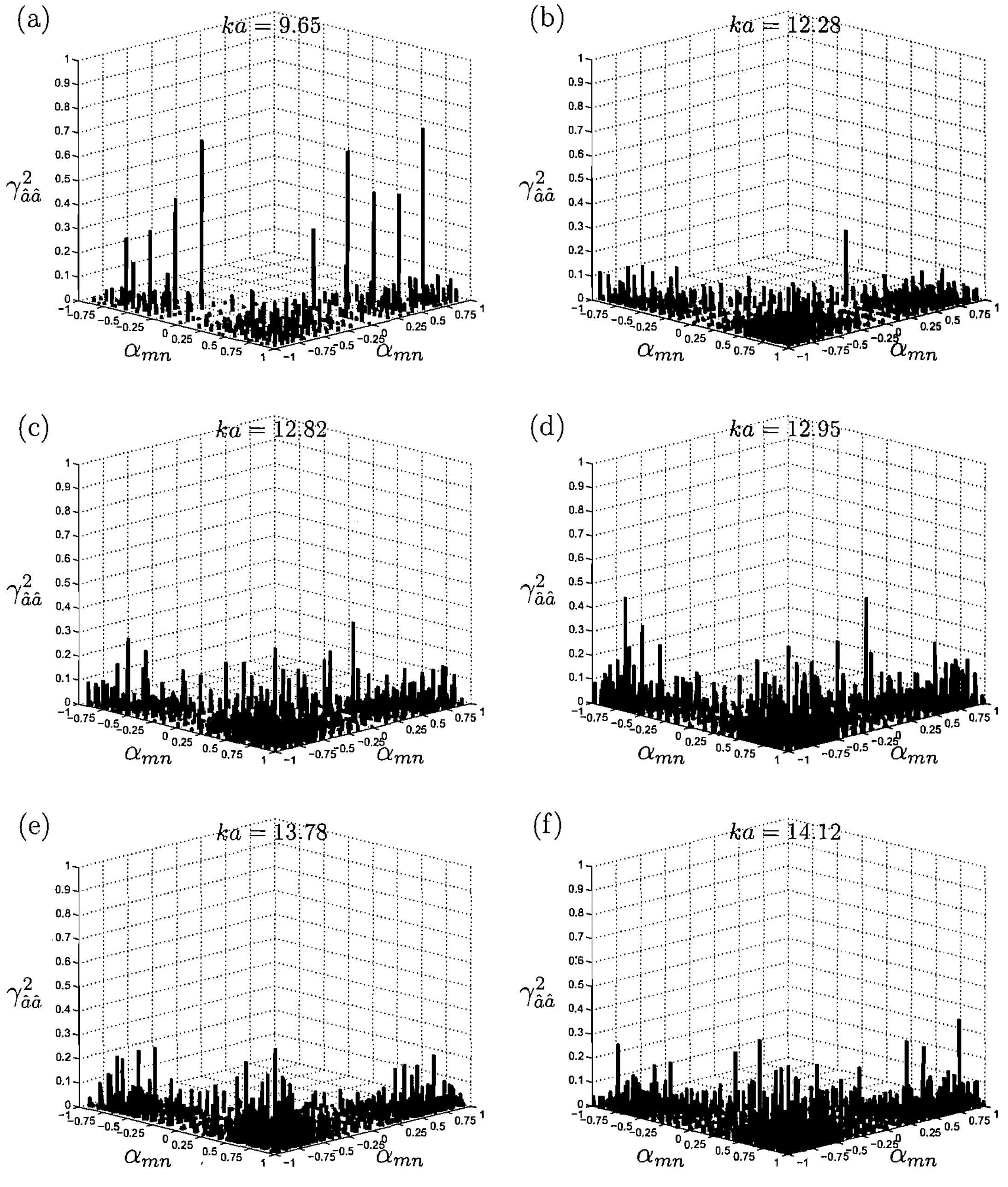

Figure 8.11: Modal coherence function against α_{mn} detected by the Geodesic array (a) $ka = 9.65$,(b) $ka = 12.28$, (c) $ka = 12.82$, (d) $ka = 12.95$ (e) $ka = 13.78$ and (f) $ka = 14.12$

8.3 The mean square mode amplitudes deduced from in-duct modal analysis

In order to provide independent validation of the mode amplitude inversion results obtained using the TCS measurements, a single ring of 24 wall flush-mounted microphones is used in the duct to perform a spinning modal decomposition. This measurement only allows the determination of amplitudes of each spinning mode number at the duct wall and not individual radial modes. The maximum spinning mode number m_{max} that can be inverted from the 24 microphones according to the sampling theorem is $m_{max} = 11$. In the present duct, this allows the determination of the amplitudes of all cut-on modes up to $ka = 13.8$. The cut-off frequency $ka = 14.12$ studied in the previous sections is therefore not investigated in this section. Comparison will also be made at the cut-on frequency $ka = 11.35$.

At a single frequency, the in-duct pressure field at the i^{th} microphone may be written as

$$p(\theta_i) = \sum_{m=-M}^{+M} a_m e^{-jm\theta_i} \tag{8.3.1}$$

where a_m are the pressure mode amplitudes at the duct wall. Comparison of equation 8.3.1 with equation 2.1.16 allows the amplitudes a_m to be related to the mode amplitudes a_{mn} by

$$a_m = \sum_{n=1}^{+N} a_{mn} \frac{J_m\left(\kappa_{mn} a\right)}{\sqrt{\Lambda_{mn}}} \tag{8.3.2}$$

where M and N are the maximum and spinning and radial mode numbers cut-on at a given frequency. Inverting equation 8.3.1 and taking the expectation $E\left[\overline{a_m^2}\right]$, the mean square mode amplitudes at the ring of microphones is given by

$$\overline{a_m^2}(\omega) = \left(\frac{1}{K}\right)^2 \sum_{i=1}^{K}\sum_{j=1}^{K} S_{pp}(\theta_i, \theta_j, \omega) e^{jm(\theta_i - \theta_j)} \tag{8.3.3}$$

where $S_{pp}(\theta_i, \theta_j, \omega)$ is the cross-spectrum of measured pressures between any two microphones located at θ_i and θ_j at the duct wall. Assuming incoherent radial modes, as demonstrated in figure 8.11, the mean square mode amplitudes at the in-duct microphones can readily be compared to that from the TCS microphones by the following relationship

$$\overline{a_m^2} = \sum_{n=1}^{+N} \overline{a_{mn}^2} \left| \frac{J_m(\kappa_{mn} a)}{\sqrt{\Lambda_{mn}}} \right|^2 \tag{8.3.4}$$

Figure 8.12 shows a comparison between the mean square mode amplitudes computed from the in-duct measurements and those from the geodesic array computed using equation 8.3.4, expressed in dB relative to arbitrary units. To allow a clearer comparison, vertical arrows are used to connect two data points at the same m-value. Note that Tikhonov regularisation using $\mathbf{R_2}$ is applied to the modal solution inverted from the TCS pressure measurements at the cut-on frequencies, namely at $ka = 11.35$ and $ka = 12.95$. Figure 8.12 shows generally good agreement between the two mode amplitude estimators to within 6dB, with many amplitudes found to agree to within 3dB or better. The largest differences between the two techniques are found in the high order spinning mode numbers at $ka = 9.65$ where a difference of about 10dB is found for the modes $m = -7$, $m = -6$ and $m = -5$. The results found in figure 8.12 provides experimental validation of the TCS-based inverse technique.

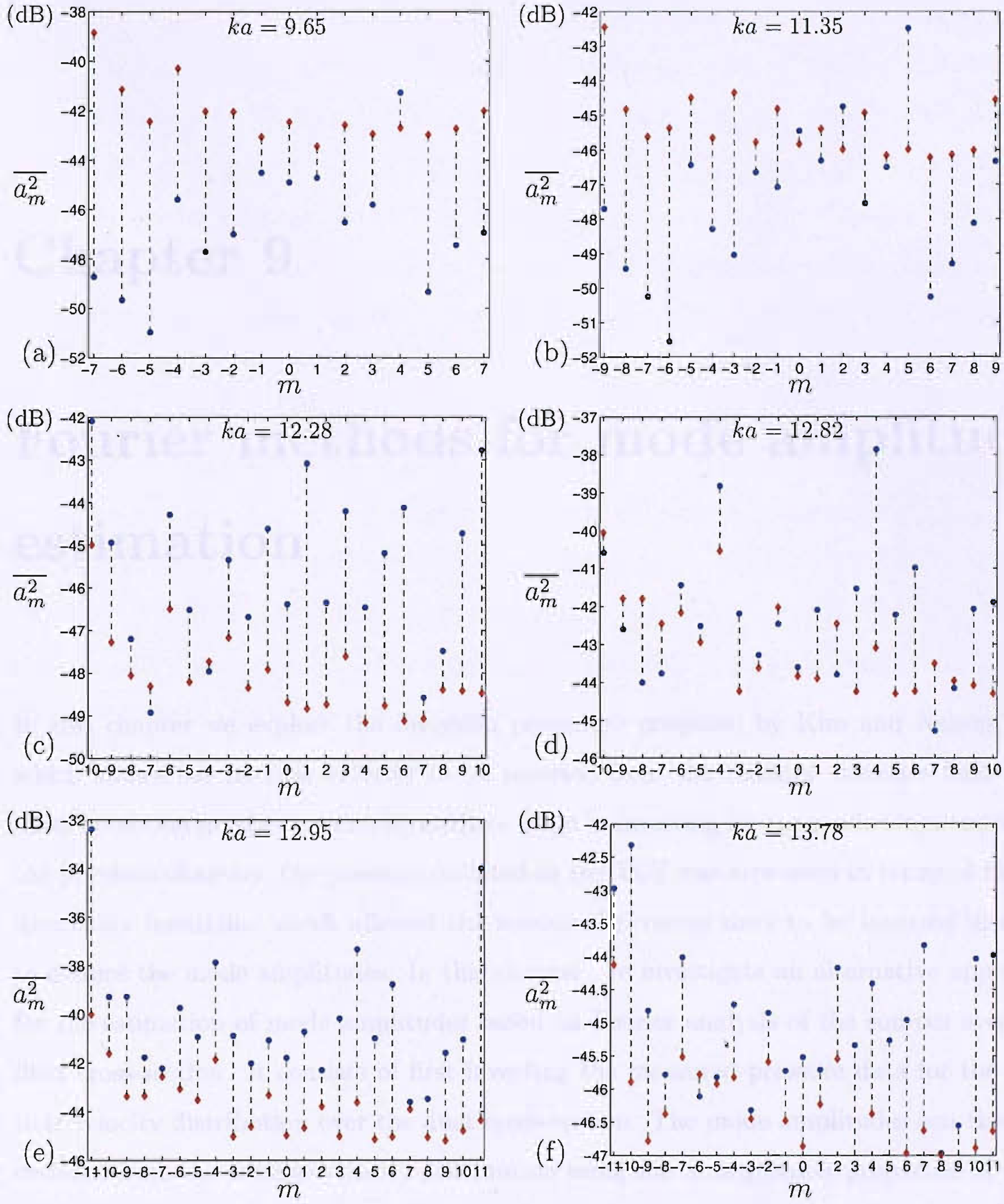

Figure 8.12: Mean square mode amplitudes against spinning mode number m inverted from ◆ In-duct microphones ● Geodesic sensor array

(a) $ka = 9.65$,(b) $ka = 12.28$, (c) $ka = 12.82$, (d) $ka = 12.95$ (e) $ka = 13.78$ and (f) $ka = 14.12$

Chapter 9

Fourier methods for mode amplitude estimation

In this chapter we explore the inversion procedure proposed by Kim and Nelson [43], which allows the particle velocity to be inverted from the radiated pressure field with unity condition number as an intermediate stage in inverting for the mode amplitudes. In the previous chapters, the pressure radiated to the TCS was expressed in terms of modal directivity functions, which allowed the measured pressure data to be inverted directly to deduce the mode amplitudes. In this chapter, we investigate an alternative approach for the estimation of mode amplitudes based on Fourier analysis of the sources over the duct cross-section. It consists of first inverting the measured pressure data for the particle velocity distribution over the duct cross-section. The mode amplitudes can then be deduced from the particle velocity distribution using the orthogonality properties of their mode shape functions. The basis for the technique is the Fourier relationship between the radiated pressure on the TCS to the axial particle velocity distribution over the duct outlet [44] as outlined in section 2.3. Using appropriate sampling of source distribution and of sensors on the TCS, the discretised Rayleigh integral becomes equivalent to a Discrete

Fourier Transform relationship, as shown by Kim and Nelson [43]. This method reviewed in section 9.1 leads to inverting a Fourier matrix for the particle velocity distribution. This Fourier matrix has singular values that are all unity and thus the condition number is a minimum of exactly unit. It will be shown in section 9.1 that this Fourier relationship, valid for far-field approximations, holds within a limited range of spatial resolution. Section 9.2 will show that the mode amplitudes can be readily deduced from the Hankel transform of the reconstructed particle velocity distribution. An optimal robustness in the solution is thus obtained. However, a fundamental issue that arises is whether this information is sufficient to obtain accurately the mode amplitudes. An overview of the relationship between radiated pressure **p**, velocity distribution **u** and duct mode amplitudes **a** is given in figure 9.1. In this figure, the matrix **G** is the transfer matrix relating the modelled pressure to the source distribution and under particular conditions is proportional to a Fourier matrix. This chapter investigates a different method by first deducing the particle velocity distribution using the right-hand side of figure 9.1 meanwhile taking care to satisfy the best trade-off between accuracy and robustness.

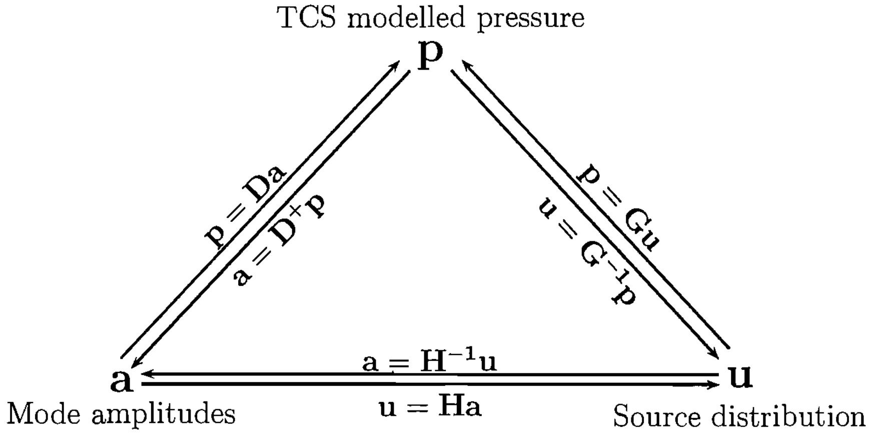

Figure 9.1: Different methods for inverting the mode amplitudes

9.1 Source and TCS sampling requirements for DFT

First recall the Fourier relationship between the far field pressure and the velocity distribution over the duct cross-section exit $u_z(x_s, y_s)$ given in equation 2.3.5 as

$$\begin{aligned} p(r,\theta,\phi) &= j\rho ck\frac{e^{-jkr}}{r}\int_{-\infty}^{+\infty}\int_{-\infty}^{+\infty} u_z(x_s,y_s)\, e^{j(k_x x_s + k_y y_s)} dx_s dy_s \\ &= j\rho ck\frac{e^{-jkr}}{r} U_z(k_x,k_y) \end{aligned} \tag{9.1.1}$$

where $U_z(k_x, k_y)$ is the spatial Fourier transform (or wavenumber transform) of $u_z(x_s, y_s)$. A discrete Fourier Transform (DFT) can relate the sampled source distribution and the radiated far field. Kim and Nelson propose an array that allow the sampled velocity distribution to be deduced from the measured pressure by the inverse of a Fourier matrix with unit condition number, whose inversion is therefore optimally robust.

9.1.1 Sampling source distribution and projection of sensors on a Cartesian grid

Kim and Nelson [43] suggest arranging microphones in the far field such that the projection of the inter-sensor spacing on the source plane is constant, as in figure 9.2. Since $\vec{k}$ and $\vec{r}$ have the same direction in the far-field, we have

$$\begin{cases} k_x = k\sin\varphi\cos\theta \\ k_y = k\sin\varphi\sin\theta \end{cases} \qquad \begin{cases} x_m = r\sin\varphi\cos\theta \\ y_m = r\sin\varphi\sin\theta \end{cases} \tag{9.1.2}$$

where x_m and y_m denote the positions of the projected sensors onto the source plane and k_x and k_y denote the respective components of the wavenumber vector.

Introducing equation 9.1.2 into equation 9.1.1, the far-field pressure at each sensor may be written as

$$p(r,\theta,\phi) = j\rho ck\frac{e^{-jkr}}{r}\int_{-\infty}^{+\infty}\int_{-\infty}^{+\infty} u_z(x_s,y_s)\, e^{j\frac{k}{r}(x_m x_s + y_m y_s)} dx_s dy_s \tag{9.1.3}$$

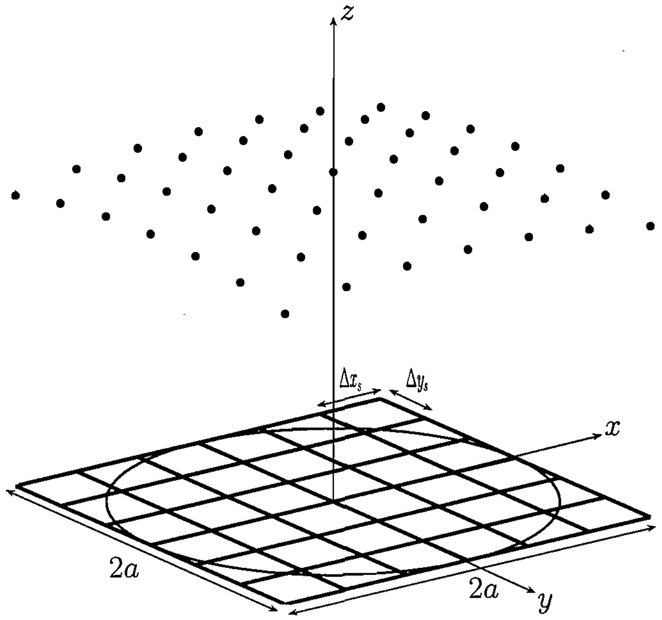

Figure 9.2: Schematic of a hemispherical array and its projection onto the rectangular source plane

In order to transform this Fourier integral into a DFT, appropriate sampling of the axial velocity distribution and appropriate distribution of sensors on the TCS is required. As shown in figure 9.2, the velocity is sampled over a rectangular grid at equal increments Δx_s and Δy_s in both directions. The velocity for is assumed to be zero for the positions on the grid which $r_s > a$. Using the properties of the Dirac delta function, equation 9.1.1 becomes

$$U_z(k_x, k_y) = \int_{-\infty}^{+\infty}\int_{-\infty}^{+\infty}\sum_{p=-\infty}^{+\infty}\left(\sum_{q=-\infty}^{+\infty} u_z(x_s, y_s)\,\delta(y_s - q\Delta y_s)\right) \delta(x_s - p\Delta x_s)\, e^{j(k_x x_s + k_y y_s)} dx_s dy_s \tag{9.1.4}$$

which reduces to

$$U_z(k_x, k_y) = \sum_{p=-\infty}^{+\infty}\sum_{q=-\infty}^{+\infty} u_z(p\Delta x_s, q\Delta y_s)\, e^{j(k_x p\Delta x_s + k_y q\Delta y_s)} \tag{9.1.5}$$

Sampling the source plane at P equally spaced position in the x-direction and Q points in the y-direction over the interval $(-a \leq x_s \leq a,\ -a \leq y_s \leq a)$ corresponds to sampling increments of

$$\Delta x_s = \frac{2a}{P} \qquad \Delta y_s = \frac{2a}{Q} \tag{9.1.6}$$

with sampling positions defined by

$$\begin{aligned} x_{sp} &= -\left(a - \frac{\Delta x_s}{2}\right) + p\Delta x_s \quad p = 0, \ldots P-1 \\ y_{sq} &= -\left(a - \frac{\Delta y_s}{2}\right) + q\Delta y_s \quad q = 0, \ldots Q-1 \end{aligned} \tag{9.1.7}$$

The Fourier transform of the sampled velocity distribution is then given as

$$U_z\left(k_x, k_y\right) = \sum_{p=0}^{P-1}\sum_{q=0}^{Q-1} u_z\left(x_{sp}, y_{sq}\right) e^{j\left(k_x p\Delta x_s + k_y q\Delta y_s\right)} \tag{9.1.8}$$

Since the spatial frequency ranges between $\left[-\frac{\pi}{Lx}, \frac{\pi}{Lx}\right]$ and $\left[-\frac{\pi}{Ly}, \frac{\pi}{Ly}\right]$ in each direction respectively, the DFT evaluates equation 9.1.8 at P and Q values in each component of the spatial frequency at the following wavenumber increments

$$\Delta k_x = \frac{2\pi}{P\Delta x_s} \qquad \Delta k_y = \frac{2\pi}{Q\Delta y_s} \tag{9.1.9}$$

The DFT of the axial velocity distribution is then written as

$$U_z\left(\mu\Delta k_x, \nu\Delta k_y\right) = \sum_{p=0}^{P-1}\sum_{q=0}^{Q-1} u_z\left(x_{sp}, y_{sq}\right) e^{j2\pi\left(\frac{p\mu}{P} + \frac{q\nu}{Q}\right)} \tag{9.1.10}$$

Similar to equation 9.1.8, the Fourier integral given in equation 9.1.3 is then written as

$$U_z\left(k_x, k_y\right) = \sum_{p=0}^{P-1}\sum_{q=0}^{Q-1} u_z\left(x_{sp}, y_{sq}\right) e^{j\frac{k}{r}\left(x_m p\Delta x_s + y_m q\Delta y_s\right)} \tag{9.1.11}$$

Following Kim and Nelson, the sensors are distributed such that their projection x_m and y_m are spaced at intervals Δx_m and Δy_m respectively,

$$x_m = \mu\Delta x_m = \mu\frac{L_x}{P} \qquad y_m = \nu\Delta y_m = \nu\frac{L_y}{Q} \tag{9.1.12}$$

Equation 9.1.11 then becomes

$$U_z\left(\mu\Delta k_x, \nu\Delta k_y\right) = \sum_{p=0}^{P-1}\sum_{q=0}^{Q-1} u_z\left(x_{sp}, y_{sq}\right) e^{j\frac{k}{r}\left(\frac{p\mu}{P}L_x\Delta x_s + \frac{q\nu}{Q}L_y\Delta y_s\right)} \tag{9.1.13}$$

In order for equation 9.1.13 to be equivalent to the DFT relationship of equation 9.1.10, we must have

$$\Delta x_s = \frac{\lambda r}{L_x} \qquad \Delta y_s = \frac{\lambda r}{L_y} \tag{9.1.14}$$

Equation 9.1.14 is the sampling condition which allows the far-field pressure at the sensors to be expressed in terms of a DFT of the velocity distribution sampled over the duct inlet cross-section on a Cartesian grid. This can be written in matrix form as follows:

$$\mathbf{p} = \mathbf{G}\mathbf{u} = g\mathbf{W}\mathbf{u} \tag{9.1.15}$$

where $g = j\rho cke^{-jkr}/r$.

$\mathbf{W}$ is the $K \times K$ matrix for the two dimensional Fourier transform given by

$$\mathbf{W} = \begin{bmatrix} [\tilde{\mathbf{W}}] & [\tilde{\mathbf{W}}] & [\tilde{\mathbf{W}}] & \cdots & [\tilde{\mathbf{W}}] \\ [\tilde{\mathbf{W}}] & w_K [\tilde{\mathbf{W}}] & w_K^2 [\tilde{\mathbf{W}}] & \cdots & w_K^{K-1} [\tilde{\mathbf{W}}] \\ [\tilde{\mathbf{W}}] & w_K^2 [\tilde{\mathbf{W}}] & w_K^4 [\tilde{\mathbf{W}}] & \cdots & w_K^{2(K-1)} [\tilde{\mathbf{W}}] \\ \cdot & \cdot & \cdot & \cdots & \cdot \\ \cdot & \cdot & \cdot & \cdots & \cdot \\ [\tilde{\mathbf{W}}] & w_K^{K-2} [\tilde{\mathbf{W}}] & w_K^{2(K-2)} [\tilde{\mathbf{W}}] & \cdots & w_K^{(K-2)(K-1)} [\tilde{\mathbf{W}}] \\ [\tilde{\mathbf{W}}] & w_K^{K-1} [\tilde{\mathbf{W}}] & w_K^{2(K-1)} [\tilde{\mathbf{W}}] & \cdots & w_K^{(K-1)(K-1)} [\tilde{\mathbf{W}}] \end{bmatrix} \tag{9.1.16}$$

where

$$\tilde{\mathbf{W}} = \begin{bmatrix} 1 & 1 & 1 & \cdots & 1 \\ 1 & w_K & w_K^2 & \cdots & w_K^{K-1} \\ 1 & w_K^2 & w_K^4 & \cdots & w_K^{2(K-1)} \\ \cdot & \cdot & \cdot & \cdots & \cdot \\ \cdot & \cdot & \cdot & \cdots & \cdot \\ 1 & w_K^{K-2} & w_K^{2(K-2)} & \cdots & w_K^{(K-2)(K-1)} \\ 1 & w_K^{K-1} & w_K^{2(K-1)} & \cdots & w_K^{(K-1)(K-1)} \end{bmatrix} \tag{9.1.17}$$

and $w_K = e^{j2\pi/K}$.

It is important to note that equation 9.1.15 is only valid when the sound field is sampled by Δx_s and Δy_s given by equation 9.1.14. The interest of such a relationship lies in the fact that the transfer matrix **H** relating the radiated pressure to the source distribution has a unity condition number since all the singular values of **W** are unity [25]. When $\Delta x_s \neq \frac{\lambda r}{L_x}$ and $\Delta y_s \neq \frac{\lambda r}{L_y}$, the transfer matrix **H** differs from **W** and its condition number will consequently increase. When the projection of the sensor array onto the source plane is made a square with dimensions equal to the diameter of the TCS [43], $L_x = L_y = L = \sqrt{2}r$ and the hemispherical sensor array shown in figure 9.2 consists of $P \times P$ sensors, the optimal sensor spacing is given by

$$\Delta x_s = \Delta y_s = \frac{\sqrt{2}}{2}\lambda \tag{9.1.18}$$

Equations 9.1.14 and 9.1.18 specify the spatial resolution of the source distribution over the duct cross-section. These limitations are frequency dependent. The extraction of mode amplitudes from the velocity distribution sampled according to equation 9.1.18 is discussed in section 9.3.

The sound field that propagates in a duct comprises modes that have cylindrical characteristic behaviour. It is therefore interesting to investigate the sampling of the velocity distribution as well as the projection of sensors on a polar grid.

9.1.2 Sampling source distribution and projection of sensors on a polar grid

Equation 9.1.1 specifies the 2D Fourier transform relationship between p and u_z providing the source distribution lies over a rectangular region. However, the geometry of the source distribution over the duct inlet is circular and the far field pressure is proportional to the Polar Fourier Transform of u_z as given by equation 2.3.9

$$U_z\left(k_r, \theta\right) = \int_0^{2\pi}\int_0^{\infty} u_z\left(r_s, \theta_s\right) e^{jk_r r_s \sin(\theta_s + \theta)} r_s dr_s d\theta_s \tag{9.1.19}$$

The velocity distribution and the projection of sensors onto the source plane are now sampled on a polar grid as shown in figure 9.3.

Unlike section 9.1.1, This section shows that there is no equivalent unique sampling criterion which would satisfy a discrete version of equation 9.1.19. It was shown in section 2.3 (i.e. equation 2.3.14) that equation 9.1.19 may be written as the Fourier series expansion

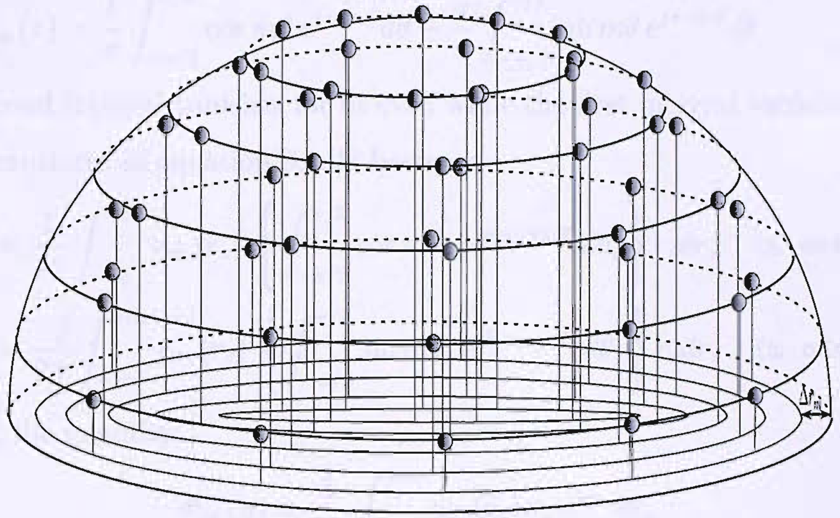

Figure 9.3: Schematic of a hemispherical array and its projection onto the circular source plane

$$U_z(k_r,\theta)=2\pi\sum_{m=-\infty}^{+\infty}\tilde{U}_{mm}(k_r)\,e^{jm\theta} \tag{9.1.20}$$

The coefficients $\tilde{U}_{mm}(k_r)$ are the Hankel transforms of order m of the m^{th} Fourier component of the radial surface velocity distribution given by equation 2.3.15

$$\tilde{U}_{mm}(k_r)=\int_0^{\infty}u_m(r_s)\,J_m(k_r r_s)\,r_s dr_s \tag{9.1.21}$$

Algorithms for computing discrete Hankel transforms can be found in the literature [45], which essentially involve variations of one dimensional Fourier transforms.

Since for $k_r \geq 0$ and $r_s \in [0;a]$, the term $r_s J_m(k_r r_s)$ in equation 9.1.21 is an even function for m even and an odd function for m odd, we can write

$$\tilde{U}_{mm}(k_r)=\frac{1}{2}\int_{-\infty}^{+\infty}u_m(r_s)\,J_m(k_r r_s)\,r_s dr_s \tag{9.1.22}$$

Using the integral identity for $J_m(k_r r_s)$,

$$J_m(z) = \frac{1}{\pi}\int_{-\pi/2}^{\pi/2} \cos m\theta \, e^{jz\sin\theta} d\theta - \frac{j}{\pi}\int_{-\pi/2}^{\pi/2} \sin m\theta \, e^{jz\sin\theta} d\theta \tag{9.1.23}$$

where the second integral vanishes for m even while the first integral vanishes for m odd, the Hankel transform in equation 9.1.22 becomes

$$\begin{aligned} \tilde{U}_{mm}(k_r) &= \frac{1}{2\pi}\int_{-\infty}^{+\infty} u_m(r_s)\left\{\int_{-\pi/2}^{\pi/2} \cos m\theta_s \, e^{jk_r r_s \sin\theta_s} d\theta_s\right\} r_s dr_s \quad \texttt{(m even)} \\ \tilde{U}_{mm}(k_r) &= \frac{-j}{2\pi}\int_{-\infty}^{+\infty} u_m(r_s)\left\{\int_{-\pi/2}^{\pi/2} \sin m\theta_s \, e^{jk_r r_s \sin\theta_s} d\theta_s\right\} r_s dr_s \quad \texttt{(m odd)} \end{aligned} \tag{9.1.24}$$

Now defining the quantity,

$$\Phi_m(\eta) = \frac{1}{2\pi}\int_{-\infty}^{+\infty} u_m(r_s)\, r_s \, e^{j\eta r_s} dr_s \tag{9.1.25}$$

which is a Fourier transform of $u_m(r_s)\, r_s$, the Hankel transform of equation 9.1.24 is now written as

$$\begin{aligned} \tilde{U}_{mm}(k_r) &= \int_{-\pi/2}^{\pi/2} \Phi_m(k_r \sin\theta_s) \cos m\theta_s \, d\theta_s \quad \texttt{(m even)} \\ \tilde{U}_{mm}(k_r) &= -j\int_{-\pi/2}^{\pi/2} \Phi_m(k_r \sin\theta_s) \sin m\theta_s \, d\theta_s \quad \texttt{(m odd)} \end{aligned} \tag{9.1.26}$$

The function $r_s u_m(r_s)$ is even for m even and odd for m odd, implying that Φ_m is even and odd for m even and odd respectively. This in turn implies that for m even or odd, the integrands in equation 9.1.26 are even. This property enables the intervals of integration in equation 9.1.26 to be halved. Thus,

$$\begin{aligned} \tilde{U}_{mm}(k_r) &= 2\int_0^{\pi/2} \Phi_m(k_r \sin\theta_s)\, \Re e\left\{e^{-jm\theta_s}\right\} d\theta_s \quad \texttt{m even} \\ &= 2j\int_0^{\pi/2} \Phi_m(k_r \sin\theta_s)\, \Im m\left\{e^{-jm\theta_s}\right\} d\theta_s \quad \texttt{m odd} \end{aligned} \tag{9.1.27}$$

In order to express equation 9.1.20 in terms of DFT relationships, the coefficients $\tilde{U}_{mm}(k_r)$ of equation 9.1.20 must be written in terms of the DFT as shown by equation 9.1.25. Sampling in the radial direction at increments of Δr_s,

$$\Phi_m(\eta) = \frac{1}{2\pi}\int_{-\infty}^{+\infty} u_m(r_s)\, r_s \sum_{p=-\infty}^{+\infty} \delta(r_s - p\Delta r_s)\, e^{j\eta r_s} dr_s \tag{9.1.28}$$

which gives

$$\Phi_m(\eta) = \frac{1}{2\pi} \sum_{p=-\infty}^{+\infty} u_m(p\Delta r_s)\, p\Delta r_s e^{j\eta p\Delta r_s} \tag{9.1.29}$$

and assuming P points of non-zero source strength in the interval $[0; a]$, the sampling points are defined at each increment $\Delta r_s = a/P$

$$r_{sp} = p\Delta r_s + \frac{\Delta r_s}{2} \qquad p = 0, 1, ..., P-1 \tag{9.1.30}$$

equation 9.1.28 becomes

$$\Phi_m(\eta) = \frac{1}{2\pi} \sum_{p=0}^{P-1} u_m(r_{sp})\, r_{sp} e^{j\eta p\Delta r_s} \tag{9.1.31}$$

Now the DFT of equation 9.1.31 is evaluated at all q values $\Delta\eta = \eta_s/P$, $q = 0, 1, ..., P-1$ where $\eta_s = 2\pi/\Delta r_s$

$$\Phi_m(q\Delta\eta) = \frac{1}{2\pi} \sum_{p=0}^{P-1} u_m(r_{sp})\, r_{sp} e^{j2\pi\frac{pq}{P}} \tag{9.1.32}$$

Since r_m denotes the radial position of the TCS sensors projected onto the source plane, it is straightforward to see that $r_m = r\sin\varphi$. Since $k_r = k\sin\varphi = kr_m/r$, evaluating $\eta = k_r \sin\theta_s$ at discrete values thus involves sampling r_m at equal increments $\Delta r_m = r/P$ (i.e. see figure 9.3). The increment at which equation 9.1.31 is evaluated is given by

$$\Delta\eta = \frac{k}{r}\Delta r_m \sin\theta_s \tag{9.1.33}$$

Thus equation 9.1.31 for the discrete Hankel transform of $u_m(r_s)$ becomes

$$\Phi_m(q\Delta\eta) = \frac{1}{2\pi} \sum_{p=0}^{P-1} u_m(r_{sp})\, r_{sp} e^{jq\frac{k}{P}\sin\theta_s p\Delta r_s} \tag{9.1.34}$$

$$\Phi_m(q\Delta\eta) = \frac{1}{2\pi} \sum_{p=0}^{P-1} u_m(r_{sp})\, r_{sp} e^{j2\pi\frac{pq}{P}\frac{\sin\theta_s\Delta r_s}{\lambda}}$$

In order for equation 9.1.34 to be equivalent to a DFT, (i.e. equation 9.1.32), the function $u_m(r_s)$ to be Hankel transformed in equation 2.3.15 needs to be sampled at non uniform increments of

$$\Delta r_s = \frac{\lambda}{\sin\theta_s} \tag{9.1.35}$$

The optimal sampling of the source distribution in the radial direction therefore depends on the polar coordinate θ_s. Equation 9.1.35 suggests that there is no unique sampling criterion on the radial direction for the Discrete Hankel Transform that are exactly analogous to that of equation 9.1.14 for rectangular source geometries, in which the radiation matrix has a unit condition number. Therefore, the sampling of the source distribution on a polar grid does not provide a DFT relationship between the far field pressure and the velocity distribution.

9.2 Mode amplitudes from Hankel transforms

In this section we investigate the feasibility of deducing the mode amplitude distribution over the duct inlet. The source distribution on the duct cross-section can be related to mode amplitudes by rewriting equation 2.2.8

$$u_z\left(r_s,\theta_s\right) = \frac{k}{\omega\rho}\sum_{m=-\infty}^{+\infty}\sum_{n=1}^{+\infty}\sqrt{1-\alpha_{mn}^2}a_{mn}\Psi_{mn}\left(r_s,\theta_s\right) \tag{9.2.1}$$

where $\Psi_{mn}\left(r_s,\theta_s\right)$ is the mode shape function defined in equation 2.1.20. Multiplying both sides of equation 9.2.1 by the complex conjugate of the mode shape function and integrating over the duct cross-section gives

$$\frac{1}{S}\int\int_S u_z\left(r_s,\theta_s\right)\,\Psi_{mn}^*\left(r_s,\theta_s\right)\,dS = \frac{1}{\rho c}\sqrt{1-\alpha_{mn}^2}a_{mn} \tag{9.2.2}$$

Therefore the mode amplitudes are given by

$$a_{mn} = X_{mn}\int\int_S u_z\left(r_s,\theta_s\right)\,\Psi_{mn}^*\left(r_s,\theta_s\right)\,dS \tag{9.2.3}$$

where X_{mn} is

$$X_{mn} = \frac{\rho c}{S}\sqrt{\frac{1}{\left(1-\alpha_{mn}^2\right)}} \tag{9.2.4}$$

For a particular mode (m_0, n_0), equation 9.2.3 can be rewritten as

$$a_{m_0n_0} = X_{m_0n_0}\int_0^{2\pi}\left\{\int_0^{\infty} u_z\left(r_s,\theta_s\right)\Pi\left(r_s\right)J_{m_0}\left(\kappa_{m_0n_0}r_s\right)r_s dr_s\right\}e^{jm_0\theta_s}d\theta s \tag{9.2.5}$$

where $\Pi(r_s)$ is defined as

$$\Pi(r_s) = \begin{cases} 0 & r_s \notin [\,0\,;\,a\,] \\ 1 & r_s \in [\,0\,;\,a\,] \end{cases} \tag{9.2.6}$$

Note that $u_z(r_s, \theta_s)$ denotes the axial velocity multiplied by the above window function for ease of notation. Introducing equation 2.3.10 into equation 9.2.5 yields

$$a_{m_0 n_0} = X_{m_0 n_0} \int_0^{2\pi} \left\{ \sum_{m=-\infty}^{+\infty} \int_0^{\infty} u_m(r_s)\, J_{m_0}(\kappa_{m_0 n_0} r_s)\, r_s dr_s \right\} e^{j(m_0 - m)\theta_s} d\theta_s \tag{9.2.7}$$

Since the integration over θ_s vanishes when $m \neq m_0$ and equals 2π when $m = m_0$, the amplitude for any mode (m, n) can be recovered from the source distribution over the duct outlet as

$$a_{mn} = 2\pi X_{mn} \tilde{U}_{mm}(\kappa_{mn}) \tag{9.2.8}$$

Thus, similar to equation 2.3.15

$$\tilde{U}_{mm}(\kappa_{mn}) = \int_0^{\infty} u_m(r_s)\, J_m(\kappa_{mn} r_s)\, r_s dr_s \tag{9.2.9}$$

Equations 9.2.8 and 9.2.9 show that the mode amplitudes may be obtained from the Hankel transform of order m of the radial velocity distribution evaluated at $k_r = \kappa_{mn}$. The Hankel transform of the radial velocity distribution is related to the Fourier transform of the axial velocity distribution in polar coordinates by equation 2.3.14. Since equation 2.3.14 is a Fourier expansion, the Hankel transforms of the radial velocity distribution of order m given by equations 2.3.15, and more particularly by equation 9.2.9, are simply the Fourier coefficients of this Fourier Series

$$\tilde{U}_{mm}(k_r) = \int_0^{2\pi} U_z(k_r, \theta)\; e^{-jm\theta} d\theta \tag{9.2.10}$$

In discrete form, equations 2.3.14 can be rewritten as

$$U_z(k_r, \theta) = 2\pi \sum_{m=-m_{\max}}^{+m_{\max}} \tilde{U}_{mm}(k_r)\; e^{jm\theta} \tag{9.2.11}$$

where m_{max} is the maximum spinning mode number cut-on under consideration. Let $q = m + m_{max}$ and $Q = 2m_{max}+1$, equation 9.2.11 can be rewritten for ease of computation as

$$U_z\left(k_r, \theta\right) = 2\pi \sum_{q=0}^{Q-1} \tilde{U}_{mm}\left(k_r\right) e^{j(q-m_{max})\theta} \tag{9.2.12}$$

Sampling in the azimuthal direction as $\theta_p = p\,2\pi/Q$ with $p = 0, 1, ..., Q-1$, equation 9.2.10 can be rewritten as

$$\tilde{U}_{mm}\left(k_r\right) = \sum_{p=0}^{Q-1} U_z\left(k_r, \theta_p\right) e^{-j(q-m_{\mathrm{max}})\theta_p} \tag{9.2.13}$$

If the sampling criterion given by equation 9.1.14 is satisfied, the Fourier transform of the velocity distribution can be computed exactly from the radiated pressure as in equation 9.1.15 for sets of wavenumber components (k_x, k_y), which from equations 9.1.9 and 9.1.18 is given by

$$\Delta k_x = \Delta k_y = \frac{\sqrt{2}\,k}{\pi P} \tag{9.2.14}$$

It is however required to interpolate the data provided by $U_z\left(k_x, k_y\right)$ such that a new set of wavenumber components (k_x, k_y) corresponds to θ_p given as in equation 9.2.13. The wavenumber components k_r are freely chosen and will therefore be evaluated at the values of the radial wavenumber of each mode (i.e. $k_r = \kappa_{mn}$).

9.3 Mode amplitudes from discretised velocity distribution

Kim and Nelson [43], as reviewed in section 9.1.1, have shown that the particle velocity distribution over the duct outlet can be inverted from the radiated pressure with optimal conditioning sampled at $\lambda/2$ in the two orthogonal directions. We now attempt to use this sampled velocity to deduce the mode amplitudes. This section discusses the different methods for determining the mode amplitudes from the source distribution.

9.3.1 Mode amplitudes matching the source distribution

The first method consists of inverting for the source distribution according to equation 9.1.15,

$$\hat{\mathbf{u}} = \mathbf{G}^{+}\hat{\mathbf{p}} \tag{9.3.1}$$

The source distribution $\mathbf{u}$ can then be related to the mode amplitudes $\mathbf{a}$ by

$$\mathbf{u} = \mathbf{H}\mathbf{a} \tag{9.3.2}$$

where $\mathbf{H}$ is a $K \times L$ matrix, which relates the particle velocity distribution to the mode amplitudes as described in the section 9.2. The velocity distribution found from equation 9.3.1 may be written as the sum of the exact velocity distribution over the duct outlet plus errors due to either noise or modelling imperfections. In this case, the complex error vector can be written as

$$\mathbf{n} = \hat{\mathbf{u}} - \mathbf{u} = \hat{\mathbf{u}} - \mathbf{H}\mathbf{a} \tag{9.3.3}$$

Minimising the cost function defined as the sum of the squared errors of equation 3.1.7, (i.e. min $\|\hat{\mathbf{u}} - \mathbf{H}\mathbf{a}\|_2^2$), the least square estimate of the mode amplitudes vector that minimises this cost function is given by

$$\mathbf{a} = \mathbf{H}^{+}\hat{\mathbf{u}} \tag{9.3.4}$$

Introducing equation 9.3.1 into equation 9.3.4, the mode amplitudes can be deduced from the radiated pressure via the product of two matrix inversions

$$\mathbf{a} = \mathbf{H}^{+}\mathbf{G}^{+}\hat{\mathbf{p}} \tag{9.3.5}$$

Although the solution to equation 9.3.5 optimises the errors found in the velocity distribution, the choice of the cost function is useful because the matrix $\mathbf{G}$ is optimally well-conditioned, i.e. $\kappa(\mathbf{G}) = 1$. The advantage of this approach is that $\mathbf{G}$ is proportional to a Fourier matrix and of unit condition number so that as long as the sampling criterion given by equation 9.1.14 is satisfied, the inverted vector of source distribution $\hat{\mathbf{u}}$ is robust to any errors found in the pressure measurements. However the accuracy in inverting the source distribution for the mode amplitudes may not be sufficiently high. As previously mentioned, an overdetermined system is required if the mode amplitudes are to be accurately detected. From equation 9.1.18 we can deduce the number P and Q of non-zero source strengths in the x and y directions respectively.

$$P = Q \leq \frac{\sqrt{2}}{\pi} ka \tag{9.3.6}$$

Since the matrix $\mathbf{G}$ is square, the number of sampling points equals the number of sensors on the TCS. Therefore the number of sensors, which depends on frequency, required with that technique is

$$K = PQ \leq \frac{2}{\pi^2} (ka)^2 \tag{9.3.7}$$

The number of cut-on modes also depends on frequency and is given by

$$L \geq \frac{1}{2} ka + \left(\frac{1}{2} ka \right)^2 \geq \frac{1}{4} (ka)^2 \tag{9.3.8}$$

The ratio of the number of sensors required to deduce $\mathbf{u}$ with unit condition number to the number of modes to be inverted is therefore given by

$$\frac{K}{L} \leq \frac{8}{\pi^2} \leq 1 \tag{9.3.9}$$

Thus the method for inverting with unit condition number the source distribution over the duct outlet from pressure measurements, and then inverting for the mode amplitudes requires approximately 80% less sensors than modes. It is therefore not possible to determine $\mathbf{a}$ from $\mathbf{p}$ via $\mathbf{u}$ with optimal conditioning. It is thus necessary to invert for 'sources' over the duct outlet that is finer than the $\lambda/2$ optimal resolution limit identified by Kim and Nelson. However, this is only done at the expense of increasing conditioning since the matrix $\mathbf{G}$ will no longer be related to the Fourier matrix and hence its condition number will be greater than unity.

9.3.2 Mode amplitudes matching the pressure measurements

This section describes another method of deducing the mode amplitudes based on similar principles to that in section 9.3.1 but the solution is now fitting in the least squares sense the pressure data. The radiated pressure may be related to the mode amplitudes by

$$\mathbf{p} = \mathbf{GHa} \tag{9.3.10}$$

such that $\mathbf{D} = \mathbf{GH}$. Now minimising the cost function resulting from the least square solution given in appendix B gives the optimal mode amplitude vector estimate via a single matrix inverse

$$\hat{\mathbf{a}} = [\mathbf{GH}]^{+}\,\mathbf{p} \tag{9.3.11}$$

Because of the underdetermined system, the same trade-off between robustness and accuracy required in the previous section needs to be satisfied. This method features the advantage of minimising the errors found in the pressure measurements whereas the method described in section 9.3.1 minimises errors found in the source distribution, which can only be useful if $\mathbf{G}$ is well-conditioned.

9.4 Conclusion

Alternative methods for mode determination in a cylindrical environment have been presented in this chapter 9. These methods based on far-field approximations use Fourier properties to express the radiated pressure field in terms of the source distribution at the inlet cross-section. This allows the reconstruction of the source distribution at the exit cross-section with an optimal minimisation of noise in the pressure measurements. This method requires, however, a underdetermined system of equations which may not be sufficient for an accurate determination of mode amplitudes from the reconstructed velocity distribution. The work undertaken in this chapter has not been completed. Numerical simulations could be performed to support the evidence that more sensors are required for an accurate determination of the mode amplitudes which in the same time will damage the optimal conditioning that these methods offer. These simulations will allows us to determine the best trade-off between conditioning and reconstruction accuracy. Furthermore, the mode amplitudes deduced from these methods require the interpolation of the reconstructed velocity to compute its Hankel transform which also introduces a source of errors. Therefore numerical simulations could be carried out in order to optimise this interpolation such that minimum errors are introduced.

Chapter 10

Conclusion

An inverse technique for determining the mode amplitudes of a circular hard-walled duct using pressure measurements made in the radiated near field has been described. This technique may be applied on turbofan engines with the use of the TCS during ground testing for mounting microphones. Although the technique presented in this thesis was expressed in terms of a simple model of a hollow duct with no flow, the technique remains valid for a more realistic model of an engine inlet with the presence of flow and liners. The technique uses a directivity matrix **D** which is inverted to compute a least-square estimate of the mode amplitudes both for tonal and broadband sound field.

10.1 Robust sensor array for accurate modal inversion

The influence of sensor positioning on inversion robustness and accuracy was investigated by means of computer simulations. Generally, this investigation showed that two essential requirements had to be satisfied in order to obtain a good estimate for the mode amplitudes:

1. The number of microphones used in the inversion is at least 1.3 the number of cut-on modes to be inverted
2. A uniform spreading of the microphones in both the azimuthal and polar directions

A sensor array geometry was designed from these requirements and was shown to couple best with the modal information radiated from the inlet. This array geometry, which resembles a geodesic sphere, is referred to as a 'Geodesic array' and has the fundamental property that each microphone occupies an equal surface area on the TCS. It was shown that the inversion performed by this array geometry leads to levels of solution errors that are of the same order of magnitude as the SNR acquired during the measurements. The reason for this has been explained.

10.2 Analysis of the modal inversion

An analytical study of the behaviour of the solution robustness was carried out. It showed that measurement noise affects strongly the solution at frequencies in the vicinity of the modal cut-on frequencies. At these frequencies, it was shown that the presence of nearly cut-off modes are responsible for large inaccuracies in the modal solution.

A physical interpretation of the SVD of the directivity matrix **D** was presented that enabled an understanding of the cause of the ill-conditioning at these frequencies. The SVD allowed the analysis of the modal radiation problem to be carried out into another set of basis functions. The singular values were interpreted as a measure of radiation efficiencies of the transformed modes and the singular vectors were found to determine the content of acoustic modes within these transformed modes. The efficiently radiating transformed modes associated with large singular values were found to contain well cut-on modes, while very inefficiently transformed modes associated with the smallest singular values contained nearly cut-off modes. The latter were shown to be responsible for large inaccuracies found in the solution. The SVD analysis also allowed the determination of the detection performance of the radiated sound field by a given sensor array, which may be of interest if one is to design an array to detect particular modes generated by a particular source mechanism in the engine inlet.

10.3 Robustness and accuracy improvement of the modal inversion

Methods for improving inversion robustness and accuracy were devised and investigated. They were shown to be effective when applied to geodesic sensor arrays at frequencies in the vicinity of the cut-on frequencies. It was found that regularisation was limited in enhancing the solution accuracy at the frequencies at which the inversion was already well-conditioned. The errors which resulted from the various constraints imposed on the solution were found to be greater than the minimisation of the errors due to the residuals. Consequently, the design of a geodesic array geometry offered the most efficient way to obtain the lowest overall solution inaccuracies. The additional constraints introduced by regularisation were found to have a considerable effect on the large inaccuracies found at the frequencies around the cut-on frequencies. It was shown that good reconstruction accuracy was achieved if the constraints were applied mainly to the nearly cut-off modes. The use of geodesic sensor arrays were found to allow accurate mode amplitude with a minimal amount of regularisation required.

10.4 Laboratory-scale fan inlet TCS measurements

The modal directivities of a laboratory-scale fan inlet were modelled using a FE/IE analysis, which included the lip effect. Although only small differences in magnitude and phase were introduced by the presence of the lip, the low values of condition number obtained with the geodesic sensor array remained unaltered between the cut-on frequencies. The experimental pressure measurements were conducted in nearly free field conditions on the laboratory-scale fan inlet using a hemispherical structure to mount the microphones. Broadband noise was measured and a cross-spectral matrix of pressure measurements was computed. The sound power radiated from the inlet comprised tones at multiples of the BPF. These tones occurring at the blade passing frequencies correspond to distortion tones with a significant bandwidth. The estimated mean square mode amplitudes were plotted against their cut-on ratio. The distribution of the mode amplitudes was found to closely follow a model in which there is equal energy per mode. The modal inversion from the geodesic sensor array was compared with the results from conventional spinning mode decomposition using a ring of in-duct microphones. Results for the spinning mode amplitudes were found to agree to within 6dB, with many of the modes found to agree to within 3dB or less. The inverse technique also allowed an estimate for the modal coherence function, which measures the level of statistical inter-dependence between any two modes. Small coherence functions were observed between most of the modes at most frequencies. The absence of modal cross coherence at the pseudo tones indicates that the sound field generated by the fan inlet is essentially broadband. To the author's knowledge, this information has not been possible before.

10.5 Future work

The inverse technique using phased array measurements in the near field, with microphones arranged in a geodesic geometry, has enabled a robust detection of mode amplitudes generated within the fan inlet with an accuracy of similar order to that of the measurement SNR level over a large band of frequencies. This measurement technique which allows for the first time an accurate estimate of broadband mode distribution, is a stepping-stone for a better understanding of source mechanisms of broadband fan noise and forms an essential tool in developing strategies to control the sound field radiating at the inlet of the engine.

However, there is significant scope for improving the accuracy of the technique. A forward problem which models the effects of realistic flows as well as the presence of liners within the inlet could be implemented. Such forward problem would increase the number of cut-on modes. The robustness and accuracy of the inverse problem will then have to be studied. The unique microphone spreading of geodesic sensor arrays allows good detection of complicated modal radiation patterns. Therefore, further investigation of other classes of geodesic geometry [27] could allow a better coupling of the TCS sensor array with the modal information radiated by the inlet with different flow and liner configurations.

A detailed investigation of the effects of the TCS structure on the sound field is also to be carried out. The diffraction effects of the steel bars from the laboratory-scale TCS rig would certainly need to be controlled by applying some absorbent material over the entire hemispherical surface.

Furthermore, the procedure detailed in this study is also to be validated against full-scale static engine tests. This would convince engine manufacturers to perform such type of measurements to gain some knowledge of the noise produced by their aircraft engines and hence develop new designs which would enable considerable reduction of noise emission.

Finally, other measurements using the TCS array in the near field could be performed such as beamforming for source localisation or near-field holography to determine quantitative aspects of the sources of sound at the inlet of the engine.

Appendix A

Far field analytical solution

Using the assumption of equation 2.2.16 and introducing equation 2.1.20 into equation 2.2.11, the far-field modal directivity factor can be approximated as

$$D_{mn}(r,\theta,\varphi) = \frac{jk\sqrt{1-\alpha_{mn}^2}}{\sqrt{\Lambda_{mn}}} \frac{e^{-j(k_{mnz}l+kr)}}{2\pi r} \int_S J_m(\kappa_{mn} r_s) e^{-jm\theta_s} e^{jkr_s \sin\varphi \cos(\theta_s-\theta)} dS \quad \text{(A.1)}$$

The integral term above is now to be solved

$$\int_0^a \int_0^{2\pi} J_m(\kappa_{mn} r_s) e^{-jm\theta_s} e^{jkr_s \sin\varphi \cos(\theta_s-\theta)} r_s dr_s d\theta_s \quad \text{(A.2)}$$

Consider first the integral with respect to θ_s.

$$\int_0^{2\pi} (\cos m\theta_s - j\sin m\theta_s) e^{jkr_s \sin\varphi \cos(\theta_s-\theta)} d\theta_s \quad \text{(A.3)}$$

First of all, it may be shown that the Bessel function can be written in power series for m as:

$$J_m(z) = \sum_{q=0}^{\infty} (-1)^q \frac{(\frac{1}{2}z)^{m+2q}}{q!(m+q)!} \quad \text{(A.4)}$$

and that

$$J_{-m}(z) = (-1)^m J_m(z) \quad \text{(A.5)}$$

If one considers the exponential term $e^{\frac{1}{2}z(t-1/t)} = e^{\frac{1}{2}zt}e^{-\frac{1}{2}z/t}$ and one expands it as

$$\left[1+\frac{1}{2}zt+\frac{1}{2!}(\frac{1}{2}zt)^2+\frac{1}{3!}(\frac{1}{2}zt)^3+...\right]\left[1-\frac{1}{2}z/t+\frac{1}{2!}(\frac{1}{2}z/t)^2-\frac{1}{3!}(\frac{1}{2}z/t)^3+...\right]$$

These two convergent series when multiplied to each other leads to terms involving t^0, t^1, t^2,...,t^n and t^{-1}, t^{-2},... t^{-n}.

If one considers only terms involving t^0 and t^1, one finds, respectively, the following

$$1-\frac{z^2}{2^2}+\frac{z^4}{2^4\cdot 2!\cdot 2!}-\frac{z^6}{2^6\cdot 3!\cdot 3!}+...$$
$$\frac{z}{2}-\frac{z^3}{2^3\cdot 2!}+\frac{z^5}{2^5\cdot 3!\cdot 2!}-...$$

and can be identified as the power series of equation A.4 namely $J_0(z)$ and $J_1(z)$. Generalising for all m, one finds $J_m(z)$ and $J_{-m}(z)$ are the coefficients of terms involving t^m and t^{-m}. Therefore,

$$e^{\frac{1}{2}}z(t-t^{-1}) = \sum_{m=-\infty}^{+\infty} t^m J_m(z) \tag{A.6}$$

If one writes in the above exponential index $t = e^{j\theta_s}$, one gets $e^{\frac{1}{2}z(e^{j\theta_s}-e^{-j\theta_s})} = e^{jz\sin\theta_s}$. Then from equation A.6

$$e^{jz\sin\theta_s} = J_0(z) + \left(J_1(z)e^{j\theta_s} + J_{-1}(z)e^{-j\theta_s}\right) + \left(J_2(z)e^{j2\theta_s} + J_{-2}(z)e^{-j2\theta_s}\right) + ...$$

and from using the property of equation A.5

$$e^{jz\sin\theta_s} = J_0(z) + 2\sum_{m=1}^{+\infty} J_{2m}(z)\cos 2m\theta_s + 2j\sum_{m=1}^{+\infty} J_{2m-1}(z)\sin(2m-1)\theta_s \tag{A.7}$$

If one substitutes θ_s by $\frac{\pi}{2}-\theta_s$ in equation A.7, then

$$\begin{aligned}
e^{jz\sin(\pi/2-\theta_s)} &= e^{jz\cos\theta_s}\\
&= J_0(z) + 2\sum_{m=1}^{+\infty}(-1)^m J_{2m}(z)\cos 2m\theta_s + 2j\sum_{m=1}^{+\infty}(-1)^{m+1}J_{2m-1}(z)\cos(2m-1)\theta_s\\
&= J_0(z) - 2\left(J_2(z)\cos 2\theta_s - J_4(z)\cos 4\theta_s + ...\right) + 2j\left(J_1(z)\cos\theta_s - J_3(z)\cos 3\theta_s + ...\right)\\
&= J_0(z) + 2\sum_{m=1}^{+\infty} j^m J_m(z)\cos m\theta_s
\end{aligned} \tag{A.8}$$

Thus the exponential term in equation A.3 can be expanded as in equation A.8 to give

$$e^{jkr_s\sin\varphi\cos(\theta_s-\theta)} = J_0(kr_s\sin\varphi) + 2\sum_{m=1}^{+\infty} j^m J_m(kr_s\sin\varphi)\cos m(\theta_s-\theta) \tag{A.9}$$

Introducing equation A.9 into equation A.3 leads to

$$\begin{aligned} &2\sum_{m=1}^{+\infty} j^m J_m(kr_s\sin\varphi)\left[\int_0^{2\pi}\cos m(\theta_s-\theta)\cos m\theta_s d\theta_s - j\int_0^{2\pi}\cos m(\theta_s-\theta)\sin m\theta_s d\theta_s\right] \\ &= \sum_{m=1}^{+\infty} j^m J_m(kr_s\sin\varphi)\left[\int_0^{2\pi}\cos 2m(\theta_s-\theta/2)d\theta_s + \int_0^{2\pi}\cos m\theta d\theta_s\right. \\ &\qquad\left. + j\int_0^{2\pi}\sin 2m(\theta_s-\theta/2)d\theta_s - j\int_0^{2\pi}\sin m\theta d\theta_s\right] \\ &= 2\pi\sum_{m=1}^{+\infty} j^m J_m(kr_s\sin\varphi)(\cos m\theta - j\sin m\theta) \\ &= 2\pi\sum_{m=1}^{+\infty} j^m J_m(kr_s\sin\varphi)e^{-jm\theta} \end{aligned} \tag{A.10}$$

Substituting equation A.10 into equation A.2 yields

$$2\pi j^m e^{-jm\theta_s}\int_0^a J_m(\kappa_{mn}r_s)J_m(kr_s\sin\varphi)r_s dr_s \tag{A.11}$$

The above Bessel functions $J_m(\kappa_{mn}r_s)$ and $J_m(kr_s\sin\varphi)$ are solutions of Bessel equations of the form

$$r_s^2\frac{\partial^2\phi_1(r_s)}{\partial r_s^2} + r\frac{\partial\phi_1(r_s)}{\partial r_s} + (\kappa_{mn}^2 - m^2)\phi_1(r_s) = 0 \tag{A.12}$$

$$r_s^2\frac{\partial^2\phi_2(r_s)}{\partial r_s^2} + r\frac{\partial\phi_2(r_s)}{\partial r_s} + (k^2\sin^2\varphi - m^2)\phi_2(r_s) = 0 \tag{A.13}$$

A.12$\cdot\frac{\phi_1}{r_s}$–A.13$\cdot\frac{\phi_2}{r_s}$ gives

$$\begin{aligned} r_s\phi_2(r_s)\frac{\partial^2\phi_2(r_s)}{\partial r_s^2} - r_s\phi_1(r_s)\frac{\partial^2\phi_1(r_s)}{\partial r_s^2} + \phi_2(r_s)\frac{\partial\phi_1(r_s)}{\partial r_s} - \phi_1(r_s)\frac{\partial\phi_2(r_s)}{\partial r_s} &= \\ (\kappa_{mn}^2 - (k\sin\varphi)^2)\phi_1(r_s)\phi_2(r_s)r_s& \\ \frac{\partial}{\partial r_s}\left[r_s\left(\phi_2(r_s)\frac{\partial\phi_1(r_s)}{\partial r_s} - \phi_1(r_s)\frac{\partial\phi_2(r_s)}{\partial r_s}\right)\right] &= \\ (\kappa_{mn}^2 - (k\sin\varphi)^2)\phi_1(r_s)\phi_2(r_s)r_s& \end{aligned} \tag{A.14}$$

As $\phi_1(r_s)$ and $\phi_2(r_s)$ are solutions of Bessel equations A.12 and A.13, they can be respectively written as $J_m(\kappa_{mn}r_s)$ and $J_m(kr_s\sin\varphi)$. Then integration of equation A.14 for all r_s leads to

$$\begin{aligned}&(\kappa_{mn}^2-(k\sin\varphi)^2)\int_0^a J_m(\kappa_{mn}r_s)J_m(kr_s\sin\varphi)r_s dr_s\\ &=a\left(J_m(ka\sin\varphi)\frac{\partial J_m(\kappa_{mn}a)}{\partial r_s}-J_m(\kappa_{mn}a)\frac{\partial J_m(ka\sin\varphi)}{\partial r_s}\right)\end{aligned}\tag{A.15}$$

Using the following recurrence formula

$$z\frac{\partial J_m(z)}{\partial z}=mJ_m(z)-zJ_{m+1}(z)\tag{A.16}$$

and equation A.15, equation A.11 can be rewritten

$$\begin{aligned}&2\pi j^m e^{-jm\theta}\frac{a}{\kappa_{mn}^2-(k\sin\varphi)^2}\big(\kappa_{mn}J_m(ka\sin\varphi)J_{m+1}(\kappa_{mn}a)\\ &\qquad-k\sin\varphi J_m(\kappa_{mn}a)J_{m+1}(ka\sin\varphi)\big)\end{aligned}\tag{A.17}$$

This result is only valid for $(\kappa_{mn})^2\neq(k\sin\varphi)^2$. When $(\kappa_{mn})^2=(k\sin\varphi)^2$, the integral term of equation A.11 becomes

$$\begin{aligned}&2\pi j^m e^{-jm\theta}\frac{a^2}{2}\left[J_m'^2(\kappa_{mn}a)+\left(1-\frac{m^2}{(\kappa_{mn}a)^2}\right)J_m^2(\kappa_{mn}a)\right]\\ &=2\pi j^m e^{-jm\theta}\frac{a^2}{2}\left[\frac{m}{\kappa_{mn}a}J_m(\kappa_{mn}a)-J_{m+1}(\kappa_{mn}a)+\left(1-\frac{m^2}{(\kappa_{mn}a)^2}\right)J_m^2(\kappa_{mn}a)\right]\\ &=2\pi j^m e^{-jm\theta}\frac{a^2}{2}\left[J_m^2(\kappa_{mn}a)-\frac{2m}{\kappa_{mn}a}J_m(\kappa_{mn}a)J_{m+1}(\kappa_{mn}a)+J_{m+1}^2(\kappa_{mn}a)\right]\end{aligned}\tag{A.18}$$

Introducing equation A.17 and equation A.18 into equation A.1 leads to the far-field pressure to be written as

- $\kappa_{mn}^2\neq(k\sin\varphi)^2$

$$\begin{aligned}D_{mn}(r,\theta,\varphi)=j^{m+1}\frac{k\sqrt{1-\alpha_{mn}^2}}{\sqrt{\Lambda_{mn}}}\frac{e^{-j(k_{mnz}l+kr)}}{r}e^{-jm\theta}\frac{a}{\kappa_{mn}^2-(k\sin\varphi)^2}\\ \left[\kappa_{mn}J_m(ka\sin\varphi)J_{m+1}(\kappa_{mn}a)-k\sin\varphi J_m(\kappa_{mn}a)J_{m+1}(ka\sin\varphi)\right]\end{aligned}\tag{A.19}$$

- $\kappa_{mn}^2 = (k\sin\varphi)^2$

$$D_{mn}(r,\theta,\varphi) = j^{m+1}\frac{k\sqrt{1-\alpha_{mn}^2}}{\sqrt{\Lambda_{mn}}}\frac{e^{-j(k_{mnz}l+kr)}}{r}e^{-jm\theta}\frac{a^2}{2}$$
$$\left[J_m^2(\kappa_{mn}a) - \frac{2m}{\kappa_{mn}a}J_m(\kappa_{mn}a)J_{m+1}(\kappa_{mn}a) + J_{m+1}^2(\kappa_{mn}a)\right] \tag{A.20}$$

Equation A.20 represents the analytic solution for directivity factor in the far field on the main radiation lobe. Elsewhere, the directivity factor is computed by equation A.19. Using the recursive relation in equation A.16 and the hard wall boundary condition of equation 2.1.14, equation A.19 may take a useful reduced form

$$D_{mn}(r,\theta,\varphi) = j^{m+1}\frac{\sqrt{1-\alpha_{mn}^2}}{\sqrt{\Lambda_{mn}}}\frac{e^{-j(k_{mnz}l+kr)}}{r}e^{-jm\theta}\frac{a\sin\varphi}{\alpha_{mn}^2-\sin^2\varphi}J_m(\kappa_{mn}a)J_m'(ka\sin\varphi) \tag{A.21}$$

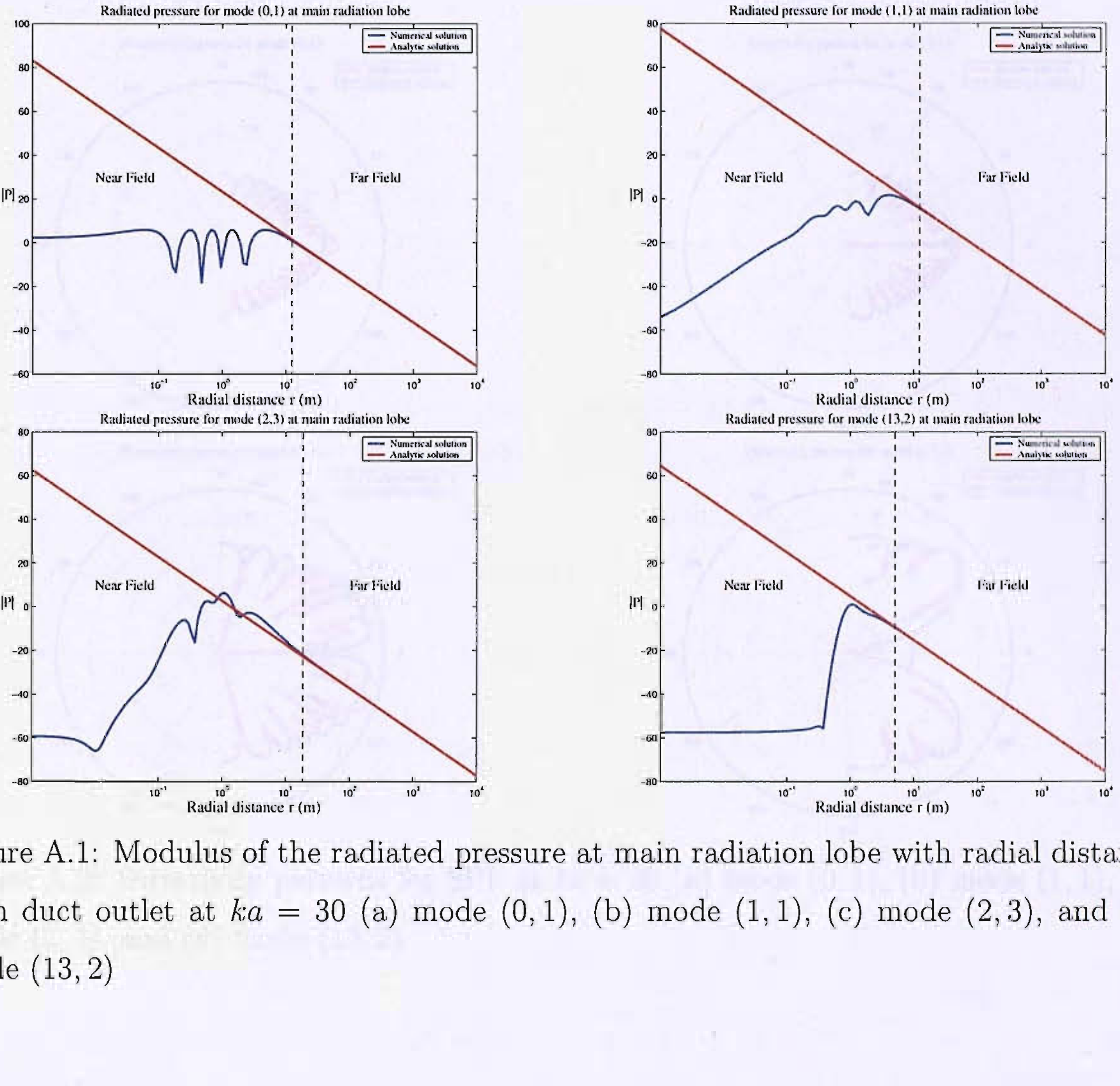

Figure A.1: Modulus of the radiated pressure at main radiation lobe with radial distance from duct outlet at $ka = 30$ (a) mode $(0, 1)$, (b) mode $(1, 1)$, (c) mode $(2, 3)$, and (d) mode $(13, 2)$

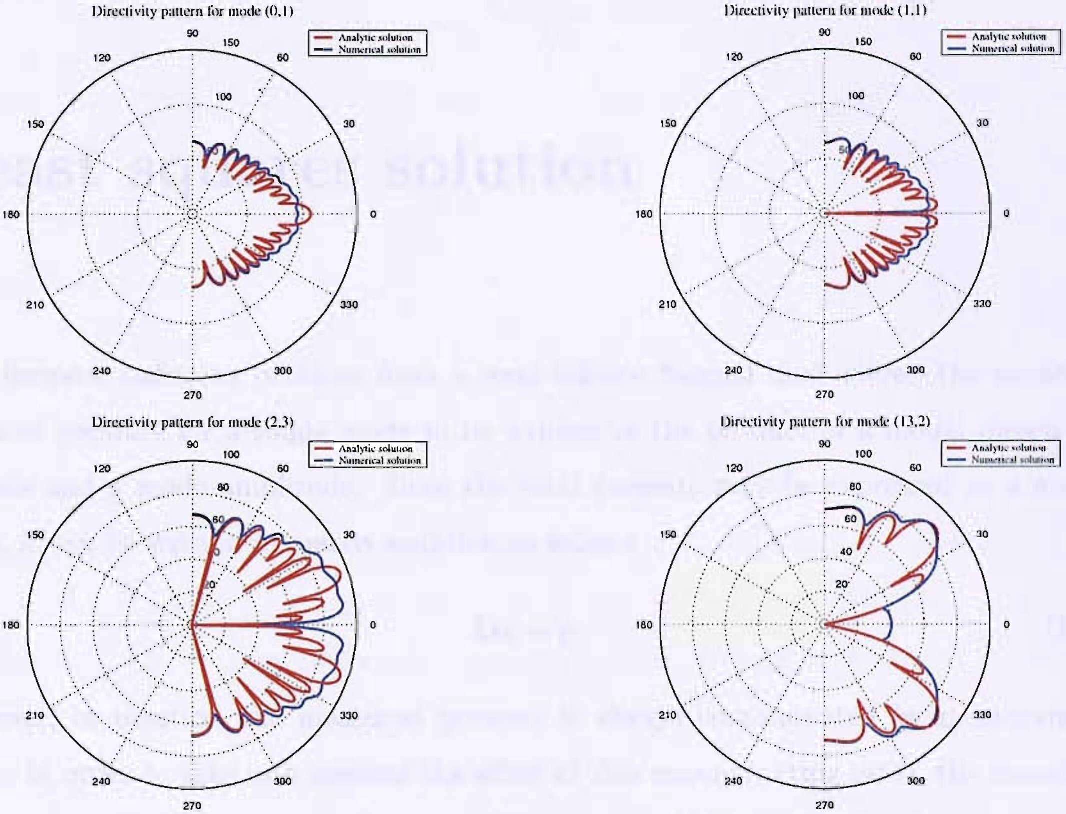

Figure A.2: Directivity patterns for SPL at $ka = 30$ (a) mode $(0, 1)$, (b) mode $(1, 1)$, (c) mode $(2, 3)$, and (d) mode $(13, 2)$

Appendix B

Least squares solution

The forward radiation problem from a semi-infinite flanged duct allows the modelled radiated pressure for a single mode to be written as the product of a modal directivity pattern and a mode amplitude. Since the total pressure may be expressed as a modal basis, it can be written in matrix notation as follows

$$\mathbf{D}\mathbf{a} = \mathbf{p} \tag{B.1}$$

However, in practice, the measured pressure is always contaminated by measurement noise. In order to take into account the effect of this contaminating noise, the measured pressure $\hat{\mathbf{p}}$ may be written as the sum of the modelled pressure vector $\mathbf{p}$ and an error vector $\mathbf{n}$

$$\hat{\mathbf{p}} = \mathbf{D}\mathbf{a} + \mathbf{n} \tag{B.2}$$

In this case the complex error vector can be written as

$$\mathbf{n} = \hat{\mathbf{p}} - \mathbf{p} = \hat{\mathbf{p}} - \mathbf{D}\mathbf{a} \tag{B.3}$$

In order to deduce the vector of mode amplitudes $\mathbf{a}$ that ensures the best fit of the modelled pressure field to the measured data, the minimisation of the sum of the squared errors ('residuals') between the measured sensor outputs and the model sensor outputs is required. This vector is called the least squares solution and satisfies

$$\min \|\hat{\mathbf{p}} - \mathbf{Da}\|_2^2 \tag{B.4}$$

which, equivalently may be written as

$$J = \sum_{k=1}^{K} |n_k(\omega)|^2 = \mathbf{n}^{\mathbf{H}}\mathbf{n} \tag{B.5}$$

In order to find the modal amplitude vector that minimises this cost function, the derivatives of the cost function with respect to each element of the modal amplitude vector are to be evaluated and to equal zero. Namely

$$\frac{\partial J}{\partial \mathbf{a}} = \left(\frac{\partial J}{\partial a_1}, \frac{\partial J}{\partial a_2}, \ldots, \frac{\partial J}{\partial a_L}\right)^T = 0 \tag{B.6}$$

Introducing equation B.3 into equation B.5 leads to

$$J = \mathbf{a}^{\mathbf{H}}\mathbf{D}^{\mathbf{H}}\mathbf{Da} - \hat{\mathbf{p}}^{\mathbf{H}}\mathbf{Da} - \mathbf{a}^{\mathbf{H}}\mathbf{D}^{\mathbf{H}}\hat{\mathbf{p}} + \hat{\mathbf{p}}^{\mathbf{H}}\hat{\mathbf{p}} \tag{B.7}$$

If one lets the matrix $\mathbf{G}$ be $\mathbf{D}^{\mathbf{H}}\mathbf{D}$ and Hermitian (must thus have real elements along its principal diagonal), the vector $\mathbf{b}$ be $-\mathbf{D}^{\mathbf{H}}\hat{\mathbf{p}}$ and the real scalar quantity c be $\hat{\mathbf{p}}^{\mathbf{H}}\hat{\mathbf{p}}$, equation B.7 can be identified as the general quadratic Hermitian form [46] defined as follows

$$J = \mathbf{a}^{\mathbf{H}}\mathbf{Ga} + \mathbf{a}^{\mathbf{H}}\mathbf{b} + \mathbf{b}^{\mathbf{H}}\mathbf{a} + c \tag{B.8}$$

Because of the Hermitian property of $\mathbf{G}$ (i.e. $\mathbf{G}^{\mathbf{H}} = \mathbf{G}$ or $\mathbf{G}^* = \mathbf{G}^{\mathbf{T}}$), the first term in equation B.8 can be shown to be equal to its complex conjugate as follows

$$\begin{aligned}
\mathbf{a}^{\mathbf{H}}\mathbf{Ga} &= \left(\mathbf{a}^{\mathbf{H}}\mathbf{Ga}\right)^{\mathbf{T}} \\
&= \mathbf{a}^{\mathbf{T}}\mathbf{G}^{\mathbf{T}}\mathbf{a}^* \\
&= \mathbf{a}^{\mathbf{T}}\mathbf{G}^*\mathbf{a}^* \\
&= \left(\mathbf{a}^{\mathbf{H}}\mathbf{Ga}\right)^*
\end{aligned}$$

and therefore to be a real scalar.

The third term in equation B.8 can be expressed as follows

$$\begin{aligned}\mathbf{b}^{\mathrm{H}}\mathbf{a} &= \left(\mathbf{b}^{\mathrm{H}}\mathbf{a}\right)^{\mathrm{T}} \\ &= \mathbf{a}^{\mathrm{T}}\mathbf{b}^{*} \\ &= \left(\mathbf{a}^{\mathrm{H}}\right)^{*}\mathbf{b}^{*} \\ &= \left[\mathbf{a}^{\mathrm{H}}\mathbf{b}\right]^{*}\end{aligned}$$

Thus, the second and third terms in equation B.8 sum to give a real scalar as

$$\mathbf{a}^{\mathrm{H}}\mathbf{b} + \mathbf{b}^{\mathrm{H}}\mathbf{a} = \mathbf{a}^{\mathrm{H}}\mathbf{b} + \left[\mathbf{a}^{\mathrm{H}}\mathbf{b}\right]^{*} \tag{B.9}$$

From this, one can see that the cost function to minimise is a real scalar which agrees with its definition (i.e. $\sum |\mathbf{e}|^2$).

The general Hermitian quadratic form may be expressed as a function of entirely real quantities by defining the real and imaginary parts of **a**, **G** and **b** such as

$$\mathbf{a} = \mathbf{a}_{\mathrm{r}} + \jmath\mathbf{a}_{\mathrm{i}} \qquad \mathbf{G} = \mathbf{G}_{\mathrm{r}} + \jmath\mathbf{G}_{\mathrm{i}} \qquad \mathbf{b} = \mathbf{b}_{\mathrm{r}} + \jmath\mathbf{b}_{\mathrm{i}} \tag{B.10}$$

Again since **G** is Hermitian, $\mathbf{G}_{\mathrm{r}} = \mathbf{G}_{\mathrm{r}}^{\mathrm{T}}$, $\mathbf{G}_{\mathrm{i}} = -\mathbf{G}_{\mathrm{i}}^{\mathrm{T}}$ and from equation B.9, the general Hermitian quadratic form can be expanded as

$$\begin{aligned}J &= \left(\mathbf{a}_{\mathrm{r}}^{\mathrm{T}} - \jmath\mathbf{a}_{\mathrm{i}}^{\mathrm{T}}\right)\left(\mathbf{G}_{\mathrm{r}}^{\mathrm{T}} + \jmath\mathbf{G}_{\mathrm{i}}^{\mathrm{T}}\right)\left(\mathbf{a}_{\mathrm{r}}^{\mathrm{T}} + \jmath\mathbf{a}_{\mathrm{i}}^{\mathrm{T}}\right) + 2\mathbf{a}_{\mathrm{r}}^{\mathrm{T}}\mathbf{b}_{\mathrm{r}} + 2\mathbf{a}_{\mathrm{i}}^{\mathrm{T}}\mathbf{b}_{\mathrm{i}} + c \\ &= \mathbf{a}_{\mathrm{r}}^{\mathrm{T}}\mathbf{G}_{\mathrm{r}}\mathbf{a}_{\mathrm{r}} - \jmath\mathbf{a}_{\mathrm{i}}^{\mathrm{T}}\mathbf{G}_{\mathrm{r}}\mathbf{a}_{\mathrm{r}} + \jmath\mathbf{a}_{\mathrm{r}}^{\mathrm{T}}\mathbf{G}_{\mathrm{r}}\mathbf{a}_{\mathrm{i}} + \mathbf{a}_{\mathrm{i}}^{\mathrm{T}}\mathbf{G}_{\mathrm{r}}\mathbf{a}_{\mathrm{i}} + \jmath\mathbf{a}_{\mathrm{r}}^{\mathrm{T}}\mathbf{G}_{\mathrm{i}}\mathbf{a}_{\mathrm{r}} + \mathbf{a}_{\mathrm{i}}^{\mathrm{T}}\mathbf{G}_{\mathrm{i}}\mathbf{a}_{\mathrm{r}} \\ &\quad - \mathbf{a}_{\mathrm{r}}^{\mathrm{T}}\mathbf{G}_{\mathrm{i}}\mathbf{a}_{\mathrm{i}} + \jmath\mathbf{a}_{\mathrm{i}}^{\mathrm{T}}\mathbf{G}_{\mathrm{i}}\mathbf{a}_{\mathrm{i}} + 2\mathbf{b}_{\mathrm{r}}^{\mathrm{T}}\mathbf{a}_{\mathrm{r}} + 2\mathbf{b}_{\mathrm{i}}^{\mathrm{T}}\mathbf{a}_{\mathrm{i}} + c \\ &= \mathbf{a}_{\mathrm{r}}^{\mathrm{T}}\mathbf{G}_{\mathrm{r}}\mathbf{a}_{\mathrm{r}} + \mathbf{a}_{\mathrm{i}}^{\mathrm{T}}\mathbf{G}_{\mathrm{r}}\mathbf{a}_{\mathrm{i}} - 2\mathbf{a}_{\mathrm{r}}^{\mathrm{T}}\mathbf{G}_{\mathrm{i}}\mathbf{a}_{\mathrm{i}} + 2\mathbf{b}_{\mathrm{r}}^{\mathrm{T}}\mathbf{a}_{\mathrm{r}} + 2\mathbf{b}_{\mathrm{i}}^{\mathrm{T}}\mathbf{a}_{\mathrm{i}} + c\end{aligned} \tag{B.11}$$

This real scalar quantity can now be differentiated with respect to each of the real and imaginary components of the modal amplitude vector **a**.

$$\begin{aligned}\frac{\partial J}{\partial \mathbf{a}_{\mathrm{r}}} &= \left(\frac{\partial J}{\partial a_{r1}}, \frac{\partial J}{\partial a_{r2}}, \ldots, \frac{\partial J}{\partial a_{rL}}\right)^{T} \\ \frac{\partial J}{\partial \mathbf{a}_{\mathrm{i}}} &= \left(\frac{\partial J}{\partial a_{i1}}, \frac{\partial J}{\partial a_{i2}}, \ldots, \frac{\partial J}{\partial a_{iL}}\right)^{T}\end{aligned}$$

Using two properties of such derivatives for entirely real $\mathbf{x}$, $\mathbf{y}$ and real symmetric $\mathbf{B}$ [25]

$$\frac{\partial\left(\mathbf{y}^T\mathbf{x}\right)}{\partial\mathbf{x}}=\mathbf{y} \qquad \frac{\partial\left(\mathbf{x}^T\mathbf{B}\mathbf{x}\right)}{\partial\mathbf{x}}=\left(\mathbf{B}+\mathbf{B}^{\mathbf{T}}\right)\mathbf{x}=2\mathbf{B}\mathbf{x} \tag{B.12}$$

the cost function may be differentiated with respect to the real and imaginary parts of $\mathbf{a}$ to give

$$\frac{\partial J}{\partial\mathbf{a_r}}=2\mathbf{G_r}\mathbf{a_r}-2\mathbf{G_i}\mathbf{a_i}+2\mathbf{b_r} \tag{B.13}$$

$$\frac{\partial J}{\partial\mathbf{a_i}}=2\mathbf{G_r}\mathbf{a_i}+2\mathbf{G_i}\mathbf{a_r}+2\mathbf{b_i} \tag{B.14}$$

A complex gradient vector $\mathbf{w}$ is now defined by the following equation

$$\mathbf{w}=\frac{\partial J}{\partial\mathbf{a_r}}+j\frac{\partial J}{\partial\mathbf{a_i}} \tag{B.15}$$

Using equations B.13 and B.14, the complex gradient vector $\mathbf{w}$ can be written

$$\begin{aligned}\mathbf{w}&=2\left(\mathbf{G_r}\mathbf{a_r}-\mathbf{G_i}\mathbf{a_i}\right)+2j\left(\mathbf{G_r}\mathbf{a_i}+\mathbf{G_i}\mathbf{a_r}\right)+2\left(\mathbf{b_r}+j\mathbf{b_i}\right)\\ \mathbf{w}&=2\left(\mathbf{G}\mathbf{a}+\mathbf{b}\right)\end{aligned} \tag{B.16}$$

If $\mathbf{G}$ is positive definite (i.e. $\mathbf{a^H}\mathbf{G}\mathbf{a}>0$), the cost function J will have a unique global minimum when the complex gradient vector $\mathbf{w}$ is set to zero

$$\mathbf{G}\mathbf{a_0}+\mathbf{b}=\mathbf{0} \tag{B.17}$$

leading to

$$\mathbf{a_0}=-\mathbf{G}^{-1}\mathbf{b} \tag{B.18}$$

Substituting expressions for $\mathbf{G}$ and $\mathbf{b}$ into equation B.18, the optimal estimate of the modal amplitude vector that minimises this cost function is found to be

$$\begin{aligned}\mathbf{a_0}&=\left[\mathbf{D^H}\mathbf{D}\right]^{-1}\mathbf{D^H}\hat{\mathbf{p}}\\ &=\mathbf{D}^{+}\hat{\mathbf{p}}\end{aligned} \tag{B.19}$$

where $\mathbf{D}^{+}$ is the pseudo-inverse of the directivity matrix $\mathbf{D}$.

Appendix C

The condition number

From the definition of the 2-norm matrix

$$\|\mathbf{D}\|_2 = \max \|\mathbf{Du}\|_2 \tag{C.1}$$

where $\mathbf{u}$ is any vector of unit 2-norm (i.e. $\|\mathbf{u}\|_2 = 1$). The square of the 2-norm above can be written in terms of the dot product

$$\|\mathbf{Du}\|_2^2 = (\mathbf{Du})^{\mathbf{H}} \mathbf{Du} = \mathbf{u}^{\mathbf{H}}\mathbf{D}^{\mathbf{H}}\mathbf{Du} \tag{C.2}$$

Thus

$$\|\mathbf{D}\|_2 = \max \left(\mathbf{u}^{\mathbf{H}}\mathbf{D}^{\mathbf{H}}\mathbf{Du}\right)^{1/2} \tag{C.3}$$

Consider the function $h(\mathbf{u}) = \mathbf{u}^{\mathbf{H}}\mathbf{D}^{\mathbf{H}}\mathbf{Du} - \lambda\mathbf{u}^{\mathbf{H}}\mathbf{u}$ for any real scalar λ. The expression $\mathbf{u}^{\mathbf{H}}\mathbf{D}^{\mathbf{H}}\mathbf{Du}$ is maximised, as required by equation C.3, when the differential of h with respect to $\mathbf{u}$ equals zero, i.e.

$$\frac{\partial h}{\partial \mathbf{u}} = 2\left(\mathbf{D}^{\mathbf{H}}\mathbf{D}\right)\mathbf{u} - \mathbf{2}\lambda\mathbf{u} = 0 \tag{C.4}$$

which leads to

$$\left(\mathbf{D}^{\mathbf{H}}\mathbf{D} - \lambda\mathbf{I}\right)\mathbf{u} = 0 \tag{C.5}$$

Equation C.5 can be identified as the eigenvalue problem equation. Therefore, the λ's are the eigenvalues of the symmetric matrix $\mathbf{D^H D}$, which is the matrix appearing in the least square solution 3.1.9.

It therefore follows that

$$\|\mathbf{D}\|_2 = \max \|\mathbf{Du}\|_2 = \max \left(\mathbf{u^H D^H D u}\right)^{1/2} = \sqrt{\lambda_{\max}} \tag{C.6}$$

where λ_{max} is the maximum eigenvalue of the matrix $\mathbf{D^H D}$.

Since it was shown in section 4 that the singular values σ of the modal directivity matrix $\mathbf{D}$ are the square root of the eigenvalues λ of $\mathbf{D^H D}$ (i.e. see equation 4.1.4),

$$\|\mathbf{D}\|_2 = \sigma_{\max} \tag{C.7}$$

Similarly it may be shown that

$$\left\|\mathbf{D}^{+}\right\|_2 = \frac{1}{\sigma_{\min}} \tag{C.8}$$

where σ_{max} and σ_{min} are the maximum and minimum singular values of the matrix $\mathbf{D}$ respectively. Introducing equations C.7 and C.8 into equation 3.3.1 enables the condition number of the directivity matrix to be expressed in terms of its maximum and minimum singular values as

$$\kappa\left(\mathbf{D}\right) = \frac{\sigma_{\max}}{\sigma_{\min}} \tag{C.9}$$

Appendix D

Asymptotic behaviour of the condition number for the inversion of 3 modes by 3 microphones at a cut-on frequency

Consider the inversion of three modes by three microphones with at least the pair of least cut-on modes at a cut-on frequency. These least cut-on modes have a cut-on ratio $\alpha_1 = \alpha_2 = \alpha_0 \approx 1$. For this problem the directivity matrix **D** is then given by

$$\begin{bmatrix} \sqrt{1-\alpha_0^2}F_{11} & \sqrt{1-\alpha_0^2}F_{12} & F_{13} \\ \sqrt{1-\alpha_0^2}F_{21} & \sqrt{1-\alpha_0^2}F_{22} & F_{23} \\ \sqrt{1-\alpha_0^2}F_{31} & \sqrt{1-\alpha_0^2}F_{32} & F_{33} \end{bmatrix} \tag{D.1}$$

where F_{ij} is a factor which is written from equations 4.3.2 and 4.3.3 for the mode j at microphone i.

If these factors are combined as the following

- $H_1 = F_{11}^2 + F_{21}^2 + F_{31}^2$
- $H_2 = F_{12}^2 + F_{22}^2 + F_{32}^2$
- $H_3 = F_{13}^2 + F_{23}^2 + F_{33}^2$
- $H_4 = F_{11}^* F_{12} + F_{21}^* F_{22} + F_{31}^* F_{32}$
- $H_4 = F_{11}^* F_{13} + F_{21}^* F_{23} + F_{31}^* F_{33}$
- $H_4 = F_{12}^* F_{13} + F_{22}^* F_{23} + F_{32}^* F_{33}$

and one lets $\gamma_0 = \sqrt{1 - \alpha_0^2}$, the matrix $\mathbf{G}$ defined by equation 4.3.6 is now written as

$$\begin{bmatrix} \gamma_0^2 H_1 & \gamma_0^2 H_4 & \gamma_0 H_5 \\ \gamma_0^2 H_4^* & \gamma_0^2 H_2 & \gamma_0 H_6 \\ \gamma_0 H_5^* & \gamma_0 H_6^* & H_3 \end{bmatrix} \tag{D.2}$$

The eigenvalues of this matrix are found from equation 4.3.7, namely

$$\det\left(\mathbf{G} - \lambda \mathbf{I}\right) = 0 \tag{D.3}$$

which leads to the following cubic characteristic equation

$$\lambda^3 - \left(H_3 + \gamma_0^2 K_1\right)\lambda^2 - \left(\gamma_0^4 K_2 + \gamma_0^2 K_3\right)\lambda - \gamma_0^4 K_4 = 0 \tag{D.4}$$

where

- $K_1 = H_1 + H_2$
- $K_2 = H_4^2 - H_1 H_2$
- $K_3 = H_5^2 + H_6^2 - H_1 H_3 - H_2 H_3$
- $K_4 = H_1 H_2 H_3 + H_4^* H_5 H_6 + H_4 H_5^* H_6 - H_1 H_6^2 - H_2 H_5^2 - H_3 H_4^2$

are factors that are independent of γ_0. In order to study how the behaviour of the condition number is influenced by the pair of least cut-on modes it is necessary to find an approximate solution for the eigenvalues when $\alpha_0 \mapsto 1$ or consequently when $\gamma_0 \mapsto 0$. It is therefore necessary to expand the solution of equation D.4 in to a regular series in γ_0

$$\lambda = \lambda_0 + \lambda_1 \gamma_0^2 + \lambda_2 \gamma_0^4 + \cdots \tag{D.5}$$

Introducing equation D.5 into equation D.4 and solving for the terms of order $O\left(\gamma_0^0\right)$ yields

$$\lambda_0^2 \left(\lambda_0 - H_3\right) = 0 \tag{D.6}$$

The coefficients of order $O\left(\gamma_0^0\right)$ for the three eigenvalues are

$$\lambda_0 = 0,\ 0,\ H_3 \tag{D.7}$$

Equation D.4 is now solved for the terms of order $O\left(\gamma_0^2\right)$

$$\left(3\lambda_0^2 - 2\lambda_0 H_3\right)\lambda_1 - \lambda_0\left(K_1\lambda_0 + K_3\right) = 0 \tag{D.8}$$

The coefficients of order $O\left(\gamma_0^2\right)$ for the three eigenvalues are given by

$$\lambda_1 = \frac{K_1\lambda_0 + K_3}{3\lambda_0 - 2H_3} \tag{D.9}$$

The maximum and minimum eigenvalues on second order approximation (i.e. $O\left(\gamma_0^2\right)$) are found to be respectively

$$\begin{aligned} \lambda_{\max} &= H_3 + \frac{K_1 H_3 + K_3}{H_3}\gamma_0^2 \\ \lambda_{\min} &= -\frac{K_1}{2H_3} \end{aligned} \tag{D.10}$$

When $\gamma_0 \mapsto 0$, one can deduce from the above equation

$$\frac{\lambda_{\max}}{\lambda_{\min}} \approx -\frac{2H_3^2}{K_1\gamma_0^2} + O\left(1\right) \tag{D.11}$$

Therefore the behaviour of the condition number of the directivity matrix at cut-on frequencies is given by

$$\kappa\left(\mathbf{D}\right) \mapsto \frac{1}{\sqrt{1-\alpha_0^2}} \tag{D.12}$$

Appendix E

Inversion robustness and accuracy for random sensor arrays

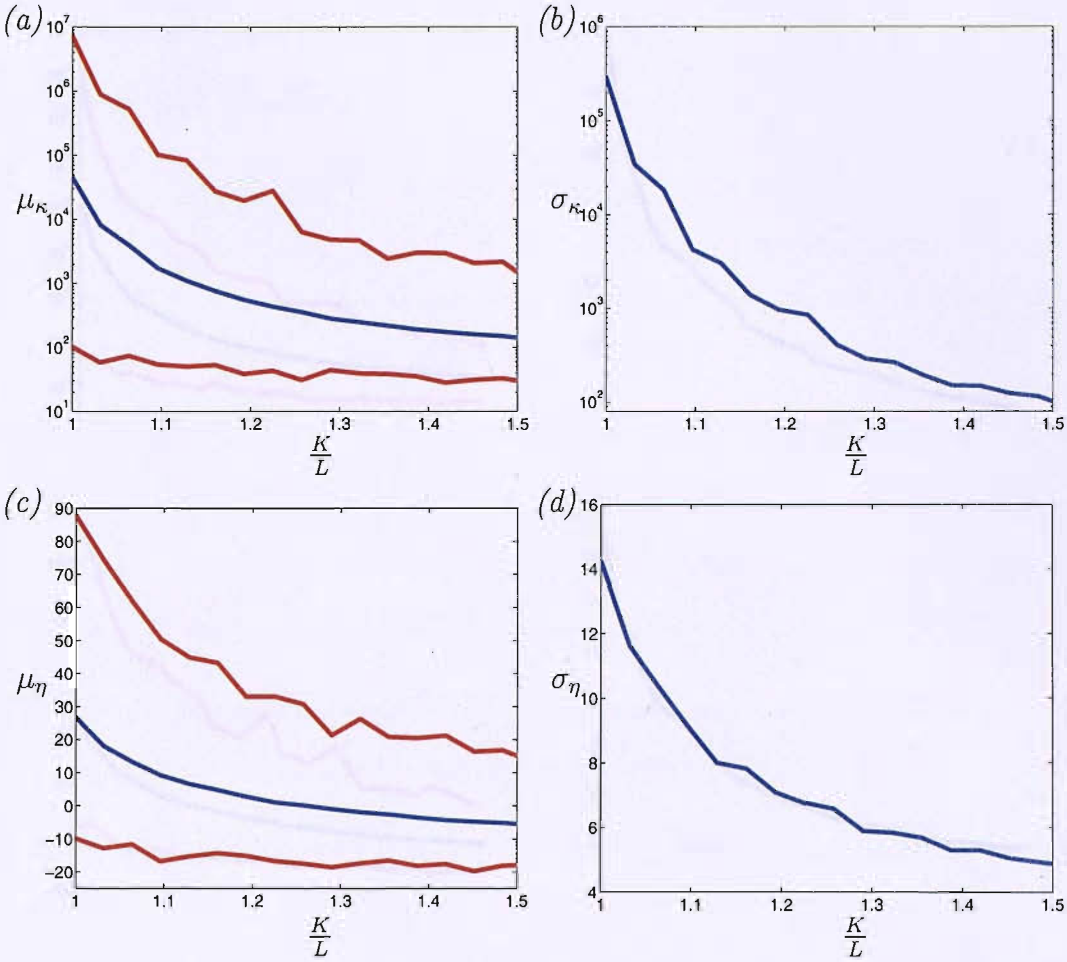

Figure E.1: (*a*) Mean value and (*b*) standard deviation of $\kappa(\mathbf{D})$, (*c*) Mean value and (*d*) standard deviation η at $ka = 10$ of 2000 randomly distributed sensor arrays —— gives the minimum and maximum values of μ_κ and μ_η

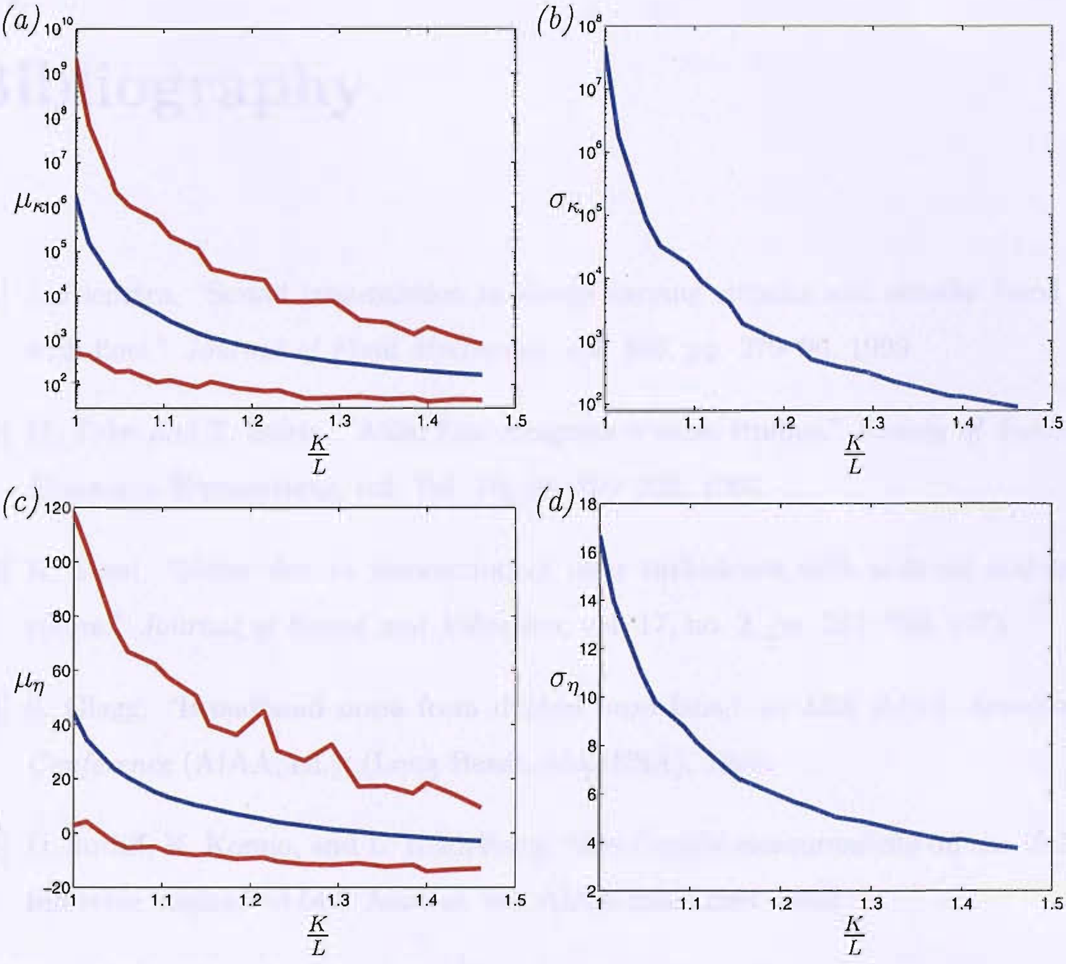

Figure E.2: (*a*) Mean value and (*b*) standard deviation of $\kappa(\mathbf{D})$, (*c*) Mean value and (*d*) standard deviation η at $ka = 15$ of 2000 randomly distributed sensor arrays —— gives the minimum and maximum values of μ_κ and μ_η

Bibliography

[1] S. Rienstra, "Sound transmission in slowly varying circular and annular lined ducts with flow," *Journal of Fluid Mechanics*, vol. 380, pp. 279–96, 1999.

[2] M. Tyler and T. Sofrin, "Axial flow compressor noise studies," *Society of Automotive Engineers Transactions*, vol. Vol. 70, pp. 309–332, 1962.

[3] R. Mani, "Noise due to interaction of inlet turbulence with isolated stators and rotors," *Journal of Sound and Vibration*, vol. 17, no. 2, pp. 251–260, 1971.

[4] S. Glegg, "Broadband noise from ducted prop fans," in *15th AIAA Aeroacoustics Conference* (AIAA, ed.), (Long Beach, CA, USA), 1993.

[5] D. Sutliff, K. Konno, and L. Heidelberg, "Duct mode measurements on the tfe731-60 full scale engine," *AIAA Journal*, vol. AIAA 2002-2564, 2002.

[6] D. Hall, L. Heidelberg, and K. Konno, "Acoustic mode measurements in the inlet of a model turbofan using a continuously rotating rake: data collections/analysis techniques," 1993.

[7] R. Thomas, F. Farassat, L. Clark, C. Gerhold, J. Kelly, and L. Becker, "A mode detection using the azimuthal directivity of a turbofan model," in *5th AIAA/CEAS Aeroacoutics Conference*, (Bellevue, WA, USA), 1999.

[8] F. Farassat, D. Nark, and H. Russel, "The detection of radiated modes from ducted fan engine," in *7th AIAA/CEAS Aeroacoustics Conference*, (Maastricht, The Netherlands), 2001.

[9] S. Lewy, "Inverse method predicting spinning modes radiated by a ducted fan from free-field measurements," *Journal of the Acoustical Society of America*, vol. 117, no. 2, pp. 744–50, 2005.

[10] C. Bewick, M. Adams, P. Schwaller, , and L. Xu, "Noise and aerodynamic design and test of a low tip speed fan," in *7th AIAA/CEAS Aeroacoustics Conference*, (Maastricht, The Netherlands), pp. AIAA Paper 2001–2268, 2001.

[11] J. Lan, J. Premo, and D. Sutliff, "Inlet mode measurements with an inflow control device microphone array," in *8th AIAA/CEAS Aeroacoustics Conference*, (Breckenridge, CO, USA), 2002.

[12] L. Enghardt, L. Neuhaus, and C. Lowis, "Broadband sound power determination in flow ducts," in *AIAA/CEAS Aeroacoustics Conference*, (Monterey, CA, USA), 2004.

[13] F. Farassat and M. Myers, "A study of wave propagation in a duct and mode radiation," in *American Institute of Aeronautical and Astronautics*, vol. 2nd AIAA/CEAS Aeroacoustics Conference, 1996.

[14] G. Borgiotti, "The power radiated by a vibrating body in an acoustic fluid and its determination from boundary measurements," *Journal of Acoustical Society of America*, vol. Vol.88, pp. 1884–1893, 1990.

[15] G. Borgiotti and E. Rosen, "The determination of the far field of an acoustic radiator from sparse measurement samples in the near field," *Journal of the Acoustical Society of America*, vol. 92, no. 2, pt.1, pp. 807–18, 1992.

[16] G. Borgiotti and K. Jones, "The determination of the acoustic far field of a radiating body in an acoustic fluid from boundary measurements," *Journal of the Acoustical Society of America*, vol. 93, no. 5, pp. 2788–97, 1993.

[17] M. Currey and K. Cunefare, "The radiation modes of baffled finite plates," *Journal of the Acoustical Society of America*, vol. 98, no. 3, pp. 1570–80, 1995.

[18] P. Nelson and S. Yoon, "Estimation of acoustic source strength by inverse methods: Part i, conditioning of the inverse problem," *Journal of Sound and Vibration*, vol. 233, no. 4, pp. 643–668, 2000.

[19] E. Williams, B. Houston, and P. Herdic, "Fast fourier transform and singular value decomposition formulations for patch nearfield acoustical holography," *Journal of the Acoustical Society of America*, vol. 114, no. 3, pp. 1322–33, 2003.

[20] C. Morfey, "A note on the radiation efficiency of acoustic duct modes," *Journal of Sound and Vibration*, vol. 9, pp. 367–372, 1969.

[21] M. Goldstein, *Aeroacoustics.* McGraw-Hill, 1976.

[22] M. Abramowitz and I. Stegun, *Handbook of mathematical functions.* Dover Publications, 1972.

[23] N. McLachlan, *Bessel functions for engineers.* Oxford engineering science series, Clarendon P, 2nd ed ed., 1955.

[24] C. Groetsch, *The theory of tikhonov regularization for fredholm equations of the first kind.* Research Notes in Mathematics 105, Pitman, Boston, 1984.

[25] G. Golub and C. Van Loan, *Matrix computations.* Oxford: North Oxford Academic, 1983.

[26] B. Fuller, "The age of the dome," *BUILD INTERNATIONAL*, vol. 2, no. 6, pp. 7–15, July/August 1969.

[27] H. Kenner, *Geodesic math and how to use it.* University of California Press, 1976.

[28] C. Hansen, "Rank-deficient and discrete ill-posed problems," SIAM Monographs on Mathematical Modeling and Computation, p. 243, 1998.

[29] F. Bromwell, "Extended asymptotic eigenvalue distributions for bounded domains in n-space," *Journal of Mathematics and Mechanics*, vol. 6, pp. 119–166, 1957.

[30] W. Veronesi and J. Maynard, "Digital holographic reconstruction of sources with arbitrarily shaped surfaces," *Journal of the Acoustical Society of America*, vol. 85, no. 2, pp. 588–98, 1989.

[31] C. Hansen, "Perturbations bounds for discrete tikhonov regularization," *Inverse Problems*, vol. 5, pp. L42–L44, 1989.

[32] C. Hansen, "Regularization, gsvd and truncated gsvd," *BIT*, vol. 29, pp. 491–504, 1989.

[33] E. Schock, "What are the proper condition numbers of discretized ill-posed problems?," *Linear Algebra and its Application*, vol. 81, pp. 129–136, 1986.

[34] F. Ihlenburg and G. Lloyd, *Finite Element Analysis Of Wave Propagation And Scattering: With Applications To Accoustic Fluid-Structure Interaction.* Applied Mathematical Sciences, Springer-Verlag New York Inc, 1998.

[35] K. Gerdes and F. Ihlenburg, "On the pollution effect in finite-element solutions of the helmholtz equation in three dimensions," *Computer Methods in Applied Mechanics and Engineering*, vol. 170, pp. 155–172, 1999.

[36] O. Zienkiewicz, *The Finite Element Method : Basic Formulation and Linear Problems.* 4th edition, McGraw-Hill College, 1985.

[37] E. Rice and M. Heidmann, "Modal propagation angles in a cylindrical duct with flow and their relation to sound radiation," in *17th Aerospace Sciences meeting*, (New Orleans, LA, USA), AIAA, 1979.

[38] A. Oppenheim, R. Schafer, and J. with Buck, *Discrete-Time Signal Processing.* Upper Saddle River, NJ: Prentice-Hall, Inc., 2nd ed., 1999.

[39] G. Jenkins and D. Watts, *Spectral Analysis and Its Applications.* 1698.

[40] P. Welch, "The use of fast fourier transform for the estimation of power spectra: A method based on time averaging over short, modified periodograms," *IEEE Trans. Audio Electroacoustics*, vol. AU-15, pp. 70–73, 1967.

[41] P. Joseph, C. Morfey, and C. Lowis, "Multi-mode sound transmission in ducts with flow," *Journal of Sound and Vibration*, vol. 264, pp. 523–544, 2003.

[42] U. Ganz, P. Joppa, T. Patten, and D. Scharpf, "Beoing 18-inch fan rig broadband noise test," Tech. Rep. NASA / CR - 1998 - 208704, Boeing Commercial Airplane Group, 1998.

[43] Y. Kim and P. Nelson, "Spatial resolution limits for the reconstruction of acoustic source strength by inverse methods," *Journal of Sound and Vibration*, vol. 265, no. 3, pp. 583–608, 2003.

[44] E. Williams, *Fourier acoustics, sound radiation and nearfield acoustical holography.* San Diego: Academic, 1999.

[45] A. Oppenheim, G. Frisk, and D. Martinez, "Computation of the hankel transform using projections," *Journal of the Acoustical Society of America*, vol. 68, no. 2, pp. 523–529, 1980.

[46] P. Nelson and S. Elliott, *Active control of sound.* London: Academic Press, 1992.